

## ABSTRACT

Title of dissertation: An Astrometric Analysis of  $\eta$  Carinae's Eruptive History Using HST WF/PC2 and ACS Observations

Bryan N. Dorland, Doctor of Philosophy, 2007

Dissertation directed by: Professor Doug Currie  
Department of Physics

$\eta$  Carinae is one of the most massive and enigmatic stars in our galaxy. The star, estimated to be well over a hundred times more massive and millions of times brighter than our sun, is shrouded in an expanding cloud of gas and debris that was ejected around 1843 during its so-called "Great Eruption" and surrounded by what appear to be fields of debris from previous eruptions.

The fundamental nature of the star is not well understood. Quite basic questions remain, such as: is the star a binary? Various questions and disagreements are also present in the literature regarding the various debris features, their physical characteristics, and what they tell us about the star's history.

In this dissertation, Hubble Space Telescope (HST) observations spanning nearly a decade and utilizing both the Wide Field/Planetary Camera 2 (WFPC2) and the Advanced Camera for Surveys (ACS) instruments—the most accurate visible imaging data yet taken of  $\eta$  Carinae—are used to address many of these fundamental issues. In the first section, HST/ACS data taken during 2003–2005 is used

<b>Report Documentation Page</b>			<i>Form Approved OMB No. 0704-0188</i>	
<p>Public reporting burden for the collection of information is estimated to average 1 hour per response, including the time for reviewing instructions, searching existing data sources, gathering and maintaining the data needed, and completing and reviewing the collection of information. Send comments regarding this burden estimate or any other aspect of this collection of information, including suggestions for reducing this burden, to Washington Headquarters Services, Directorate for Information Operations and Reports, 1215 Jefferson Davis Highway, Suite 1204, Arlington VA 22202-4302. Respondents should be aware that notwithstanding any other provision of law, no person shall be subject to a penalty for failing to comply with a collection of information if it does not display a currently valid OMB control number.</p>				
1. REPORT DATE <b>2007</b>	2. REPORT TYPE	3. DATES COVERED <b>00-00-2007 to 00-00-2007</b>		
<b>4. TITLE AND SUBTITLE</b> <b>An Astrometric Analysis of n Carinae's Eruptive History Using HST WF/PC2 and ACS Observations</b>			5a. CONTRACT NUMBER	
			5b. GRANT NUMBER	
			5c. PROGRAM ELEMENT NUMBER	
<b>6. AUTHOR(S)</b>			5d. PROJECT NUMBER	
			5e. TASK NUMBER	
			5f. WORK UNIT NUMBER	
<b>7. PERFORMING ORGANIZATION NAME(S) AND ADDRESS(ES)</b> <b>U.S. Naval Observatory, Dr. Bryan Dorland, Chief, Astrometric Satellite Division, Washington, DC, 20392</b>			8. PERFORMING ORGANIZATION REPORT NUMBER	
<b>9. SPONSORING/MONITORING AGENCY NAME(S) AND ADDRESS(ES)</b>			10. SPONSOR/MONITOR'S ACRONYM(S)	
			11. SPONSOR/MONITOR'S REPORT NUMBER(S)	
<b>12. DISTRIBUTION/AVAILABILITY STATEMENT</b> <b>Approved for public release; distribution unlimited</b>				
<b>13. SUPPLEMENTARY NOTES</b>				
<b>14. ABSTRACT</b>				
<b>15. SUBJECT TERMS</b>				
<b>16. SECURITY CLASSIFICATION OF:</b>			<b>17. LIMITATION OF ABSTRACT</b> <b>Same as Report (SAR)</b>	<b>18. NUMBER OF PAGES</b> <b>269</b>
<b>a. REPORT</b> <b>unclassified</b>	<b>b. ABSTRACT</b> <b>unclassified</b>	<b>c. THIS PAGE</b> <b>unclassified</b>		
<b>19a. NAME OF RESPONSIBLE PERSON</b>				

to address the question of binarity. Based on an astrometric analysis of the data, binary reflex motion is detected in the primary and, by combining these results with those of other authors, allows us to derive the physical parameters of the resultant system.

In the second section, 1995 WFPC2 and 2003 ACS data are used to make the most precise measurements yet of the debris around the central star. A date of origin is derived for the Homunculus, and a new, much shorter interval for the duration of the Great Eruption. Certain equatorial features, previously associated with an 1890 eruptive event are instead shown to be coeval with the Homunculus features and are thus associated with the Great Eruption. New debris associations outside the Homunculus are identified and their dates of origin are determined, implying eruptive events that preceeded the Great Eruption.

These results add both significant new insight into our understanding of  $\eta$  Carinae and its history and introduce important new constraints for any theoretician who seeks to model the star, the Great Eruption, or earlier events.

An Astrometric Analysis of  $\eta$  Carinae's Eruptive History Using HST  
WF/PC2 and ACS Observations

by

Bryan N. Dorland

Dissertation submitted to the Faculty of the Graduate School of the  
University of Maryland, College Park in partial fulfillment  
of the requirements for the degree of  
Doctor of Philosophy  
2007

Advisory Committee:

Professor Doug G. Currie, Chair/Thesis Advisor  
Professor Jean-Paul J. E. Richard  
Professor Jordan Goodman  
Professor Philip Roos  
Professor Michael A'Hearn

© Copyright by  
Bryan N. Dorland  
2007

## DEDICATION

I would like to dedicate this dissertation to my family, especially my wife Lorna and my children Natalya, Ciaran, and Emma. To my wife, I say thank you for all your understanding and help in achieving this lifelong goal; to my children, a bit of advice: don't ever let anyone convince you not to strive for *your* goals. I apologize for all the time I missed while trying to work on this; hopefully, you won't regret it if I am around more after this is completed.

I would also like to dedicate this to my mother and father who gave me everything I needed and everything they could, each differently and according to their own interests and abilities. Finally, I would also like to dedicate this to my Aunt Eileen, who spent many a night with me both as a little boy and as an adult looking at the stars. The *only* drawback to sitting in a field in rural Maine looking at the stars is that you can't see  $\eta$  Car<sup>1</sup>. Of course, I love all of you.

---

<sup>1</sup>On second thought, perhaps the thick clouds of mosquitoes also fall into this category.

## ACKNOWLEDGMENTS

Some of the data presented in this thesis were obtained from the Multimission Archive at the Space Telescope Science Institute (MAST). STScI is operated by the Association of Universities for Research in Astronomy, Inc., under NASA contract NAS5-26555. Support for MAST for non-HST data is provided by the NASA Office of Space Science via grant NAG5-7584 and by other grants and contracts.

I would like to acknowledge Warren Hack and Max Mutchler at the Space Telescope Science Institute (STScI) for help in using the STSDAS analysis package with both HST/WFPC2 data and ACS/HRC data. I would like to acknowledge Jay Anderson of Rice University for helpful discussions on HRC astrometry and access to his software package for distortion correction.

I would like to acknowledge the assistance of David Frew, who provided electronic versions of his tables describing the photometric history of  $\eta$  Carinae.

Some images used in this thesis were obtained from external sources. In all cases, these sources have been cited and are used in accordance with the Fair Use right as set forth in §107 of the United States Copyright Act.

I would like to thank the U. S. Naval Observatory, specifically Drs. Ken Johnston and Ralph Gaume, for supporting this research. I would also like to thank my thesis advisor, Prof. Doug Currie, for his insight and suggestions.

## TABLE OF CONTENTS

List of Figures	viii
1 $\eta$ Carinae: History and Overview	1
1.1 Introduction . . . . .	1
1.2 Observational History . . . . .	5
1.2.1 Historical Light Curve . . . . .	5
1.2.2 Interpretation and Discussion of Historical Light Curve . . . . .	9
1.3 Is $\eta$ Car a Luminous Blue Variable (LBV)? . . . . .	12
1.4 Objective and Organization of the Thesis . . . . .	16
1.5 Data Used in Thesis . . . . .	18
I IS $\eta$ CARINAЕ A BINARY?	20
2 Is $\eta$ Car a Binary? A review of the literature	21
2.1 Introduction . . . . .	21
2.1.1 A note on orbital elements . . . . .	23
2.2 The Models . . . . .	23
2.2.1 Damineli 1996 . . . . .	26
2.2.2 Damineli et al. 1997 . . . . .	26
2.2.3 Davidson 1997 . . . . .	28
2.2.4 Ishibashi et al. 1999 . . . . .	29
2.2.5 Damineli et al. 2000 . . . . .	30
2.2.6 Davidson et al. 2000 . . . . .	31
2.2.7 Corcoran et al. 2001 . . . . .	32
2.2.8 Ishibashi 2001 . . . . .	33
2.2.9 Pittard & Corcoran 2002 . . . . .	33
2.2.10 Smith et al. 2004 . . . . .	34
2.2.11 Verner et al. 2005 . . . . .	35
2.2.12 Iping et al. 2005 . . . . .	35
2.2.13 Hillier et al. 2006 . . . . .	36
2.3 Summary of Proposed Binary Models . . . . .	36
3 Development of an Astrometric Methodology for Analyzing Binarity	41
3.1 Introduction . . . . .	41
3.2 Differential Astrometry: Overview of Problem . . . . .	43
3.3 HRC Data and Processing . . . . .	47
3.4 HRC Local Astrometric Accuracy . . . . .	49
3.4.1 Grid Search Method (GSM) Centroiding Algorithm . . . . .	50
3.4.2 Pixel Phase Error (PPE) Correction Algorithm . . . . .	51
3.5 HRC Global Astrometric Accuracy . . . . .	55
3.6 Composite Results . . . . .	57
3.7 Confirmation with Earlier Epoch Data . . . . .	62

3.8	Summary: Accuracy of HRC Astrometry . . . . .	65
4	Astrometric Analysis of Central Star Reflex Motion	66
4.1	Data . . . . .	66
4.2	Methodology . . . . .	67
4.2.1	Error Estimation for New Coordinates . . . . .	70
4.2.2	Implications for Binary Detection . . . . .	71
4.3	Observations . . . . .	71
4.3.1	Saturation . . . . .	71
4.3.2	Possible Parallax Considerations . . . . .	75
4.3.3	Basic Astrometric Results . . . . .	75
4.4	Orbital vs. Linear Motion: Best Fit . . . . .	76
4.4.1	Orbit Modeling . . . . .	78
4.4.2	Problematic November 2003 Data Point . . . . .	81
4.4.3	Quantitative Model/Data Results . . . . .	82
4.5	Discussion of Results . . . . .	82
4.5.1	Astrometric Constraints . . . . .	83
4.5.2	Possible $\eta$ Car A Orbit . . . . .	88
4.5.3	Discussion of Measurement Limitations . . . . .	90
4.5.4	Resolving the astrometric limitations: suggested future observations . . . . .	92
5	Astrophysical Implications of Binary Measurement Results	96
5.1	Primary Luminosity and Mass . . . . .	96
5.2	Secondary Mass and Luminosity . . . . .	98
5.3	Secondary Orbit . . . . .	100
5.4	Comparison of Results with Earlier Binary Models . . . . .	100
5.5	Primary–Secondary Distance . . . . .	102
5.6	Periastron passage . . . . .	105
5.6.1	Orbital Configuration at Periastron . . . . .	105
5.6.2	Mass exchange across L1 . . . . .	106
5.6.3	Wind penetration and opacity considerations . . . . .	109
5.6.4	Tidal considerations . . . . .	110
5.6.5	Roche Lobe “Holes” and Mass Ejection . . . . .	115
5.7	Implications for History and Evolution of $\eta$ Car . . . . .	119
5.7.1	Formation of Binary System . . . . .	119
5.7.2	Stellar Evolution Implications . . . . .	119
5.7.3	Orbital Implications: Binary Capture as Explanation for Great Eruption? . . . . .	121
6	Binarity: Summary and Conclusions	124

II	ASTROMETRIC EXPANSION OF THE EJECTA FIELDS	128
7	The Ejecta Field Around $\eta$ Car: The Fossilized Historical Record of Its Eruptions	129
7.1	A Review of the Literature . . . . .	130
7.1.1	Gaviola 1950 . . . . .	130
7.1.2	Ringuelet 1958 . . . . .	132
7.1.3	Walborn, Blanco, & Thackery 1978 . . . . .	132
7.1.4	Currie & Dowling 1996 . . . . .	133
7.1.5	Smith & Gehrz 1998 . . . . .	134
7.1.6	Morse et al. 2001 . . . . .	136
7.2	Discussion . . . . .	136
8	Astrometric Methodology	143
8.1	Observational Data . . . . .	143
8.2	Creation of Reference Images . . . . .	144
8.2.1	1995.5 F658N Reference Image . . . . .	145
8.2.2	2003.9 F660N Reference Image . . . . .	148
8.3	The cross-correlation procedure . . . . .	152
8.3.1	Patch extraction and preparation . . . . .	152
8.3.2	Cross-correlation . . . . .	156
8.3.3	Expansion velocity/date-of-origin calculation . . . . .	158
8.3.4	Inter-epoch/inter-instrument plate-scale correction . . . . .	159
8.4	Simulation results . . . . .	160
8.5	Error Estimates . . . . .	162
8.5.1	Random centroiding . . . . .	162
8.5.2	Residual distortion . . . . .	164
8.5.3	Deconvolution effects . . . . .	164
8.5.4	Central star position . . . . .	164
8.5.5	Single-Patch Separation Estimated Total Error . . . . .	166
8.5.6	Estimated single-patch expansion rate error . . . . .	167
8.5.7	Estimated single-patch age error . . . . .	167
8.5.8	Algorithm Error and Calculation of the Total Error . . . . .	168
8.5.9	Summary . . . . .	169
9	Homunculus and Equatorial Debris: Astrometric Measurement Results	170
9.1	NW Lobe: Initial Results . . . . .	170
9.2	SE Lobe: Initial Results . . . . .	174
9.3	Disagreements in Expansion Rates and Dates of Origin Between Lobes	176
9.4	Revised Integrated Measurements and Results . . . . .	179
9.5	The Paddle and the Equatorial Debris . . . . .	184
9.6	Confirmation of Integrated Results with Patch Alignment Method (PAM) . . . . .	186
9.6.1	Overview of PAM . . . . .	186
9.6.2	PAM Results . . . . .	187

9.7	Summary of Measurement Results . . . . .	194
10	Analysis and Discussion of Homunculus Results	196
10.1	Answering the Astrometric Questions . . . . .	196
10.1.1	What is the date-of-origin for the Homunculus ejecta? . . . . .	196
10.1.2	What is the ejection interval for the Great Eruption? . . . . .	199
10.1.3	What is (are) the ejection dates for the equatorial features? .	200
10.2	Additional discussions . . . . .	201
10.2.1	Deceleration of leading edge of NW lobe . . . . .	201
10.2.2	Possible Great Eruption-Induced Impulse . . . . .	203
10.2.3	Evidence of c. 1841 Ejecta? . . . . .	204
10.2.4	Equatorial Disk vs. Equatorial Streams . . . . .	205
11	Outer Debris: Astrometric Results	206
11.1	Northeast Quadrant . . . . .	208
11.2	Northwest Quadrant . . . . .	212
11.3	Southwest Quadrant Features . . . . .	214
11.4	Southeast Quadrant Features . . . . .	217
11.5	What are the ejection dates for the debris outside the Homunculus? .	217
11.5.1	1840s Great Eruption . . . . .	219
11.5.2	c. 1790 Polar Ejection . . . . .	221
11.5.3	c. 1730 South Ridge Ejection . . . . .	222
11.5.4	c. 1400 ejection . . . . .	222
11.5.5	Correlation with Photometry . . . . .	223
12	Conclusions: Astrometric Results for both Binarity and Ejecta Fields	225
12.1	Binarity: Summary . . . . .	225
12.2	Ejecta Fields: Summary . . . . .	227
12.3	Towards an integrated picture . . . . .	228
	Appendices	231
A	Glossary	231
B	Distance to $\eta$ Car	234
C	Gaussian Centroiding and Pixel Phase Effects	236
C.1	Centroiding for Well-Sampled PSFs: FWHM and SNR Dependency .	236
C.2	Centroiding under-sampled PSFs: Pixel Phase Error . . . . .	240
C.3	Optimal Sampling: A Simulation . . . . .	243
	Bibliography	246

## LIST OF FIGURES

1.1	Ground based images of $\eta$ Car	2
1.2	HST Color Image of $\eta$ Car	4
1.3	$\eta$ Car's Historical Lightcurve	6
1.4	$\eta$ Car's Historical Lightcurve during the Great Eruption period	8
1.5	LBVs on the H-R	14
2.1	Orbital Elements	24
2.2	Magnified Orbital Elements	25
3.1	Differential Astrometry	44
3.2	HST Focal Plane Layout	46
3.3	F330W empirical pixel phase error correction	53
3.4	Reference star proper motion: case 1	58
3.5	Reference star proper motion: case 2	59
3.6	Reference star proper motion: case 3	60
3.7	Reference star proper motion: early epoch data	64
4.1	Reference Frame	68
4.2	Saturated F330W images	73
4.3	Blooming in F330W image	74
4.4	Central Star Y Positions	76
4.5	Central Star X Positions	77
4.6	Astrometric Reflex Constraints	85
4.7	Central Star Orbit	89
4.8	Trumpler star field	94

5.1	Comparison of binary models	101
5.2	Separation vs. time of components	103
5.3	Binary orbits	104
5.4	Binary configuration at periastron	107
5.5	Effective height of $\eta_A$ 's surface during periastron	113
5.6	Binary effective potential contours	116
5.7	Potential energy cross section	117
7.1	Ejecta diagram	131
8.1	Process for generating F658N reference image.	146
8.2	F658N Reference Image	149
8.3	F658N Reference Image: Homunculus	150
8.4	Process for generating F660N reference image.	151
8.5	F660N Reference Image	153
8.6	Cross-correlation procedure.	154
8.7	Visualization of patch expansion	155
8.8	Simulated expansion images	161
9.1	NW Lobe patch locations	171
9.2	NW Lobe projected velocites.	173
9.3	SE Lobe patch locations	174
9.4	SE Lobe projected velocites.	175
9.5	Comparison of NW and SE lobe expansion velocities.	178
9.6	Homunculus expansion velocity and date of origin	180
9.7	Equatorial patch locations	185
9.8	Velocity field	189

9.9	Avg. separation vs. time . . . . .	190
9.10	Time history of expansion . . . . .	191
9.11	Central region for 1848.2 . . . . .	192
9.12	Alternate expansion rates . . . . .	193
11.1	Outer debris difference image . . . . .	207
11.2	Outer debris patches . . . . .	209
11.3	NE Quadrant outer debris . . . . .	210
11.4	NW Quadrant outer debris . . . . .	213
11.5	SW Quadrant outer debris . . . . .	215
11.6	SE Quadrant outer debris . . . . .	218
11.7	Cartoon view of ejecta dates of origin . . . . .	220
C.1	Pixel phase error . . . . .	242
C.2	Total centroiding error . . . . .	244

# Chapter 1

## $\eta$ Carinae: History and Overview

### 1.1 Introduction

$\eta$  Carinae (henceforth:  $\eta$  Car) is generally considered an extreme member of an extreme class of stars—the Luminous Blue Variables (LBVs). As viewed from Earth,  $\eta$  Car is in the Keyhole region of the Carinae Nebula (fig. 1.1), and is a member of the Trumpler 16 association, located at a distance of approximately 2.25 kpc<sup>1</sup>. It is near the tangent point to the Carina arm at Galactic longitude  $\approx 280^\circ$  [Dame et al.(2001)]. LBVs inhabit the upper left corner of the Hertzsprung-Russel diagram (see, for example, [Carroll & Ostlie(1996)]), being the most massive and luminous stars known. Even within the select group of LBVs, however,  $\eta$  Car ( $M_\eta \approx 130 M_\odot$ ,  $L_\eta \approx 10^{6.7} L_\odot$ , see references cited in this work) is the largest of the large, one of the most massive<sup>2</sup> and luminous stars known within our galaxy. This rarified group also appears to be atypical with respect to their not-quite-so-massive LBV cousins—for example, they all violate the Humphreys-Davidson (H-D) limit ([Humphreys & Davidson(1979)])<sup>3</sup>.

---

<sup>1</sup>See discussion in Appendix B.

<sup>2</sup>Along with LBV candidates the “Pistol Star” ( $M_{PS} \approx 150 M_\odot$ ,  $L_{PS} \approx 10^{6.6} L_\odot$ , [Figer et al.(1998)]) and LBV 1806-20 ( $M_{1806-20} \approx 130 M_\odot$ ,  $L_{1806-20} \approx 10^{6.3} L_\odot$ , [Figer et al.(2004)]).

<sup>3</sup> The H-D limit is an empirical limit to how bright stars can be as a function of their spectral type. In general, the brightest stars are blue. The position of the H-D limit is shown in fig. 1.5.

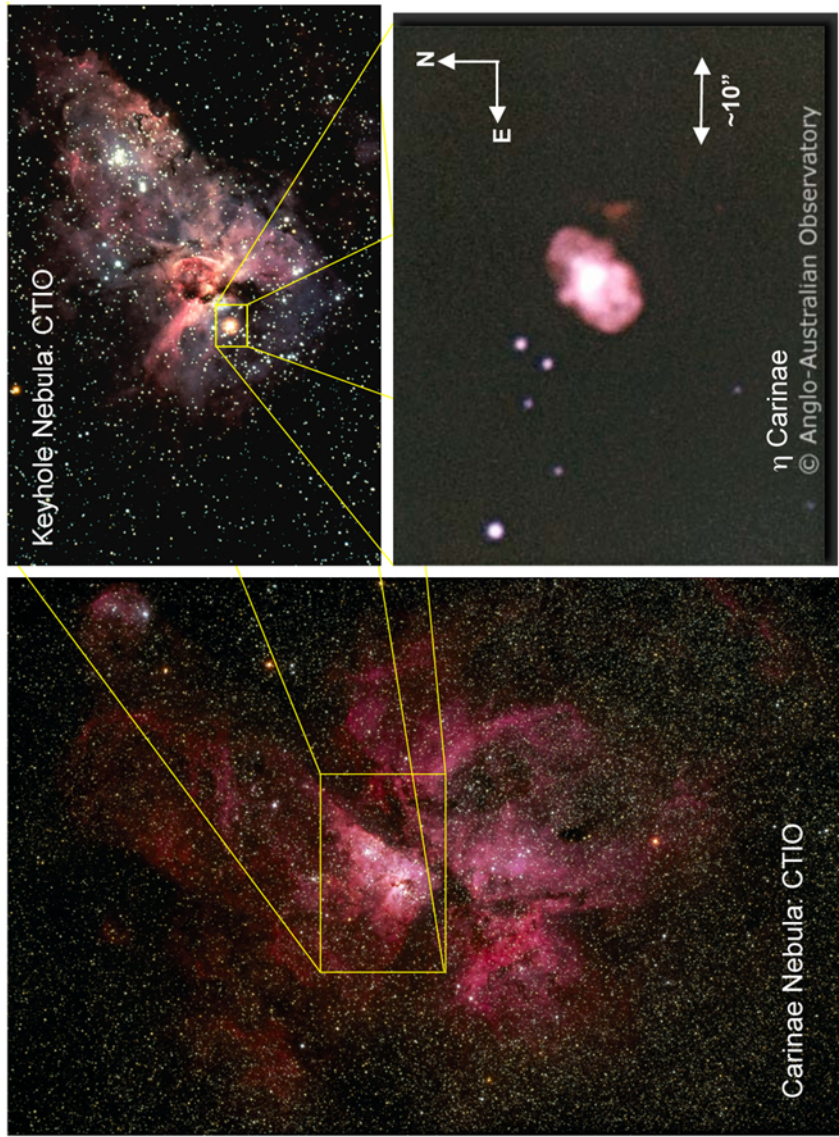


Figure 1.1: Ground based visible light images of  $\eta$  Car. (Left) Carinae nebula from the Curtis-Schmidt telescope at CTIO; (Upper right) Magnified view of the Keyhole region, taken by the 4-m Blanco telescope at CTIO (both images credit: NOAO/AURA/NSF); (Bottom right)  $\eta$  Car and neighboring Tr16 stars observed using the AAT (credit: AAO).

Understanding the LBV hypergiants is critically important for a number of fields within astrophysics. They appear to represent an upper stellar mass limit and thus they test and constrain theories of star formation. The uncertain relation between O, LBV and Wolf-Rayet (WR) stars pushes the limits of our understanding of stellar evolution. Their proclivity for “dancing” back and forth over both the Eddington and Humphreys-Davidson limits strains both stellar evolution models and our fundamental understanding of stellar atmospheres at these extremes of mass and luminosity<sup>4</sup>.

$\eta$  Car, being the closest and least extincted of this class of LBV hypergiant, is the one most easily studied. In fact, over the last one hundred and sixty years, it has been very well observed indeed (§1.2), especially so since the early 1990s with many *Hubble Space Telescope* (HST) observations dedicated to observing  $\eta$  Car. These include GO 9721 (PI: B. Dorland; see fig. 1.2) and the HST  $\eta$  Car “Treasury” campaign (PI: K. Davidson), spanning over three years (Oct. 2002–Nov. 2005), nine observing epochs, and hundreds of exposures across multiple filter bands.

In addition, a significant number of southern hemisphere observations have been made of  $\eta$  Car, most notably with the European Southern Observatory’s (ESO) *Very Large Telescope* (VLT) array of 8-m telescopes at Cerro Paranal, Chile. Despite this concerted effort to probe its nature with the most advanced astronomical instrumentation currently available,  $\eta$  Car has jealously guarded her secrets, with new observations not only failing to definitively address questions regarding the na-

---

<sup>4</sup>See [Humphreys & Davidson(1994)] for an extensive review of LBVs, including some discussion of  $\eta$  Car.

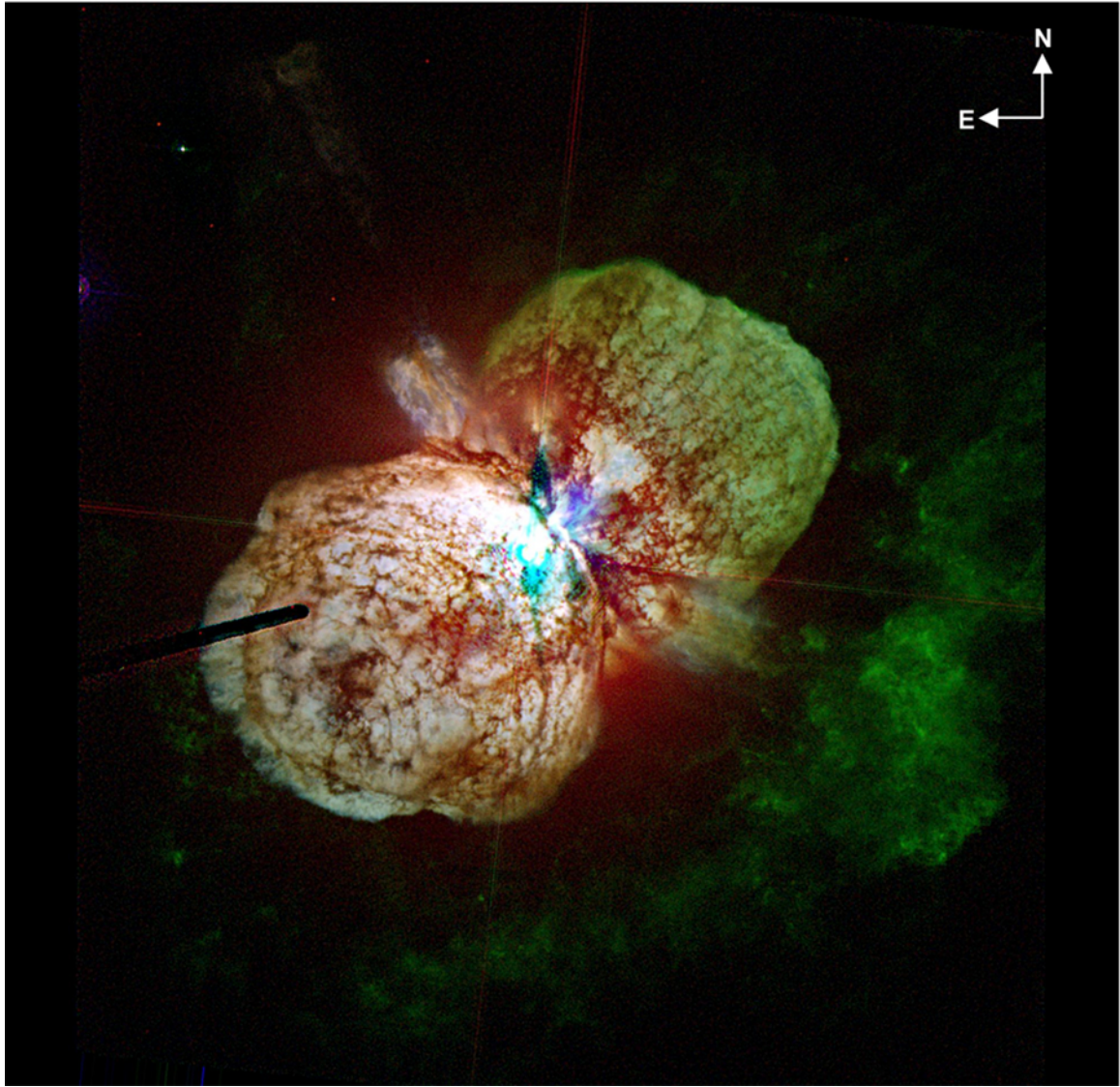


Figure 1.2: Three color (NUV-Vis-NIR) composite image of  $\eta$  Car. The central star (or stars) are in the region that appears saturated. The two large “lobes” extending from the central star in the NW and SE directions make up the “Homunculus” nebula, the material ejected during  $\eta$  Car’s ”Great Eruption” of the 1840s [Currie et al.(1996)]. The NW lobe is receding from and the SE lobe is approaching us. Sparse-disk-like equatorial features are also seen; some authors associate them with the so-called ”Lesser Eruption” around 1890 [Davidson & Humphreys(1997)]. In the SW direction a ridge of material exists that appears to have been ejected much earlier than the 1840s. *Composite color image from HST GO 9721 (PI: B. Dorland) observations. Four sets of 0.1, 1, and 10 second images were taken in Nov. 2003 with ACS/HRC. Multiple exposures were combined using STSDAS/MultiDrizzle, deconvolved, cross-correlated, and combined (details in the text). Blue=F330W (330 nm), Green=F660N (660 nm), and Red=FR914 (1.012  $\mu$ m). The dark area across the SE lobe of the Homunculus is the HRC occulting finger. Compare to lower right image from fig. 1.1. Image is approximately 30 arcsec across.*

ture of the star (or stars), but frequently raising new questions and problems. Even now, after all of these observations, it is generally agreed that we do not understand the underlying physical mechanisms that are responsible for the unique history and behavior of  $\eta$  Car. It is the goal of this thesis to better understand some of these critical phenomena, using a combination of astrometry, spectroscopy and velocimetry data obtained using some of the most capable instruments currently available to astronomers.

## 1.2 Observational History

### 1.2.1 Historical Light Curve

Any discussion of  $\eta$  Car should begin with its historical light curve. Figure 1.3 is a plot of the historical data as compiled by [Frew(2004)]. The plot displays the best estimate for the V-band magnitude as a function of observation date.

Based on Frew’s review of the historical record, there was an underlying trend of at least two centuries of slight secular brightening ( $\approx 1.5^m$  over 230 years, or  $\dot{m} < 0.01 \text{ m yr}^{-1}$ ) ending during the 1830s<sup>5</sup>. Based on observations by Herschel, Frew finds that  $\eta$  Car brightened from  $+2^m$  to  $+1^m$  over the first seven years of the decade ( $\dot{m} \approx 0.1 \text{ m yr}^{-1}$ ); then, at the end of 1837, it experienced a sudden increase (less than two weeks in duration) to  $0^m$  ( $\dot{m} \approx 25 \text{ m yr}^{-1}$ ) (see fig. 1.4). This marked the beginning of a twenty year period (1837–1856) termed “the Great Eruption” during which  $\eta$  Car fluctuated between 0 and  $-1^m$ . The peak brightness was reached

---

<sup>5</sup>Frew suggests relative quiescence during this period, but given the temporally sparse nature of his data, this may not be the case.

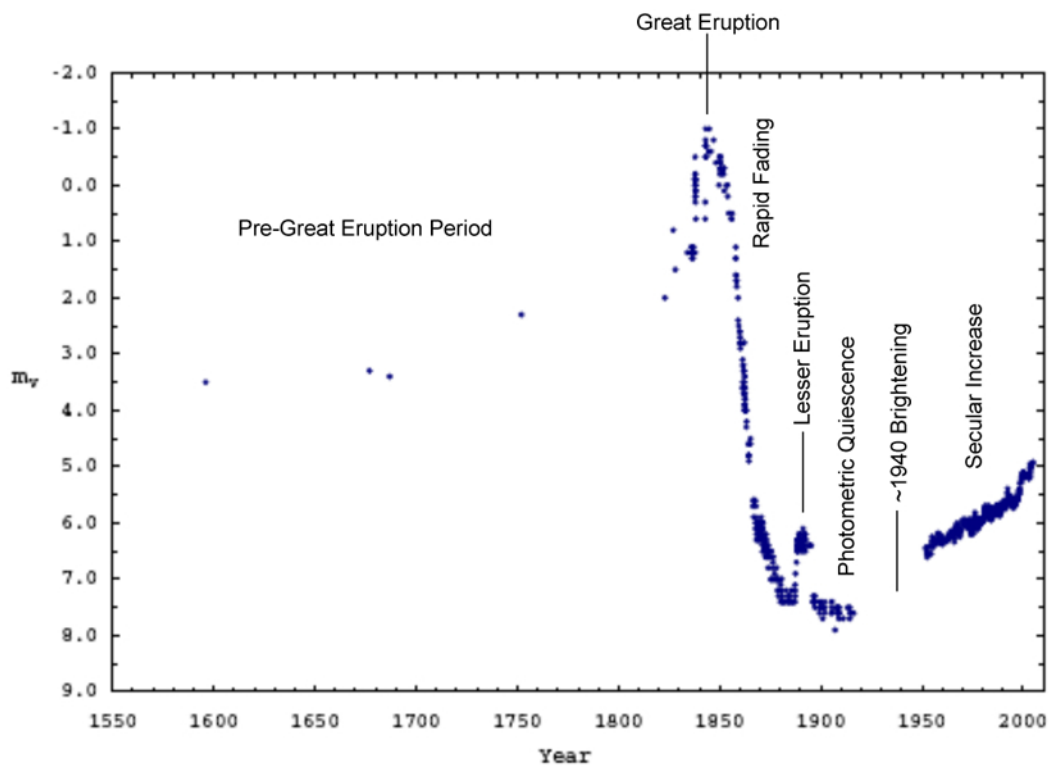


Figure 1.3: The historical lightcurve of  $\eta$  Car, taken from [Frew(2004)]. V-band magnitude is shown as a function of time. The major known photometric events and periods are marked.

in April, 1843 and December 1844, with significant variations on timescales of days to weeks during the entire period. Beginning in 1844, a fading trend was present that reduced  $\eta$  Car's brightness to approximately  $0.5^m$  by 1856 ( $\dot{m} \approx -0.15 \text{ m yr}^{-1}$ ).

The “Homunculus” Nebula is, perhaps, the most prominent persistent feature associated with the Great Eruption. The Homunculus is the two-lobed nebula of material surrounding  $\eta$  Car, prominent in fig. 1.2. Gaviola gave the nebula this name because its physical appearance reminded him of a small, fat man with crossed arms (see the lower right panel in fig. 1.1) [Gaviola(1950)]. It is a primarily a reflection nebula [Davidson & Humphreys(1997)] and consists of ejecta from the Great Eruption [Currie et al.(1996)].

Beginning in approximately 1856–1857, rapid fading began, with  $\eta$  Car dropping to  $6.0^m$  by 1869 ( $\dot{m} \approx -0.4 \text{ m yr}^{-1}$ ). Between 1869 and 1872, the fading plateaued briefly, then resumed once again through 1886, when it reached  $7.6^m$  ( $\dot{m} \approx -0.1 \text{ m yr}^{-1}$ ).

In 1887,  $\eta$  Car suddenly brightened to  $m_V \approx 6.2$ , followed by a plateau around  $m_V \approx 6.5$  lasting approximately 8 years. This event is known as “the Little Eruption.” It was followed by a return to the gradual fading trend, with  $\eta$  Car reaching  $m_V \approx 8$  by 1920. In 1940, De Vaucouleurs reported a 1-mag brightening over a one month period ([de Vaucouleurs(1952)], [de Vaucouleurs & Eggen(1952)]). Photographic plate evidence from circa 1940 indicates a sudden brightening of  $1^m$  in one month<sup>6</sup>. This was followed by a secular brightening trend of  $1^m$  to  $m_V \approx 5.5$  by

---

<sup>6</sup>The data from the 1940s period were not included by Frew due to the problematic nature of estimating photometric magnitude precisely using photographic plates.

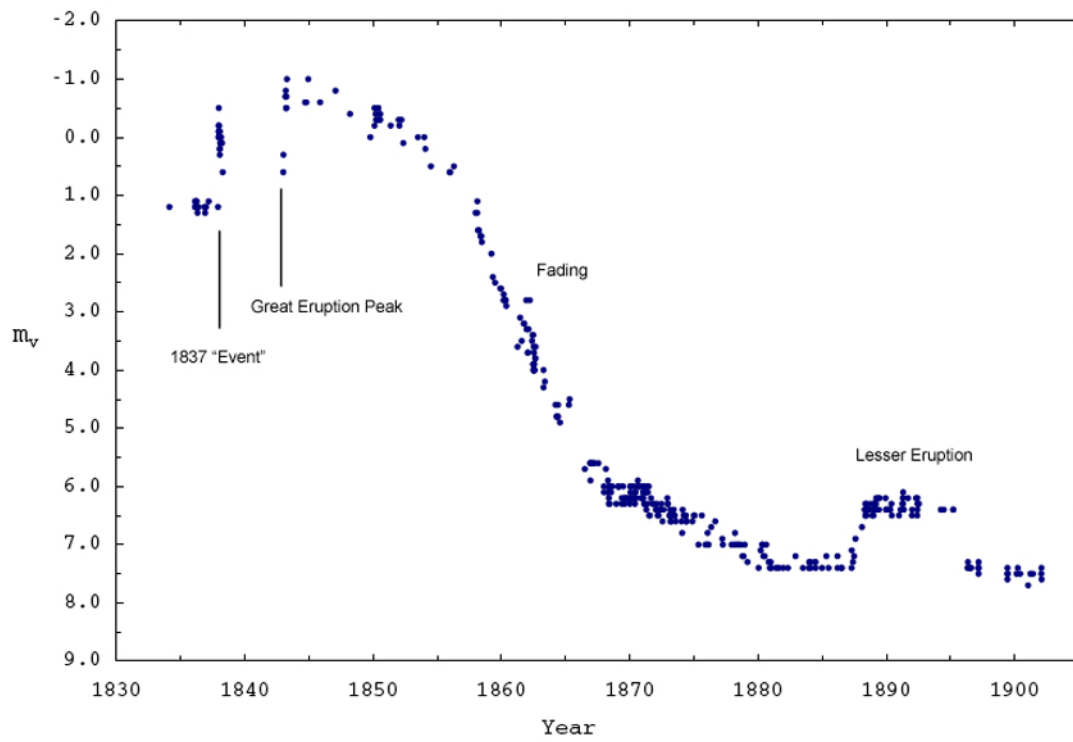


Figure 1.4: The historical lightcurve of  $\eta$  Car during the period immediately before the Great Eruption through the Lesser Eruption, taken from [Frew(2004)]. V-band magnitude is shown as a function of time. The major photometric events and periods are marked.

1997 ( $\dot{m} \approx 0.02 \text{ m yr}^{-1}$ ).

At this point, the secular trend continued for the overall extended structure of the central star and Homunculus. In 1998, the central star brightened rapidly ([Davidson et al.(1999)]) relative to the Homunculus, going from  $8.4^m$  (1991) to  $7.4^m$  (2000) to  $6.8^m$  (2004).

It should be noted that many authors dispute Frew's conclusion that there is no support for a pre-Great Eruption history of large V-band fluctuations. This group includes [Innes(1903)], [Davidson(1989)], and [van Genderen & The(1984)], who all argue that fluctuations of up to three visual magnitudes exist in the historical record. The latter also infers outbursts back in time at least to 1000 A.D., based on the presence of multiple ejecta shells around  $\eta$  Car in the context of proper motion studies of [Walborn et al.(1978)]. Frew does not rule out the possibility of earlier photometric events, but rather finds no evidence of them in the historical record.

### 1.2.2 Interpretation and Discussion of Historical Light Curve

The canonical interpretation of the light curve ([Davidson & Humphreys(1997)]) is as follows: Prior to the Great Eruption,  $\eta$  Car behaved more or less like a canonical LBV (see §1.3), that is, it underwent periodic shell ejection events manifested as color changes and with a relatively constant bolometric luminosity. The Great Eruption was a cataclysmic event, representing a massive release of both energy and material and was marked with a significant increase in bolometric luminosity over the period of the Eruption. As [Dowling(1996)] and [Currie et al.(1996)] found,

essentially all of the Homunculus material was ejected during the Great Eruption. By combining the light curve data with estimates for the total mass ejected and its velocity, the total energy released during the Great Eruption has been estimated at  $10^{49} - 10^{50}$  ergs [Davidson & Humphreys(1997)] and mass ejected  $\dot{m} \approx 10 M_{\odot}$  ([Smith et al.(2004)])<sup>7</sup>. The mechanism for the release of all of this energy is not understood.

After the subsidence of the Great Eruption, the rapid fading phase is attributed to condensation of dust from the material ejected during the Great Eruption. The dust obscured the central star (which, presumably, returned to  $m_V \approx 2-4$  sometime after the eruption) by approximately visible magnitudes. It has been suggested that the Lesser Eruption is related to the Great Eruption and represents some sort of adjustment related to a heretofore undiscovered 50-year time scale associated with the star. Various authors have proposed that the equatorial debris [Davidson & Humphreys(1997)] (see fig. 1.2 and Chapter 4), the Weigelt blobs [Davidson et al.(1997)] (see Chapter 3), and the so-called “Little Homunculus” [Ishibashi et al.(2003)] were all emitted from the central star during this period, much in the same way the Homunculus material was emitted during the Great Eruption, strongly suggesting that the Lesser Eruption was closer in nature to the Great Eruption than it was to an S Doradus-type event<sup>8</sup>.

After the Lesser Eruption,  $\eta$  Car appears to have returned to relative quiescence for approximately 50 years. The 1940 brightening remains unexplained. Frew

---

<sup>7</sup>The presence “quiescent” rate of energy release (see discussion in §5.1 which is based on [Cox et al.(1995)] observations) is  $L_{\odot} \approx 5 \times 10^{47}$  ergs/year, thus the Great Eruption release represents 20–200 years worth of energy.

<sup>8</sup>See §1.3 and the glossary for definition and further discussion of of S Doradus (S Dor) eruptions.

cites circumstantial evidence that it was due to the sudden appearance of the expanding Humunculus lobes by the central star<sup>9</sup>, but does not offer any substantive thoughts on the mechanism responsible for this transition. A secular brightening has occurred since the 1940s photometric event; it is generally thought that this brightening is due to the dissipation of the local dust<sup>10</sup> around  $\eta$  Car that is responsible for the heavy extinction [Davidson & Humphreys(1997)]. This would be manifested as a redistribution of the spectral energy from the IR to the visible bands rather than a gradual increase in the bolometric luminosity, though [van Genderen et al.(2001)] looked for evidence of this effect in the photometric record from 1974–1991 and did not find it. In addition to the underlying trend, small, sub-magnitude photometric variations of varying time scales have also observed (see e.g., [van Genderen et al.(1994)], [van Genderen et al.(2001)]).

The sudden 1998–1999 brightening of the central star in V-band remains unexplained. Both [Davidson et al.(1999)] and [Smith et al.(2000)] suggest that a slight increase in intrinsic luminosity could result in grain destruction that would reduce extinction and, in effect, amplify the luminosity increase. No detailed mechanism for an underlying increase in bolometric luminosity has been proposed, though [Smith et al.(2000)] conjectures that the central star may still be “adjusting from its Great Eruption.”

---

<sup>9</sup>By the 1900, the Great Eruption ejecta had expanded to a mean distance of 2 arcsec from the Central Star (see §9.6, particularly figs. 9.9 and 9.10); it should have been visible before that. Frew’s argument is that the material became *illuminated* at that point; he cites lack of observations of the Homunculus before 1940 as his circumstantial evidence.

<sup>10</sup>Consisting of circumstellar, Homunculus, and other local concentrations.

### 1.3 Is $\eta$ Car a Luminous Blue Variable (LBV)?

$\eta$  Car's behavior has been associated with its membership in the class of stars known as LBVs. What is an LBV? A comprehensive review of the nature of LBVs is given in [Humphreys & Davidson(1994)]. In that reference, an LBV is defined as:

...an evolved, *very luminous, unstable* hot supergiant which suffers *irregular eruptions* like S Dor and AG Car or more rarely the *giant eruptions* as in  $\eta$  Car and P Cyg [emphases in original].

The position of LBVs on the H-R diagram (fig. 1.5) makes some of these essential characteristics clear. As shown, LBVs have evolved off the main sequence. They occupy a region called the “instability strip” (the hatched region in the figure) during quiescence. LBVs are observed to go through “S-Dor”-type eruptions, which are manifested by redward changes in color but not changes in total luminosity. When an LBV undergoes an S Dor-type eruption<sup>11</sup>, it is thought to eject an opaque “psuedo-photosphere”, i.e. an expanding shell of material that reprocesses<sup>12</sup> the light of the star as it expands. As total flux is approximately constant, the expanding shell appears redder as it expands. This is shown in the figure as “rightward” horizontal motion. This reddening ends at what Wolf terms the “opacity wind limit” [Wolf(1989)], the point at which the shell effectively becomes transparent once again to the light of central star, and the star appears once more to be in its quiescent state. Wolf’s empirical value of 8000K is in reasonable agreement with

---

<sup>11</sup>See glossary for additional discussion of S-Dor events.

<sup>12</sup>By “reprocess” I mean the shell material absorbs the light, warms up, and re-emits the light at longer wavelengths.

the opacity temperature limit derived analytically in [Davidson(1987)].

These shell ejection events or S Dor eruptions are to be distinguished from the “Plinian” class<sup>13</sup> or eruptions, typified by the Great Eruption. In these cases, the bolometric luminosity increases significantly, with the eruption showing up as a significant vertical shift in the stars position in the H-R diagram.

The question of how LBVs are related to Wolf-Rayet (WR) stars is also suggested by the diagram. WRs are highly evolved stars with an exposed He core; i.e., most or all of the star’s hydrogen has been either consumed or ejected via intense winds combined with mass ejection events. The current model, suggested by many authors, is that LBVs represent an evolutionary stage in the evolution of O stars into WRs and ultimately into supernovae [Maeder(1989)], that is:

$$O \rightarrow Of \rightarrow LBV \rightarrow WR \rightarrow SN$$

In this model, the removal of mass that is necessary in the transformation from a zero age main sequence (ZAMS) O star to WR is accomplished during the LBV stage by a combination of wind and both S Dor and—perhaps only for the larger LBVs—Plinian eruptions. From the main sequence, stars evolve redward up to the H-D limit, at which point they enter into their LBV phase, oscillating back and forth between the instability strip and the opacity limit, losing mass with each

---

<sup>13</sup>This term is borrowed from Geology where it is used to describe large volcanic eruptions. It is a reference to the eruption of Mt. Vesuvius in 79 A.D. which killed Pliny the Elder [Pliny the Younger (c. 100 AD)].

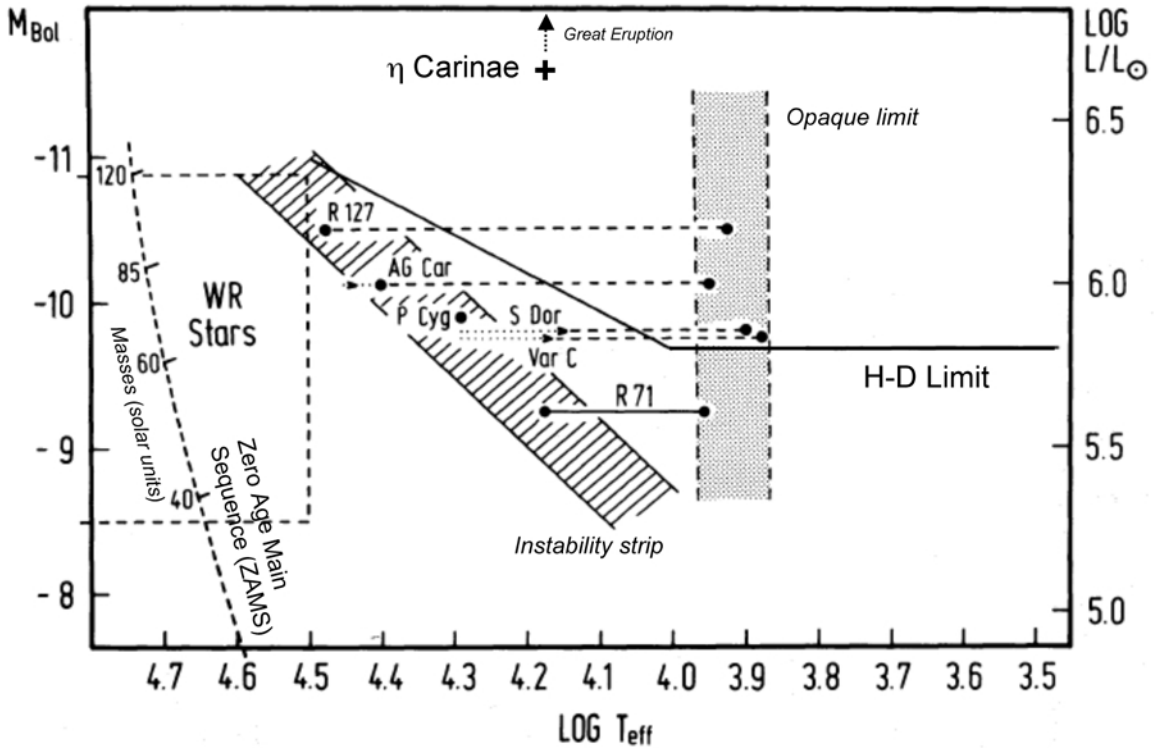


Figure 1.5: The positions of Luminous Blue Variables on the H-R Diagram. The dashed line indicates Zero Age Main Sequence (ZAMS), with specific stellar masses (in solar units) indicated. LBVs have evolved off the ZAMS, and specific LBVs are indicated in the plot. The hatched box is the so-called “instability” strip (i.e., the LBV quiescent states) and the vertical shaded box is the so-called “opaque wind limit.” LBVs are thought to spend most of their time in the instability strip; during S Dor-type eruptions, the move redward (horizontally on the diagram) to the opaque wind limit where they eject a shell, then return back to the instability strip. The location of  $\eta$  Car on the diagram has been added, with an arrow indicating the direction of evolution during the Great Eruption. Also shown is the Humphreys-Davidson (H-D) empirical limit (see text) and a box indicating the region of Wolf-Rayet (WR) stars. Underlying plot is fig. 1 from [Wolf(1989)].

oscillation<sup>14</sup>. Assuming a star maintains the same approximate luminosity, it evolves through a series of S Dor shell ejections, losing a bit of mass during each event. As it does so, it begins to approach the Eddington limit ( $L_{Edd}$ ). At some point, it may reach  $L_{Edd}$  and even cross it. This event may trigger a larger non-luminosity conserving eruption, resulting in even more mass loss for the star. In this model, the star eventually loses sufficient hydrogen that its He core becomes exposed and it begins to move blueward, transitioning from LBV to WR, and beginning its evolution within the WR class towards its ultimate SN fate.

This model is not universally accepted. Many authors have noted that the distinction between LBV and WR is not altogether obvious, with more than one example of a star previously classified as WR now having been reclassified as LBV after undergoing an S Dor event. This is to say that WRs look very much like LBVs in their quiescent state.

Does  $\eta$  Car satisfy the Davidson definition of an LBV? Based on IR photometry ([Cox et al.(1995)]), it meets the luminosity requirement. Based on spectroscopic evidence ([Davidson & Humphreys(1997)]), it meets the requirement for an evolved, post-main sequence star. It is manifestly unstable, and certainly meets the criterion for massive eruptions. It is not clear, however, if it undergoes semi-regular S Dor shell ejection events. As will be discussed in some detail in Chapter 2, there is direct evidence of spectroscopic variability on a 5.52 year cycle which a minority of authors attribute to S Dor events. There remains no direct evidence of S Dor-like variability,

---

<sup>14</sup>Note that stars can temporarily cross the H-D limit, but cannot reside for any length of time in the region beyond the limit.

however.  $\eta$  Car thus appears to be similar to other LBVs, but perhaps different at the same time; it may be *sui generis* because it is so much larger and more luminous than the other well-studies LBVs. Nevertheless, the LBV categorization seems to be the best available and will be adopted as a working model which provides some explanatory power for purposes of this thesis.

## 1.4 Objective and Organization of the Thesis

I address two major questions in this thesis: “Is  $\eta$  Car a binary system?” and “What does the motion of the ejecta tell us about its eruptive history?” The thesis is divided into two major parts, with each part addressing one of the questions. Each part is essentially self contained; Chapter 12 will examine how combined results from the first two parts of the thesis improve our understanding of  $\eta$  Car.

Each of the two major parts are composed of multiple chapters. The specific organization of the parts and component chapters are as follows:

### 1. *Is $\eta$ Car a binary system?*

The first part consists of Chapters 2–6. Chapter 2 is a review of the binary literature, Chapter 3 is a description of a methodology for obtaining 250- $\mu$ arcsec narrow-field astrometry with Hubble Space Telescope (HST)/Advanced Camera for Surveys (ACS)/High Resolution Channel (HRC) data, Chapter 4 describes the application of this methodology to the available  $\eta$  Car data, and Chapter 5 is a discussion of the results of the investigation. Chapter 6 is a discussion of the physical implications of the measurements in terms of  $\eta$  Car’s component masses, orbits, and physical

conditions. In this part, the following questions are addressed: (1) is  $\eta$  Car a binary system?, (2) if so, what is the most likely physical description (masses, orbits, etc.) of the binary system?, (3) what are the physical conditions during periastron?, and (4) do the binary results help explain the history of outbursts we see in  $\eta$  Car's light curve?

*2. What does the motion of the ejecta tell us about its eruptive history?*

The second section includes chapters 7–11 and addresses the eruptive history of  $\eta$  Car by examining the motion of the ejecta in the surrounding nebula. Chapter 7 is a review of the Homunculus and outer-ejecta proper motion literature, Chapter 8 is a description of the methodology used in this thesis, Chapter 9 describes the application of this methodology to both HST/Wide Field Planetary Camera 2 (WFPC2) and HST/ACS/HRC data of the Homunculus, Chapter 10 is a discussion of the implications of the Homunculus measurements, and Chapter 11 describes application of the methodology to the outer debris fields and the resultant implications to  $\eta$  Car's eruptive history. In Part II, the following questions are addressed: (1) with what eruptive event or events can the various nebular (both Homuncular and outer) features be associated?, (2) how tightly constrained (in time) were these eruptive events, (3) is there any evidence of temporal structure in the eruptions, and (4) what does the eruptive history that is inferred from the ejecta field tell us about the physical nature of  $\eta$  Car? The analysis code, written in Interactive Data Language (IDL), is available as an appendix to this dissertation from the author.

In addition, three Appendices are included after Chapter 12. A glossary of terms is presented in Appendix A. Appendix B is a discussion of the distance to

$\eta$  Car. A description of astrometric centroiding is presented in Appendix C; this description expands on concepts described in Chapter 3 includes details regarding the somewhat esoteric process of centroiding astronomical imagery at very high precision.

## 1.5 Data Used in Thesis

In Part I, the analysis of possible binarity, the primary data set consisted of eight epochs of very short exposure, near UV (NUV) data taken with the HST/ACS/HRC instrument between 2002–2005 as part of the HST  $\eta$  Car “Treasury” program (P.I.: K. Davidson). As discussed in Chapter 3, these data are the best available astrometric data for measuring small scale, reflex-type motions. All of these data were extracted from the HST Multimission Archive at the Space Telescope Institute (MAST) system. Descriptive details and a discussion of data processing and reduction for these data are given in Chapter 3.

For Part II, the astrometric analysis of the ejecta fields, two data sets were used. The first epoch consisted of WFPC2 data taken in 1995 (GTO/WFC 5239, PI: J. Westphal) and was retrieved via MAST; the second set consisted of a dedicated HST General Observer program GO 9721 (PI: B. Dorland). GO 9721 was executed over three HST orbits during November, 2003. The filter and exposure time combinations used are shown in Table 1.1.

Data were collected in three filters (F330W, F660N, and FR914M) spanning the available dynamic range, from the faint outer ejecta fields to the very bright cen-

Table 1.1: GO 9721 Filter and exposure combinations. All observations were run using a “box dither” pattern in order to optimize sampling of PSF.

Filter	0.1 s	1.0 s	10. s	Deep exp.(s)	Total int.(s)
F330W	$\times 4$	$\times 4$	$\times 4$	$238 \times 4$	996.4
FR459M		$\times 4$			4.0
FR505N	$\times 4$	$\times 4$			4.4
F550M	$\times 4$	$\times 4$			4.4
FR656N	$\times 4$	$\times 4$			4.4
F660N	$\times 4$	$\times 4$	$\times 4$	$412 \times 4$	1692.4
FR914M		$\times 4$	$\times 4$	$265 \times 4$	1104

tral star. Additional filter data were collected only for the brighter regions (central star and close-in ejecta) using the remaining filters, with these filters chosen to best match the earlier epoch WFPC/2 filters used for earlier observations of  $\eta$  Car, to allow for long temporal baseline proper motion calculations for the brighter features. For each filter/exposure time combination, a total of four exposures were taken using the standard ACS/HRC “box dither” pattern in order to optimally sample the PSF. The reduction and processing of the data are described in detail in Chapter §3. A total of 60 separate HRC exposures were made, spanning a total integration time of  $\approx 1.1$  hours. Of primary interest for the work in this thesis are the F660N data which constitute the core of the second-epoch data and which match well the F656N data from the Westphal 1995 observations.

## Part I

### IS $\eta$ CARINAE A BINARY?

## Chapter 2

### Is $\eta$ Car a Binary? A review of the literature

#### 2.1 Introduction

Prior to 1996, binarity was one of many possible explanations put forth to explain  $\eta$  Car’s luminosity variations and ejecta. As Davidson and Humphreys note ([Davidson & Humphreys(1997)]), there was no reason to prefer a binary model. It did not explain the observed phenomena (variations in luminosity and spectral characteristics) any better than a model of a single, unstable star near (and, at times, crossing over) the Eddington limit, regularly undergoing shell ejection events.

This changed when Damineli discovered a 5.52 year periodicity in  $\eta$  Car’s spectroscopic data that extended from 1994 back at least to 1948 and perhaps all the way back to the early 19th century ([Damineli(1996)]). The “spectroscopic event” occurred when specific high excitation lines (specifically, [Ne III], [Fe III], [Ar III], and He I) that were characteristic of  $\eta$  Car’s “normal” spectrum were seen to fade completely for relatively short periods of time (a few weeks to a few months) with respect to the 5.52 period. These events anti-correlated quite closely with near NIR (H-band<sup>1</sup>) photometry ([Damineli(1996)]), so the event was not merely restricted to being spectroscopic in nature and suggested some fundamental, highly periodic phenomenon was occurring.

---

<sup>1</sup> $\lambda_{\text{center}} = 1.65 \mu\text{m}$

Damineli argued that previous models of  $\eta$  Car that invoked shell ejections as the source of irregular variations could not explain the regularity of the spectroscopic event. He noted that if these eruptions were S Doradus in nature,  $\eta$  Car would be unique in terms of the stability of the variation cycle. Instead, Damineli suggested that a binary system with a 5.52 year orbital period could explain the regularity of the spectroscopic events. Damineli’s predictions of subsequent spectroscopic events have been borne out in 1998.0 and 2003.5; as a result, the binary model has been adopted by most  $\eta$  Car researchers as the preferred model. Damineli also offered a conjecture of what such a system might look like: a  $120 M_{\odot}$  primary, a small secondary, and an elliptical orbit.

Since Damineli’s paper, the binary hypothesis has been adopted by most researchers. A variety of new constraints and revised models of what a binary configuration might consist of have been proposed in the intervening decade in order to explain new observational results. Short descriptions of the evolution of the binary model and development of constraints for  $\eta$  Car are given in §2.2. They are covered in order of publication.

A summary is given in §2.3. If the details of the specific models are of limited interest, the reader can skip directly to that section for a summary discussion of the evolution of the binary models and the “current” (c. 2006) composite model.

### 2.1.1 A note on orbital elements

Throughout the discussion of binaries, standard Campell notation for binary orbits (as opposed to the Thiele–Innes notation) (see, for example, the discussion in [Heintz(1978)]) will be used. The relevant Campbell orbital elements are shown in fig. 2.1.

The value of  $\alpha$ , the projection of  $a$  onto the PoS is a useful metric for astrometric observations. Based on geometrical considerations shown in fig. 2.2, we have:

$$\alpha = a \cos \gamma \quad (2.1)$$

where  $\gamma$  is the angle between  $\vec{a}$  and the PoS. Based on simple geometric considerations, we get:

$$\alpha = a \sqrt{\cos^2 \omega + \sin^2 \omega \cos^2 i} \quad (2.2)$$

which, normalized to unit  $a$ , is referred to in the following text as  $a_{proj}$  and is equivalent to  $\cos \gamma$ .

## 2.2 The Models

The following subsections describe the development of the binary models over the last decade. It should be noted that most of the interest in this section is directed at those models and/or observations that describe orbital elements and

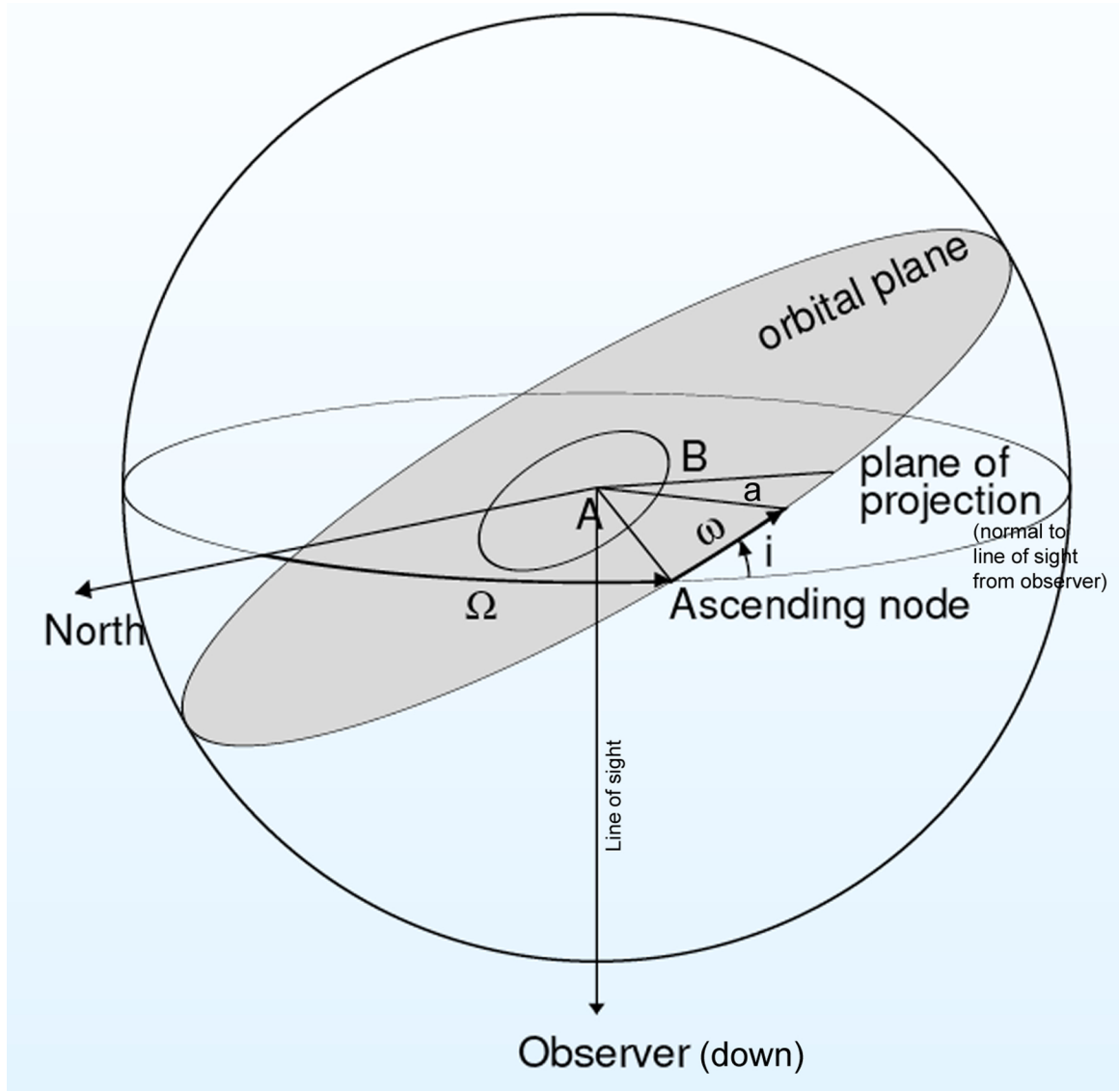


Figure 2.1: Campbell orbital elements. Here, the plane of projection is the Plane of the Sky (PoS);  $a$  is the semi-major axis of the true orbit;  $i$  is the inclination of the orbital plane with respect to the PoS;  $\omega$  is the argument of periastron, defined as the angular difference between the line of nodes and the semi-major axis through periastron; and  $\Omega$  is the longitude of the ascending node, defined as the angular difference between north and the ascending node. Not explicitly shown is  $e$ , the eccentricity of the true orbit. The line of sight to the observer is also shown; this line is normal to the plane of projection and forms a right angle with the line marked “North” at A. Illustration is from [Pourbaix (2005)].

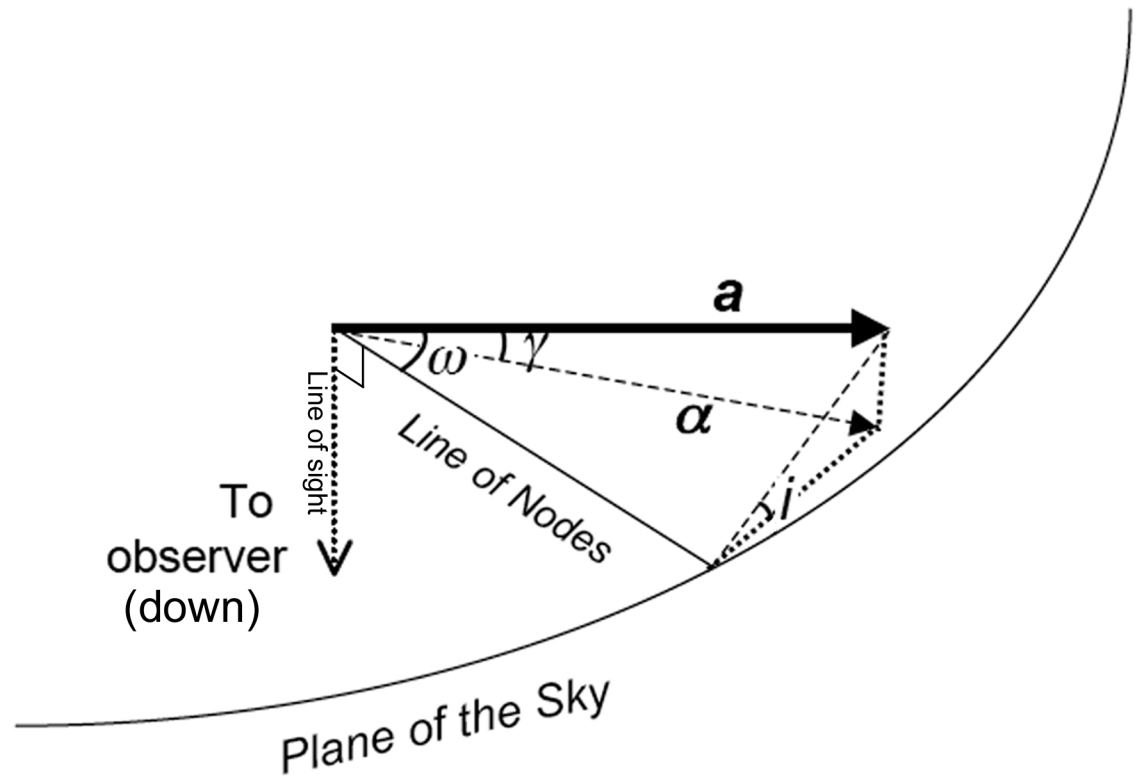


Figure 2.2: Enhanced view of  $a$ ,  $\alpha$ ,  $i$ , and  $\gamma$ . The observer is located “below” the plane of the sky, with the indicated line of sight normal to the plane of sky. The actual orbital semi-major axis  $a$  can be on either side of the plane of the sky as defined by the plane normal to the line of sight.

basic binary parameters (e.g., masses). While reading the details of each model, the reader should note that summary information is presented in Tables 2.1 (orbital elements) and 2.2 (binary parameters).

### 2.2.1 Damineli 1996

This refers to Damineli's first, qualitative model described above, and is included for completeness. Based on both spectroscopic and NIR photometric observations, Damineli derived an orbital period of  $P = 5.52$  years. Damineli also noted the relatively brief duration of the event, and conjectured that a small secondary in an elliptical orbit that resulted in variable mass accretion might be invoked to explain the NIR light curves.

### 2.2.2 Damineli et al. 1997

Damineli et al. ([Damineli et al. (1997)]) observed  $\eta$  Car spectroscopically between 1989 and 1996 using the 1.6 m National Astrophysical Laboratory (LNA/CNPq) telescope in Brazil. Observations of the Pa  $\gamma$  line were used to derive Doppler<sup>2</sup> velocimetric data for specific features in the spectra<sup>3</sup>.

Damineli et al. found radial velocity variations of order  $\pm 50$  km/sec (peak to peak) in the narrow components of the Pa  $\gamma$  line that strongly correlated with phase across multiple spectroscopic events. They argued that this represented radial motion in the central star indicating reflex motion due to the presence of binary

---

<sup>2</sup>i.e. line-of-sight

<sup>3</sup>Other lines (e.g., Pa  $\delta$ , He) were cited to show “consistency [with the] Pa  $\gamma$ ” measurements [Damineli et al. (1997)].

companion. They derived an orbit for the primary (henceforth:  $\eta_A$ ) that include the following elements: eccentricity  $e = 0.63$ , argument of periastron  $\omega = 286^\circ$ , semi-major axis/inclination angle product of  $a \sin(i) = 7.6$  AU. They assume an inclination angle of  $i = 60^\circ$  and derive a semi-major axis  $a = 8.8$  AU.

The mass function for the companion (henceforth:  $\eta_B$ ) is defined as:

$$f_{m,B} \equiv M_B \frac{\sin^3 i}{(1 + \frac{M_A}{M_B})^2} = \frac{P}{2\pi G} \nu_{A,r}^3 \quad (2.3)$$

(see, for example, eqn. 7.8 [Carroll & Ostlie(1996)]), where  $P$  is the period,  $G$  is the gravitational constant, and  $\nu_{A,r}$  is the observed radial velocity of  $\eta_A$ . The equation relates the masses of the binary components to the observed quantities  $\nu$  and  $P$  for only one component. Given a mass and inclination, one can solve for the mass of the “hidden” companion. Without inclination, the mass function gives the lower limit to the companion mass. Damineli et al. calculate  $f_{m,B} = 14.6 M_\odot$ .

Damineli et al.’s results for  $i$  and  $\omega$  indicate that the semi-major axis of the binary is oriented more parallel to our line of sight rather than perpendicular. That is, the secondary appears to be coming towards and receding from us rather than moving back and forth across the sky.

Using the derived orbital elements and mass function and arguments based on luminosity and age, they derive mass ranges of  $64 M_\odot < M_A < 68 M_\odot$  for  $\eta_A$  and  $65 M_\odot < M_B < 71 M_\odot$ , where  $M_B$  is the mass of the companion. They argue that  $\eta_A$  has passed the hydrogen core burning stage while  $\eta_B$  is still in that stage, with progenitors for  $\eta_A$  and  $\eta_B$  of masses  $M_A \approx 115 M_\odot$  and  $M_B \approx 90 M_\odot$ . A spectral

type range of O9 to B3 and temperatures of 18,000-33,000 K are estimated for  $\eta_A$ , and O9 to B3 and a temperature of 27,500 K are estimated for  $\eta_B$ . These parameters are listed in Tables 2.1 and 2.2. This will be referred to as the “first generation” model. The paper concludes with a prediction of strongly phase-dependent wind-wind interaction given the derived orbital elements and masses and suggests this phenomenon may be apparent in X-ray observations.

### 2.2.3 Davidson 1997

Davidson re-examined the observational data published by Damineli et al. and derived two modified models of the binary system. Using the same methodology as Damineli et al., he found that the fit could be improved by adopting slightly different parameters. Davidson referred to this as his “Model 1” and the revised values are shown in Tables 2.1 and 2.2. He found slightly higher eccentricity than Damineli et al., and a smaller mass function.

Davidson then goes on to note that for highly elliptical orbits, the data near periastron (i.e., zero phase) are the most important. He includes the Pa  $\delta$  and He lines *not* used by Damineli et al. to increase the density of data around zero phase. Davidson refers to the resultant fit as “Model 2.” His mass function  $f_{m,B} = 12.5 M_\odot$  is smaller than Damineli et al.’s and his eccentricity  $e = 0.8$  is much larger. He adopts an inclination  $i = 55^\circ$ , and concludes that both stars are massive, consistent with Damineli’s model. Davidson argues that Model 2 is to be preferred over Model 1 (and the Damineli et al. model) not only on empirical grounds, but also because

the much higher eccentricity allows for a brief period near periastron where the two stars are close enough to tidally interact, thus providing some mechanism for triggering the event—though Davidson does not speculate on the nature of the event.

It should also be noted that in the same paper, Davidson also argues that the binary model does *not* provide a better explanation for the behavior of  $\eta$  Car than the single star/shell ejection event. As such, he takes a neutral stance in this paper on the question of binarity.

#### 2.2.4 Ishibashi et al. 1999

Ishibashi et al. ([Ishibashi et al.(1999)]) describe x-ray observations of  $\eta$  Car made with the Rossi X-Ray Timing Explorer (RXTE, see [Bradt et al.(1993)]) during the 1998 event. These observations show hard, highly absorbed X-rays. The flux obeys the 5.52 year spectroscopic cycle first described by Damineli, with a peak in x-ray flux right before the “event” followed by a collapse to near zero flux immediately after this peak. The observations seem to confirm the previous ([Damineli(1996)]) prediction for strongly phase dependent x-ray emissions.

They argue that the hard, absorbed emission is typical of colliding winds from two components in a binary system rather than the softer, less absorbed emissions usually seen for single, massive stars. They hypothesize that the collapse of the flux system near zero phase is the result of an occultation of the hard emission region due to the presence of a dense disk of material around the central star. As the secondary approaches the primary, the x-ray luminosity increases as the distance

between the stars decreases, then suddenly plunges to near zero when the emission region is eclipsed by the disk as seen from Earth.

The Ishibashi et al. colliding-winds binary (henceforth: CWB) model lends credence to the binary model. Although the paper is somewhat qualitative in nature (at least in so far as no real model of the binary system is derived), a new set of observations—viz., the x-ray observations—are introduced that appear to support as well as constrain the binary model.

### 2.2.5 Damineli et al. 2000

Damineli et al. ([Damineli et al.(2000)]) report the results of spectroscopic observations made during the 1998 spectral event using telescopes at the European Southern Observatory (ESO) and the National Astrophysical Laboratory, Brazil (details of which are given in [Damineli et al.(1999)]). The observations were a continuation of the ones first described in the original spectroscopic event paper ([Damineli(1996)]). Pa  $\gamma$  and  $\delta$  lines were used to calculate radial velocity as a function of observing date. The 1998 results were found to correlate strongly with the previous (1992) event, allowing the value of the period to be refined to  $P = 2020 \pm 5$  days ( $5.53 \pm 0.01$  years).

The authors derive a revised binary model (see Tables 2.1 and 2.2) based on the new results. The primary differences with the previous models [Damineli et al. (1997)] are an increased eccentricity (in better agreement with Davidson's model) and a significantly smaller mass function for the companion. Damineli et al. do not derive a

mass for  $\eta_B$ , but suggest that  $\eta_B$  may be a smaller, hotter, less evolved star than  $\eta_A$ . The authors thus allow for the possibility of an highly asymmetric mass distribution in the system, a significant departure from previous models.

### 2.2.6 Davidson et al. 2000

Using the HST/Space Telescope Imaging Spectrograph (STIS), Davidson et al. report on spectroscopic observations made during the 1998 event ([Davidson et al.(2000)]). Davidson et al. examined Pa  $\delta$ , Pa  $\epsilon$ , Pa  $\eta$  and Pa  $\theta$  lines (the STIS instrument was not able to access the Pa  $\gamma$  line). The Damineli-based models predicted a radial velocity shift of +35 km/sec over the period of STIS observations near periastron (1998.2–1999.1). Davidson et al. noted the difficulty in deriving a “velocity” for the relatively broad Pa lines and rejected template fitting and flux weighting (i.e., centroiding) as viable methods due to the real variations in the line profile as a function of spectroscopic cycle phase. Instead, they calculated the midpoint for a parameter  $h$ , which ranged from 0.0 to 1.0, and represents the “height” above the continuum relative to normalized peak flux. So, for example, the FWHM for a given line would be equivalent to  $h = 0.5$ . Davidson et al. argued that  $h$  would be much less sensitive to line profile variations than other methods, and thus, provide a much more robust measurement of velocity.

Using  $0.5 < h < 0.7$ , Davidson et al. measured velocity changes that ranged from -23 km/sec (Pa  $\theta$ ,  $h = 0.7$ ) to +4 km/sec (Pa  $\eta$ ,  $h = 0.5$ ), with a mean shift of  $\delta v = -7 \pm 10$  km/sec. The authors suggest that the Damineli et al. results

were most likely due to contamination of the central star spectrum by nearby ejecta which ground-based instruments were not able to resolve spatially from the central star. They speculate that what appear to be changes in velocity may actually be the effects of changing illumination conditions during the spectroscopic event. The authors conclude their results invalidate the [Damineli et al. (1997)]. model—two very massive stars orbiting more-or-less along our line of sight—based on the apparently inaccurate interpretation of the ground-based velocimetry data. Davidson et al. suggest that a binary model consisting of a massive primary and a much smaller secondary remains feasible.

### 2.2.7 Corcoran et al. 2001

[Corcoran et al.(2001)] provide a quantitative model of the RXTE x-ray observations made during the 1998 spectral event, previously described by Ishibashi et al. [Ishibashi et al.(1999)]. In the earlier paper, a CWB model was proposed in which the winds from the primary and secondary collide, producing orbital phase-dependent x-ray flux in the process. Corcoran et al. refine that work by generating orbital elements and inferring astrophysical properties directly from the observational results rather than assuming the values proposed in earlier models. Furthermore, they propose variable mass loss (induced by tidal forces near periastron) as the cause of the few months drop off in x-ray flux immediately after the putative periastron, rather than the thick circumstellar disk proposed by Ishibashi et al.

The revised binary model parameters are given in Tables 2.1 and 2.2. Using

an inclination of  $i = 50^\circ$ , Corcoran et al. find a much higher eccentricity ( $e = 0.9$ ) and a much smaller mass function,  $f_{m,B} = 1.5 M_\odot$ . Based on inferred mass loss rates from the secondary, the authors suggest that  $\eta_B$  may be a Wolf-Rayet (WR) rather than an unevolved O star. This model is important in that it confirms some of the important trends in the evolution of the binary star models: the secondary is smaller and the eccentricity larger for the second generation, as compared to the first generation models.

### 2.2.8 Ishibashi 2001

Using the RXTE x-ray data [Corcoran et al.(2001)], Ishibashi derived a revised set of binary orbital elements [Ishibashi(2001)]. Most notably, the combined revised  $i$  and  $\omega$  values suggest the semi-major axis of the orbit is closer to perpendicular to our line of sight rather than parallel as previous models had suggested. Ishibashi also derived a significantly larger primary mass ( $M_A = 130 M_\odot$ ) than previous authors.

### 2.2.9 Pittard & Corcoran 2002

Pittard & Corcoran [Pittard & Corcoran(2002)] analyzed Chandra x-ray spectroscopic data and derived improved estimates of mass loss rates due to wind for both  $\eta_A$  and  $\eta_B$ . They did not attempt to solve for the orbital elements but rather used values previously published [Corcoran et al.(2001)]. A mass loss rate of  $\dot{M}_B = 0.98 \times 10^{-5} M_\odot \text{ yr}^{-1}$  was derived directly from the model results, and a mass loss rate of  $\dot{M}_A \approx 2.5 \times 10^{-4} M_\odot \text{ yr}^{-1}$  was inferred for the primary. From the

former, they deduce that the companion is an Of supergiant or WR star. They prefer the Of classification due to inferred subsolar abundances in the x-ray spectrum, which they attribute to the secondary.

### 2.2.10 Smith et al. 2004

Smith et al., using HST/ACS/HRC ultraviolet (UV) and visible observations (filters F220W, F250W, F330W, and F550M) analyzed the distribution of flux in the vicinity of the central star during the 2003.5 spectral event [Smith et al.(2004)]. Using six independent epochs, they found that a UV shadow appeared to move across the ejecta near the central star over the course of one year. They concluded that the shadowing was due to UV flux from the secondary being occulted by the primary as it passed through periastron.

From these observations, Smith et al. generated a series of qualitative constraints on the orbit. They prefer a highly elliptical orbit ( $e = 0.8\text{--}0.9$ ). The variable illumination is consistent with  $\eta_B$  passing “behind” A (as viewed from Earth) prior to periastron and in front of  $\eta_A$  post-periastron and with the Plane-of-Sky (PoS) orientations of the orbit running from NE (periastron) to SW (apastron) (position angle  $PA_a \approx 225^\circ$ ), with an orientation of the semi-major axis  $a$  more perpendicular to our line of sight than parallel, in agreement with [Ishibashi(2001)].

### 2.2.11 Verner et al. 2005

Using Space Telescope Imaging Spectrograph (STIS) observations of the Weigelt blobs B and D during the 2003.5 spectroscopic event, Verner et al. [Verner et al.(2005)] argue that the variations in low and high excitation states observed in the blobs can be explained with a binary model consisting of a cooler primary ( $T_{eff} \approx 15,000$  K) and a hotter secondary ( $34,000$  K  $< T_{eff} < 38,000$  K). In their model, the secondary is in a highly elliptical orbit, and periodically (at periastron) passes through a UV-thick gas that effectively blocks its UV emission in the direction of the B and D blobs. Verner et al. conclude that the primary is a B star and the secondary is a post-main sequence O7.5 supergiant of age  $\approx 10^6$  yr.

### 2.2.12 Ipingle et al. 2005

Ipingle et al. describe Far Ultraviolet Spectroscopic Explorer (FUSE) observations of  $\eta$  Car before, during, and after the 2003.5 spectroscopic event [Ipingle et al.(2005)]. Hillier et al. ([Hillier et al.(2001)]) showed that the primary should have a pre-reddened  $t_{eff} = 15,000$  K, while Verner et al. [Verner et al.(2005)] (see previous section) showed that the secondary must have a  $t_{eff} > 34,000$  K. Ipingle et al. conclude that any flux from the central star region shortward of Ly $\alpha$  must originate from the secondary. They report that FUSE observations show that FUV flux disappeared approximately one month prior to the spectral event date and reappeared in observations after the event, indicating an eclipse of the FUV source, i.e., the secondary. Furthermore, they argue that the pre- and post-event spectra *with* FUV

flux represent the inherent spectrum of  $\eta_B$  itself, thus providing the first *direct* observational evidence of  $\eta_B$ . Based on the presence of specific spectral lines in the FUV spectrum of  $\eta_B$  (most notably N II 1084), they infer that the companion is an evolved, late-type nitrogen-rich O or WR star.

### 2.2.13 Hillier et al. 2006

Hillier et al. present a more detailed analysis of the FUSE results. They find that the FUV features previously reported [Iping et al.(2005)] are not direct observations of  $\eta_B$ , but rather due to contamination by nebular and other sources [Hillier et al.(2006)] located some distance ( $r > 0.3''$ ) from the central star. They reject neither the binary hypothesis nor the model parameters, but rather argue that FUV emission from the central star region is reprocessed by the primary's dense wind and re-emitted in longer wavelengths where it is lost in the glare of the much brighter primary.

## 2.3 Summary of Proposed Binary Models

Originally proposed as an explanation of the periodic spectroscopic variations first described by [Damineli(1996)], the binary model has evolved significantly over the last decade. The “first generation” models were based on ground-based spectroscopic velocity measurements made during 1994 and 1998 events. These models suggested two massive ( $M_A \approx M_B \approx 70 M_\odot$ ) stars (see Tables 2.1 and 2.2) orbiting each other in moderately elliptical orbits with the major axes oriented more paral-

lel to our line-of-sight than to the plane of the sky. These models were eventually rejected when HST/STIS highly spatially resolved spectral data indicated that the ground-based spectroscopic data were most likely contaminated by flux from nearby ejecta [Davidson et al.(2000)] and did not reflect actual velocity shifts in the central star due to reflex motion.

Table 2.1: Orbital elements and mass function for binary models described in this section. An orbital period of  $P = 5.52$  years is assumed for all models.  $i$  and  $\omega$  are given in degrees,  $a_A$  and  $a_B$  are given in AU and the mass function  $F_{M,B}$  is given in solar mass units.  $a_{proj}$  is the length a semi-major axis  $a$  with unit value projected onto the plane of the sky using the given values of  $i$  and  $\omega$ . Most models are not complete. Some models have additional astrophysical parameters, given in Table 2.2.

Reference	$e$	$i$	$\omega$	$a_A$	$a_B$	$a_{proj}$	$f_{M,B}$
Dam. et al. 97 (Dam97)	0.63	60	286	8.8	[8.8]	0.55	14.6
Dav. 97 (Model 1) (Dav97.1)	0.67	55–60	293	8.3	[8.3]	0.64	10.1
Dav. 97 (Model 2) (Dav97.2)	0.80	55–60	286	8.8	[8.8]	0.59	12.5
Dam. et al. 00 (Dam00)	0.75		275			0.50	7.5
Corcoran et al. 01 (Cor01)	0.90	50	275			0.65	1.5
Ishibashi 01 (Ish01)	0.80	45	200			0.97	
Pitt. & Cor.. 02 (PC02)	0.90	50	275			0.65	1.5
Smith et al. 04 (Sm04)	0.8–0.9	42	200			0.97	
Werner et al. 05 (W05)						15	
Iping et al. 05 (Ip05)							
Hillier et a. 06 (H06)						15	

At approximately the same time the velocimetry-based binary models were being called into question, it was shown that a binary system provided a good model for explaining the variation in x-ray flux observed by RXTE ([Ishibashi et al.(1999)], [Corcoran et al.(2001)], [Ishibashi(2001)]) as well as the x-ray spectrum observed using Chandra [Pittard & Corcoran(2002)]. These “second-generation” models favored a highly elliptical orbit with major axes oriented more parallel to the plane

of the sky than to our line of sight and a much smaller mass function (see Table 2.1). As a result, the stellar mass distribution became more asymmetric, with a supermassive primary ( $M_A \geq 80 M_\odot$ ) and a much less massive (though still huge by solar standards) secondary ( $M_B \approx 30 M_\odot$ ) (see Table 2.2).

Table 2.2: Astrophysical parameters for binary models described in this section. Mass ( $M$ ) and luminosity ( $L$ ) are given in solar units, temperature ( $t$ ) in Kelvin. Not all models are complete. Full references are given in Table 2.1

Ref.	$M_A$	$t_A$ $\times 10^3$	$L_A$ $\times 10^6$	Spectral Class (A)	$M_B$	$t_B$ $\times 10^3$	$L_B$ $\times 10^6$	Spectral Class (B)
Dam97	64–68	18–33		O9–B3	65–71	27.5	1.5	O9–B3
Dav97.1								
Dav97.2	$\approx 70$	$< 20$	2–2.7	(NA)	$\approx 70$	$> 20$	$< 2$	
Dam00	70				$\ll 70$			
Cor01	80		$< 3$		30		$< 1.1$	WR
Ish01	130				30			
PC02	80				30			Of (WR)
W05		15		B		37.2	0.9	O7.5 I
Ip05								O/WR
H06			5.0		30	33.7	1.0	O

The recent work in the UV (imaging: [Smith et al.(2004)]; spectroscopic: [Iping et al.(2005)]) are consistent with the second-generation models, though some of the conclusions of the latter paper have recently been called into question ([Hillier et al.(2006)]). Similarly, Verner et al.’s results regarding photoionization modeling based on UV/Visible/NIR STIS data have produced results convergent with the second-generation models.

This evolution and multi-wavelength convergence suggests that while the first-generation models were most likely incorrect (based, as they were, on an apparently specious interpretation of the data), the more recent models are more likely to be better representations of the actual physical conditions. Using the data from Tables

2.1 and 2.2, we can synthesize a “standard” binary model that best represent the current state of affairs. This 2006 combined model is shown in Table 2.3.

Table 2.3: Combined 2006 Binary Model. As described in the text, recent models based on multi-wavelength observations using a variety of different instruments have tended to converge on a single solution. The values listed in the table are representative values for this “combined” solution.

Parameter	Value	Notes
$P$	5.52 years	
$e$	0.8–0.9	
$i$	$\leq 45^\circ$	
$\omega$	$\approx 200^\circ$	
$a_A$	$\leq 4$ AU	
$a_B$	$\geq 11$ AU	
$a_{proj}$	0.97	<i>Implies PoS–major axis angle <math>\gamma \approx 14^\circ</math></i>
$f_{M,B}$	1.5	
$M_A$	$\geq 80 M_\odot$	<i><math>L_{Eddington}</math> implies <math>M_A \geq 105 M_\odot</math></i>
$t_A$	$\approx 15,000$ K	
$L_A$	$\approx 4 \times 10^6 L_\odot$	
Spect. Class (A)	$\approx$ B	
$M_B$	$\approx 30 M_\odot$	
$t_B$	$\geq 35,000$ K	
$L_B$	$\leq 1 \times 10^6 L_\odot$	
Spec. Class (B)	O/WR	

The combined model thus prefers a supermassive, B–type primary and a massive, very hot O or WR–type secondary in a highly elliptical orbit. The lower limit on the mass of the primary is  $M_B \geq 80 M_\odot$  based on the early x-ray CWB fits [Corcoran et al.(2001)], but based purely on luminosity considerations, a larger mass ( $M_B \geq 105 M_\odot$ ) is preferred on the assumption that the star is currently below the Eddington limit, in agreement with at least one model [Ishibashi(2001)]. The major axes of the orbits are inclined such they are nearly in the plane of the sky with respect to our line of sight, thus minimizing the reflex motion Doppler signal

but maximizing its astrometric signal. This raises the possibility of detection of the companion by astrometric means, which will be explored in the next two sections.

A small minority of researchers continue to argue that  $\eta$  Car is a single star undergoing periodic mass ejection events. As noted at the beginning of the chapter, however, the strong periodicity of the spectroscopic events (which is undisputed) argues strongly for binarity, as orbital motion is generally considered the only obvious example of *such* precise regularity in nature. Furthermore, though the early spectroscopic/velocimetric observations appear now to have been flawed (at least in terms of their interpretation), subsequent observations over multiple phenomenological regimes all seem to have converged on binarity as the best explanation for the the disparate phenomena. It is important to note, however, that no *direct observation* of the companion star has been made to date (2006)<sup>4</sup>.

---

<sup>4</sup>Assuming that the criticism by [Hillier et al.(2006)] of [Ipingle et al.(2005)] is valid—an assumption that is lent weight by the fact that Hillier was a co-author on Ipingle et al. and Ipingle was a co-author on Hillier et al.

## Chapter 3

### Development of an Astrometric Methodology for Analyzing Binarity

#### 3.1 Introduction

One standard method for detecting binaries, noticeably absent from the methods described in the previous section, is astrometric detection of reflex motion. If we adopt the parameters listed in Table 2.3, are there, in principle, any instruments capable of detecting the reflex motion of the primary?

The astrometric signal of the primary  $\alpha_A$  is given (in arcseconds) by the product of the semi-major axis  $a$ , given in astronomical units (AU), and the cosine of the angle  $\gamma$  between the semi-major axis  $a$  and the plane of the sky<sup>1</sup>, divided by the distance in parsecs, or:

$$\alpha_A = \frac{a_A a_{proj}}{d} \quad (3.1)$$

where  $a_{proj} = \cos \gamma$ . The “combined model” (see Table 2.3) gives us a minimum mass, but, for reasons discussed in §2.3, there is good reason to believe that the primary is larger than the minimum mass; three cases are considered:  $M_A = 80, 105, 130 M_\odot$ . From Newton and Kepler, the two equations that govern the relations between masses, semi-major axes and periods are:

---

<sup>1</sup>See §2.1.1 for a detailed discussion of the geometry.

$$M_A a_A = M_B a_B \quad (3.2)$$

and

$$(M_A + M_B)P^2 = (a_A + a_B)^3 \quad (3.3)$$

where mass  $M$  is in solar masses, period  $P$  is in years and semi-major axis  $a$  is in AU.

Using a value of  $M_B = 30 M_\odot$  for the companion and the three mass cases described above, eqn 3.3 and Kepler's equation can be solved simultaneously, i.e.:

$$M(t) = E(t) - e \sin E(t) \quad (3.4)$$

where  $M(t)$  is the “mean anomaly,”  $e$  is the orbital eccentricity, and  $E(t)$  is the “eccentric anomaly.”<sup>2</sup> Adopting a value of 2.2 kpc for the distance and  $a_{proj} = 0.97$  from Table 2.3, the astrometric signal can then be calculated using eqn 4.1. The results for the three cases are shown in Table 3.1.

Table 3.1: Astrometric signal  $\alpha$  for three  $M_A$  cases.  $\alpha$  represents the projection of the orbital semi-major axis on the plane of the sky in units of milliarcseconds.

$M_A$	$a_A$ (AU)	$a_B$ (AU)	$\alpha_A$ (mas)	$\alpha_B$ (mas)
$80 M_\odot$	4.1	10.9	1.8	4.8
$105 M_\odot$	3.6	12.5	1.6	5.4
$130 M_\odot$	3.2	13.8	1.4	6.0

I am concerned primarily with the astrometric signal for the primary, shown

---

<sup>2</sup>This equation and the numerical evaluation of it are discussed in detail in §4.4.1.

in the fourth column in the table. If the combined model is correct, it varies from 1.4 mas (largest  $M_A$  case) to 1.8 mas (smallest  $M_A$  case). In other words, the reflex motion should be detectable for measurements with an accuracy at the sub-1 mas level<sup>3</sup>. Is there an instrument that can perform differential astrometry at this level of precision?

The Hubble Space Telescope’s Advanced Camera for Surveys High Resolution Camera (HST/ACS/HRC) is a UV/Visible/NIR imaging instrument with a pixel subtense of approximately 25 mas on the sky; if we want a  $3\sigma$  detection for a 1.5 mas signal, then we need 0.5 mas, or 1/50 pixel precision, an achievable level on many optical instruments . In this section, the level of differential astrometry the HRC supports is discussed and a method for achieving the required level of precision is developed.

### 3.2 Differential Astrometry: Overview of Problem

In order to detect motion with sub-mas accuracy, the ability to measure astrometric position with an *accuracy* (not simply precision) across multiple epochs at the sub-mas level must be demonstrated. In this section, such a methodology is described along with the steps that have been taken to validate it. In the next chapter, the methodology is applied to examining the motion of  $\eta$  Car’s central star.

Differential astrometry using imaging instruments can be broken down into two separate problems, each of which can be a significant source of error. As shown in fig. 3.1, determining the separation between two stars in a single exposure involves

---

<sup>3</sup>“Sub” because we want a multi-sigma result.

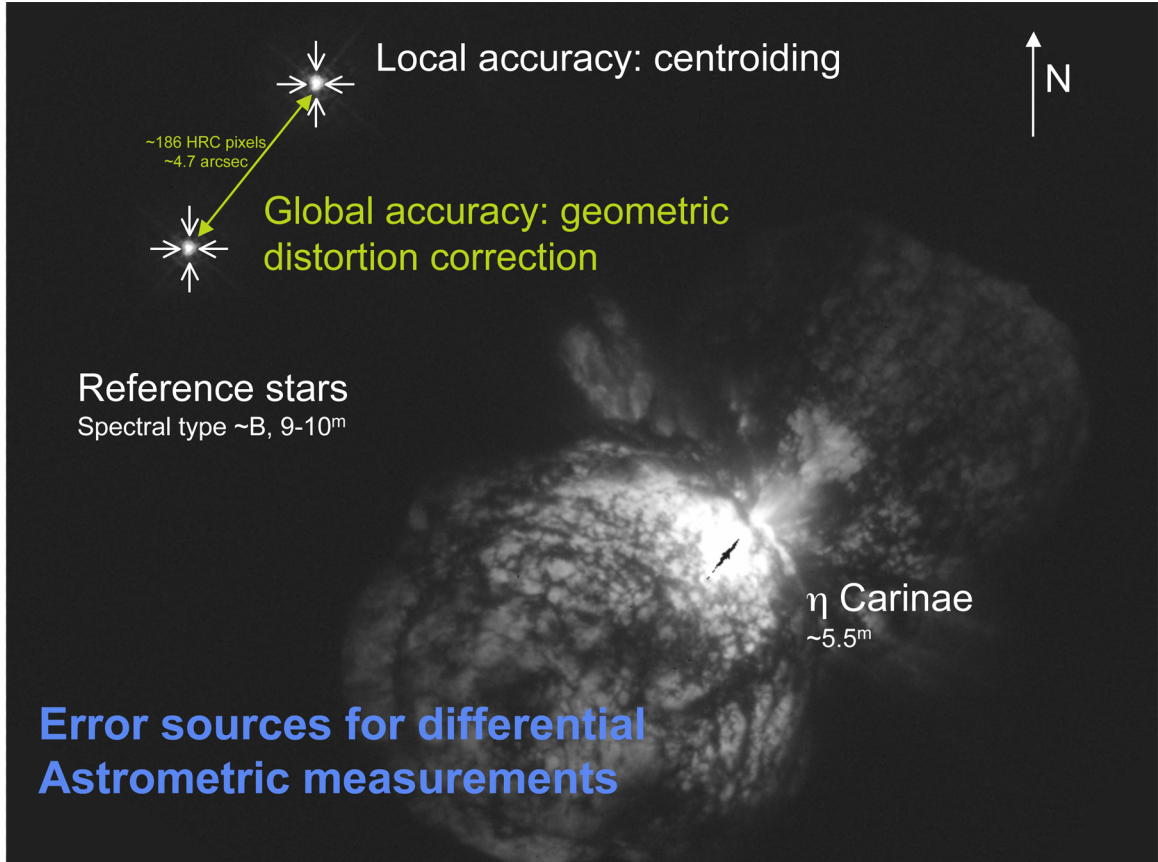


Figure 3.1: Differential astrometry using HRC images. The two dominant sources of error are shown: first, the “local” error based on the ability to centroid stars, and second, the “global” error due to effects such as distortion corrections that limit the ability to relate positions between pixels. The image is a 0.1 second HRC UV exposure (F330W) of  $\eta$  Car; it also shows the two field reference stars (“RSN” and “RSS”, Trumpler 16-64 and -65, respectively).

a three step process: first, the “local” positions of each star are determined in the detector frame of reference by precise centroiding<sup>4</sup>. Next, these positions are corrected for “global” effects such as distortion and asymmetric pixel dimensions. These corrected positions are then differenced to yield a relative separation.

Different HST instruments have different astrometric strengths and weaknesses. The WFPC2/PC instrument has relatively straightforward distortion cor-

<sup>4</sup>Note: a detailed discussion of centroiding is presented in Appendix C

rection because the instrument is positioned along the HST’s optical axis, as shown in fig. 3.2, and subject predominantly to radial (i.e., Seidel) distortion. On the other hand, the older PC detector undersamples stellar PSFs by a factor of nearly two with respect to the newer ACS/HRC instrument<sup>5</sup>. The ACS/HRC, on the other hand, is critically sampled in the mid-optical, but is subject to large, non-radial, field-dependent distortion that is much more difficult to correct. The two instruments are, in a certain sense, complementary. For purposes of astrometry, however, we will restrict our focus to the HRC, based on the assessment that overcoming the distortion correction to the required level of accuracy is feasible, while overcoming fundamental resolution and undersampling problems is more problematic. The HRC is also a newer, more capable instrument with lower noise and much larger dynamic range.

In the following sections, the methodology is described for high-precision differential measurements across multiple observing epochs. The two reference stars shown in fig. 3.1 (RSN and RSS for “Reference Stars North” and “South”)<sup>6</sup> are used as a test case, and positions measured and separations calculated for eight epochs of HRC data spanning a 2.75 year period from 2003 to 2005. The results are then used to calculate a relative proper motion of RSN with respect to RSS. The methodology and results are then validated by using 1995 WFPC2 data to calculate proper motion using a ten-year temporal baseline. In following sections, the methodology will be applied to the central star and other objects in the inner region.

---

<sup>5</sup>For example, for WFPC2/F656N,  $R_{Airy} \approx 1.5$  pixels; for HRC/F660N,  $R_{Airy} \approx 2.7$  pixels.

<sup>6</sup>These stars are also referred to as Trumpler 16-64 and 16-65 based on their membership in the Trumpler 16 association; see e.g. [Ipingle et al.(2005)].

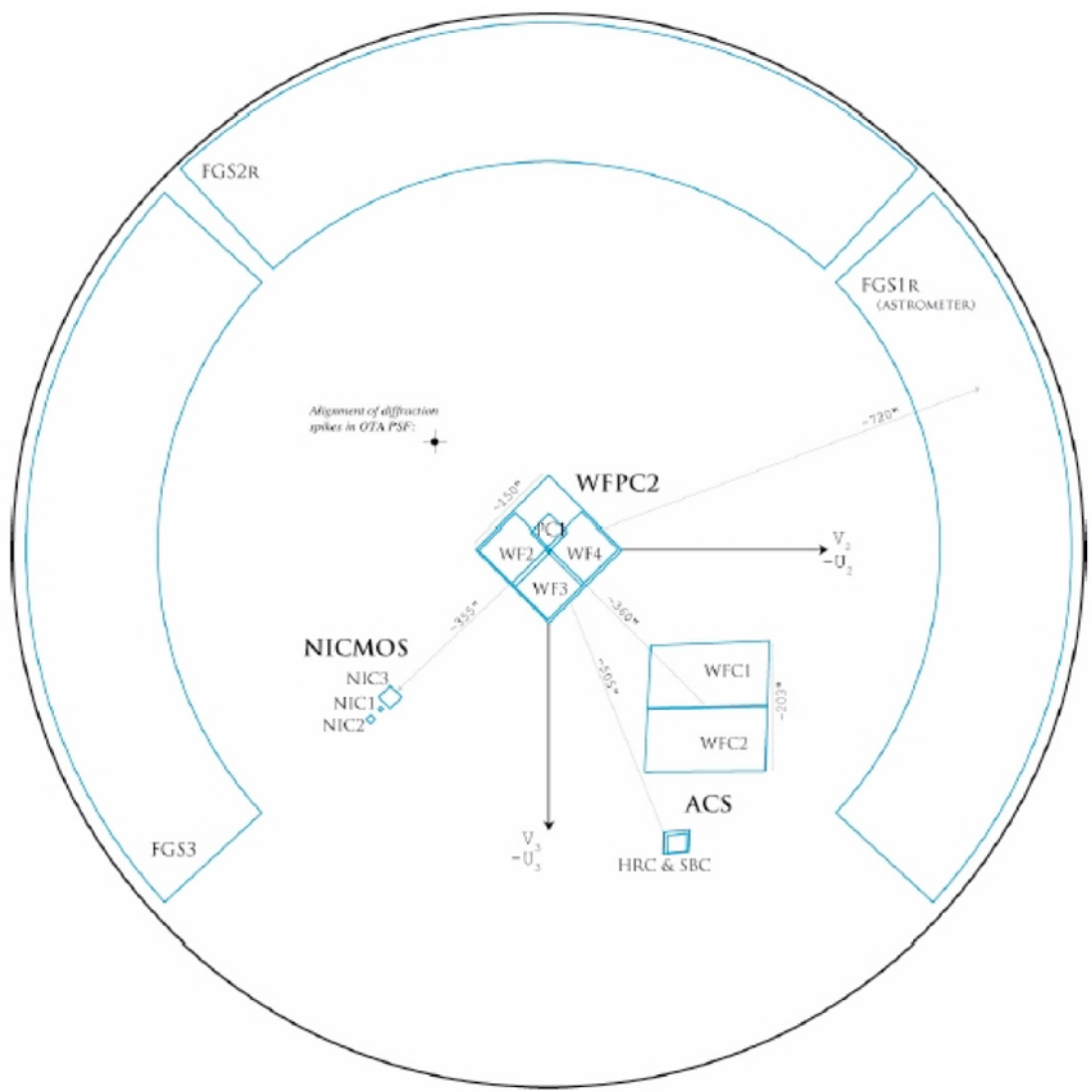


Figure 3.2: HST focal plane layout. Shapes indicate the instrument apertures as projected onto the sky. The scale is in arcsec. Contrast WFPC2 position along optical axis with the off axis ACS/HRC position. The images is reproduced from the *ACS Instrument Handbook* (Gonzaga [Gonzaga(2005)]).

### 3.3 HRC Data and Processing

The method adopted for geometric distortion correction only covers ten (out of 32) HRC filters (see §3.5 for details). The intersection of this set of ten filters with all filters used for HRC  $\eta$  Car observations is F220W and F330W. The F330W PSFs are undersampled with  $FWHM \approx 1.0$  and 1.2 pixels in  $x, y$ , respectively; the F220W observations are further undersampled, with  $FWHM \approx 0.7$  and 0.8 pixels in  $x, y$ . In order to avoid additional pixel phase error problems associated with the increased undersampling for the F220W filter, the analysis is limited to using just F330W data. The available F330W data<sup>7</sup> were taken during the eight epochs spanning nearly three years; these are listed in Table 3.2.

Table 3.2: Datasets used in developing HRC astrometry and for central star motion analysis (§4).

Epoch date	Filter	Exposures	HRC file type	Notes
2003.118 (Feb.)	F330W	0.1 sec $\times 4$	*_flt.fits	
2003.449 (June)	F330W	0.1 sec $\times 4$	*_flt.fits	
2003.550 (July)	F330W	0.1 sec $\times 4$	*_flt.fits	
2003.701 (Sept.)	F330W	0.1 sec $\times 4$	*_flt.fits	
2003.871 (Nov.)	F330W	0.1 sec $\times 4$	*_flt.fits	
2004.931 (Dec.)	F330W	0.1 sec $\times 4$	*_flt.fits	<i>Central star saturation</i>
2005.534 (July)	F330W	0.1 sec $\times 4$	*_flt.fits	<i>Central star saturation</i>
2005.849 (Nov.)	F330W	0.1 sec $\times 4$	*_flt.fits	<i>Central star saturation</i>

As noted in the table, only “\*\_flt.fits” files are used for astrometric measurements. The HRC data processing consists of two steps: CALACS and MultiDRIZ-ZLE. As described in detail in [Pavlovsky et al. (2005)], CALACS, which is a standard component of the HST MAST data archive, takes raw HRC images (\*\_raw.fits)

<sup>7</sup>These observations were made as part of a “Hubble Treasury” program (GO 9973, PI: K. Davidson).

as input, and performs the following calibration steps: flags bad and saturated pixels; subtracts overscan bias; subtracts bias image; scale and subtracts dark image; divides by flat field and multiplies by gain; calculates photometry headers for flux conversion and calculates image statistics. The output from CALACS is the “flat” file (“\*\_flt.fits”), a calibrated exposure (in units of photons) corrected for detector response and artifacts.

The file is *not* corrected for optical distortion. The files used are also not cosmic-ray cleaned. These two functions are performed by the MultiDRIZZLE task, which is distributed as part of STSDAS/PyRAF (see [Fruchter & Hook(2002)] and [Koekemoer et al.(2002)] for more information on both DRIZZLE and MultiDRIZZLE and the STSDAS implementations). In general, MultiDRIZZLE takes as input multiple files, performs cosmic ray rejection on them by comparing the input images, then combines them together into a single, distortion corrected, output “drizzled” image (“\*\_drz.fits”).

A typical next processing step with HST data is to deconvolve the data using a standard technique such as Lucy–Richardson deconvolution ([Lucy(1974)], [Richardson(1972)]). The resultant output file is then a deconvolved, geometrical distortion-corrected, detector response-corrected image.

In performing high accuracy astrometry, however, one must be cautious about the introduction of new sources of systematic error. Both the drizzling and deconvolution processes are sources of this error. Based on the analysis described in the appendix, applying both processes to point sources can introduce astrometric position systematic errors  $\sigma_{sys} \geq 0.1$  pixel. For the HRC, this is equivalent to 2.5 mas,

much larger than the astrometric signals we are trying to detect. For this reason, we restrict the high precision astrometric analysis of point-source positions to the `*_flt.fits` (i.e., pre-distortion corrected) files. A similar conclusion was reached by Anderson and King ([Anderson & King (2004)]), who indicate that high precision astrometry ( $\sigma \approx 0.01$  pix) with the HRC is only possible if one uses the `*_flt.fits` files in order to avoid the systematic errors introduced by drizzling and deconvolution.

### 3.4 HRC Local Astrometric Accuracy

I define “local” astrometric accuracy as the accuracy with which the local (intra-pixel) location of a PSF photocenter can be determined. Centroiding accuracy is a function of both the signal-to-noise of the observed PSF and the PSF sampling as well as other factors (e.g., intra-pixel QE uniformity). In the case of the HRC/F330W data, the PSF is undersampled. Simulations using TinyTim<sup>8</sup>-generated PSFs indicated uncorrected peak-to-valley pixel phase errors of  $\pm 70$  and  $\pm 30$  mpix (1.7 and 0.8 mas) in x and y directions, respectively<sup>9</sup>. This suggests strongly that simply Gaussian centroiding is not sufficiently precise to support position measurement at the sub-mas level.

The local position measurement is therefore a two-step process: centroiding followed by pixel phase error correction. Centroiding is accomplished by what I term the Grid Search Method (GSM). The GSM uses a constrained<sup>10</sup> 2D Gaussian

---

<sup>8</sup>TinyTim is a point spread function simulator developed specifically for HST instruments. See Krist [Krist(1995)], [Krist(2003)].

<sup>9</sup>“Pixel phase error” is the systematic error that results from fitting a Gaussian distribution to an undersampled PSF. See discussion in Appendix C.

<sup>10</sup>By “constrained” I mean that some of the fitting parameters are not free, and are either

fitting algorithm over a regular sub-pixel grid, with the centroid determined by the  $\chi^2$  minimum. Because of the undersampling, the GSM centroid is then corrected using a pixel phase error correction algoraithm tied to empirical data. I discuss each of these in turn.

### 3.4.1 Grid Search Method (GSM) Centroiding Algorithm

Centroiding is the determination of the photocenter of the detector response to a given source. In this case, I am centroiding point sources. In order to accomplish this, I use a Levenberg-Marquardt least-squares minimization alogorithm with a 2-D Gaussian model as the “fitting kernel.” The specific set of algorithms is available in the Markwardt IDL Library<sup>11</sup>. This algorithm is more stable and flexible than the standard 2-D Gaussian fitting routine available in IDL.

Previous work ([Dorland et al.(2004b)]) found that unconstrained centroiding using this type of fitting algorithm in the cluttered background of  $\eta$  Car was highly sensitive to the starting guess for the centroid. This was determined to be caused by the centroiding kernel’s sensitivity to clearly “inappropriate” features that are frequently present in noisy and cluttered data, resulting in convergence on highly localized  $\chi^2$  local minima, the selection of which is strongly dependent on input starting position. The solution was to force the kernel to systematically examine the entire region in question using a constrained set of parameters (widths, amplitude) in order to ensure that the resultant centroid was a global minimum for the region.

---

constant or allowed to vary over a limited range.

<sup>11</sup>See <http://cow.physics.wisc.edu/~craigm/idl/idl.html>

To effect this systematic approach, the “grid search method” (GSM) algorithm was created. The GSM calculates a  $\chi^2$  surface over a regular grid for the region in question using the Levenberg-Marquardt centroiding kernel. In order to use the GSM, the user specifies a starting position to the nearest integer pixel; the GSM generates a grid over a user-specified range of pixels and resolution setting and then executes the centroiding kernel at each and every grid position with the given set of constrained parameters, including a requirement that the fit amplitude be positive. The “centroid” is taken to be the position that minimizes  $\chi^2$ , that is, the selection of the smallest of the various local minima. For purposes of these analyses, the grid was run at 5 mpix ( $\approx 0.1$  mas) or finer resolution.

### 3.4.2 Pixel Phase Error (PPE) Correction Algorithm

Using a Gaussian fitting approach to calculate centroids for undersampled data will result in systematic offsets between the actual and measured photocenters that are dependent on where in the pixel the photocenter is actually located. This concept is not necessarily obvious at first glance<sup>12</sup>. For didactic purposes, we construct the following extreme example:

*Pixel Phase Error Example:* Consider a PSF of width 0.01 pixels. I can position the photocenter of the PSF over a range of intra-pixel  $x, y$  positions, fit an unconstrained 2D Gaussian and derive centroids. Because of the extreme undersampling in this example, only PSFs that lie on the outer pixel boundaries will result in a calculated centroid at any distance from the pixel center. As a result,

---

<sup>12</sup>See discussion in Appendix C for a more detailed discussion.

a random distribution of input centroids will have an output (calculated) distribution that is sharply peaked near the center of the pixel, with secondary (and much smaller) peaks near the edges. It is this offset between the inputs and outputs that is the PPE; a position-dependent PPE correction term can be calculated given a comprehensive set of known input (i.e., truth) and output (i.e., measured) positions.

Since the F330W data are undersampled, use of a Gaussian-fitting approach to calculating photocenter centroid will result in a PPE. Initial attempts to derive and apply PPE error correction using TinyTim-generated PSFs resulted in inferior (i.e., increased  $\chi^2$ ) results. This suggests that the idealized TinyTim PSFs are not sufficiently realistic to be useful for PSF PPE correction.

A second approach for calculating PPE is to adopt an empirical method. With only two stars, the HRC data I analyzed was severely underdetermined with respect to generating an empirical PSF. Anderson & King [Anderson & King (2004)], however, using HRC observations of 47 Tucanae covering thousands of stars, developed an empirical model of the HRC PSF for ten filters, including F330W, at a sub-1 mas resolution. I adopt the Anderson & King results as “truth” and calculated the difference between the GSM and A&K for all centroiding measurements of the two reference stars. The results are shown in fig. 3.3 as a function of A&K centroid position within a pixel.

In the figure, the differences between the GSM and Anderson & King methods are plotted as triangles. For a given pixel phase, there is some vertical spread in the offset due to random errors associated with the noise of the centroiding process. The characteristic sine-like PPE trend is clearly present in the data. The solid line

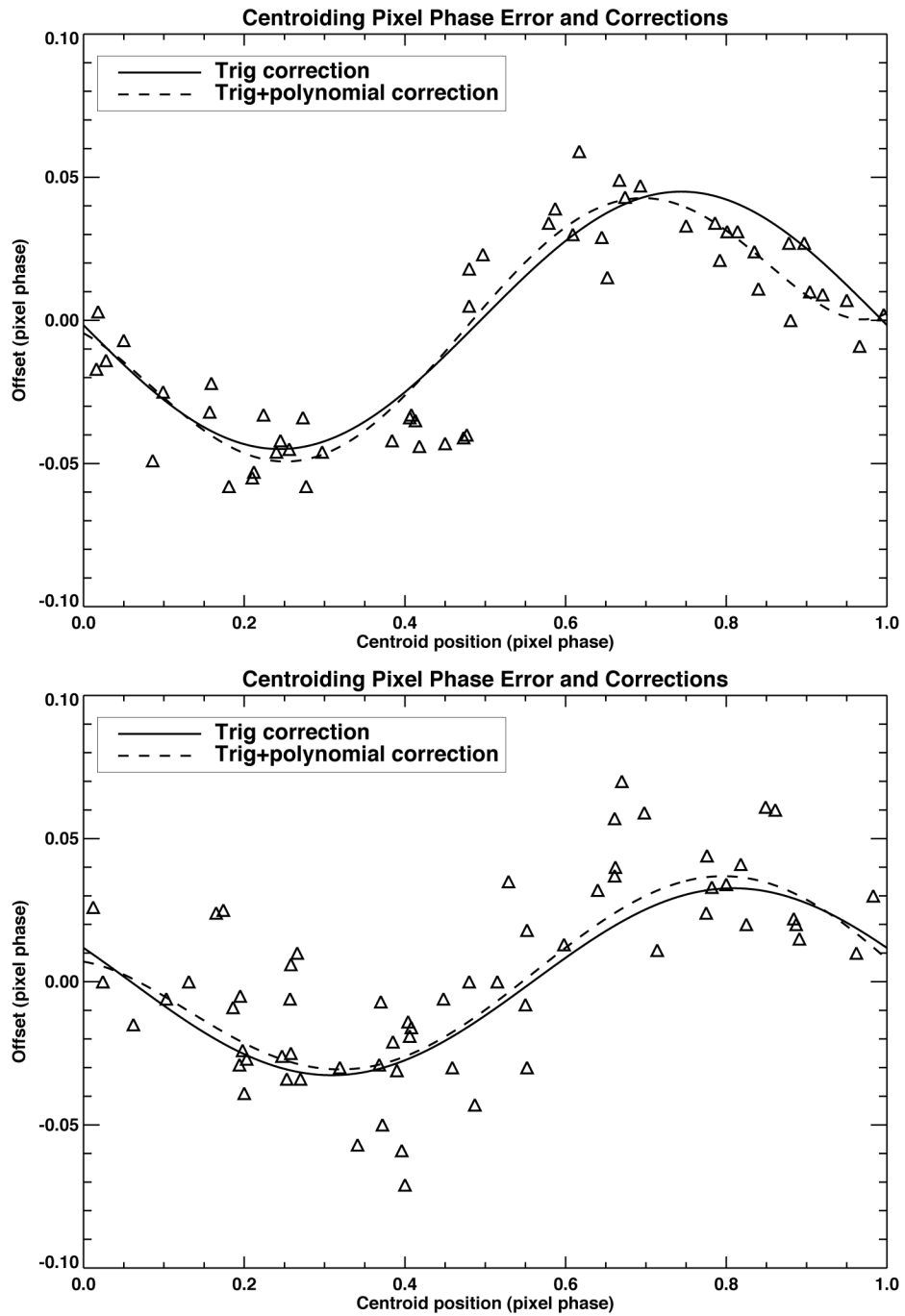


Figure 3.3:  $O - C$  values for pixel phase measurements. Pixel phase offset between the GSM and A&K methods is shown a function of A&K pixel phase. (Top) X-direction; (bottom) Y-direction. Triangles are the measured differences between the two methods; solid line is the best-fit sine function; dashed line is the best-fit sine function, with an additional third-order polynomial correction.

represents the best-fit sine function, with the constraint that the period close over one pixel. This correction is termed “PPE1.”

Uncorrected systematic structure is still present in the residual data after correction with PPE1. This is seen most clearly in the X-direction data; for example, in the region between pixel phase = 0.7 and 1.0, PPE1 clearly overestimates the offset. The X-direction data are steeper near the center of the pixel (phase = 0.5) and shallower towards the edges. This is an artifact of fitting a Gaussian function to the relatively narrow core of an Airy PSF<sup>13</sup>. There is also an obvious asymmetry, with the deviations from PPE1 much larger in the right half (pixel phase = 0.5-1.0) of pixels than in the left half (pixel phase = 0.0-0.5). To correct for these deviations from PPE1, a third-order polynomial was fit to the PPE1 residual data. The sine+polynomial fit function is shown as a dashed line. This second correction is termed “PPE2.”

Table 3.3: Effectiveness of PPE Corrections. RMS errors shown for uncorrected, sine corrected (PPE1) and sine+polynomial corrected (PPE2) data. “%” columns indicate corrected error as a percent of raw error.

		$\sigma_x$		$\sigma_y$		
	(mpix)	(mas)	(%)	(mpix)	(mas)	(%)
Raw	164	3.94	–	127	3.56	–
PPE1	21	0.50	13	23	0.64	18
PPE2	11	0.26	7	14	0.39	11

Employing the PPE1 correction, the PPE error is reduced to about approximately one-sixth the uncorrected error. Use of PPE2 further reduces PPE by another factor of two, and, perhaps more importantly, as shown clearly in fig.3.3,

<sup>13</sup>To leading approximation, the HRC PSFs are Airy- rather than Gaussian-like.

the residuals are distributed randomly around the fitted function, in contrast to the PP1 results, which show significant residual systematic trends. Based on the results presented in Table 3.3 and assuming a sufficiently large signal, the final *systematic* error due to uncorrected PPE alone is estimated to approach 10 mpix ( $\approx 0.26$  mas) per axis.

### 3.5 HRC Global Astrometric Accuracy

The second major component of differential astrometry is that of relating the local positions derived through centroiding to one another over the entire detector. As described above (§3.2), this is made difficult for the HRC by the very large and complex field-position dependent distortion the detector is subject to. A complete solution to distortion at the level of accuracy I require would necessitate observations of many hundreds or thousands of stars with multiple orientations. This is beyond the scope of this analysis.

Fortunately, the Anderson & King analysis addressed this problem<sup>14</sup>. As mentioned previously, Anderson & King analyzed HRC observations of 47 Tucanae spanning three HST General Observer (GO) campaigns. These data were originally analyzed by Meurer et al. [Meurer et al. (2002)], and a fourth-order polynomial solution with a global accuracy  $\approx 0.1$  pixels ( $\approx 2.5$  mas) was obtained. Anderson & King sought in their analysis to improve Meurer et al.’s accuracy by an order of magnitude. They developed a method that includes filter and field-dependent fine-scale distortion corrections to supplement the fourth-order approach developed

---

<sup>14</sup>In fact, the Anderson & King PSFs were originally derived to support the analysis of distortion.

by Meurer et al. They estimate the final global accuracy of their approach  $\approx 0.01$  pixels for the ten HRC filters covered.

Their methodology was adopted by STScI for use in the Space Telescope Data Analysis System (STSDAS) software package for reducing ACS/HRC data [Pavlovsky et al. (2005)]. Specifically, Anderson & King was implemented in both the STSDAS PyDRIZZLE and TRAN tasks, both of which are components of the ANALYSIS.DITHER package. PyDRIZZLE is the PyRAF implementation of the DRIZZLE task that resamples and regrids HST data, correcting for geometric distortion as part of the functionality. TRAN is a coordinate transformation program that converts coordinates on the non-corrected detector into distortion-corrected coordinates (and vice-versa). Both tasks utilize the IDCTAB files for the fourth-order geometric distortion correction, and “tweak” files (the actual nomenclature is “\*\_dxy.fits”) that contain the field-dependent fine structure adjustments. In principle, TRAN should produce distortion correction results with global accuracies equal to the accuracies achieved by Anderson & King, i.e. 0.01 pixels ( $\approx 0.25$  mas).

Two algorithms thus exist for correcting HRC geometric distortion, ostensibly to the 10 mpix ( $\approx 0.25$  mas) level of global accuracy. Both of these algorithms are based on the same underlying data and analysis, only their implementations differ. In the next section, I analyze the differences that arose when the two methods were used on this same input set of centroids.

### 3.6 Composite Results

The total differential astrometric error is composed of error from both the local and the global processes. In order to select the optimal combination of methodologies for performing differential astrometry using HRC, I considered three cases: 1)  $\text{PPE2}_{local} + \text{TRAN}_{global}$ ; 2)  $\text{A\&K}_{local} + \text{A\&K}_{global}$ ; and 3)  $\text{PPE2}_{local} + \text{A\&K}_{global}$ , where A&K refers to the software developed by Anderson based on the analysis work done in Anderson & King.

The analyses covered all eight epochs of HRC  $\eta$  Car F330W data, with each epoch consisting of four 0.1 sec exposures taken within a few hours of each other. The local (centroding) method was applied to each exposure for both stars using the pre-geometric distortion corrected HRC images. The local centroid results were then transformed using the global method into distortion-corrected coordinates. Intra-epoch separation was calculated by taking the mean value for each epoch. Intra-epoch uncertainty was calculated by taking the standard deviation (SD) of the distribution of centroids about the mean for a given epoch.

The results for all three cases are shown in figs. 3.4, 3.5, and 3.6 and summarized in Table 3.4.

Both cases 1 and 3 display smaller intra-epoch SDs, and the SDs are more consistent across multiple epochs than the A&K SDs, which vary significantly from epoch to epoch. The smaller, more consistent SDs suggest that the PPE2 is a more robust centroding algorithm than the A&K one, which shows much larger variations in the spread of the separation data between epochs.

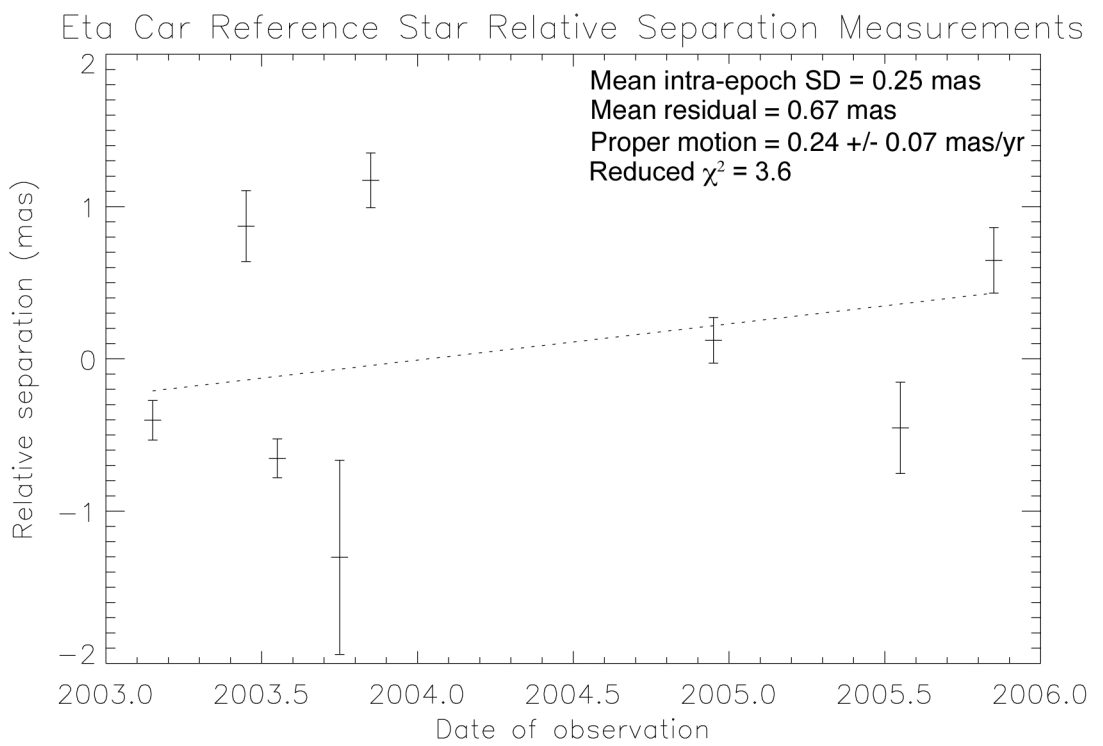


Figure 3.4: Relative separation and proper motion calculated using PPE2+TRAN combination (case 1). Intra-epoch proper mean separations are shown, along with intra-epoch standard deviations (SD). Dotted line is best linear fit to mean inter-epoch separations inversely weighted by its SD.

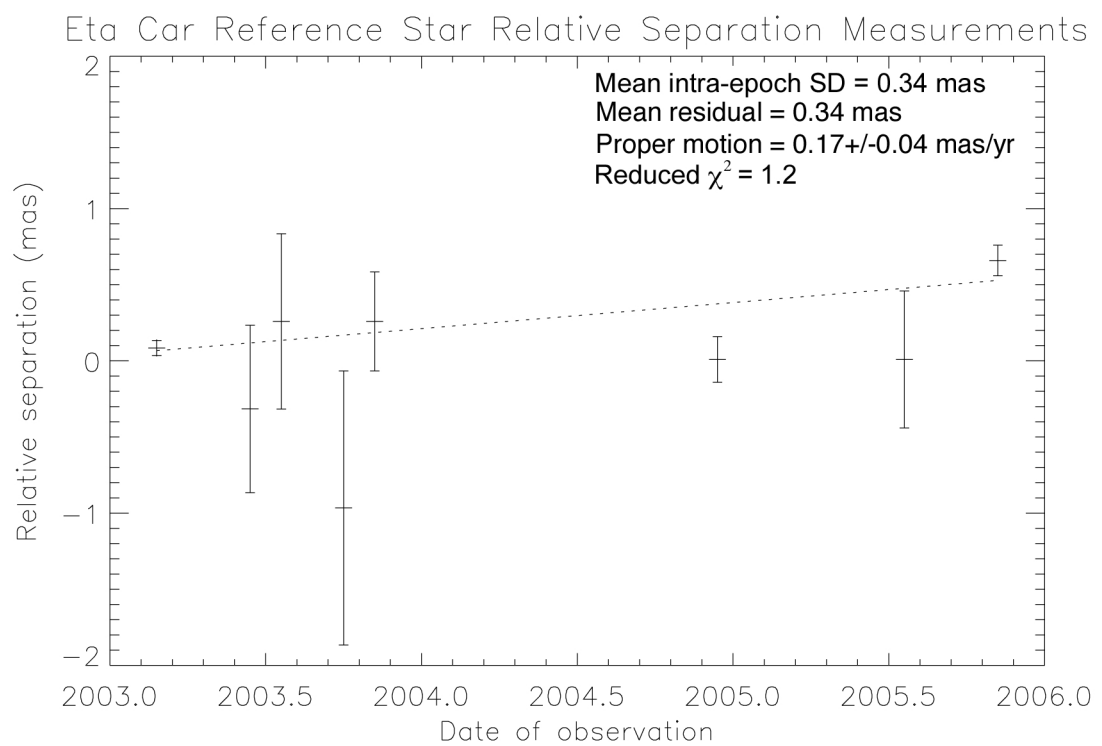


Figure 3.5: Relative separation and proper motion calculated using A&K+A&K combination (case 2).

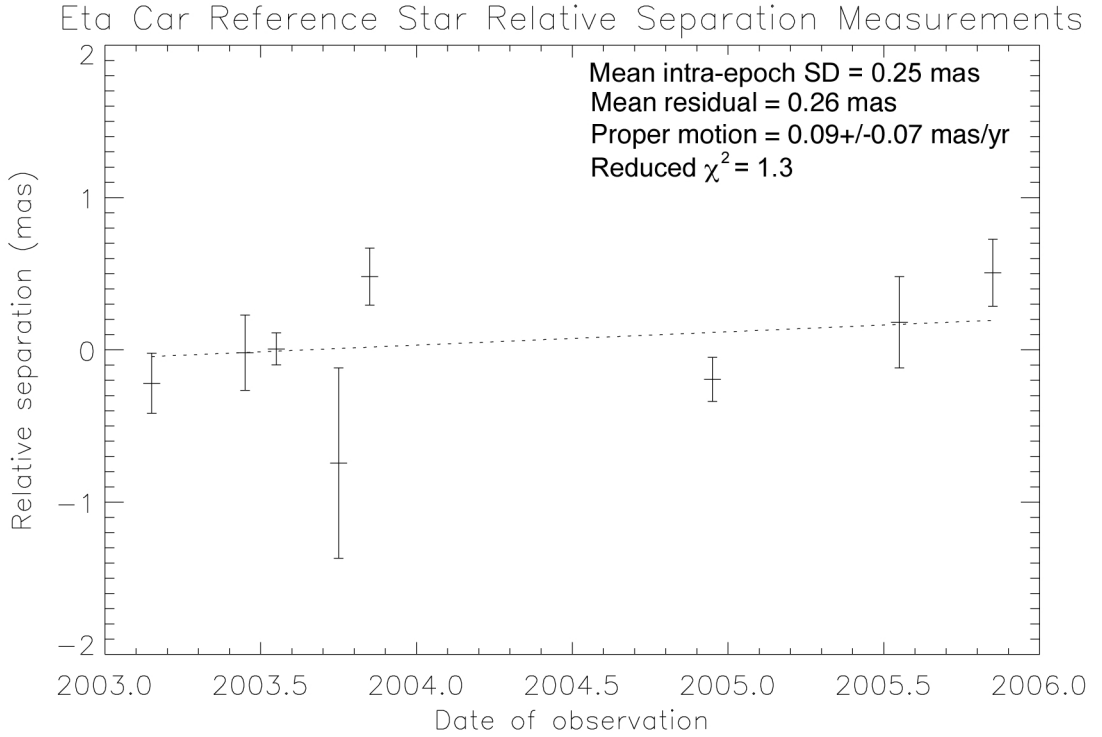


Figure 3.6: Relative separation and proper motion calculated using PPE2+A&K combination (case 3). This combination had the smallest, most consistent errors.

On the other hand, the mean residuals for both A&K distortion correction cases (2 and 3) are smaller and more closely match the average SDs than the TRAN case (1). In fact, the average TRAN residuals are two and a half times larger than the SDs, suggesting that the geometric transformations algorithm in TRAN has a systematic limit of approximately 0.03 pixels (0.7 mas), nearly three times the goal of the distortion correction work for HRC.

These results (see Table 3.4) suggest that the best combination of local and global astrometric processes is case 3, PPE2 *local* + A&K *global*. The results are consistent with global astrometric position measurement at the 0.01 pixels (0.25 mas), level. The derived proper motion has an error of 70 *microarcseconds* per year.

I thus provisionally adopt this as the optimal method pending further confirmation (see next section, §3.7).

Table 3.4: Comparison of astrometric (local and global) accuracies for three techniques.

Local	Global	$< SD >$ (mas)	Fit residual (mas)	$\chi^2_{\text{red}}$	Proper motion (mas year $^{-1}$ )
PPE2	TRAN	0.25	0.67	3.6	$0.24 \pm 0.07$
A&K	A&K	0.39	0.34	1.2	$0.17 \pm 0.04$
PPE2	A&K	0.25	0.26	1.3	$0.09 \pm 0.07$

Adopting case 3, I note that there are still residuals. What is the nature of these residuals? Given eight epochs, we would expect two or three measurements to be between one and two standard deviations from the mean. In fig. 3.6, two epochs (November, 2003 and December, 2004) appear to fall under this category, consistent with the statistics. Based on these results, I conclude that remaining residuals are consistent with Gaussian statistics and thus most likely due to natural measurement limitations. I note, however, that the A&K methodology does not include temporal effects such as changes in the instrument focal length due to breathing, etc., that could have an effect on the size of the distortion correction. One *caveat*: while these effects do not seem to appear in these data, I note that the separation we are measuring is approximately 20% of the total size of the detector. If the errors scale as the measurement distance, (i.e., by a factor of three in the case of central star motion—see §4), then they could be sufficiently large to preclude the targeted measurement accuracy. This will be discussed in more detail in §4.4.2.

### 3.7 Confirmation with Earlier Epoch Data

The results from the previous section indicate that the PPE2+A&K methodology results in the smallest “internal” errors for the proper motion calculation. This does not mean, however, that the derived proper motion is actually valid. In order to confirm the proper motion and validate (or not) the methodology, earlier epoch data are needed with a long enough temporal baseline to allow for independent calculation of proper motion with the required accuracy.

I consulted USNO’s Naval Observatory Merged Astrometric Database (NOMAD) [Zacharias et al.(2004)] in an attempt to locate either proper motion values or earlier epoch position information for the two reference stars. NOMAD is a merged catalog system of over a billion visible and NIR stars. It contains the following component catalogs: UCAC2 [Zacharias(2003)], USNO-B [Monet et al.(2003)], Hipparcos [Perryman et al.(1997)], Tycho-2 [Høg et al.(2000)], and 2MASS [Cutri et al.(2003)].

NOMAD reports only a single source at the approximate location of the two reference stars. Discussions with N. Zacharias [Zacharias (2006)] indicate that that two stars are most likely merged into a single source in all ground-based catalogs due to their relatively small separation ( $< 5$  arcseconds) and proximity to  $\eta$  Car. The best current catalogs are therefore of no use in determining either proper motion or earlier epoch positions.

A second source of earlier epoch data are the mid-1990s observations made of  $\eta$  Car using the WPFC2/PC instrument. While the PC in general is more poorly

sampled than the HRC for the corresponding filter, archival data from observations made by Westphal et al. in 1995 were found that extend out to  $1 \mu\text{m}$  using the F1042M PC filter. These data are approximately 1.8x *better* sampled than the HRC F330W data, thus do not need PPE correction in order to achieve a 0.01 pixel systematic local centroiding floor.

The two reference stars are early-type B stars, thus are relatively dim at 1 micron. However, the Westphal data include two 200-sec exposures, which is enough to get large signal-to-noise on both of the reference stars. The brighter of the two (RSN) is slightly saturated in a single pixel, but as shown in the Appendix, the centroiding accuracy is driven by the pixels in an annulus of width FWHM. As a result, centroiding is relatively insensitive to *slight* central pixel saturation.

Using the two 200-sec exposures, I centroided using the GSM method, and did not correct for pixel phase error. The local coordinates were converted to global coordinates using TRAN (in the WFPC2 case, there is no other option; also, due to the fundamentally different nature of the distortion for the WFPC instrument, there is strong reason to believe TRAN is capable of achieving the quoted 0.01 pixel accuracy for its WFPC2 transformations). Separations were then determined from the transformed coordinates, and a mean separation calculated.

Figure 3.7 plots the results from the analysis of the WFPC2/PC F1042M data along with the later HRC F330W data. I have adopted 0.01 pixels (=0.5 mas) as the error bars for the WFPC2 data based on discussions with STScI and the close agreement of the local (centroiding) results. Proper motion has been calculated using all of the data, properly weighted, and is shown in the figure with a dotted

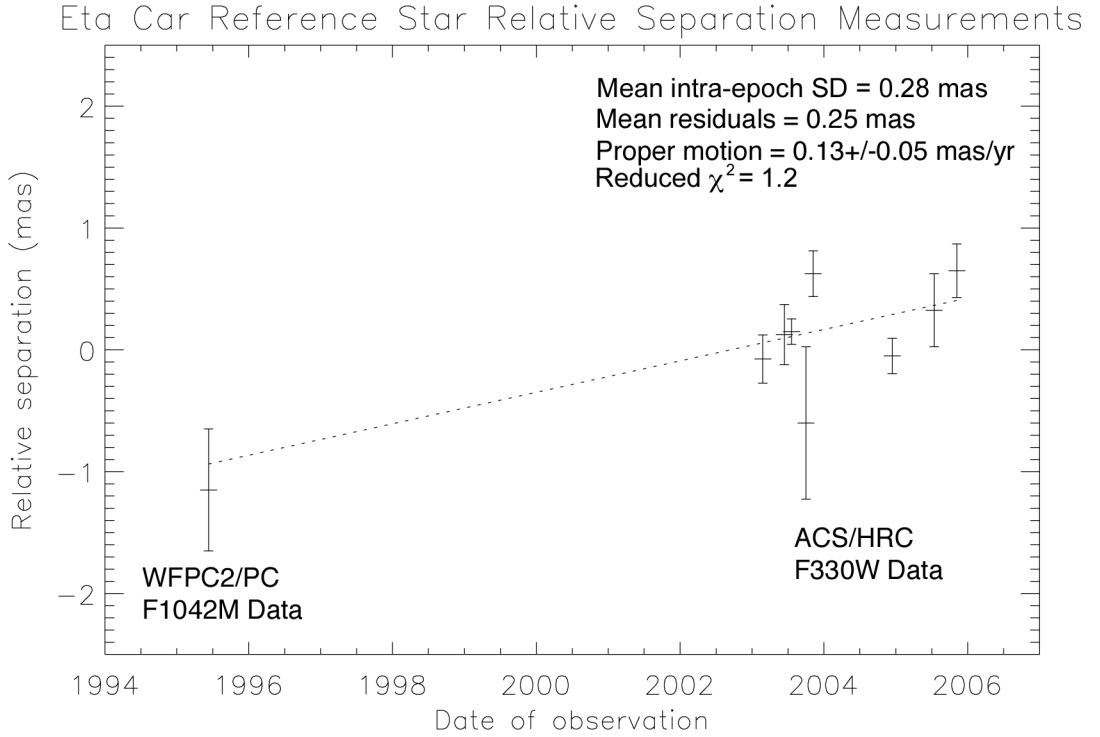


Figure 3.7: Relative separation and proper motion calculated using PPE2+A&K combination (HRC) and GSM+TRAN (WFPC2). The WFPC2 data were observed in 1995, while the HRC data were observed over a 2.75 year period from early 2003 to late 2005. The revised, long-baseline proper motion result is consistent with the internal PPE2+A&K proper motion.

line.

The long-baseline proper motion value of  $pm_{rel} = 0.13 \pm 0.05$  mas/year is consistent with both the PPE2+A&K and the A&K+A&K results (see figs. 3.6 and 3.5). The former method, however, results in smaller residuals (0.26 mas vs. 0.34 mas) and smaller and more consistent intra-epoch SDs (0.26 mas vs. 0.39 mas). It is thus preferred to the latter.

### 3.8 Summary: Accuracy of HRC Astrometry

I have developed a method for calculating with high accuracy the positions and relative separations of sources from HRC/F330W data. Using a test case of the two  $\eta$  Car reference stars (RSN and RSS), I have derived position measurements with an accuracy of approximately 0.25 mas (= 0.01 pixels ), and calculated internal proper motions over a 2.75-year period to an accuracy of 0.07 mas/year. I have also demonstrated a method for performing differential astrometry at the 0.01 pixel (0.5 mas) level for WFPC2/PC in the F1042M band. Relating the derived positions across the two epochs (1995 for WFPC2 and 2003–2005 for HRC), I find the resultant proper motion is consistent with the internal proper motion values calculated using HRC data only and the much smaller HRC temporal baseline. I thus conclude that the earlier epoch WFPC2 analysis confirms the methods and accuracies of the HRC data analysis.

## Chapter 4

### Astrometric Analysis of Central Star Reflex Motion

The goal of the previous section was to develop and validate a methodology for differential astrometry using HST/HRC data that was sufficiently accurate to detect relative motion over multiple observing epochs at the  $\sigma \approx 0.5$  mas (or better) level. This level of accuracy would make the technique sufficiently precise for detecting astrometric reflex motion given the binary model described in Table 2.3. In this section, the methodology for measuring  $\eta$  Car's central star position and, using successive observations, relative motion is described. First, the data are reviewed; next, the methodology is described and errors estimated; finally, results are described and possible interpretations discussed.

#### 4.1 Data

For reflex motion analysis, the same ACS/HRC F330W data described in §3.2, and shown in Table 3.2 were used. The data set consisted of eight observing epochs (Feb., June, July, Sept., and Nov. 2003; Dec. 2004; and July and Nov. 2005), each one of which was composed of four 0.1 sec HRC exposures observed using the ACS F330W filter. In each of these exposures, the two reference stars (RSN and RSS) were present and unsaturated.

Photometry of the central star over this three-year period reveals that it is

brightening in the UV. As a result, since the same exposure times were used over this period, the 2004 and 2005 central star data were saturated, as denoted in the table. This limited the utility of the post-2003 epochs as discussed in more detail in §4.3.1.

## 4.2 Methodology

In order to assess possible astrometric reflex motion, the PPE2 local (centroding) methodology (2D Gaussian centroding, with observed pixel phases corrected using the functions shown in fig. 3.3), was employed along with the A&K method for global coordinate transformations that include full geometric distortion correction as described in §3.

Because multiple epochs of data observed over several months are being used, the HRC fields are rotated at various angles<sup>1</sup>. This is not normally a problem, as the DRIZZLING/MultiDRIZZLING tasks are typically used to rotate the image so that North is up. In this case, however, the very high metric accuracy requirements preclude the use of DRIZZLE.

The motion (or lack thereof) of the central star must be measured with respect to something. In this case, the two reference stars present in the image (see fig. 4.1) allow me to define a reference frame.

I define the origin vector  $\vec{O}$  as the midpoint between RSN and RSS vectors ( $\vec{N}$  and  $\vec{S}$ , respectively), i.e.:

---

<sup>1</sup>The angle of the HST OTA axes is a strong function of date of observation due to solar panel illumination constraints on the spacecraft bus.

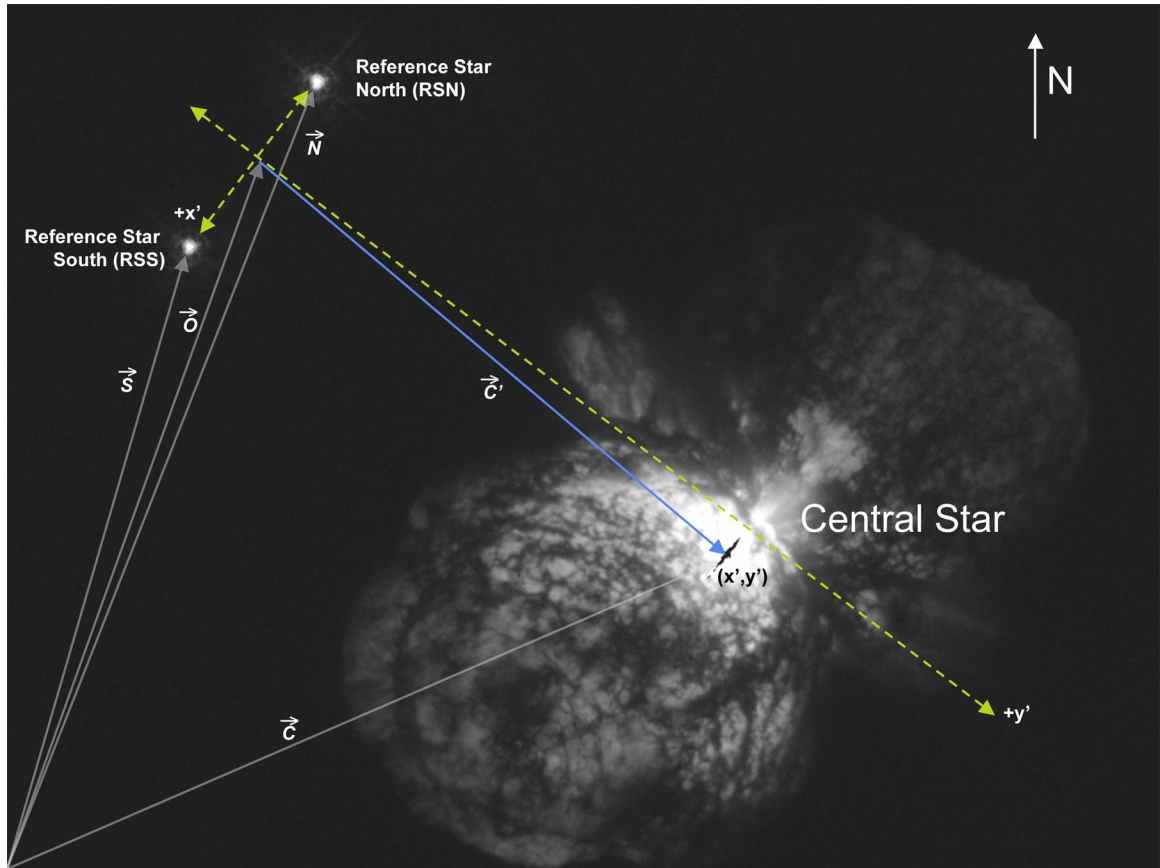


Figure 4.1: Reference frame for F330W ACS/HRC observations.  $x'$  and  $y'$  axes are defined with respect to the two reference stars (“RSN” and “RSS”, Trumpler 16-64 and -65, respectively), as shown in the figure, and are independent of a given epoch’s rotation. Vectors are discussed in text.  $PA_{\hat{x}'} = 142^\circ$  and  $PA_{\hat{y}'} = 232^\circ$ .

$$\vec{O} = \frac{\vec{N} + \vec{S}}{2} \quad (4.1)$$

The offset vector from the origin to the central star is given by:

$$\vec{C}' = \vec{C} - \vec{O} \quad (4.2)$$

where  $\vec{C}$  is the central star position vector and  $\vec{C}'$  is the central star offset from the reference frame origin, both in image coordinates.

The basis unit vectors for the stellar reference frame are given by:

$$\hat{x}' = \frac{\vec{S} - \vec{N}}{\|\vec{S} - \vec{N}\|} \quad (4.3)$$

$$\hat{y}' = \mathbf{R}(90^\circ) \hat{x}' = \begin{pmatrix} 0 & -1 \\ 1 & 0 \end{pmatrix} \hat{x}' \quad (4.4)$$

where  $\mathbf{R}(90^\circ)$  represents the rotation matrix for a  $90^\circ$  rotation. The coordinates  $(x', y')$  for the Central Star in the stellar reference frame are then given by:

$$x' = \vec{C}' \cdot \hat{x}' \quad (4.5)$$

$$y' = \vec{C}' \cdot \hat{y}' \quad (4.6)$$

and are independent of the specific epoch's instrument orientation. Based on measurements from distortion-corrected images, the position angles (PAs) of  $\hat{x}'$  and  $\hat{y}'$

are  $PA_{\hat{x}'} = 142^\circ$  and  $PA_{\hat{y}'} = 232^\circ$ .

#### 4.2.1 Error Estimation for New Coordinates

From the previous section, we have an estimate of 0.25 mas for the per-epoch position accuracy using the PPE2+A&K methodology. How does this position error translate into  $(x', y')$  measurement errors for  $\eta$  Car in the stellar reference frame?

For any function  $f(x_1, \dots, x_n)$ , the approximate total error  $\sigma$  can be written as:

$$\sigma = \sqrt{\sum_{i=1}^n \left( \frac{\partial f}{\partial x_i} \sigma_{x_i} \right)^2} \quad (4.7)$$

assuming the individual errors  $\sigma_{x_i}$  are small ([Bevington & Robinson(2003)]), which, in the case of the HRC astrometric results, is a valid assumption. Applying eqn. 4.7 to eqns. 4.5 and 4.6, and evaluating using representative values for the positions of RSS, RSN and the central star, I get:

$$\sigma'_x \approx 4.4\sigma = 1.1 \text{ mas} \quad (4.8)$$

$$\sigma'_y \approx 1.2\sigma = 0.3 \text{ mas} \quad (4.9)$$

where  $\sigma$  is my measurement error from the previous section ( $\approx 0.25$  mas). Because the central star is much farther away from the origin than the width of the measurement baseline and the fact that the  $y'$ -axis is generated by rotating this baseline, the measurement *from* the central star *to* the  $y'$ -axis—that is, the  $x'$  coordinate—is  $\approx 3.7 \times$  the error of the measurement along the  $y'$  coordinate.print,

### 4.2.2 Implications for Binary Detection

The primary constraint this implies is that only binary orbits with major axes aligned along the  $y'$  axis will have sufficiently large signal for detection. The  $x'$  measurements will constrain the size of the signal (and, by implication, the orbital parameters), but are too coarse to either prove or disprove the binary model described in Table 2.3. Serendipitously, as noted in the discussion of Smith et al.'s results of UV shadowing, the current thought is that the major axes do run roughly along a  $PA_a \approx 225^\circ$ , close to parallel with my  $y'$  axis, with a  $PA_{\hat{y}'} = 232^\circ$ . Thus, my measurements are well suited for testing the current model.

## 4.3 Observations

As described in Table 3.2 (§3.3), each epoch consisted of four 0.1 sec exposures. The central star position was measured in  $x'$ ,  $y'$  coordinates for each exposure, and per-axis mean positions and standard deviations of the mean (SDOM) were calculated for each epoch. These are given in Table 4.1. Overall mean positions for both  $x'$  and  $y'$  coordinates were calculated, and the per epoch position differences with respect to these overall mean positions are shown in the  $x' - \bar{x}'$  and  $y' - \bar{y}'$  columns.

### 4.3.1 Saturation

A secular increase in integrated F330W flux over the 2.75 year observing period resulted in saturation during the last three observing epochs (2004–2005). Two of

Table 4.1: Measured central star position in  $x'$ ,  $y'$  reference frame; HRC F330W data, PPE2+A&K methodology.

Epoch	$x'$ (mas)	$x' - \bar{x}'$ (mas)	$\text{SDOM}_{x'}$ (mas)	$y'$ (mas)	$y' - \bar{y}'$ (mas)	$\text{SDOM}_{y'}$ (mas)	Notes
2/2003	395.7	1.8	0.4	13,699.9	-0.3	0.3	
6/2003	396.8	0.7	1.1	13,700.3	0.1	0.3	
7/2003	396.8	0.7	0.8	13,700.9	0.7	0.1	
9/2003	395.7	1.8	1.4	13,701.5	1.3	0.5	
11/2003	396.2	1.4	1.2	13,699.1	-1.1	0.2	
12/2004	400.5	-3.0	1.7	...	...	...	<i>Sat. in <math>y'</math> direction</i>
7/2005	...	...	...	13,699.5	-0.7	0.9	<i>Sat. in <math>x'</math> direction</i>
11/2005	396.3	1.2	3.2	...	...	...	<i>Sat. in <math>y'</math> direction</i>

the fit images are shown in Fig. 4.2.

In the absence of specific anti-blooming circuitry, CCDs respond to saturation by the “blooming” of electrons out from the saturated pixel or pixels and into neighboring pixels. Because the potential barrier between columns (i.e., “channel stops”) is higher than the potential barrier between pixels in the same column [Janesick(2001)], electrons from a given saturated pixel spill into the neighboring pixels in the same column only rather than across multiple columns. This effect is present but subtle in fig. 4.2, which show the relevant short exposure images; fig. 4.3 is a heavily overexposed image that shows the relationship between blooming and detector columns much more clearly. In the images, the image x,y axes corresponds to the detector column, row axes. The “saturation” arrows mark the direction of the CCD columns (and hence, the direction of electron blooming).

From the discussion in the appendix, the centroiding result is dominated by the pixels around the FWHM. In the HRC F330W data, FWHM is slightly more than a

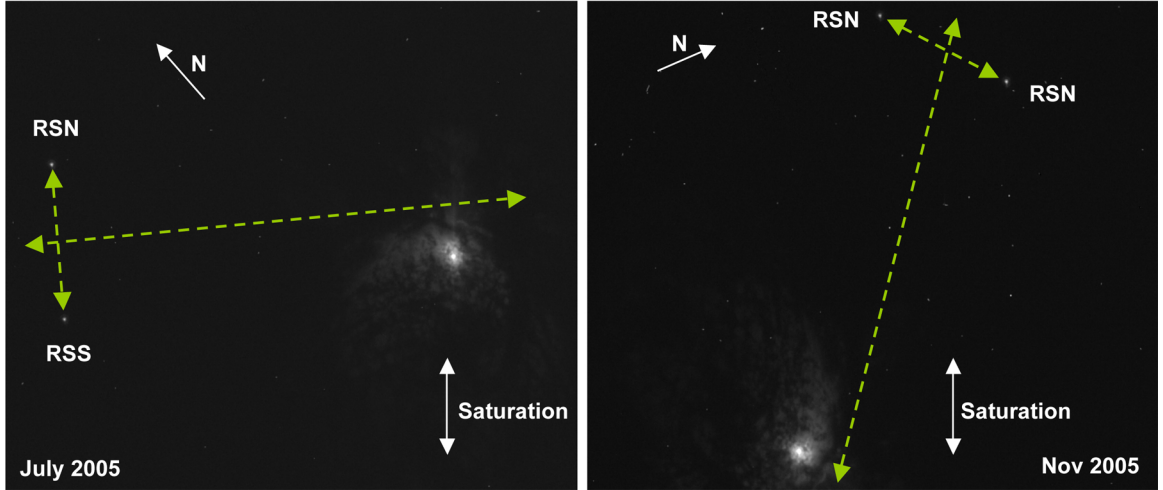


Figure 4.2: F330W 0.1 sec images for July and November 2005 epochs. Stellar reference axes are shown, along with saturation (i.e., CCD column) direction. The arrows indicate the direction of blooming. These images are pre-DRIZZLE, so have not been corrected for distortion (i.e., orthorectified).

pixel. Thus, the saturation described in these images is problematic along columns, but not across columns (i.e., the detector rows). For this analysis, I therefore reject position measurement in the column direction, but accept measurements made in the row direction.

As shown in fig. 4.2, the detector columns for the July 2005 observations are aligned very nearly in the  $\hat{x}'$  direction with the result that the saturation is nearly orthogonal to the  $y'$  measurements. The situation for the November 2005 (shown) and the December 2004 (not shown) observations are approximately reversed, with detector columns (and hence, saturation) primarily in the  $\hat{y}'$  direction, orthogonal to the  $x'$  measurements. In both cases, the saturation only extends a few pixels along a single column. The rejection of saturated data in the column direction for the 2004–2005 observations is reflected in Table 4.1 and adopted for the remainder of this chapter.

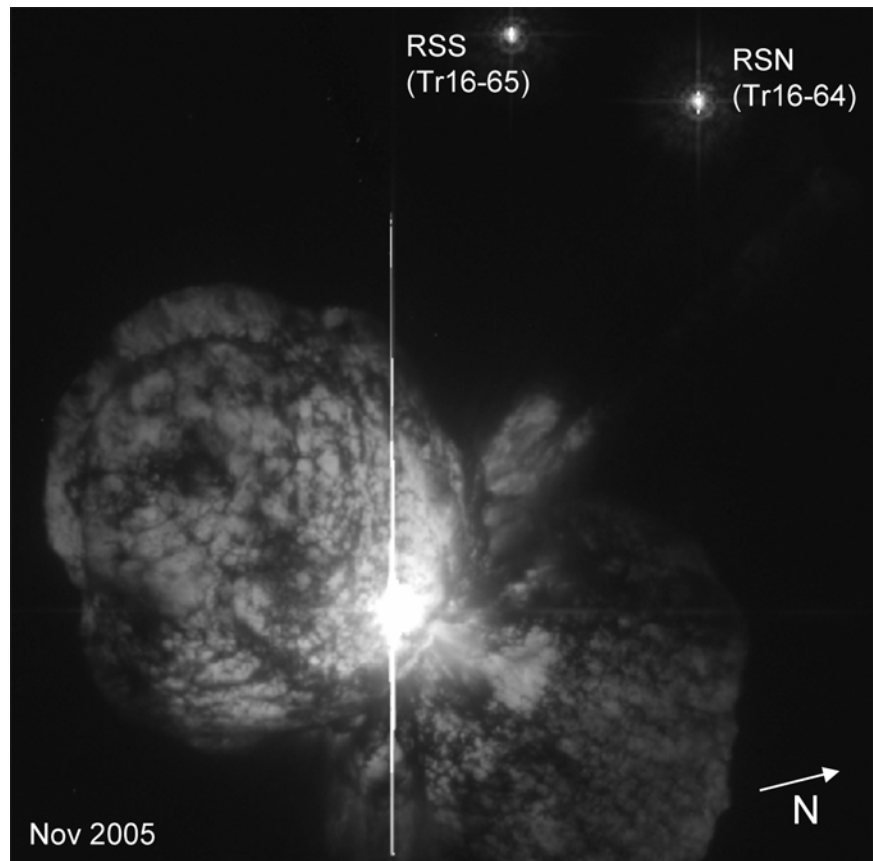


Figure 4.3: Blooming clearly shown in overexposed F330W image from Nov. 2005. Both the central star and both Tr16 field stars are saturated. The central star photoelectrons are blooming over many pixels, while the reference star saturation (which is at a much lower level) extends over a few pixels. The pixels bloom in the direction of the detector columns.

### 4.3.2 Possible Parallax Considerations

Since I am performing differential astrometry over a range of epochs that span the entire year, the effects of differing parallaxes between the two reference stars and the central star must be taken into consideration. All three stars are considered part of the Trumpler 16 association [Feinstein et al.(1973)]. Tr 16 extends across approximately 10 arcminutes in the plane of the sky [DeGioia-Eastwood et al.(2001)]. At 2250 pc, 10 arcmin subtends  $\approx 6.5$  pc. Using a spherical approximation for Tr16, and assuming the extreme case where the reference frame origin is offset from the central star along our line-of-sight by 6.5 pc (the diameter of the Tr 16 sphere), the difference in parallax would be of order a few  $\mu$ arcseconds. It can thus safely be ignored for purposes of this analysis.

### 4.3.3 Basic Astrometric Results

The results for both  $y' - \bar{y}'$  and  $x' - \bar{x}'$  measurements are shown in figs. 4.4 and 4.5, respectively. The average per epoch SDOMs are  $SDOM_{x'} = 1.40$  mas and  $SDOM_{y'} = 0.38$  mas, slightly larger than predicted in eqns. 4.9 and 4.9, but in the predicted ratio ( $\approx 3.7\times$ ). The first two statistical moments of the distribution of offsets gives mean positions and standard deviations of  $\hat{x}' = 397.5 \pm 1.7$  mas and  $\hat{y}' = 13,700.2 \pm 0.9$  mas. Adopting the errors from eqns. 4.9 and 4.9, I get reduced  $\chi^2_{x'} = 16.4$  and reduced  $\chi^2_{y'} = 44.2$ , suggesting that a more complex fitting approach is needed. The SDOM error bars for the 2004 and 2005 observations are larger than those for the 2003 observations; this is most likely due to the effects of saturation

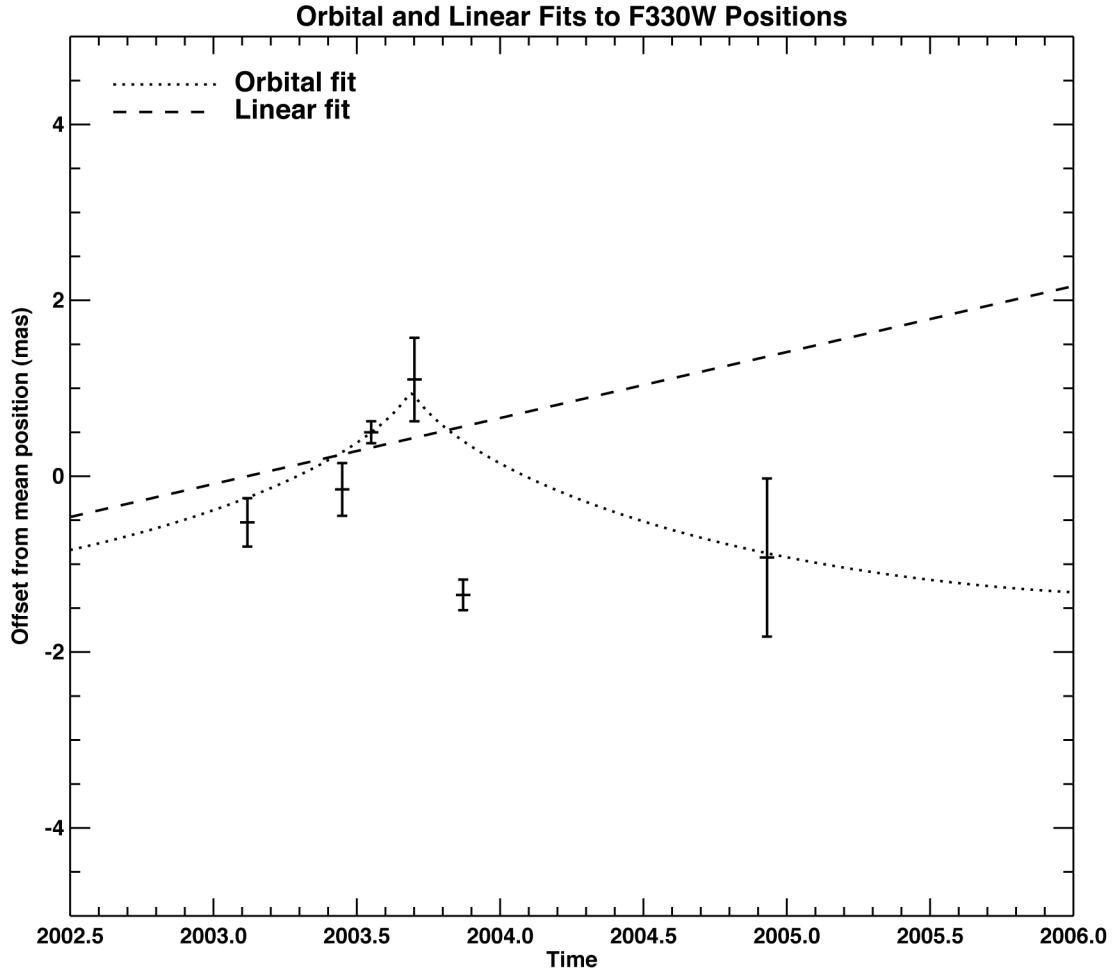


Figure 4.4: Position measurements of the central star along  $y'$  axis. Best fit solutions for linear and orbital motions (excluding Nov. 2003 measurements; see §4.4.2) also shown. Mean position  $\bar{y}' = 13,700.2$  mas.

discussed in §4.3.1.

#### 4.4 Orbital vs. Linear Motion: Best Fit

Regardless of whether or not  $\eta$  Car is a binary system, some motion with respect to the stellar reference frame defined by the Tr16 reference stars (RSN and RSS) is expected. If  $\eta$  Car is a single star, I would expect linear proper motion similar

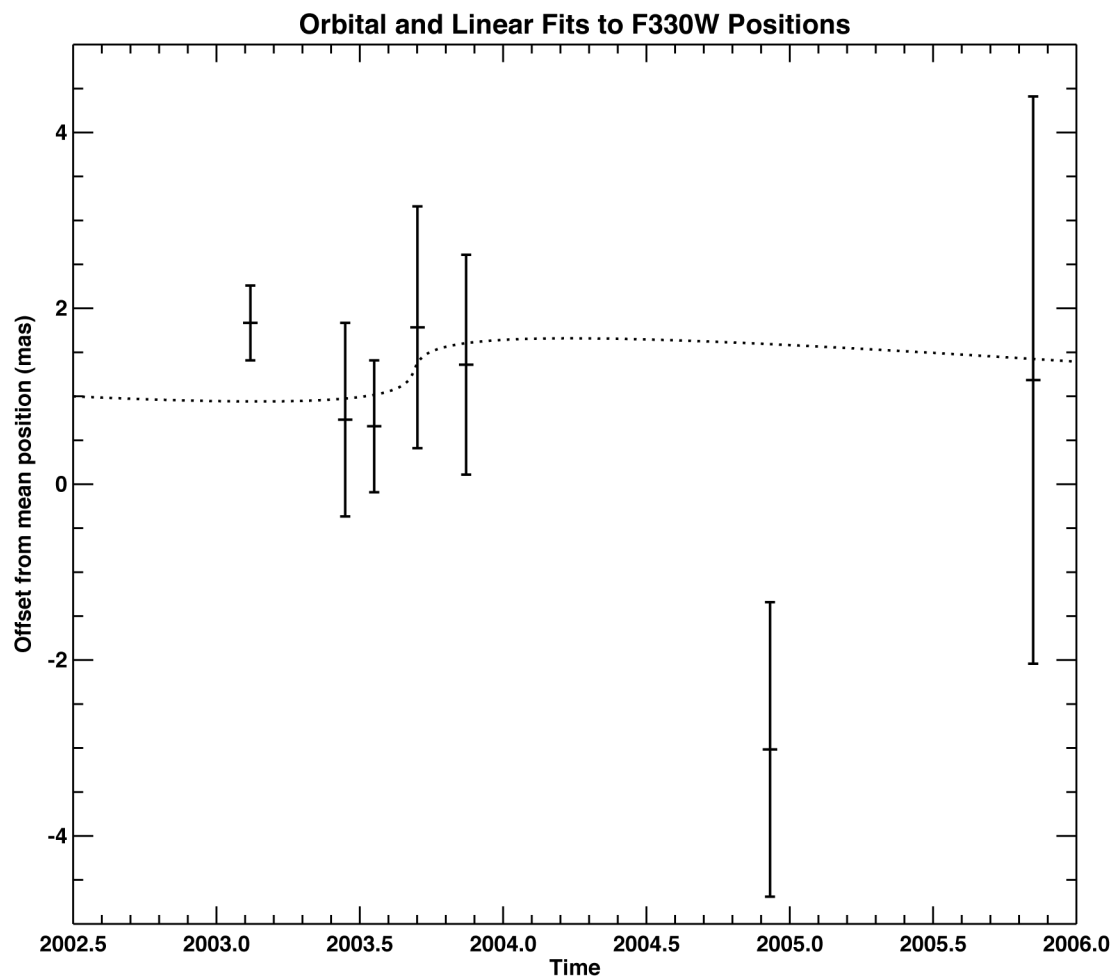


Figure 4.5: Position measurements of the central star along  $x'$  axis. Orbital solution from fig. 4.4 shown as dotted line. Mean position  $\bar{x}' = 397.5$  mas.

to that observed for the two reference stars, i.e.,  $pm \approx 0.1 \text{ mas yr}^{-1}$  (see §3.7). If, on the other hand,  $\eta$  Car is a binary, I would expect to see some combination of linear and proper motion. If the companion is sufficiently large and the orbits are oriented favorably (see Table 2.3), I would expect the astrometric reflex motion signal in the range  $1 < \alpha_a < 2 \text{ mas}$  (see Table 3.1), or approximately ten times the magnitude of the expected proper motion signal over a two-year period.

In order to compare the hypotheses, both linear and orbital motion models were fit to the  $y'$  data, with results shown in fig. 4.4. Because the accuracy in  $x'$  is so much worse than the accuracy in the  $y'$  direction, both linear and orbital models fits work equally poorly. As a result, no systematic attempt was made to fit those data. Unless otherwise noted, for the remainder of this section, the discussion is restricted to  $y'$  measurements.

#### 4.4.1 Orbit Modeling

The equation of motion for a body traveling along an elliptical orbit cannot be expressed in simple analytical form as a function of the orbital elements. To obtain the position of the body as a function of time, the transcendental Kepler's equation must be solved, i.e.:

$$M(t) = E(t) - e \sin E(t) \quad (4.10)$$

where  $M(t)$  is the “mean anomaly,” or mean motion around the center of mass for a idealized circular orbit with the same period;  $e$  is the orbital eccentricity; and  $E(t)$  is the “eccentric anomaly,” a parametrization of polar angle, related to the so-called

“auxiliary circle.”  $M(t)$  is given by the product of the mean orbital angular rate of the orbit and the time from periastron, or:

$$M(t) = \frac{2\pi}{5.52}(t - T) \quad (4.11)$$

where  $t$  and  $T$  are given in years.

For a given  $M(t)$ , eqn. 4.10 can be solved iteratively using the Newton-Raphson method, i.e.:

$$E_{i+1}(t) = \frac{M(t) - e(E_i(t) \cos E_i(t) - \sin E_i(t))}{1 - e \cos E_i(t)} \quad (4.12)$$

The “true anomaly”  $\nu(t)$  of the orbit, i.e., the angle from periastron from the focus is then given by:

$$\nu(t) = \tan^{-1} \left( \sqrt{\frac{1+e}{1-e}} \tan \left( \frac{E(t)}{2} \right) \right) \quad (4.13)$$

where  $E(t)$  is the final iteration of eqn. 4.12 after the convergence criterion is met<sup>2</sup>.

The radius  $r(t)$  of the orbit is then given by:

$$r(t) = a \frac{1 - e^2}{1 + e \cos \nu(t)} \quad (4.14)$$

and the position projections along the orbital semi-major ( $y''$ ) and semi-minor ( $x''$ )

---

<sup>2</sup>I used a convergence criterion of  $|E_{i+1} - E_i| < 1 \times 10^{-6}$

axes are:

$$y''(t) = r(t) \cos \nu + ae \quad (4.15)$$

$$x''(t) = r(t) \sin \nu \quad (4.16)$$

If I assume that the semi-major axis is approximately parallel to my  $y'$  axis, that the orbit is highly elliptical, and given the much larger errors associated with my  $x'$  measurements, I can ignore the effects of  $x''$  on measurements for the time being.

The projection of the  $y''$  orbital motion onto my  $y'$  measurement axis is thus:

$$y'(t) = y''(t) \cos \gamma \cos \delta \quad (4.17)$$

where  $\gamma$  is the previously defined angle between the semi-major axis and the plane of the sky and  $\delta$  is the angle between the projected semi-major axis ( $y''(t) \cos \gamma$ ) and the measurement  $y'$  axis, that is, the projection of the semi-major axis onto the  $y'$  measurement axis.

In order to determine the best fit, a spanning set of  $e$ ,  $a$  and  $T$  initial conditions were combined with a 5.52 year period and resultant orbits generated. For each discrete set of parameters, the  $\chi^2$  metric calculated using:

$$\chi^2 = \sum_{i=1}^6 \left( \frac{O_i - C_i}{\sigma_i} \right)^2 \quad (4.18)$$

where  $O_i$  is the measured  $y'$  position,  $C_i$  is the orbital model position (given by eqn. 4.17 for  $t(i)$ ), and  $\sigma_i$  is the SDOM for the epoch  $i$ . The “best fit” solution was taken to be that choice of parameters that minimized  $\chi^2$ .

#### 4.4.2 Problematic November 2003 Data Point

Initial fit results were poor for either model, with  $\chi^2_{reduced} = 31.9$  and 23.6 for the orbital and linear fits, respectively. The problem centers around the Nov. 2003 data point. Due to the combined effects of the epoch’s relatively small SDOM and the large distance from either the linear or orbital fits, the anomalous data point has an inordinately large impact on the  $\chi^2$  values for both models.

Measurement results have been re-checked and the raw data visually inspected for any obvious explanation of why this particular measurement appears to lie so far ( $\approx 5 - 6\sigma$ ) from where we would expect it, regardless of whether or not  $\eta$  Car is a binary. There does not appear to be a ready explanation for the data point. Using Chauvenet’s criterion for identifying illegitimate data [Taylor(1997)], this data point is rejected for both the orbital and linear motion solutions. Thus, for the remainder of this section, I will ignore the Nov. 2003 data point. I will discuss it again in the context of systematic limits to the accuracy of the reflex motion measurements (§4.5.3).

### 4.4.3 Quantitative Model/Data Results

The best fit linear and orbital solutions (not including the Nov. 2003 data point) are shown in fig. 4.4 as dashed (linear) and dotted (orbital) lines. The fit solutions resulted in the following parameters:

*Linear (proper motion) results:* The linear solution has a  $\chi^2_{reduced} = 5.3$ . The proper motion solution of the central star in the reference frame is  $pm_{y'} = 0.75$  mas  $\text{yr}^{-1}$ .

*Orbital results:* The orbital solution has a  $\chi^2_{reduced} = 1.0$ . The resultant solution parameters are:  $e = 0.95$ ,  $a = 1.15$  mas, and  $T = 2003.69$ .

In fig. 4.5, the projection of the orbital solution (derived from the observed  $x'$  motion) has been plotted as a dotted line over the actual measurements. No fitting was involved; the solution is shown simply to assess the feasibility of the  $y'$ -based orbital solution given the  $x'$  measurements.

## 4.5 Discussion of Results

The best fit to the  $y'$  data is a high-eccentricity orbit rather than a simple proper motion model. The data show a shift of approximately +1 mas ( $\approx 2$  AU) during the six months *preceding* periastron, followed by a shift of approx.  $-1.5$  mas ( $\approx 3$  AU) in the 1.5 years *after* periastron. These shifts are consistent with astrometric reflex motion caused by a high-eccentricity binary orbit lying nearly orthogonal to our line-of-sight; the resultant binary orbit model is quite similar to the second generation models, e.g. [Corcoran et al.(2001)], [Ishibashi(2001)], and

[Smith et al.(2004)], and described in Table 2.3. The  $x'$  data is, in general, consistent with this conclusion (fig. 4.5), but the measurement errors along the  $x'$  axis are too large to assign much confidence to this statement.

#### 4.5.1 Astrometric Constraints

One goal of this analysis is to determine which binary models, if any, are favored by the current results. In §5.4, I will present results that use derived physical parameters of the two stars (viz., their masses) to argue that the current data is more consistent with second generation models rather than first.

In this section, I use a simpler approach and ask if the basic observational data prefers one class of binary models over the other. I can eschew orbit fitting and simply use the mean position and standard deviation from §4.3.3 to develop very basic astrometric constraints on possible orbits and orientations. By way of example, from the discussion in §4.3.3, the  $\text{SDOM}_{y'} = 0.9$  mas. An orbit with a projected semi-major axis  $\alpha_{y'} = 1.8$  mas would therefore be excluded at the  $2\sigma$  ( $\approx 96\%$ ) level.

If I adopt a 95% confidence criterion ( $= \pm 1.96\sigma$ ), I can use the values of  $\text{SDOM}_{x'}$  and  $\text{SDOM}_{y'}$  to describe an ellipse about the mean position of the central star (see fig. 4.6). The region inside this ellipse defines the range of possible orientations and lengths of the the projected semi-major axis of the primary. The region outside the ellipse represents orientations and lengths for the projected semi-major axis that are excluded above the 95% confidence level based on the basic astrometric

results. Using the results from §4.3.3, the astrometric constraint ellipse is defined as having a semi-major axis  $a = 2.9$  mas, oriented at  $PA_a = 232^\circ$  and semi-minor axis  $b = 1.8$  mas, oriented at  $PA_b = 142^\circ$ .

I can use this approach to “test” the binary orbital models described in §2.3. Using the values listed in Tables 2.1 and 2.2, I can calculate the expected astrometric signal  $\alpha_A$  due to reflex motion in the primary.

For cases where  $\alpha_A$  is not stated explicitly, I have calculated it from the masses and period. Solving eqns. 4.12 and 3.3 simultaneously for the semi-major axis  $a_A$ , I get:

$$a_A = \frac{P^{2/3}(M_A + M_B)^{1/3}}{(1 + M_A/M_B)} \quad (4.19)$$

where  $a_A$  is given in AU. To convert to astrometric signal  $\alpha_A$  in mas, the following equation is used:

$$\alpha_A = 2.25(a_A \cos \gamma) \quad (4.20)$$

where  $\gamma$  is the angle between the semi-major axis and the plane-of-the-sky and 2.25 is the conversion from AU to mas at a distance of 2.25 kpc. The results are shown in Table 4.2

The first four models in the table have astrometric signals greater than 1.8 mas. They all thus have “exclusion regions” where the predicted astrometric signal is greater than the distance from the central star to the error ellipse. The exclusion half-angles ( $eha$ ) are calculated for each of the four cases, and the corresponding

## Astrometric Constraints on Primary Reflex Motion

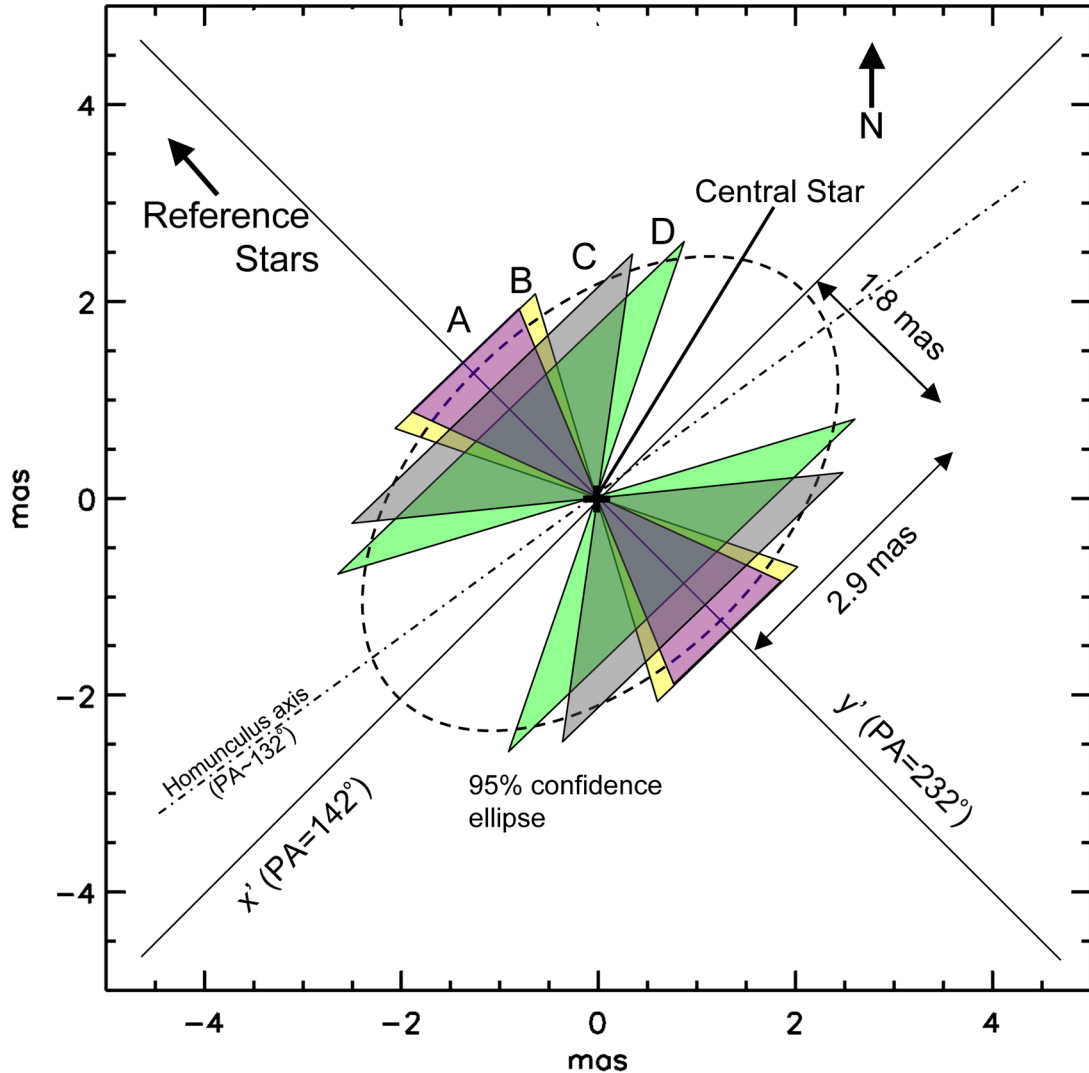


Figure 4.6: Astrometric constraints on reflex motion of primary. Astrometric motion outside the ellipse over the course of the HRC observations is excluded at the 95% confidence level. The colored regions indicate exclusion zones for semi-major axis orientation for different models (see text); half angles for the colored regions are:  $A = 25^\circ$ ,  $B = 30^\circ$ ,  $C = 49^\circ$ ,  $D = 53^\circ$ . The approximate symmetry axis of the Homunculus  $PA \approx 132^\circ$  is also shown [Davidson et al.(2001)].

Table 4.2: Effects of astrometric constraints on binary models.  $eha$  refers to the exclusion half angle defining the region where the required astrometric signal  $\alpha_A$  is less than the size of the astrometric 95% confidence ellipse (i.e., an orientation with the semi-major axis inside the given region is not allowed). Exclusion regions are shown in fig. 4.6. The first four models are constrained by the astrometric results; the last four are not.

Model	$\alpha_A$ (mas)	$eha$ ( $^{\circ}$ )	Exclusion Region	angle range 1 ( $^{\circ}$ )	angle range 2 ( $^{\circ}$ )
Dam. et al. 97	2.0	30	B	22 – 82	202 – 262
Dav. 97 (Model 1)	2.3	53	D	–1 – 105	179 – 285
Dav. 97 (Model 2)	2.2	49	C	3 – 101	183 – 281
Dam. et al. 00	1.9	25	A	27 – 77	207 – 257
Corcoran et al. 01	1.2	...	...	...	...
Ishibashi 01	1.4	...	...	...	...
Pitt. & Cor.. 02	1.2	...	...	...	...
Smith et al. 04	1.7	...	...	...	...

exclusion regions are shown as colored-in triangles in fig. 4.6 and are cross-referenced to the table with the letters A–D.

The exclusion region and angular ranges refer to the angular region around the central star where the PA of the projected semi-major axis is not allowed.  $PA_A$  is given by (see figs. 2.1 and 2.2):

$$PA_A = \Omega + \tan^{-1}(\cos i \tan \omega) \quad (4.21)$$

Unfortunately, none of the modelers offer values for  $\Omega$ , though Smith et al. suggest a  $PA_A \approx 225^{\circ}$ .

Table 4.2 thus establishes constraints on possible orbital orientations for the first four models. For the two Davidson et al. 1997 models, these constraints are large, with almost 60% of the angular range (Region D) excluded due to astrometric

constraints on their model 1. As shown in the figure, the “allowed” orientations for the semi-major axes for this “first generation” of binary models all lie approximately along the Homunculus axis of symmetry  $PA \approx 132^\circ$  [Davidson et al.(2001)].

This orientation is problematic from a theoretical point of view. Both the Homunculus and equatorial debris appear (to first order) to be symmetric about the Homunculus axis of symmetry (hence the name). Occam’s razor would lead one to conclude that the symmetry of the debris should correlate with some underlying symmetry of the binary system. One obvious orientation that satisfies this is when the normal to the orbital plane is parallel to the Homunculus axis of symmetry, with the semi-major axis of the orbit orthogonal to the axis of symmetry<sup>3</sup> (see [Soker(2005)] for an example of a theoretical discussion of the generation of the Homunculus moderated by a binary configuration) . The constraint solutions imply the reverse is true in this case, with a major axis along the axis of symmetry and the normal to the orbital plane, therefore orthogonal to the axis of symmetry. There is no obvious correlation between the resultant rotational symmetries of this binary model and the rotational symmetries of the homunculus and equatorial debris. This orientation and the models that require it are thus unlikely based on arguments of symmetry.

On the other hand, the second-generation models that include both a different orientation (i.e., more parallel to the PoS) to the semi-major axis and a much smaller secondary all imply astrometric reflex signals that fall within the constraint ellipse

---

<sup>3</sup>I note, however, that the single star system can also satisfy this criterion, with either the axis of rotation or of precession aligned along the Homunculus axis of symmetry.

(i.e., are permitted by the current limits defined by the astrometric measurements).

The second-generation models are thus all allowed by the astrometric data.

#### 4.5.2 Possible $\eta$ Car A Orbit

A candidate orbit solution can be generated that is consistent with the astrometric results. Using the  $y'$  data and the resultant values for  $e = 0.95$ ,  $a = 1.15$  and  $T = 2003.69$  as well as the adopted value of  $P = 5.52$  years, fig. 4.7 represents the “overhead” view (i.e., the view looking down a line of sight normal to the orbital plane) of the resultant orbit.

With only five  $y'$  data points and lacking useful  $x'$  data, it not possible to solve for the orientation of the orbit ( $i$ ,  $\Omega$  or  $\omega$  parameters). I do adopt the assumption—consistent with both the HRC data as well as [Smith et al.(2004)]—that the semi-major axis is aligned approximately along the  $y'$  measurement axis (i.e.,  $PA_A \approx 232^\circ$ ) and that the angular separation between the semi-major axis and the plane of the sky is small (i.e., angle  $\gamma \approx 0$ ). Thus, the view of the orbit projected onto the sky should resemble that shown in fig. 4.7, with the exception that the semi-minor axis’ rotation about the semi-major axis is unknown.

There are two major differences between my results and the “combined” binary model described in Table 2.3. First, the eccentricity is higher (0.95 vs. 0.8–0.9), and second, the time of periastron passage is somewhat later (2003.69 vs. 2003.5) in my model. The former is driven by the relative sizes of the pre- and post-periastron shifts in  $y'$ . The post-periastron shift is heavily dependent on the July 2005 measurement

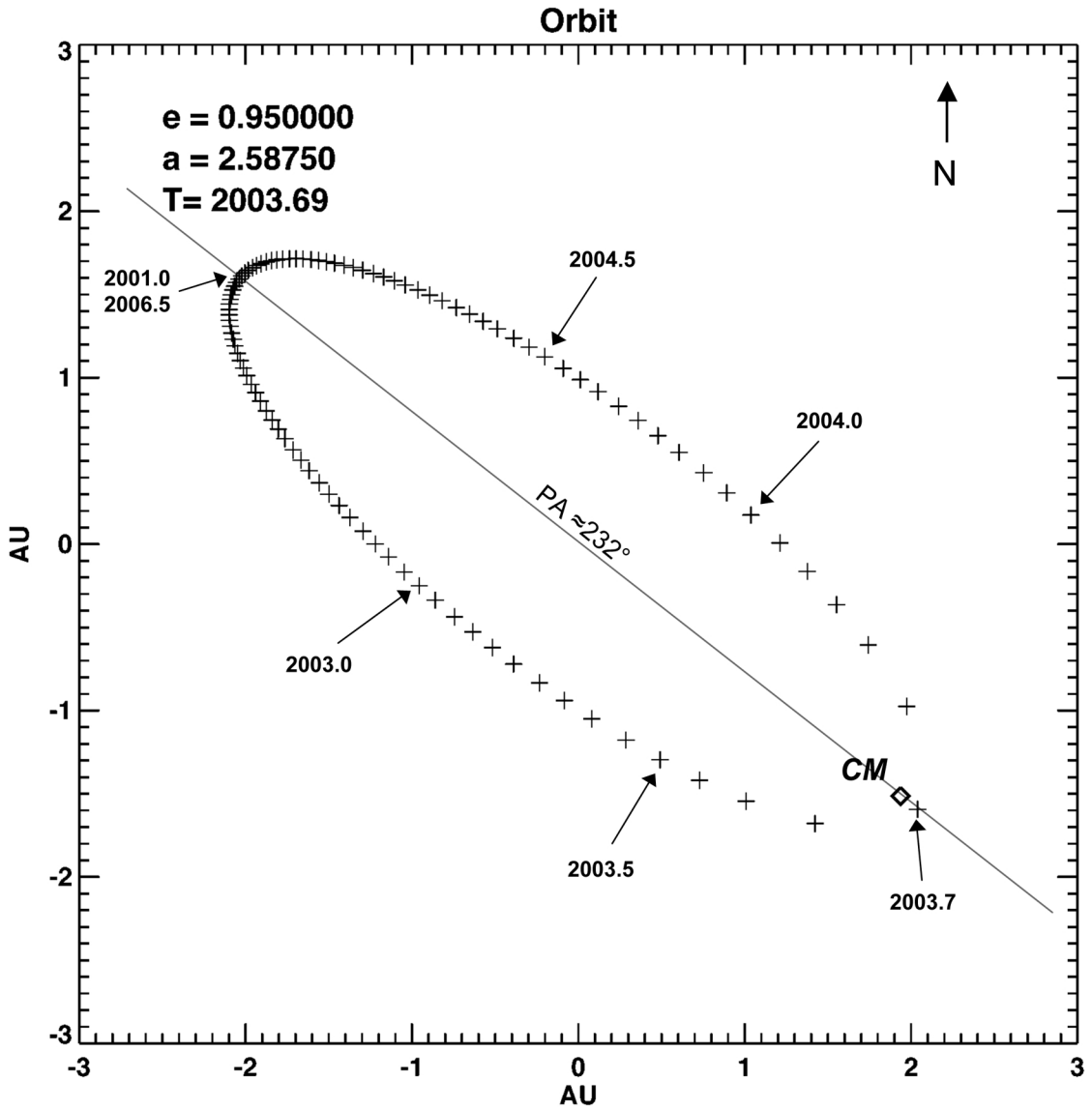


Figure 4.7: View of possible binary orbit. The solution has been scaled to a distance of 2.25 kpc and represents an “overhead” view, i.e., looking down along a line of sight normal to the orbital plane. “CM” indicates system’s center of mass. Approximate positions marked based on  $P = 5.52$  years and  $T = 2003.69$ . Each tick mark denotes 0.05 years (18.25 days). Diagonal line indicates measurement  $y'$  axis.

that was affected by saturation. I have already discussed (§4.3) the first-order effects of saturation: blooming; a higher-order effect is charge deferral due to trap-induced electron capture and subsequent release [Dorland(2004a)]. Charge deferral can introduce offsets in the opposite direction of the charge transfer (i.e., the CCD columns away from the direction of the serial register) which, since the  $y'$  is not completely orthogonal to the detector columns, would appear as a slight shift in  $y'$ . The charge deferral occurs in the anti-shift direction, which in the HRC images should result in a slight offset in the  $+y'$  direction. It is possible, therefore, that the measured  $y'$  position is slightly overestimated, and that a better value would be somewhat below the measured value on the plot. The resultant fit would have a larger semi-major axis  $a$  and a smaller eccentricity  $e$ , more in line with the combined model.

The time of periastron passage  $T$  is strongly dependent on the Sept. 2003 measurement. This measurement has the largest error associated ( $\text{SDOM}_{y'} = 0.5$  mas) when compared to the other non-saturated images, thus it is not unlikely that an overestimate of the  $y'$  measurement is skewing the value of  $T$  to be later than it actually is.

#### 4.5.3 Discussion of Measurement Limitations

The two biggest limitations to the measurements are the loss of precision in the  $x'$  direction and possible epoch-to-epoch variations in the instrument that result in uncompensated systematic errors. Both of these issues are discussed in turn.

The precision problem in the  $x'$  direction is, as described above, due to the limited number and sub-optimal configuration of reference stars present in the HRC fields. This, in turn, is due to the combined effects of the relatively small HRC field, the short exposures necessitated by the brightness of the central star, and the extinction due to the Carina nebula. As a result, only two reference stars are present in the field, with a relatively short measurement baseline between them. Fortunately, the current models seem to favor orientations along the more sensitive ( $y'$ ) of the two axes. The  $x'$  limitation appears primarily to affect the ability to determine orientation parameters of the resultant orbit.

The epoch-to-epoch variations are more serious. As discussed in §4.4.2, I argued that the problematic Nov. 2003 measurements should be rejected based on the fact that they seemed highly anomalous for either the binary or no binary models. This does not, however, explain the cause of the measurement error.

Other high-precision astrometry users of HRC data have discussed the presence of uncorrected systematics at the  $\approx 0.005$  pixel (0.125 mas) level [Anderson & King (2004)], with some reports of anomalies at the  $\approx 0.01$  pixels (0.250 mas) level [Anderson (2006)]. The methods for high-precision astrometry described in this work along with the work of [Anderson & King (2004)] represent the highest precision astrometric work done with the HRC instrument. As such, we are probing the systematic floor of the instrument. One can speculate that epoch-to-epoch variations due to changes in the telescope, ACS instrument and focal plane states due, for example, to changing illumination conditions on the spacecraft are responsible for slight changes in plate scale, distortion , etc., that appear as changes in measured separations between

epochs. In principle, these effects are “calibratable” using multiple, astrometrically stable field reference stars from epoch to epoch. In the case of the  $\eta$  Car observations, however, the requirement that we use F330W data combined with the available field stars that are observable in the NUV constrains us to just two field reference stars, even using the longest exposures.

For purposes of these observations, stability is implied by the results of the differential astrometric measurements between the two reference stars, but the Nov. 2003 anomaly suggests we may be at the limit of the instrument, and that any inferences beyond the basic constraints are not warranted. It does not appear possible to resolve this calibration issues given the data currently available. New observations will be required that are specifically designed to address the weak points in the current data set. In the next section, I provide some suggestions for improving the astrometry for any future next set of observations.

#### 4.5.4 Resolving the astrometric limitations: suggested future observations

Of what would a future HRC observing campaign aimed at minimizing astrometry errors and determining astrometrically an orbit with higher confidence consist? Based on my analysis of the HRC data, I suggest the following:

1. Temporal coverage. Temporal coverage should extend from apastron through periastron to the next apastron. The parameter  $a$  is a function of the separation between apastron and periastron. Unfortunately, apastron is scheduled

for approximately 2006.5, so it is too late to include this suggestion in an HST proposal. The next apastron will occur around 2011.8. A sequence of 2–4 unsaturated observing epochs (box dither pattern, 0.1 sec exposure times) around apastron would reduce the current position measurement error by nearly an order of magnitude ( $SDOM_{y'} = 0.9 \text{ mas} \rightarrow 0.1 - 0.2 \text{ mas}$ ), resulting in a much higher confidence estimate of the parameter  $a$ . The apastron (or, given the dates, the earliest feasible portion of the orbit after apastron) and periastron periods (to better determine  $e$ ) should receive the densest coverage, perhaps one observation a month near apastron,  $\pm 3$  months and one observation per week around periastron,  $\pm 3$  months. Intermediate observations between apastron and periastron would allow the degeneracy between simple, linear relative proper motion and orbital motion to be broken.

2. Spectral coverage. [Anderson & King (2004)] list a total of ten filters available for HRC that include the high-precision position corrections. The more redward the filter, the better the PSF sampling is, and the smaller the PPE is. Too far redward ( $\lambda > 650 \text{ nm}$ ), however, and HRC detector artifacts begin to appear (the red halo, spikes). In addition, the central star gets brighter as we go red, while the set of early-type Tr16 field-reference stars get progressively dimmer, thus creating a dynamic range problem. Of the available filters, a good compromise appears to be the F606W/F625W filters. PSF sampling is good, both the central star and the field reference stars are accessible on the same image, and the appropriate calibration corrections have been developed.

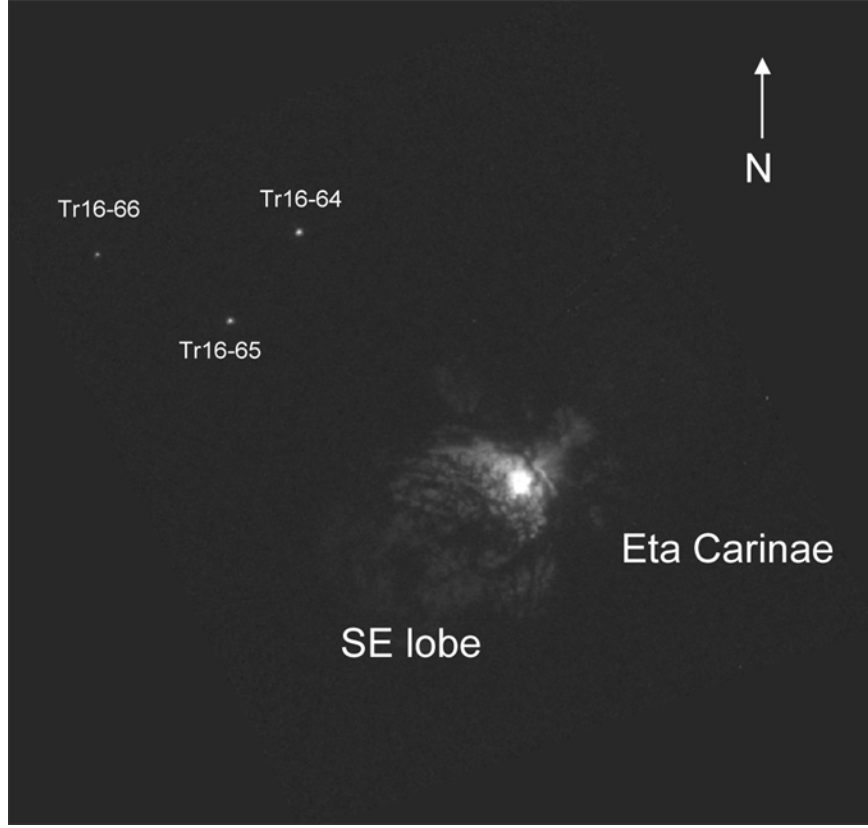


Figure 4.8: Re-centered HRC field that includes Tr16-64, 65, and 66. In this particular image (Feb 03), Tr16-66 fits into the corner of the detector. At other times, multiple overlapping fields are required to include Tr16-66.

3. Spatial coverage. Adding a third Tr16 reference star (Tr16-66) is feasible. A standard image of  $\eta$  Car would be taken, making sure to include Tr16-64 and -65. This would be followed by a re-centered field on Tr16-64. This recentered field would also include Tr16-66 (see fig. 4.8). Assuming the two overlapping fields could be tied together with minimal error, the three reference stars would enable reduction of both the  $y'$  and  $x'$  errors, reduce the likelihood that anomalous position measurements for any single star would go undetected, and support first-order calibration of the optical system due to breathing effects.

4. Integration times. The most straightforward way to increase the number of HRC stars beyond three is to integrate over much longer periods of time (hundreds of seconds) in an effort to observe background stars. In this case, extinction favors the reddest filters (F775W, F814W, F850LP). It may be possible simply to use very short and very long exposures, and use the long exposures to calibrate for plate scale and geometric distortion variations and assume the corrections are valid for the short exposures. This may be the only way to push beyond 1/100th the astrometric limits of the HRC with respect to the question of  $\eta$  Car's binarity.

## Chapter 5

### Astrophysical Implications of Binary Measurement Results

The second-generation models describe a high-eccentricity ( $e = 0.8 - 0.9$ ), relatively close-in ( $a_A + a_B \approx 15$  A.U.) binary system with at least a three-to-one asymmetry in the distribution of mass (see Table 2.3). The astrometric results from this analysis are in general agreement with these second-generation models, but with a somewhat larger eccentricity  $e = 0.95$  (see §4). If the second-generation orbital model, as adjusted by astrometric analysis of the HRC data, is adopted, do the results shed new insight on the nature of the component stars? In this section, the physical implications of the system described by the orbital parameters derived in §4 is discussed.

#### 5.1 Primary Luminosity and Mass

Since it is the reflex motion of the primary that is being observed, neither the mass of the primary nor mass ratio can be directly determined. One approach to inferring the mass of the primary is to calculate the mass range based on luminosity considerations. Cox et al. [Cox et al.(1995)] derived a bolometric luminosity of  $L_\eta = 5 \times 10^6 L_\odot$  using a combination of IR and radio data. The *in situ* value was based, however, on an estimated distance of 2.5 kpc to  $\eta$  Car. If these results are adjusted to the preferred 2.25 kpc (see Appendix B), the luminosity must be

adjusted by the square of the distance, or downward by  $\approx 30\%$ . As a result, the revised value for luminosity is  $L_\eta \approx 4 \times 10^6 L_\odot$ .

While  $\eta$  Car has most likely been in a super-Eddington state during previous periods of time, there is no evidence that it is currently undergoing significant mass eruptions that would likely characterize such a state. Its relative quiescence suggests it is below the Eddington limit. The Eddington limit is given by (e.g., [Rose(1998)]):

$$L_{Edd} \approx 3.3 \times 10^4 \frac{M}{M_\odot} L_\odot \quad (5.1)$$

which is equivalent to:

$$L_\eta \leq 3.3 \times 10^4 \frac{M}{M_\odot} L_\odot \quad (5.2)$$

This can be re-written as:

$$M \geq 3.0 \times 10^{-5} \frac{L}{L_\odot} M_\odot \quad (5.3)$$

Using  $L_A = 4 \times 10^6 L_\odot$ , eqn. 5.3 gives a minimum mass of  $M_A \geq 120 M_\odot$ . This assumes that approximately all of the luminosity is coming from the primary. If we further assume that  $\eta_A$  is currently sub-Eddington and adopt a value of  $0.9 L_{Eddington} < L_A < 1.0 L_{Eddington}$  we get mass range of  $M_A \approx 120 - 130 M_\odot$ .

## 5.2 Secondary Mass and Luminosity

The secondary mass can be calculated by solving eqn. 4.12 in terms of  $a_B$  and substituting this result into eqn. 3.3:

$$(M_A + M_B)P^2 = (a_A + a_A M_A/M_B)^3 \quad (5.4)$$

This equation can be solved numerically for  $M_B$  given values for  $a_A$ ,  $M_A$  and  $P$ . We adopt the previously derived values of  $a_A = 2.59$  A.U.,  $P = 5.52$  years and  $M_A = 125 \pm 4.2 M_\odot$ , and obtain a result of  $M_B = 23.2 \pm 0.6 M_\odot \approx 23 M_\odot$ .

This actually represents the effective mass due to the projection of the semi-major axis onto the measurement  $y'$  axis. As such, it represents a lower limit. The analysis previously assumed that this angle ( $\gamma$ ) is small<sup>1</sup>. Assuming  $\gamma < \pi/8$  ( $= 22.5^\circ$ ), the upper limit to the mass is  $M_B < 26_\odot$ . Thus, assuming the basic model is correct, the mass of the secondary is constrained to a range of  $23_\odot < M_B < 26_\odot$ .

In the discussion of luminosity in which the mass of the primary was derived (§5.1), it was assumed that all of the luminosity is coming from the primary. Given that the secondary is less massive than the primary and assuming that the two are approximately coeval (this assumption will be discussed in detail in §5.7.1), it is reasonable to assume that the secondary is less evolved than the primary. Given the relative brevity of the LBV phase ([Humphreys & Davidson(1994)]), it is not unreasonable to suppose that the secondary is either a ZAMS or very recently evolved. The bolometric absolute magnitude of a ZAMS star of mass  $25_\odot$  is  $M_{Bol} \approx$

---

<sup>1</sup>See Table 2.3 and §4.1; this assumption was shown to be self-consistent in Chapter 4.

−7.5, with a post-ZAMS maximum of  $M_{Bol} \approx -8.5$  [Burkholder et al.(1997)]. For comparison, the total luminosity of the system ( $L_\eta = 4 \times 10^6 L_\odot$ ) is equivalent to  $M_{Bol} = -11.8$ . The relationship between bolometric magnitude and luminosity is given by (e.g., [Rose(1998)]):

$$M_{Bol} = 4.72 - 2.5 \log L \quad (5.5)$$

where  $L$  is given in units of solar luminosity. This equation can be inverted to give:

$$L = 10^{\left(\frac{4.74 - M_{Bol}}{2.5}\right)} \quad (5.6)$$

Using the Burkholder values for absolute magnitude, we get a luminosity range of  $7.7 \times 10^4 L_\odot < L_B < 1.9 \times 10^5 L_\odot$ . The luminosity range and age can be further narrowed by considering the temperature constraints necessary for the observed ionization of the inner ejecta ([Verner et al.(2005)], see §2.2.11). A temperature range of 34,000–38,000 K was specified by Verner et al. for the secondary. The results from [Burkholder et al.(1997)] indicate a ZAMS or slightly post-ZAMS 23–26 $_\odot$  star with a maximum luminosity of  $L_B < 1.2 \times 10^5 L_\odot$  is necessary to meet the temperature constraints. Thus,  $L_B/L_{total} < 3 \%$ , and the assumption in §5.1 that all of the luminosity is coming from the primary is a self-consistent first-order approximation.

### 5.3 Secondary Orbit

The remaining step is to calculate the semi-major axis of the orbit of the secondary. This is done by solving eqn. 4.12 using the calculated values for  $a_A$ ,  $M_A$ , and  $M_B$ . Using upper and lower bounds for the secondary mass of  $23 < M_B < 26$ , eqn. 4.12 can be solved for  $a_B$ :

$$a_B = \frac{M_A a_A}{M_B} \quad (5.7)$$

Assuming upper and lower bounds on the mass of the primary of  $120_{\odot} < M_A < 130_{\odot}$ , eqn 5.7 indicates a range of 12 A.U.  $< a_B < 15$  A.U. for the semi-major axis of the secondary. 13 A.U. is adopted as the most likely value.

### 5.4 Comparison of Results with Earlier Binary Models

We now have sufficient information to compare the derived model of the system with the binary models described in §2. As discussed in Ch. 2, the primary discriminators between the “first” and “second generation” binary models are eccentricity and mass ratio. The earlier models tended to have smaller eccentricities and approximately equal masses between primary and secondary. The later models are characterized by higher eccentricities and asymmetric mass distributions between primary and secondary. Figure 5.1 is a scatter plot of eight of the relevant models from §2.

Also shown are these results, indicated by “This work.” Values of  $e = 0.95$ ,

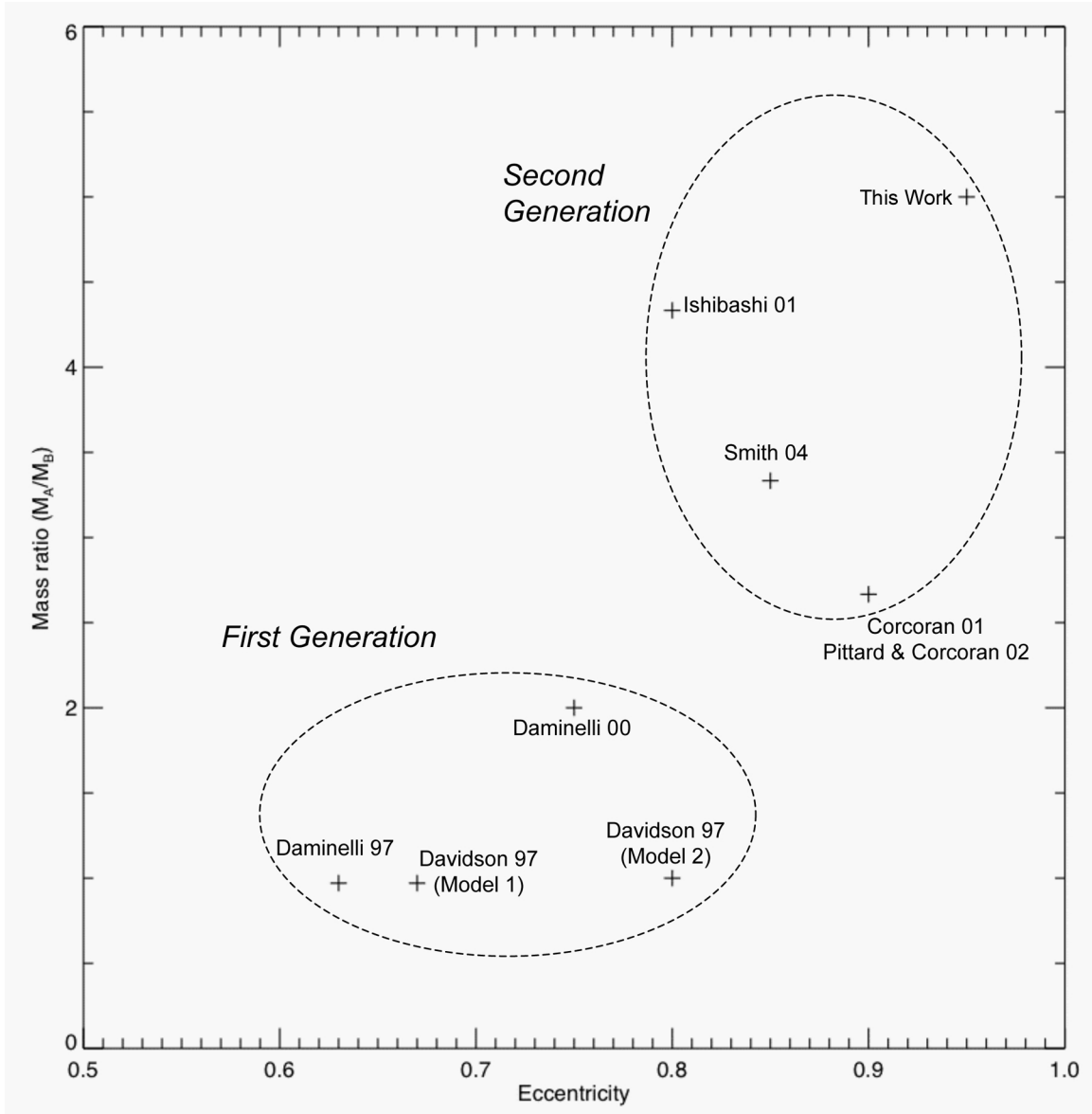


Figure 5.1: Comparison of binary models with current results. Two critical parameters, the orbital eccentricity ( $e$ ) and the mass ratio between the primary and the secondary ( $M_A/M_B$ ) are used. “First-generation” and “second-generation” groups of models are shown. The former is characterized by smaller eccentricities and mass ratios, while the latter has larger eccentricities and mass ratios.

$M_A = 125\odot$  and  $M_B = 25\odot$  are used. The current results strongly favor the second-generation models rather than the first. This conclusion is consistent with the discussion in §4.5.1, which found that pure orientation considerations strongly favored the second-generation models over the first.

## 5.5 Primary–Secondary Distance

I have now derived values for  $a_A$ ,  $M_A$ ,  $a_B$ , and  $M_B$  as well as orbital parameters for the orbit of  $\eta_A$ . The orbit of  $\eta_B$  will be identical to that of  $\eta_A$  with the exceptions that the semi-major axis will be scaled by the ratio of the masses  $M_A/M_B$  and the orientation of the semi-major axis  $a_B$  will anti-parallel to  $a_A$ . The relative separation vs. time can be calculated by adding the radial distances from the system center of mass (CM). The results are shown in fig. 5.2.

Maximum/minimum separation between the two components is 30 A.U. at apastron and 0.78 A.U. at periastron. Also show in the figure is the outer slow wind opacity radius at 4.1 A.U. described in [Hillier et al.(2006)]. This is defined as the approximate limit of the opaque wind ( $\tau = 0.67$ ). The resultant orbital geometry is shown in fig. 5.3. Within this boundary, U.V. light from  $\eta_B$  is absorbed by the wind particles coming from  $\eta_A$  and re-emitted at redder wavelengths. As shown in the figure, the secondary is within the outer opacity boundary for approximately two months during the period around periastron. As the secondary penetrates more deeply into this region, an increasingly larger portion of its U.V. light is intercepted and reprocessed as redder light. It is the U.V. light from the

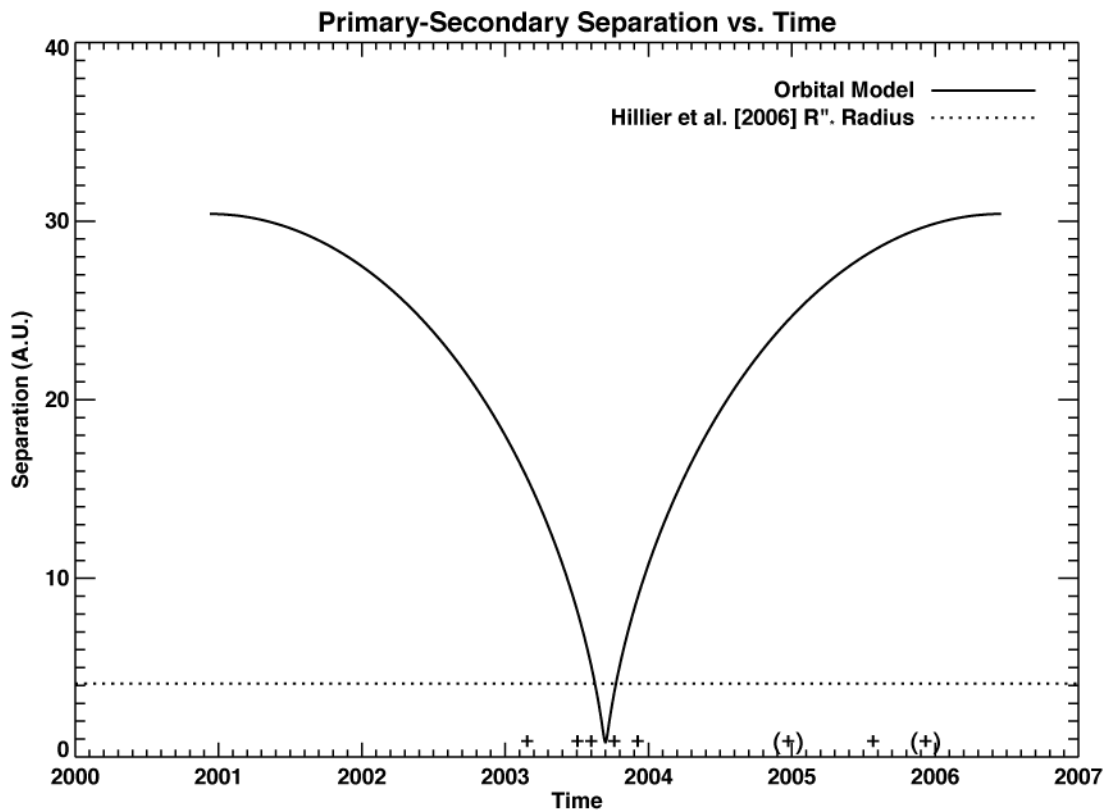


Figure 5.2: The separation between  $\eta_A$  and  $\eta_B$  shown as a function of time. The observations used in this analysis are marked with crosses; the two heavily saturated observations are marked with crosses in parentheses. Also shown is  $R''_*$ , the outer opacity boundary ( $\tau = 0.67$ ) of the slow wind (from [Hillier et al.(2006)]).

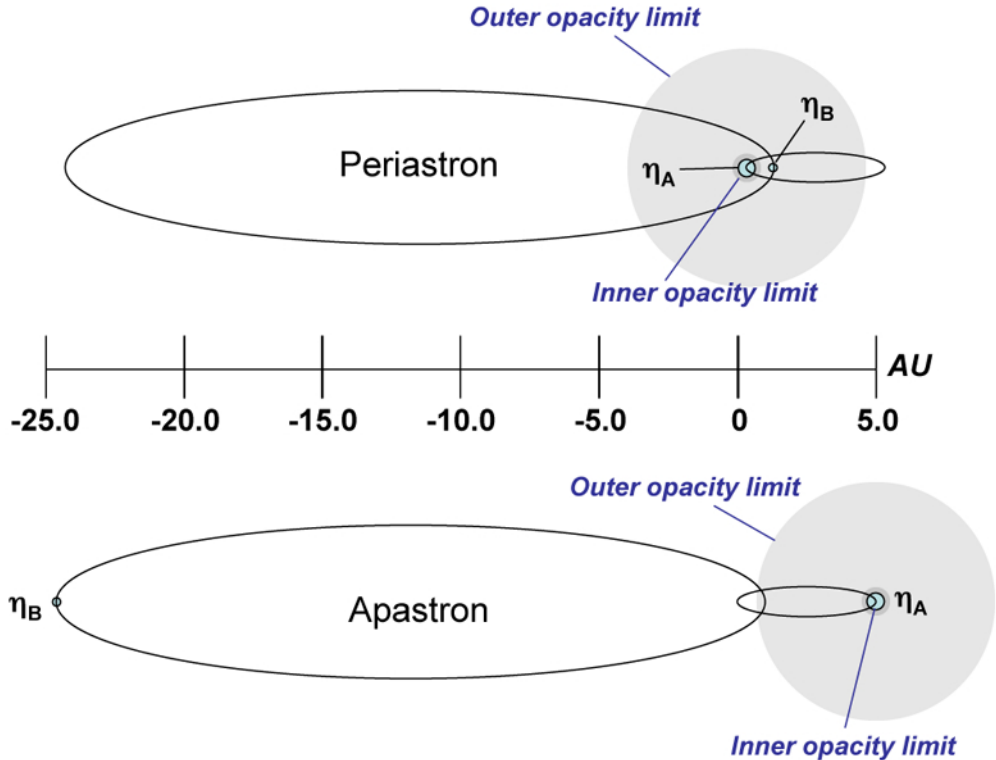


Figure 5.3: Binary orbits at periastron (top) and apastron (bottom) shown in center of mass (CM) frame. Positions of primary ( $\eta_A$ ) and secondary ( $\eta_B$ ) are shown along with Hillier et al.'s inner ( $R'_A$ ,  $\tau = 10$ ) and outer opacity radii ( $R''_A$ ,  $\tau = 0.67$ ).

secondary that excites the high excitation lines in the Weigelt blobs; as a result, these lines are seen to disappear near periastron ([Davidson et al.(1995)])<sup>2</sup>. This is consistent with the standard binary explanation of the spectroscopic cycle (see §2), specifically [Verner et al.(2005)], viz., that the UV light that is responsible for the ionization of the inner ejecta is “turned off” during periastron due to obscuration of the UV light from the secondary.

<sup>2</sup>Other lines are present at the primary or are excited by radiation from the primary; these are not extinguished at periastron.

## 5.6 Periastron passage

Given a closest approach of 0.78 A.U., what is the nature of the interaction between the two stars? How large are the tidal forces and is there any mass exchange?

### 5.6.1 Orbital Configuration at Periastron

Given the orbital parameters and masses, the total orbital energy can be computed using the Virial theorem:

$$E_{Orb} = \frac{-GM_A M_B}{2(a_A + a_B)} \quad (5.8)$$

Total energy is conserved, so the energy at periastron is given by:

$$E_{Orb} = PE_G + (KE_A + KE_B) \quad (5.9)$$

$$\frac{-GM_A M_B}{2(a_A + a_B)} = \frac{-GM_A M_B}{(a_A + a_B)} + \frac{1}{2}(M_A V_A^2 + M_B V_B^2) \quad (5.10)$$

where  $PE_G$  is the gravitational potential energy and  $KE_A$  and  $KE_B$  are the kinetic energies of  $\eta_A$  and  $\eta_B$ , respectively.

In the CM reference frame (see fig. 5.4), the radial line connecting the two stars and passing through the CM will rotate with an angular velocity  $\omega$ . The velocities can be re-written in terms of  $\omega$ <sup>3</sup>:

---

<sup>3</sup>In order to simplify the analysis, we concentrate on conditions at periastron. Quantities such as  $V$  and  $\omega$  are typically time dependent; in this case, we consider only the instantaneous values at periastron and drop the explicit time dependence for brevity.

$$V_A = a_A \omega \quad (5.11)$$

$$V_B = a_B \omega \quad (5.12)$$

These values can then be substituted into eqn. 5.10, which can then be solved for  $\omega$ :

$$\omega = \sqrt{\frac{GM_A M_B}{(a_A + a_B)(a_A^2 M_A + a_B^2 M_B)}} \quad (5.13)$$

Plugging in the values previously obtained for all the variables on the right-hand side gives  $\omega = 5.14 \times 10^{-6} \text{ sec}^{-1} \approx 5 \mu\text{radians sec}^{-1}$  as the instantaneous rotational velocity of the CM frame at periastron. As shown in the figure, this translates into velocities of 100 and 500 km sec $^{-1}$  for the primary and secondary, respectively.

### 5.6.2 Mass exchange across L1

Mass is exchanged in a binary system if the radius of either star extends beyond its Roche lobe, i.e., the surface that defines the region within which material is gravitationally bound to the star. Stellar material outside a given star's Roche lobe can be transferred to the companion via the first Lagrange point (L1), which also marks the intersection of the Roche lobes for both stars.

One way to define L1 is that it is the point along a line connecting two orbiting bodies at which a test particle in the co-rotating frame experiences no net acceleration. In the rotating frame, acceleration is thus a combination of the two

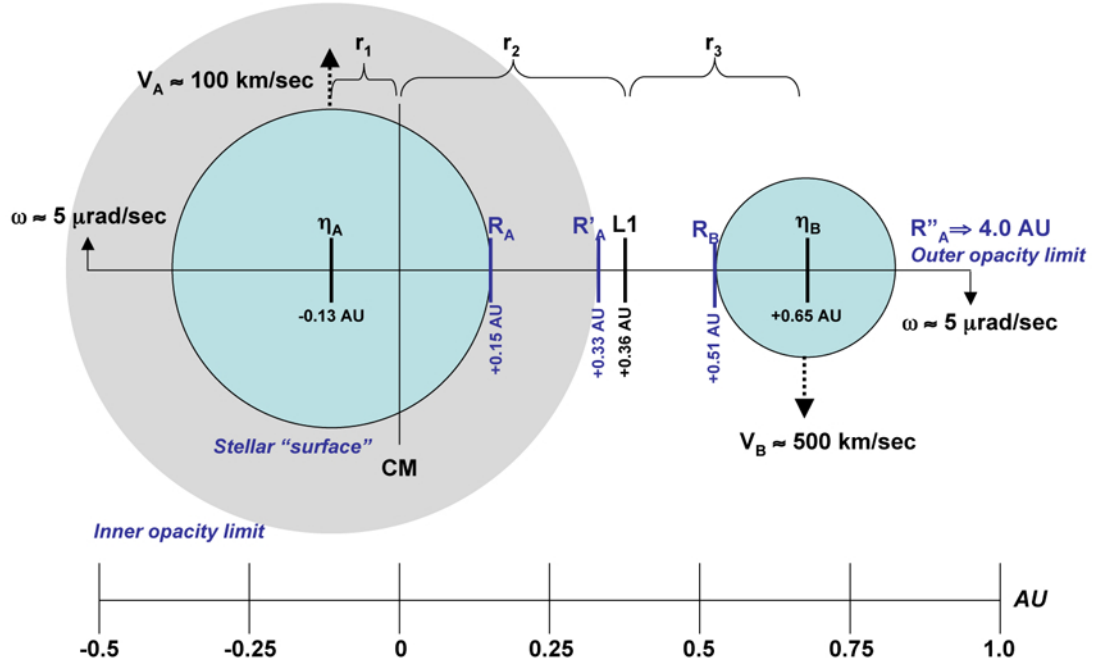


Figure 5.4: Binary configuration at periastron in center of mass (CM) frame. Positions of primary ( $\eta_A$ ) and secondary ( $\eta_B$ ) are shown properly scaled to predicted radii ( $R_A$ ,  $R_B$  from [Hillier et al.(2006)]) Also shown are the position of the first Lagrange point (L1) and Hillier et al.'s inner opacity radius ( $R'_A$ ,  $\tau = 10$ ). Hillier et al.'s outer opacity radius ( $R''_A$ ,  $\tau = 0.67$ ) extends well beyond the secondary at periastron. At periastron, the frame is rotating at an instantaneous rate of  $\omega \approx 5 \mu\text{rad sec}^{-1}$  due to orbital motion, which results in instantaneous velocities of 100 and 500  $\text{km sec}^{-1}$  for the primary and secondary respectively.  $r_1$ ,  $r_2$ , and  $r_3$  are described in the text.

gravitational forces and the centrifugal “pseudo” force due to rotation, i.e.:

$$\phi = \frac{-GM_A}{r_A^2} \hat{r}_A + \frac{-GM_B}{r_B^2} \hat{r}_B - \vec{\omega} \times (\vec{\omega} \times \vec{r}_{CM}) \quad (5.14)$$

where  $\vec{r}_A$ ,  $\vec{r}_B$  and  $\vec{r}_{CM}$  represent the distance of a test particle from  $\eta_A$ ,  $\eta_B$  and the center of mass, respectively.

Using the coordinate system shown in fig. 5.4, we can substitute  $\|\vec{r}_A\| = r_1 + r_2$ ,  $\|\vec{r}_B\| = r_3$ , and  $\|\vec{r}_{CM}\| = r_2$  and re-write 5.14 as:

$$a = \frac{-GM_A}{(r_1 + r_2)^2} + \frac{GM_B}{(r_2 + r_3)^2} + r_2 \omega^2 \quad (5.15)$$

In addition, we know:

$$r_2 + r_3 = a_B \quad (5.16)$$

Combining eqns. 5.15 and 5.16 and solving for  $r_3$ , we get:

$$r_3 = 0.29 \text{ A.U.} \quad (5.17)$$

from which it follows:

$$r_2 = 0.36 \text{ A.U.} \quad (5.18)$$

The position thus derived of L1 is marked in fig. 5.4 as well as fig. 5.6. The radii (from [Hillier et al.(2006)]) for both stars are also shown. As can be seen, neither star is close to overflowing at L1, thus the present results suggest mass exchange is unlikely even at periastron based on Hillier et al.’s analysis of

the current, quiescent state. LBVs undergoing S Dor eruptions (§1.3) experience photospheric swelling during the eruption, with the ejected shell being expelled at the conclusion of the event. A shell ejection event coincident with periastron passage would conceivably result in a significant amount of mass (either during the swelling or post-ejection) being swept up by  $\eta_B$ .

### 5.6.3 Wind penetration and opacity considerations

Also marked on the figure is  $R'_A$ , the inner high opacity ( $\tau = 10$ ) boundary from [Hillier et al.(2006)]. At periastron, the secondary comes relatively close the boundary, suggesting that it is deeply encased in the primary's wind, with minimal UV light escaping during closest approach. Mass exchange from the wind, however, is unlikely as the secondary is encased in its own high-velocity wind. The boundary region between the two stars where these winds collide is thought to be responsible for the x-ray emission [Corcoran et al.(2001)].

One other note: as described in this section, the opaque wind forms a sort of cloud around  $\eta_A$  of radius  $R''_* = 4.1$  A.U. This is large enough to contain the entire calculated orbit for  $\eta_A$ . Presumably, this cloud does not present as a uniformly illuminated disk, but shows an luminosity gradient that peaks at the true photocenter due to the variation in opacity and the presence of the strong source in the center of the cloud. Nevertheless, during periods of relatively large motion (e.g., periastron), the true motion of the star may be obscured to a certain degree by this opacity. The slow wind is thought to possess an escape velocity of  $V_{wind} \approx 500$  km

$\text{sec}^{-1}$  ([Corcoran et al.(2001)], [Hillier et al.(2006)]). It thus takes approximately two weeks for the wind to make it from the surface of  $\eta_A$  to  $R''_*$ . There is thus up to a two-week lag between the actual stellar motion and apparent motion of the outer boundary. This may partially explain the apparent delay observed between the calculated astrometric periastron and the x-ray and spectroscopic-inferred periastron dates (see §4.4).

#### 5.6.4 Tidal considerations

Tidal forces will arise on both surfaces due to the proximity of the two stars during periastron passage. The effects of these forces can be estimated by comparing the effective gravity at the surface of the star in the CM frame at apastron with periastron. In the absence of any knowledge regarding rotation, we consider only the non-rotating case.

In the case of  $\eta_A$ , the gravitational potential at the surface during apastron is approximately:

$$\phi_A \approx \frac{-GM_A}{r_A^2} \quad (5.19)$$

where both the gravitational contribution from  $\eta_B$  and effects of rotation of the CM frame are negligible due to the separation of the two components ( $\approx 30$  A.U.). Plugging in the relevant values, we get:

$$\phi_A \approx -9.4 \text{ m sec}^{-2} \quad (5.20)$$

as the gravitational potential, or, alternately, the acceleration of a test mass at the surface.

If we now consider the periastron case (fig. 5.4), the gravitational potential at the surface along the line passing through the CM is given by

$$\phi'_A \approx \frac{-GM_A}{R_A^2} + \frac{GM_B}{(r_2 + r_3 - R_A)^2} + R_A\omega^2 \quad (5.21)$$

where  $\phi'$  denotes the periastron case. Plugging in the relevant values, we get:

$$\phi'_A \approx -8.2 \text{ m sec}^{-2} \quad (5.22)$$

Thus, at periastron, the close passage has the effect of reducing the effective gravitational potential at the surface of  $\eta_A$  by nearly 13%. At and above the surface, the gravitational potential scales as one over the square of the radius. A reduction of the effective gravitational potential at the surface by 13% is thus equivalent to the gravitational potential (for the apastron case) at a radius of approximately  $1.07 \times R_A$ , or an altitude of 4 solar radii above apastron surface. To first approximation, the effect of the tidal interaction of  $\eta_B$  on  $\eta_A$  is to raise a bulge on  $\eta_A$  of height 4 solar radii above the normal surface.

Energy is required to lift this material during periastron passage. After the secondary has moved off, the primary resumes its nearly spherical shape and the gravitational potential energy is converted into other forms of energy<sup>4</sup>. Periastron

---

<sup>4</sup>This simplification implies that the following conclusions represent limits, not most likely values.

passage thus results energy transfer from the secondary to the primary and subsequent dissipation. Each orbital cycle results in loss of orbital energy due to the tidal interactions. The final configuration of the system should be a close pair in a nearly circular orbit with tidal locking between the two stars.

The tidal effects of close periastron passage on orbit evolution is an extremely complex field and detailed analysis is outside the scope of this paper. A very crude model of the process can provide some idea of the shortest possible circularization time. We can estimate the energy expended to lift the bulge material during periastron by calculating the volume of raised material and its average height. Fig. 5.5 shows the effective height of the raised surface as a function of angle from the center of mass lines connecting the primary and secondary. Total volume is obtained by integrating under this surface. The resultant volume estimate is  $\Delta V \approx 0.001 M_{\odot}$  at a mean height of  $\bar{h} \approx 1.7 R_{\odot}$ . This represents a change in gravitational potential energy of  $\delta E \approx 2 \times 10^{37}$  Joules. On the other hand, the difference between current and final orbital configurations ( $a \approx 16 \rightarrow a' \approx 0.8$  A.U.) represents a change of  $\Delta E \approx 3 \times 10^{42}$  Joules. Thus, approximately  $10^5$  ( $\approx 550,000 \approx 0.5$  Myr) are required to circularize. More detailed treatments (cf. [Fabian et al.(1975)], [Zahn(1977)]) give much shorter ( $\sim 10$  years) circularization times, while others [Mardling(1995b)] predict much longer ( $\approx 10^7$  years) times. Much of the disagreement regarding circularization times and overall evolution has to do with our understanding (or lack thereof) of the tidal effects on the interior structure of the stars and the resultant dissipation mechanisms and timescales. This issue will be revisited in the next section.

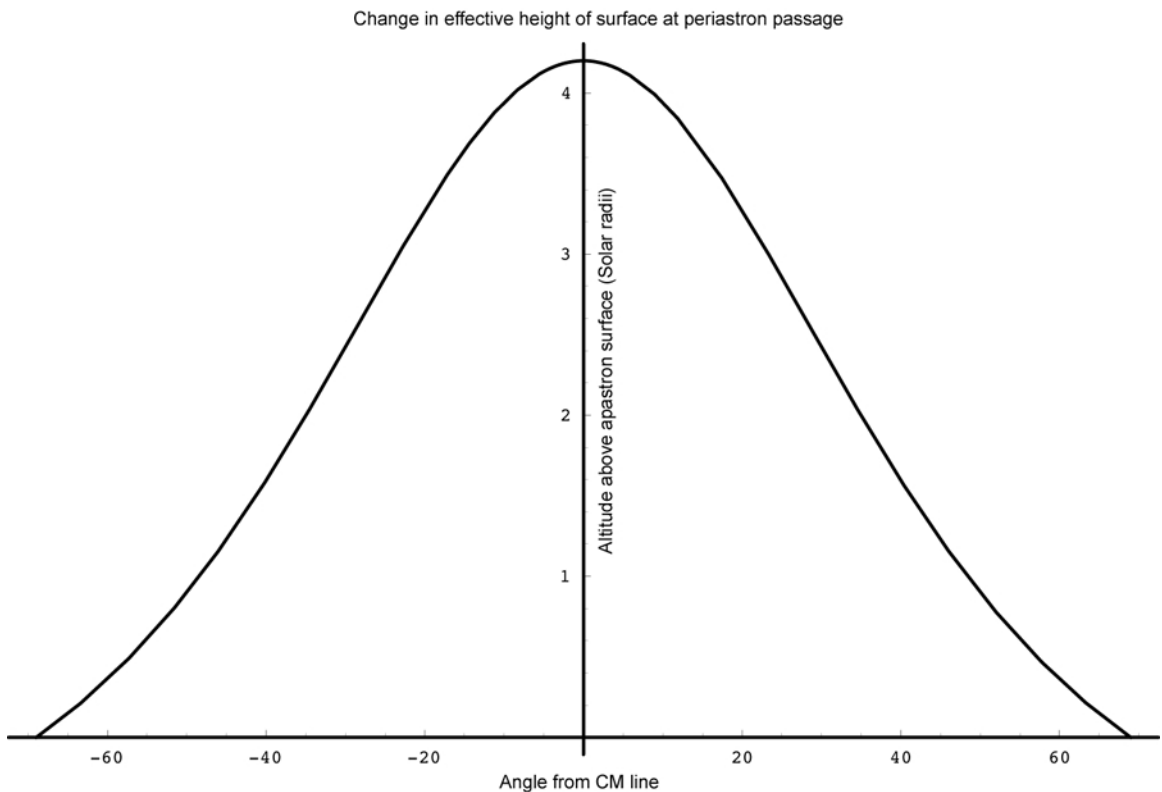


Figure 5.5: The effective height during periastron of  $\eta_A$ 's surface due to the presence of  $\eta_B$ . Effective height  $h$  is a function of angle from the lines connecting the centers of mass. Units of height are solar radii ( $R_\odot$ ); angle is given in degrees.

Performing a similar calculation for  $\eta_B$  for the point on the surface closest to the system's CM gives us:

$$\phi_B \approx 7.5 \text{ m sec}^{-2} \quad (5.23)$$

$$\phi'_B \approx 7.7 \text{ m sec}^{-2} \quad (5.24)$$

which is an interesting result in that during periastron passage, the effective potential at the surface *increases* rather than decreases. This is due to the rapid rotation of the CM frame as the companion swings by the primary. The centrifugal pseudo-force (in this case, directed towards  $\eta_B$ 's center rather than away) more than compensates for the gravitational effects of the primary.

The effects of periastron passage can be summarized thus: approximately one month before closest approach,  $\eta_B$  enters the opaque wind and the UV radiation (and associated high-energy excitation lines seen in the inner ejecta region) begin to diminish. As  $\eta_B$  nears A, the opacity due to the slow wind around A increases, with the UV flux approaching zero near periastron passage. As B approaches A, a tidal bulge of height  $h \approx 4 R_\odot$  is raised on the surface of A. Raising the bulge results in a transfer of energy and angular momentum from B to A. As B passes by A and heads towards apastron, A and B tidally decouple and the bulge begins to dissipate as the gravitational equipotential surfaces "re-sphericalize."

As the bulge collapses, gravitational potential energy will be converted to heat. Also, as the bulge collapses, the transfer of angular momentum will tend to spin up the star in the direction of motion of B. Both of these effects should tend to

destabilize a LBV-type star near the Eddington limit, the former by adding energy to the system and the latter by reducing the effective surface gravity along the orbital plane of the secondary. This suggests the potential for increased luminosity or eruptive behavior immediate after periastron. The effects on the secondary are also important—energy loss and angular momentum transfer to the primary will tend to circularize the orbit at the periastron distance, with estimate of  $t_{Circ} \approx 5 \times 10^5$  years. Implications for the evolution of the system are deferred to §5.7.

### 5.6.5 Roche Lobe “Holes” and Mass Ejection

The canonical definition of a star’s Roche Lobe is the volume enclosed by a surface of zero potential in the rotating frame. The two Roche Lobes (primary and secondary) intersect at L1. Material lying on the surface of or beyond the Lobe is lost to the source star and can be exchanged across the L1 interface given the appropriate kinematic conditions.

The potential at periastron for the  $\eta$  Car system in the rotating frame of reference is shown in fig. 5.6. The zero-level equipotential surface is marked with the dashed line.

Of greatest interest is the fact that the zero-level equipotential surfaces are not closed around the two stars. There are “holes” in the Roche Lobes stretching from point A1 to A2 (for the primary) and B1 to B2 (for the secondary). At the high instantaneous rotation rate associated with this configuration, the centrifugal pseudo-force is large enough to lower the potential in the anti-center of mass

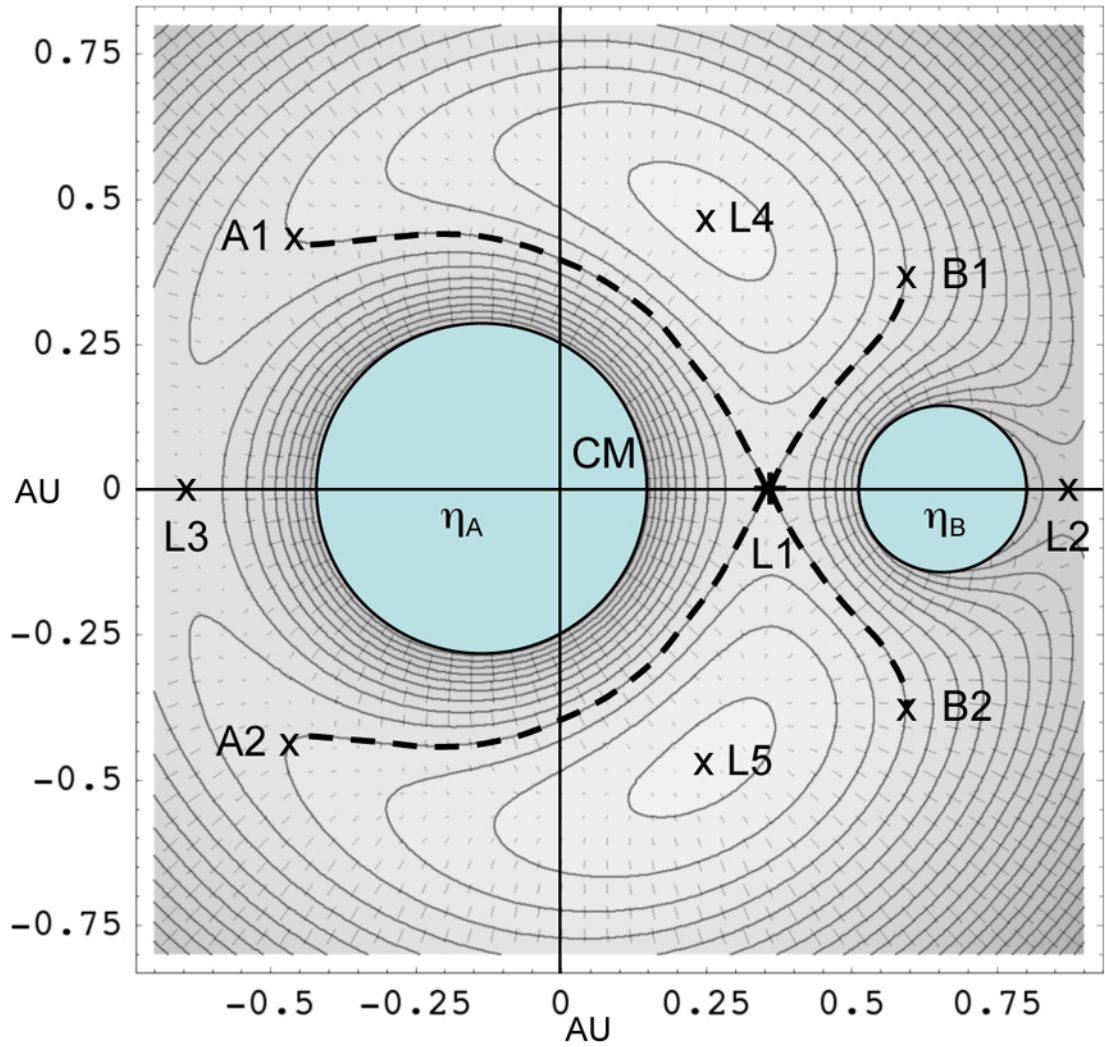


Figure 5.6: Binary configuration effective potential contours and Lagrange points for  $\eta_A$  and  $\eta_B$  at periastron. The effective potential is calculated for the rotating frame of reference using the values derived in this paper and the radii reported in [Hillier et al.(2006)]. Also shown as overplotted arrows is the gradient of the effective potential (i.e., the effective gravitational potential or acceleration vector field). The dashed lines represent the “rump” Roche Lobes; i.e., the regions near L2 and L3 have holes in them due to the very fast rotation of the system at periastron.

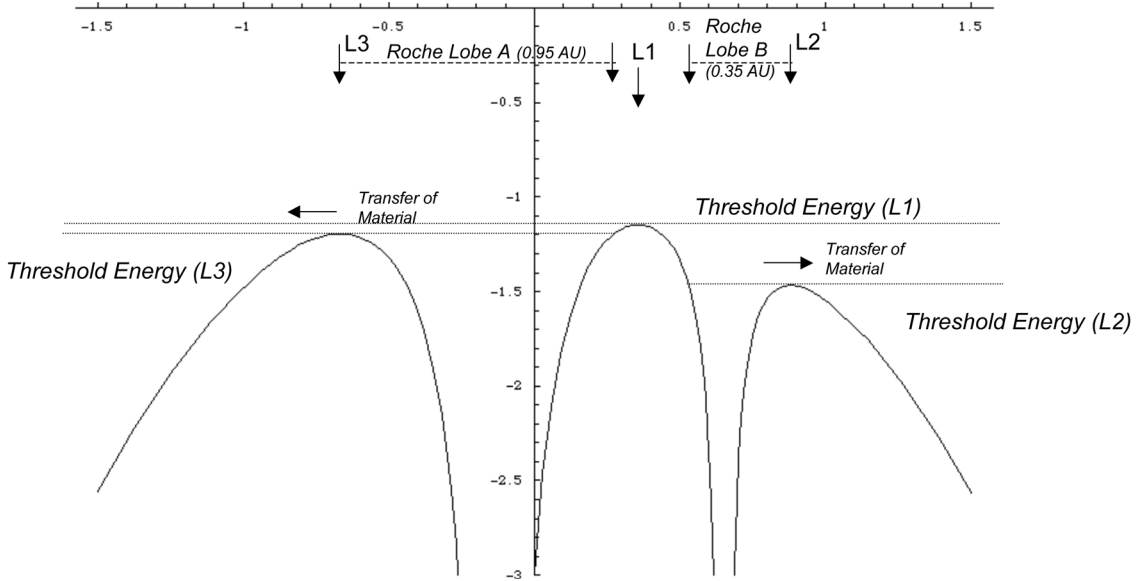


Figure 5.7: Effective potential energy cross section at periastron in the rotating frame. The three bumps represent the potential barriers between (1) space and  $\eta_A$ , (2)  $\eta_A$  and  $\eta_B$ , and (3)  $\eta_B$  and space, respectively. The very high eccentricity of the system causes the potential barriers at L2 and L3 to be *lower* than the barrier at L1, thus resulting in mass loss in the anti-CM direction rather than mass transfer between the two components as one would expect in a normal system.

directions (around L2 and L3) to below that at L1, as shown in fig. 5.7.

As shown in fig. 5.7, the potential at L2 is significantly lower than that at L3. This is due to both the great distance from the system center of mass and the smaller mass at B.

Because of this, mass transfer occurs through the lobe holes in the L2 and L3 regions rather than across L1, as is typical of the canonical Roche Lobe configuration. As a result, any mass with sufficiently high kinetic energy is ejected along the orbital plane, out through the holes in the anti-CM direction rather than transferred across L1.

These Roche lobe holes are a particular result of very high eccentricity and the

fast speed associated with periastron passage. Although a detailed analysis of this phenomenon will be the subject of future work, initial analysis indicates that the hole remains open at L3 for all  $e > 0.93$  and at L1 for all  $e > 0.91$ . In other words, even for the slightly lower eccentricities ( $e = 0.9$ ) associated with earlier models, this phenomenon can be operative.

The theoretical basis for this phenomenon is described in [Regös et al.(2005)] and [Sepinsky et al.(2007)]. The former employed smoothed particle hydrodynamic simulations to examine a variety of binary scenarios and found non-conservative mass transfer (i.e., mass loss) from both components possible in extreme cases similar to the one described in this thesis for  $\eta$  Car. The latter paper, using analytic methods, concludes that mass loss from the secondary is possible, though the paper did not consider the exact case we have described for  $\eta$  Car. These papers support the possibility that this type of non-conservative mass transfer would be relevant for  $\eta$  Car given the derived orbital parameters.

This mechanism may provide an explanation for some of the unusual phenomena associated with  $\eta$  Car. For example, the equatorial debris (see fig. 1.2) may actually be material ejected in the orbital plane by either A or B (or both). Similarly, the south ridge feature may also trace out the orbital plane, with the area of highest density marking the CM–L2 or L3 axis during the ejection event.

## 5.7 Implications for History and Evolution of $\eta$ Car

### 5.7.1 Formation of Binary System

To summarize these binary results,  $\eta$  Car consists of a high-eccentricity ( $e = 0.95$ ), relatively close ( $a \approx 13$  A.U.; periastron separation  $\approx 0.78$  A.U.), two component system, with primary and secondary masses of  $M_A \approx 125 M_\odot$  and  $M_B \approx 25 M_\odot$  respectively. The primary is an evolved LBV star, currently quiescent, with  $L_A = 4 \times 10^6 L_\odot$  and  $t_{eff} = 15,000$  K. The secondary is either a ZAMS (or newly evolved) O8/9 star (based on temperature considerations, see [Garcia & Bianchi(2004)]) or WR-type evolved star. How would such a binary come to form, and do these results constrain and/or illuminate the question of binary formation or evolution?

There are two possible mechanisms for binary formation: formation in place and capture. The standard theory is that wide separation binaries are the result of capture, while close-in binaries result from the fission of the collapsing source nebula due to local variations in density and angular momentum constraints [Heintz(1978)]. Close binaries tend towards circular orbits due to the circularization effects arising from the tidal forces and exchange of energy and momentum. In the case of  $\eta$  Car, we have what appears to be a contradiction: a close in, highly elliptical orbit.

### 5.7.2 Stellar Evolution Implications

Is the secondary a ZAMS O or a WR-type star? The Trumpler 16 association is a large collection of O-type stars, thought to have originated from the same

source nebula<sup>5</sup> [Walborn et al.(1978)]. Typical collapse times for nebular clouds during star formation is  $t_{collapse} \approx 10^4$  years [Carroll & Ostlie(1996)]<sup>6</sup>. The ZAMS lifetime is proportional to the amount of fuel divided by the rate of consumption, or ([Harwit(1988)]):

$$t_{ZAMS} \approx \frac{M}{L} t_{\odot} \quad (5.25)$$

where  $M$ ,  $L$  are in solar units and  $t_{\odot} \approx 10^{10}$  years [Carroll & Ostlie(1996)]. Using the derived parameters for  $\eta_B$  as representative of a “typical” O star in Tr16, we get a value of  $t_{ZAMS} \approx 2.5 \times 10^6$  years. With formation times of order ten thousand years and ZAMS lifetimes of order millions of years, the Tr16 members are thus effectively coeval.

What about  $\eta_A$ ? The standard mass-luminosity relationship [Harwit(1988)] is given by:

$$L = L_{\odot} \left( \frac{M}{M_{\odot}} \right)^a \text{ where } a = 3 - 4 \quad (5.26)$$

The ZAMS luminosity for a  $M = 125 M_{\odot}$  is  $L \approx 2 - 4 \times 10^6 L_{\odot}$  using a value of  $a = 3$  for a lower limit and  $L_{Eddington}$  for an upper limit. This results in a range of  $t_{ZAMS} = 3 - 6 \times 10^5$  years for  $\eta_A$ .

There is no reason to suspect that  $\eta_A$  is not a member of the Tr16 association, and strong astrometric (relative proper motion measurements, this paper) and velocimetric reasons [Davidson et al.(1997)] to suspect that it *is*. It does appear to be far and away the most *massive* member of the association. Nevertheless, the other

---

<sup>5</sup>Tr16 is now an “association” rather than a cluster because the component O stars have all been ejected from the original cluster and are no longer gravitationally bound

<sup>6</sup>The Kelvin-Helmholtz (i.e., thermal readjustment) time scale [Carroll & Ostlie(1996)] is of order hundreds of years for a star of  $\eta$  Car’s mass and luminosity

association stars are quite large in their own right. It is therefore most likely coeval with the rest of the association. Since the LBV phase is thought to occur over a few tens of thousands of years [Humphreys & Davidson(1994)], this puts the most likely upper age of the association at about 600,000 years.

An association age of 600,000 years excludes a scenario in which  $\eta_B$  is a WR-type star under any normal set of evolutionary assumptions. If it is an association member—and it most likely is for precisely the same reasons that  $\eta_A$  is—it is most likely an O8/9 star the early stages of its ZAMS lifetime.

### 5.7.3 Orbital Implications: Binary Capture as Explanation for Great Eruption?

As discussed in §5.6, the high-eccentricity orbit should decay due to energy and angular momentum transfer into a circular orbit. Given an upper limit of  $\approx 0.5$  Myr for circularization time, it seems unlikely that the binary orbit would still be in its current, highly eccentric orbit.

Pioneering work by [Fabian et al.(1975)] and [Press & Teukolsky(1977)] demonstrated that two-body tidal capture, where angular momentum and energy are transferred tidally between stars—as distinguished from capture mechanisms requiring a third star which is subsequently ejected carrying off a large amount of angular momentum—is a viable mechanism for explaining close binaries. Two-body tidal capture is most effective for stars with small relative velocities (10s of km/sec), such as within a cluster or association. Based on the analysis presented in this sec-

tion, typical velocities of the Tr16 stars in the vicinity of  $\eta$  Car are  $pm_{64-65} \approx 0.1$  mas/yr, or  $V_{64-65} \approx 1$  km/sec. This is well within the velocity constraints specified by [Fabian et al.(1975)], [Press & Teukolsky(1977)], *et seq.*, required to make tidal capture feasible.

If capture was indeed the mechanism for the formation of  $\eta$  Car's system, what was the resultant release of energy? Simulation work ([Mardling(1995a)], [Mardling(1995b)]) suggests that under certain circumstances (small periastron, high eccentricity), capture binaries experience an initial period of chaotic orbital evolution which then transitions to non-chaotic, quasi-periodic period of evolution consistent with previous treatments. During this chaotic phase, huge tides are raised on the stellar surfaces, and a large amount of energy is released in the form of luminosity and mass ejection. Total energy release of order  $1/3^{\text{rd}}$  of the final binding energy of the fully circularized system.

From [Dale & Davies(2006)], the quasi-periodic tidal evolution of a close binary system results in circularization at the periastron distance. For  $\eta$  Car, this gives me:

$$E_{\text{orb, circ}} = -\frac{GM_A M_B}{2(0.78 \text{ A.U.})} \quad (5.27)$$

$$\approx -3.6 \times 10^{49} \text{ erg} \quad (5.28)$$

for the total orbital energy at circularization. The total amount of energy released during the initial chaotic phase due to tidal interactions resulting in mass loss and increased luminosity (per [Mardling(1995a)], [Mardling(1995b)]) is  $1/3^{\text{rd}}$  of this, or

$E_{release} \approx 10^{49}$  erg. As discussed in §1.2.2, the current estimates for the energy released during the Great Eruption is  $E_{GE} \approx 10^{49} - 10^{50}$  erg ([Davidson & Humphreys(1997)]).

Is this a coincidence? Perhaps; however one can imagine a scenario in which the capture of  $\eta_B$  by  $\eta_A$  triggers a major eruptive event (or sequence of events) in  $\eta_A$  during a relatively brief chaotic phase of orbital evolution. The close passage of  $\eta_B$  would have raised very large tides on A, depositing gravitational energy on A in the form of raised material (subsequently released after post-periastron gravitational decoupling) and reduced effective gravity at the surface, both leading to some combination of mass loss and swelling of the outer photosphere of A., possibly inducing an S Dor-type event. A passage through the swollen A by a chaotically changing B could have resulted in significant mass loss for A ([Smith et al.(2003)] provide a current prediction of  $\dot{M}_{GE} \approx 10 M_{\odot}$ ), with perhaps a significant amount of the ejected mass channeled through polar jets of the secondary as suggested by [Soker(2005)]. Some of this material could also have been ejected via the Roche Lobe hole mechanism described in §5.6.5 from either A or B (or both), creating the equatorial debris features along the orbital plane. The capture and subsequent chaotic evolution of the close-binary orbit may have thus been an important causal factor in the Great Eruption. Once the eruption subsided and the orbits transitioned into the quasi-periodic evolutionary state, the system would have entered into the currently observed period of relative quiescence, with a quiescent LBV and  $a \approx 25 M_{\odot}$  O8/9 ZAMS companion in the close, highly elliptical orbit described in this work.

## Chapter 6

### Binarity: Summary and Conclusions

There are strong reasons to suspect  $\eta$  Car is a binary. The primary driver is the extreme regularity of the spectroscopic cycle, fundamentally different than the quasi-periodic S Dor-type eruptions that characterize other, smaller LBVs. There also exists, however, significant “circumstantial” evidence. This includes the disappearance of the high-ionization lines during the spectroscopic event in the close-in ejecta ([Damineli(1996)], [Damineli et al. (1997)]), the observed x-ray intensity curves over the entire cycle ([Corcoran et al.(2001)], [Ishibashi(2001)], [Pittard & Corcoran(2002)]) and the time-dependent variability of the background illumination conditions during the spectroscopic minimum ([Smith et al.(2004)]).

The earliest (first generation) orbital models ([Damineli et al. (1997)], [Davidson(1997)]) were based on ground-based velocimetry data which later proved problematic ([Davidson et al.(2000)]). These models preferred very massive, similarly sized primary and secondaries ( $M_{A,B} \approx 70 M_{\odot}$ ), with the semi-major axis oriented more along the line-of-sight rather than the plane of the sky.

The second-generation models that followed were based primarily on X-ray data ([Corcoran et al.(2001)], [Ishibashi et al.(1999)], [Ishibashi(2001)], [Pittard & Corcoran(2002)]). These models preferred a very large primary ( $M_A > 80 M_{\odot}$ ), a smaller (though still massive) secondary ( $M_B \approx 30 M_{\odot}$ ), and a semi-

major axis that is oriented more along the line-of-sight than in the plane of the sky. Refinements to these models based on spectroscopic observations ([Verner et al.(2005)], [Hillier et al.(2006)]) indicate effective temperatures of  $t_{eff} = 15,000$  K for  $\eta_A$ , and  $t_{eff} \approx 35,000$  K for  $\eta_B$ . These results suggest that  $\eta_A$  is an evolved LBV with a stellar spectral class B-like spectrum and  $\eta_B$  is either an O giant or WR-type evolved star.

I have employed a previously untried measurement technique for  $\eta$  Car—differential optical astrometry—to try to better determine if  $\eta$  Car is a binary, and if so, improve our knowledge of the range of its orbital elements and refine the orbital model. Using a synthesis of the geometrical distortion correction techniques developed by [Anderson & King (2004)] and a new method of centroiding based on fitting two-dimensional Gaussian profiles and correcting the resultant undersampling-induced pixel phase error, relative astrometry at the 1/100th pixel (0.25 mas) has been demonstrated to be possible using the the HST’s ACS/HRC instrument in the F330W filterband. The methodology was successfully tested using two reference O-type field stars (Tr16-64 and -65).

Using this methodology, the relative motion of the central star was analyzed with respect to a coordinate system defined by the two reference stars. It was found that  $\eta$  Car moves by about 2 mas over two years of observation along one of the observational axes. This motion is consistent with reflex motion of the primary in a highly elliptical orbit, with a derived eccentricity  $e = 0.95$  and semi-major axis  $a = 1.15$  mas (= 2.6 A.U. at 2.2 kpc). The astrometric results are consistent with second-generation models and inconsistent with first-generation ones.

Using these orbital results and basic arguments concerning luminosity, masses of  $M_A \approx 125 M_\odot$  and  $M_B \approx 25 M_\odot$  were derived. Using these results and the orbital elements from A, the orbit of B and the separation A–B vs. time is straightforward to derive, with a most likely value of  $a_B = 13$  A.U. for the semi-major axis, with resultant separations of 0.78 AU at periastron and 32 A.U. at apastron. This periastron separation is within the opacity boundary described by [Hillier et al.(2006)], thus validating the fundamental spectroscopic argument for the binary model: during a short period around periastron, the ionizing UV light of the secondary is “turned off” by the dense, opaque wind of the primary. Full results are presented in Table 6.1

Table 6.1: Revised binary model. The results are based on astrometric analysis presented in this thesis. Compare to Table 2.3.

Parameter	Value	Notes
$P$	$5.52 \pm 0.005$ years	
$e$	$0.95 \pm 0.025$	
$i$	$\leq 22^\circ$	
$\omega$	$\approx 200^\circ$	
$a_A$	$2.6 \pm 0.05$ AU	
$a_B$	$13.3 \pm 1.3 \approx 13$ AU	
$M_A$	$125 \pm 4.2 M_\odot$	
$t_A$	$\approx 15,000$ K	
$L_A$	$\approx 4 \times 10^6 L_\odot$	
Spect. Class (A)	$\approx$ B	<i>apparent, actually LBV</i>
$M_B$	$24.5 \pm 1.3 \approx 25 M_\odot$	
$t_B$	$36,000 \pm 1700$ K	
$L_B$	$\leq 1.2 \times 10^5 L_\odot$	
Spec. Class (B)	O8/9	<i>WR unlikely given system age</i>
Age (both A and B)	$\leq 600,000$ years	<i>Coevality likely</i>

At periastron, the secondary is well within the opacity region defined by Hillier. Close passage will also raise tides on both primary and companion which will tend

to circularize the system over time. The quiescent configuration does not overflow the Roche Lobes. A possibly new mechanism for ejection of material—holes in the Roche Lobes due to the system’s high eccentricity and velocity during periastron passage—has been uncovered, which would result in ejection of any overflow material via L2 and L3 rather than the canonical exchange of material across L1 near periastron. During periods of non-quiescence, this mechanism may explain some of the unusual ejecta features associated with  $\eta$  Car.

As discussed previously, there is strong reason to suspect that all of the very massive members of the Tr16 association are coeval. This would include both  $\eta_A$  and  $\eta_B$ . If  $\eta_A$  is an LBV (and thus post-main sequence, but pre-WR) its age (and hence, the age of the association) must be about 0.5 Myears.  $\eta_B$  is therefore most likely still a ZAMS star, and thus of spectral type O8/9 rather than WR.

Given the current configuration—a highly elliptical orbit with a relatively small (in absolute terms) periastron—it seems unlikely that the binary system was formed in place. It must therefore be the result of capture. Extensive work exists in the literature supporting the notion of capture being responsible for close-in, highly elliptical orbits. Based on some of the more recent work in the literature, the amount of energy released during the brief period following capture is approximately equivalent to the energy thought to have been released during the Great Eruption. Thus, a binary capture scenario provides one possible explanation of the cause of the Great Eruption.

## Part II

### ASTROMETRIC EXPANSION OF THE EJECTA FIELDS

## Chapter 7

### The Ejecta Field Around $\eta$ Car: The Fossilized Historical Record of Its Eruptions

As discussed in detail in §1,  $\eta$  Car has passed through a sequence both of small-scale (i.e., S-Dor type) luminosity fluctuations and large-scale eruptions (e.g., the Great Eruption, the 1890 “Lesser Eruption,” etc.). Previous authors (see §7.1) have determined that much—if not all—of the material in the vicinity of  $\eta$  Car is on ballistic trajectories, with velocity vectors tracing back to and radiating outward from the general vicinity of the central star. Analysis of the astrometric and radial motions and separations have allowed calculation of dates of origin of the various ejecta. There is strong evidence correlating ejecta with discrete events in  $\eta$  Car’s historical light curve.

Answering the question of continuous vs. discrete ejection of material is necessary for advancing our understanding of LBVs and the evolution of very massive stars. Furthermore, the sorting of the various ejecta features into event-correlated bins is critical to understanding and modeling the specific eruptive events that  $\eta$  Car (and other, similar stars) has gone through to get to its current state.

Figure 7.1 is a cartoon view of the ejecta field, taken from [Currie et al.(1996)] and modified to show the field-of-view of the GO9721 HST/ACS/HRC observations conducted in support of this thesis. The goal of this section is to use multiple as-

trometric techniques to analyze the motion of the ejecta accessible in the GO9721 HRC data and to determine, with better accuracy than previously achieved, positions, motions and dates of origins of the various accessible ejecta features. I will then use this information to correlate the ejecta features to specific events in the historical record, draw conclusions about the nature of these events, and develop constraints for modelers.

In this chapter, a summary of the current state of knowledge is provided with a review of the more important papers published regarding proper motion of the ejecta. In Chapter 8, a description is given of the methodology developed to analyze proper motion of the ejecta. Chapter 9 is a discussion of the results obtained when applying this methodology to the Homunculus data. Chapter 10 is a discussion of the Homunculus results and the physical implications. Finally, Chapter 11 describes the results of applying the methodology to the outer debris fields.

## 7.1 A Review of the Literature

### 7.1.1 Gaviola 1950

Gaviola (henceforth: G50) published photographs of  $\eta$  Car taken using the Córdoba 61-inch reflector (Córdoba Observatory, Córdoba, Argentina) in 1944 and 1945. In this paper, Gaviola first named the brightest ejecta feature the “Homunculus” because of its resemblance (at that time) to a man with his “arms folded over a fat body” [Gaviola(1950)]. In this paper, Gaviola measured radial separations between six specific nebular features, or “nubeculae.” He used earlier epoch

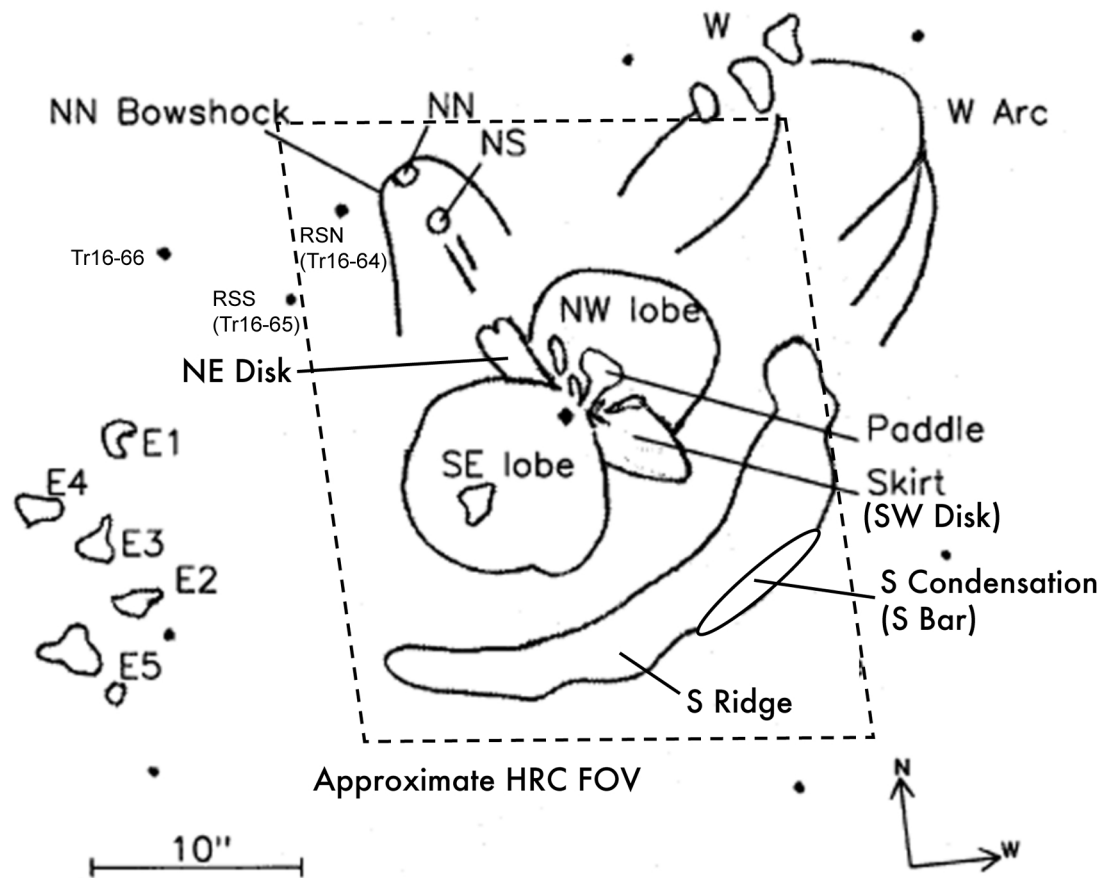


Figure 7.1: Diagram of ejecta field around  $\eta$  Car with prominent features labeled. HST/ACS/HRC field-of-view for GO9721 marked with dashed line. Compare with the color image in fig. 1.2. Illustration adapted from [Currie et al.(1996)].

(1915–1934) results from the *Southern Double Star Catalog* [Innes et al.(1927)] and the *Union Observatory Circulars*<sup>1</sup> to calculate proper motions. He found that the weighted mean proper motion of the six features was approximately 5" per century, and they were offset by 5" from the central star, thus indicating an age of one century, and concluded that the material had most likely been ejected during the 1843 Great Eruption.

### 7.1.2 Ringuelet 1958

Ringuelet (henceforth: R58) re-measured the data cited by Gaviola and performed a more quantitative analysis of the proper motion of five condensations within the Homunculus [Ringuelet(1958)]. She concluded that various features within the Homunculus actually traced back to *three* photometric events, viz., 1843 (the Great Eruption), 1857, and 1895 (the Lesser Eruption).

### 7.1.3 Walborn, Blanco, & Thackery 1978

Walborn, Blanco, & Thackery (henceforth: WBT78) used ground-based observations from 1950 and 1975 to deduce proper motions for a total of eleven nebular objects around  $\eta$  Car [Walborn et al.(1978)]. These included the outer wall of the NW lobe, the south ridge, the NN and NS condensations, the western condensation (marked “W” in fig. 7.1) and the eastern condensations (marked “E1”–“E5” in fig. 7.1). They found a spread of ejection dates, ranging from 1163 to 1873. Since the HRC FOV is restricted to the area marked out in the box (see fig. 7.1), I will not

---

<sup>1</sup>No specific references are given by Gaviola.

discuss the eastern or western condensations any further.

WBT78 determined the date of origin of the leading edge of the NW lobe to be  $1818 \pm 44$  years. The NN and NS condensations were found to have dates of origins of  $1869 \pm 11$  years and  $1873 \pm 14$  years, respectively. The central portion of the South Ridge was found to have a date of origin of  $1810 \pm 33$  years, and the eastern tip of the South ridge was dated at  $1703 \pm 51$  years. WBT concluded that some of Gaviola and Ringuelet Homunculus features correlated with the 1890 Lesser Eruption and that some, along with the leading edge of the NW lobe and the central region in the South Ridge correlated with the 1843 Great Eruption. WBT78 also suggested that NN and NS were associated with the photometric plateau of c. 1870 (barely visible in fig. 1.3; see [Frew(2004)] for a discussion of this photometric feature).

#### 7.1.4 Currie & Dowling 1996

The next major advance was obtained when Currie & Dowling (henceforth: CD96) applied feature cross-correlation to hundreds of features across multiple epochs (spanning three years) of HST Wide Field/Planetary Camera (WF/PC) and WFPC2 data [Currie et al.(1996)]. CD96 determined with high certainty that the entire Homunculus was correlated with a single event, viz. the 1843 Great Eruption. They determined a date of origin for the Homunculus to be  $1841 \pm 4$  years (standard deviation of the mean), with a distribution width of  $\pm 10$  years. CD96 took the later as an upper limit to the duration of the Great Eruption, deriving an eruption “interval” upper limit of 20 years. The CD96 results refuted the hypoth-

esis of Ringuelet (later recalled by WBT78) of multiple events associated with the material in the Homunculus.

CD96 (along with [Dowling(1996)], which contains a much more detailed exposition of the methodology and results summarized in CD96) found indications of an 1841 date of origin for the equatorial debris, though these results were less conclusive than the Homunculus results. They also report a date of origin for the NN and NS condensations with the Great Eruption and discovered that the prominent bright feature in the South Ridge—the South Bar—also had a Great Eruption-era date of origin. The remainder of the South Ridge is dated to  $1785 \pm 3$  years, again, with lower confidence than the definitive dating of the Homunculus.

### 7.1.5 Smith & Gehrz 1998

In their 1997 review of  $\eta$  Car, Davidson & Humphreys conjectured that the equatorial debris system originated in the 1890 Lesser Eruption [Davidson & Humphreys(1997)]. Smith & Gehrz (henceforth: SG98) followed this conjecture up with a new proper motion analysis of the Homunculus and the equatorial debris [Smith & Gehrz(1998)].

SG98 used two ground-based epochs (1945, 1972) along with 1995 HST observations, giving them a 50-year temporal baseline. Their methodology consisted of matching a total of 15 features (five in the NW lobe, one in the “paddle”, one in the NE branch of the equatorial debris field, two in the SW branch of the equatorial debris, and nine in the SE lobe). Because the HST data were higher resolution than the two ground-based epochs, the HST data were blurred by being convolved with

a 0.7" Gaussian kernel. The resultant data was at the same "resolution" as the ground-based data, allowing the relevant features to be matched across epochs.

Using this methodology, SG98 dates the SE lobe to  $1843.8 \pm 7.3$  years, the NW lobe to  $1858.8 \pm 6.0$  years, the paddle to  $1878 \pm 8$  years, the NE equatorial debris to  $1891 \pm 5$  years, and the SW equatorial debris to  $1885 \pm 6$  years <sup>2</sup>.

SG98 adopt the SE lobe date of  $1843.8 \pm 6.5$  years as the date of origin of the entire Homunculus. A brief assertion that "contamination by emission from faster moving equatorial features shifts the centroids of features belonging to the northwest lobe" is given by SG98 as the reason for ignoring the NW lobe result of  $1858.8 \pm 6.0$  years. This somewhat vague assertion is thus contingent on their results for the equatorial debris, and is not operative if the equatorial debris does not originate at a much later date. They thus associate the entire Homunculus with the Great Eruption.

Similarly, they associate the entire equatorial debris field with the 1890 Lesser Eruption. They are confident enough to state that "the errors associated with the measurement of the ejection times for the individual condensations positively rule out the possibility that the equatorial features could have been ejected as early as 1843."

---

<sup>2</sup>SG98 lump both NE and SW equatorial debris features along with the paddle into a single equatorial group, for which they derive a date of origin of  $1885.8 \pm 6.5$  years. There is some question about whether the paddle is a member of the equatorial debris field or the NW lobe; these components will thus be referred to separately.

### 7.1.6 Morse et al. 2001

Morse et al. (henceforth: M01) used two epochs (1994 and 1999) of HST WFPC2 data and a modified form of the cross-correlation algorithm described in CD96 to analyze proper motions and derive dates of origin for the Homunculus, equatorial, and outer debris for approximately 50 data points. They found a date of origin for the lobe material to be  $1847 \pm 1$  year. They associate the NN and NS condensations and all equatorial features with the Great Eruption. They find the South Ridge complex to be complicated, with the central region (the “South Condensation”) associated with the Great Eruption, but the remaining material dating to  $1771 \pm 31$  years, and argue that the material significantly predates the Great Eruption, indicating that significant mass loss events most likely preceded the Great Eruption.

## 7.2 Discussion

Table 7.1 summarizes the evolution of the astrometric analysis of the debris, from 1950 to 2001. Beginning with Gaviola in 1950, researchers realized that the features near  $\eta$  Car were non-stellar in nature, and further, that they may have been ejected during the 1843 Great Eruption. Work by Ringuelet and WBT78 attempted to quantify the proper motion and resultant dates of origin. It was not until CD96, however, that a definitive dating of the entire Homunculus was made, associating it with the Great Eruption. As described above, CD96 also dated the equatorial debris and NN and NS condensations to the same event. CD96 estimated the upper

limit of the GE interval to be 15 years.

Using different data and methodology, Smith & Gehrz date the Homunculus to the Great Eruption and the equatorial debris to the late 1880s, associating it with the 1890 Lesser Eruption. Morse et al.'s work contradicted this latter finding, agreeing with CD96's conclusions regarding the equatorial material. Nevertheless, this association of the equatorial debris with the 1890 event has subsequently been adopted as canon by some researchers (e.g., [Humphreys et al.(1999)], [Davidson et al.(2001)], [Smith(2006)], etc.), with the equatorial ejecta being considered a critical component of the Lesser Eruption.

Table 7.1: Astrometric dates of origins for specific ejecta fields as derived by previous authors.

Feature	Subfeature	G50 (1950)	R58 (1958)	WBT78 (1978)	CD96 <sup>a</sup> (1996)	SG98 (1998)	M01 (2001)
Homunculus	c.1845	1839 <sup>b</sup> ±18		1841±4			1847±5
	NW Lobe		1818±44		1858.8±6.0		
	SE Lobe				1843.3±7.3		
	Paddle <sup>c</sup>			1878±8		1847±5	
S Ridge			1785±3		1771±31		
	S Bar		1845±4		c.1847		
North Jet				1849±2		1847±5	
	NN			1855±5		1847±5	
	NS				c.1841	1891±5	1847±5
						1885±6	
Eq. Disk	NE Disk						
	SW Disk						

<sup>a</sup>Some results taken from [Dowling(1996)].

<sup>b</sup>Other Homunculus features dated to 1895±2.

<sup>c</sup>The Paddle is now generally considered a Homunculus feature, though some authors (SG98) conclude it is an equatorial one.

In this analysis, data from the 1995 WFPC2 observations are combined with 2003 HRC observations. The error of the derived proper motion (and hence, date of origin) measurements will (to first approximation) vary as the error of the distance divided by the temporal baseline. The combination of a much more accurate astrometric instrument (the HRC) with a relatively long temporal baseline (8 years) allows significant improvement over all previous astrometric measurements. In table 7.2, I provide estimates for single measurement accuracies, list the temporal baselines, and give the estimated proper motion accuracy. The last row in the table gives the estimates for this work and includes the improved second-epoch measurement (by using the HRC instrument) and the 8.4-year baseline.

Table 7.2: Comparison of estimated single measurement and calculated proper motion accuracies of previous data sets with expected accuracy for this work.

Data set	Epoch 1 (mas)	Epoch 2 (mas)	$\Delta t$ (years)	$\sigma_{PM}$ (mas/yr)	Proper motion degradation vs. this work
CD96	10	5	4.1	2.7	4.1x
SG98	100	100	50	2.8	4.2x
M01	5	5	5	1.4	2.1x
This work	5	2.5	8.4	0.66	—

As shown in the table, the data used in this work will allow significant improvement (factor of 2x or more) in the *per feature* position measurement, proper motion and date of origin results. Additional “bulk” accuracy improvements are achieved by using approximately four times as many data points as M01 and have a factor of two improvement in position for the second epoch.

With these improvements in proper motion and date of origin accuracies, the following questions can be addressed:

## 1. *What is the date of origin for the Homunculus ejecta?*

The photometric peak of the Great Eruption is well established.  $\eta$  Car reached peak brightness first in April 1843 and then again in December 1844. CD96 reports the eruption to have peaked in  $1841 \pm 4$ , SG98 reports  $1843.3 \pm 7.3$ , and M01 reports  $1847 \pm 5$ . All fall within the 1843.3–1844.9 period that represents the peak of the great eruption, given the reported error bounds. Is it possible, with the increased accuracy, to better determine when the ejection peak occurred? There are significant theoretical implications either if the ejection peak occurred significantly *before* or significantly *after* the photometric peak.

Furthermore, SG98 reports a *fifteen-year* difference between ejection dates for the NW and SE lobes. This is alluded to in [Dowling(1996)] as well (which described the CD96 analysis in detail), with the final 1841 value arrived at through averaging between the two lobes. Is there a significant difference between measured ejection dates for the two lobes? If so, is there an explanation for it?

## 2. *What is the ejection interval for the Great Eruption?*

CD96 derived an interval upper limit of approximately 15 years for the Great Eruption. However, as they themselves note, this may be due simply to measurement limitations. Their derived ejection-date histogram may be dominated by basic measurement error. The actual ejection interval may have been much shorter. If so, this is an important constraint for future modelers of the Great Eruption, since knowing when mass was ejected and how much was ejected will set the constraints on the

mass ejection rates during the eruption. Was the mass all blown off very quickly, did it follow the photometric curve, or was there some other distribution?

A second issue related to the distribution of ejection dates is that of the spectroscopic cycle. As both Daminelli [Damineli(1996)] and Frew [Frew(2004)] have noted (among others), one can “rewind” the spectroscopic cycle to  $1843.3 \pm 0.2$ , i.e., the photometric peak. Is this a mere coincidence, or was the Great Eruption related to the spectroscopic cycle, perhaps a manifestation of periastron passage for a binary system, as discussed in Part I of this thesis? If so, it may be possible to detect temporal structure (e.g., 5.52-year features) with a high-accuracy ejection date histogram. For example, is there any evidence of ejecta from 1838 or 1849? If so, this could suggest that binarity was an essential component of the Great Eruption.

### *3. What is (are) the ejection date(s) for the equatorial features?*

Both CD96 and M01 converge on the equatorial debris having been ejected during the Great Eruption. Nevertheless, the association of equatorial debris with the 1890 event—first conjectured in [Davidson & Humphreys(1997)], then quantified in [Smith & Gehrz(1998)]—has subsequently been adopted as canon by some researchers (e.g., [Humphreys et al.(1999)], [Davidson et al.(2001)], [Smith(2006)], etc.), with the equatorial ejecta being considered a critical component of the Lesser Eruption.

Whether the equatorial debris is associated with the Great Eruption or the Lesser Eruption is critical to theoreticians attempting to model one or the other event. Was the Great Eruption a purely bi-polar phenomenon, or did it also have an

equatorial component? Were the two events significantly different in their natures, or were they similar? It is therefore crucial to establish which event or events the equatorial features properly belong to.

*4. What are the ejection dates for the debris outside the Homunculus?*

The improved accuracy of these measurements will allow calculation of the ejection dates of certain feature outside the Homunculus with high accuracy. Are there any fast-moving features that are associated with the Great Eruption? Are there the remains of earlier events, such as the South Ridge, which appears to date from the 1700s? If so, can the current state of knowledge be improved upon, with the result that more accurate dates and associations for earlier event(s) are obtained?

These are the specific questions addressed in Part II of the thesis.

## Chapter 8

### Astrometric Methodology

Currie & Dowling demonstrated that significant improvements in astrometric accuracy for diffuse (i.e., non-stellar) objects could be achieved by cross-correlating properly scaled regions between multiple observing epochs ([Dowling(1996)], [Currie et al.(1996)]), as compared to more standard techniques (e.g., centroiding). Morse et al. then re-implemented this basic idea using higher accuracy data and a longer baseline and was able to improve upon CD96 results [Morse et al.(2001)] (see discussion in §7.1).

As shown in table 7.2, our 2003 HRC observations provide us with the opportunity to significantly improve the astrometric accuracy of the ejecta vs. previous analyses. In order to achieve this improvement, the basic concept of multi-epoch cross-correlation analysis has been re-implemented. This chapter describes the implementation and the expected accuracies.

#### 8.1 Observational Data

Table 1.1 lists the available data from our GO9721 observations. For this analysis, F660N data from G09721 is used for two primary reasons: first, by including both very short (0.1 sec) and very long (412 sec) exposures, it allowed access to the full dynamic range of the central star and the material around it; second, it is a

good spectral match for the GTO/WFC 5239 observations (PI: J. Westphal) used for Morse's second epoch (M01). Specifically, the two epochs consist of the following data sets:

*Epoch 1: 1995.4 WFPC2 F658N data*

These observations consist of a total of six exposures using WFPC2 centered on the central star. Effective post-processing instrument pixel resolution = 45.5 mas; central wavelength = 6590 Å; spectral bandwidth = 28 Å ([Heyer et al.(2004)]). Integration times =  $2 \times 0.1$ ,  $2 \times 4$ ,  $2 \times 200$  secs. No dithering pattern was used during the observations; the multiple exposures were performed for cosmic-ray rejection purposes. Combined deep exposure time = 400 sec.

*Epoch 2: 2003.9 HRC F660N data*

This data set consists of sixteen exposures using ACS/HRC, centered on the central star. Effective post-processing instrument pixel resolution = 25.0 mas; central wavelength = 6599 Å; spectral bandwidth = 35 Å ([Gonzaga(2005)]). Integration times =  $4 \times 0.1$ ,  $4 \times 1.0$ ,  $4 \times 10.0$ ,  $4 \times 412.0$  secs. The standard four-point HRC box-dither pattern [Gonzaga(2005)] was used for both cosmic ray rejection purposes and to support image reconstruction at higher resolution using the MultiDrizzle package [Koekemoer et al.(2002)]. Combined deep exposure time = 1648 sec.

## 8.2 Creation of Reference Images

The first task was to take the input images and create single, integrated images that cover the full million-to-one dynamic range of the deconvolved data at

maximum SNR. Because the detectors have much smaller dynamic ranges ( 53k e- for the WFPC2 ADC and 85k e- for the HRC full well capacity), multiple images over a range of integration times were needed. These images were co-registered and a reference image was created by selecting the highest SNR pixel below saturation. For example, the central cores of the reference images were extracted from the shortest exposure input images, while the outer debris regions were extracted from the longest exposures. In general, the longest exposure images contributed the most pixels, with only the central star and blooming regions replaced with shorter exposures. The details for each of the epoch's images follow in the next two subsections.

### 8.2.1 1995.5 F658N Reference Image

The process for creating the F658N reference images is shown in fig. 8.1. All F658N WFPC2 images were pre-processed using the standard MAST/On-the-fly retrieval option from the HST MAST archive. MAST delivered flat-fielded, dark and bias-corrected WFPC2 images. These images were at the native instrument 45.5 mas per pixel resolution and were neither distortion corrected nor cosmic ray cleansed.

The image processing on the delivered images began with running them through the PyRAF MultiDrizzle procedure. Each pair of matched integration time images was run through multidrizzle, which rotated the image to align the output y axis with celestial north, removed cosmic ray hits, corrected the data for WFPC2 distortion, and combined the two into a single image with an effective integration time

### Generation of 1995.4 F658N 400+8+0.2 sec Reference Image

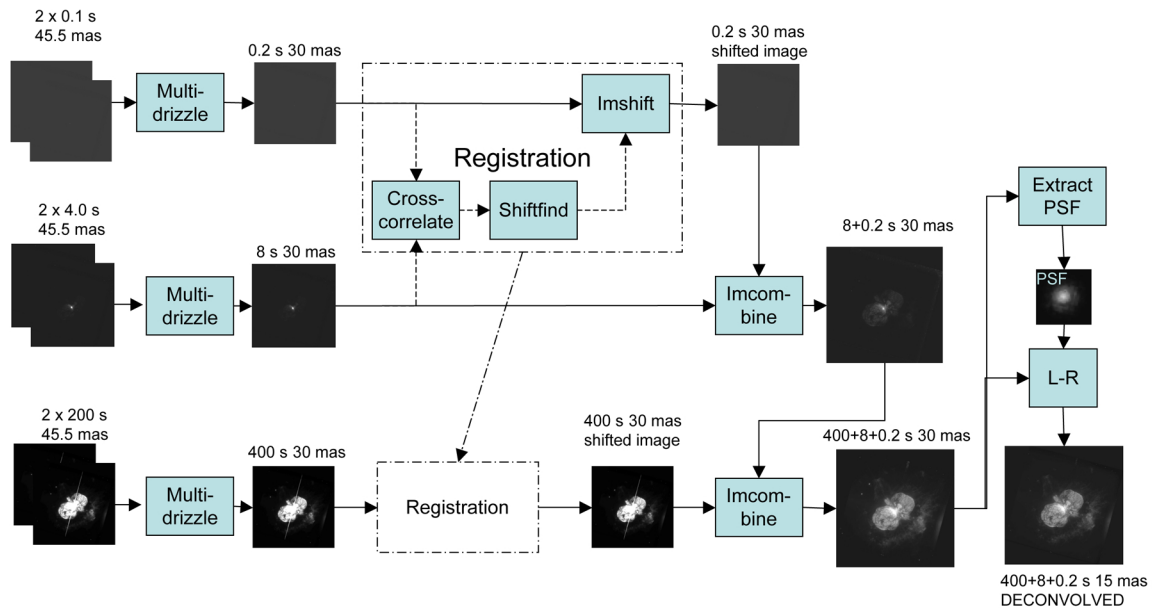


Figure 8.1: Process for generating F658N reference image. Input images are shown on left side of figure, the final output product is shown on bottom right. A description of the process is given in §8.2.1

equal to the sum of the input image integration times. The images were resampled using the MultiDrizzle algorithm from 45.5 to 30 mas per pixel in order to make them more compatible for later analysis.

Next, the Homunculus region of the 0.2-sec image was cross-correlated with the 8-sec image using the PyRAF Cross-correlate routine. This routine generates a cross-correlogram that is then used by the SHIFTFIND routine, which calculates registration translations in x and y coordinates. The 0.2-sec image and the translation coordinates are then input into the PyRAF IMSHIFT routine, which generates a new, shifted 0.2-sec image that is registered with the 8-sec image. The two images are then combined using a custom IDL routine IMCOMBINE that replaces all saturated regions in the longer exposure image with unsaturated pixels from the shorter exposure image. A combined 8+0.2 sec<sup>1</sup> unsaturated image is output from this process.

The procedure was then repeated, only now cross-correlating the Homunculus from the 400-sec image with the same region from the 8+0.2 sec image. The output image was a 400+8+0.2 combined unsaturated image.

The next step was to deconvolve the combined image to improve SNR and feature contrast. After extensive experimentation with a variety of synthetic and empirical PSF models, it was found that using the PSF from Tr16-64 produced the most satisfactory results<sup>2</sup>. Again, using the custom IDL routine EXTRACT\_PSF,

---

<sup>1</sup>The nomenclature refers to the fact that the output image is created by combining an 8 and 0.2 second images.

<sup>2</sup>Candidate PSFs from both models and *all* F660N observations were used to deconvolve F660N images. The Tr16-64 PSF was found to produce the best results across all available stars on the GO9721 composite image. Presumably this is due to the fact that the Tr16-64 PSF incorporates the instrument state information at the time the image was taken, while other PSFs do not.

the PSF was extracted from the combined image and used as the deconvolution kernel for the PyRAF implementation of the Lucy-Richardson deconvolution algorithm (see [Lucy(1974)], [Richardson(1972)]). After experimentation, it was found that 25 iterations of L-R on the WFPC2 data was optimal; additional iterations resulted in unacceptable artifacts in the output images.

The results of the reference image generation process are shown in fig. 8.2. Some residual image artifacts are visible around the edges of the PC detector, as well as faint diffraction spikes emanating from the central star. The PC detector subtends more sky than the HRC detector; a magnified region of the PC image is shown in fig. 8.3 that represents the corresponding 2003.9 HRC image. It is this latter image that is used for the first epoch analysis of ejecta separation and proper motion.

### 8.2.2 2003.9 F660N Reference Image

The process of generating the 2003.9 HRC F660N image was similar to that for the WFPC2 F658N image (§8.2.2). The F660N images were retrieved from the on-line MAST archive after being processed by the CALACS on-the-fly system. CALACS flat fields, dark and bias corrects the raw images. As shown in fig. 8.4, these calibrated images—four per exposure-time setting—were then processed using the PyRAF MULTIDRIZZLE routine. As with the WFPC2 data, MULTIDRIZZLE combined the input images into a single, cosmic-ray rejected, distortion corrected combined image rotated so that the y-axis was parallel to celestial north. The box

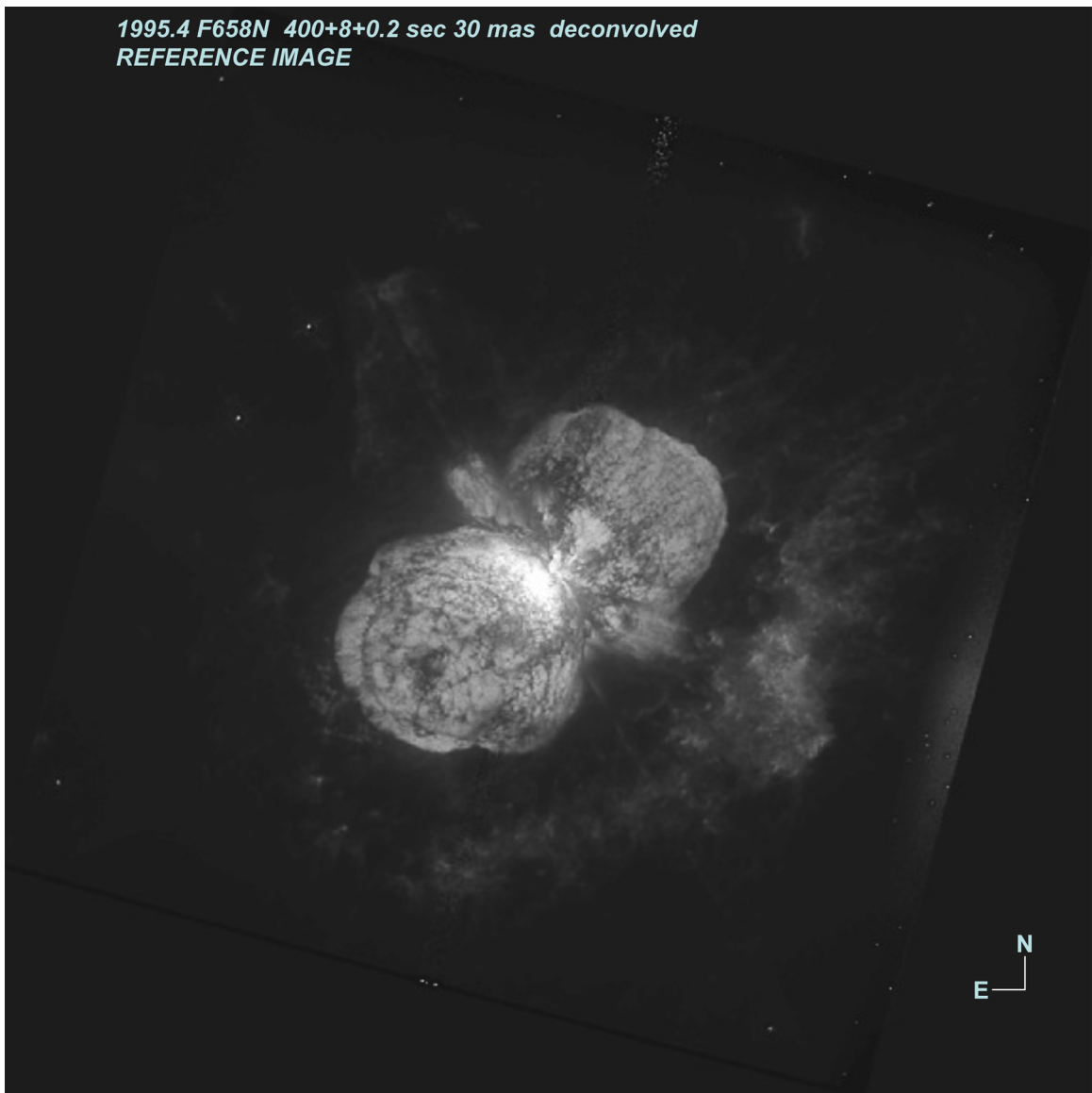


Figure 8.2: WFPC2 F658N reference image. Image includes full dynamic range from background through unsaturated central star (note, however, that for display purposes, the upper end of the dynamic range was cut off and appears saturated in the image). The central, rotated square region is the Planetary Camera (PC) detector and the dark regions outside the detector area are the padding added during image rotation. Diffraction spikes are faintly visible extending out from the central star along NE/SW and NW/SE axes.

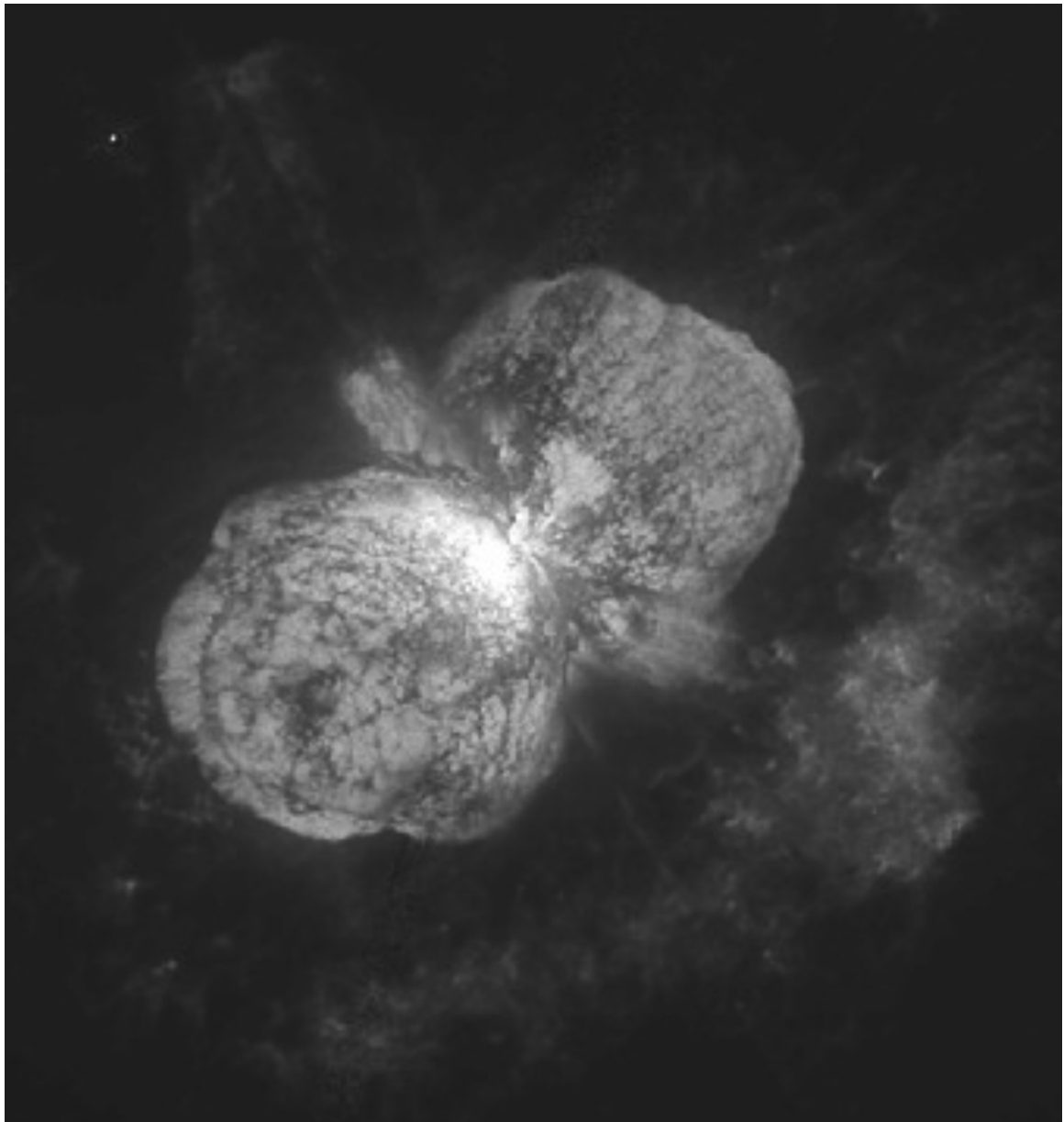


Figure 8.3: A magnified view of the Homunculus region of the WFPC2 F658N reference image (see fig.8.2), corresponding to the approximate field-of-view of the HRC (see fig. 8.5).

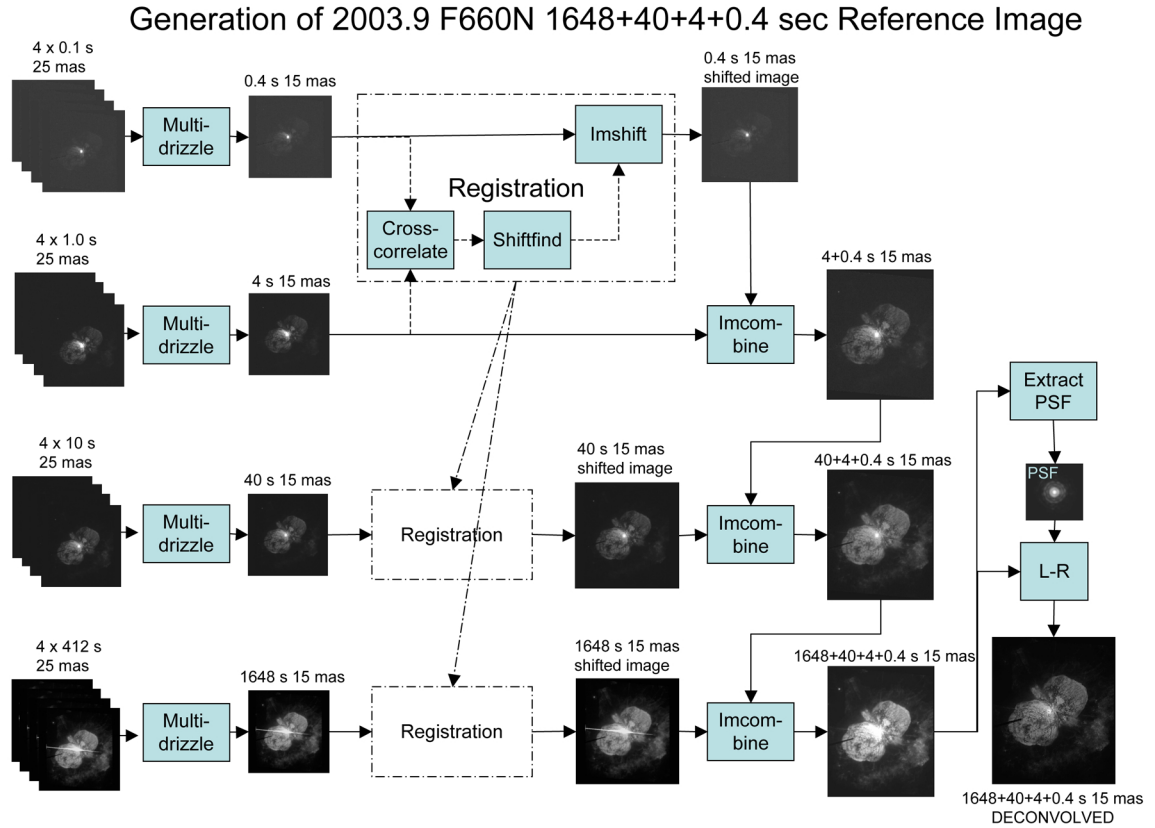


Figure 8.4: Process for generating F660N reference image. Input images are shown on left side of figure, the final output product is shown on bottom right. A description of the process is given in §8.2.2.

dithering conducted during the observations allowed generation of the final image at 15 mas/pixel resolution. The combined images effectively had integration times equal to the sum of the integration times of the input images. In the case of the HRC data, this resulted in 0.4, 4, 40 and 1648 sec images.

As shown in the fig. 8.4, the combination process was essentially the same as with the F658N WFPC2 data, with the exception that four images were combined rather than three. After all images were cross-correlated, shifted, and combined to form the 1648+40+4+0.4 15 mas non-deconvolved image, the IDL routine EX-

TRACT\_PSF was used to extract the TR16-64 PSF, which was then used to deconvolve the entire image<sup>3</sup>. Deconvolution was terminated at 100 iterations for the F660N data. Figure 8.5 is the resultant F660N reference image.

### 8.3 The cross-correlation procedure

The cross-correlation procedure (shown in fig. 8.6) is the core of the astrometric analysis task. The entire procedure consists of custom IDL subroutines written specifically for this analysis and these instruments. The overall objective of the procedure is to determine expansion velocities and dates of origin for specific nebular features. This is done by extracting “patches” from the HRC data, cross-correlating the patches with both the 1995.4 WFPC2 and 2003.9 HRC data, and using the resultant cross-correlograms to determine inter-epoch shift. The results for all patches are then compiled, allowing the calculation of the overall expansion rate and the date-of-origin distribution for the individual patches and regions. The following subsections describe specific implementation details.

#### 8.3.1 Patch extraction and preparation

The data in HRC images are of higher quality and resolution than the WFPC2 data. The first step in the procedure is to extract 0.48-arcsecond square (32 x 32 pixels at 15 mas per pixel) from the HRC reference image. The typical Homunculus features are approximately 75 mas FWHM across; the 0.48-arcsecond patch was

---

<sup>3</sup>As with the WFPC2 data, a variety of other means were tested, including a visual inspection of all other HRC F660N data sets publicly available, but the PSF from this data set appeared to be the highest quality one available.

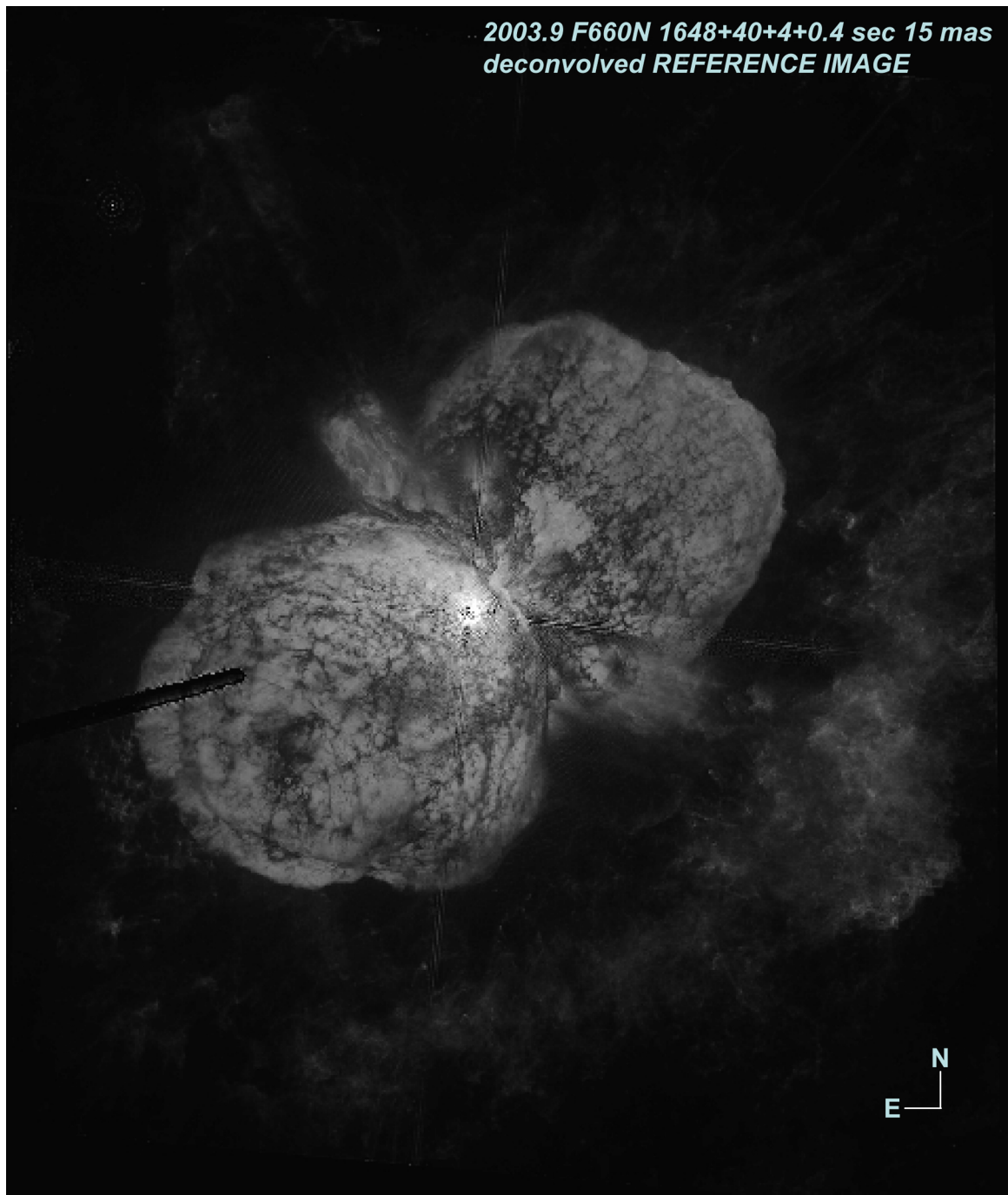


Figure 8.5: HRC F660N 2003.9 reference image. Reference image is a composite of 1648, 40, 4, and 0.4 sec images, with each pixel populated from the maximum unsaturated signal to noise value from the input images. Four diffraction spikes are visible emanating from the central star in a cross-like pattern. The HRC's "Fastie finger" occulting device is visible as a dark region covering part of the SE lobe. This image represents the full HRC frame.

## Cross-Correlation Procedure

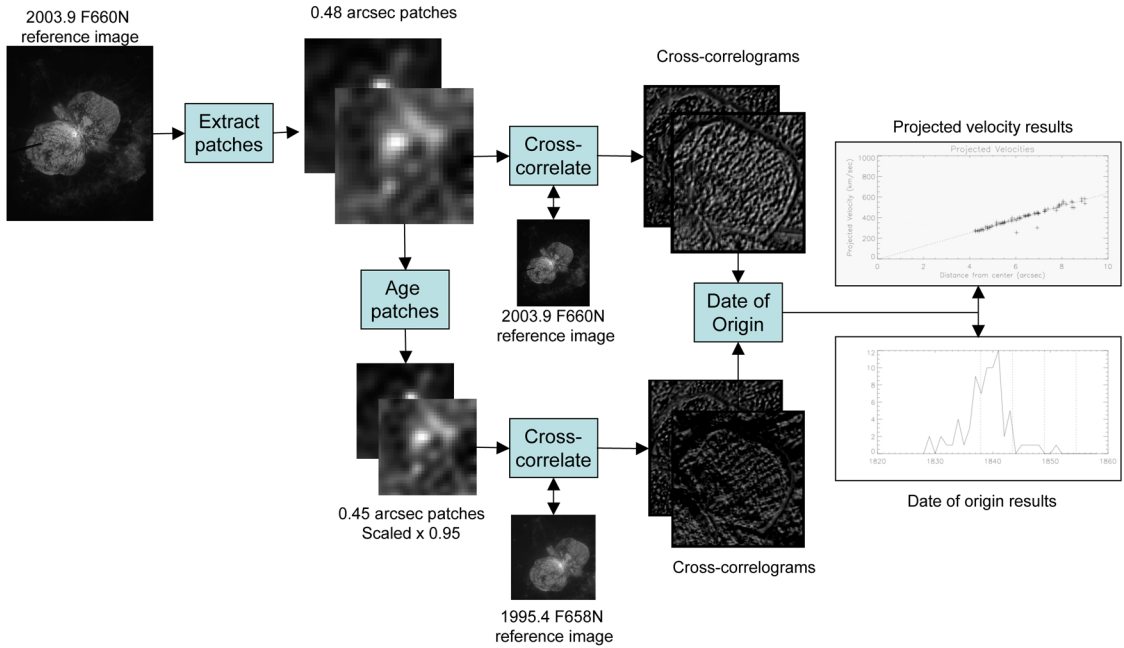


Figure 8.6: Cross-correlation procedure.

found to be large enough to include multiple features without being so large that higher-order scaling or motion effects became a problem. A total of approximately 300 patches were extracted during the data analysis process (see §9).

One set of extracted patches was retained for cross-correlation<sup>4</sup> with the 2003.9 HRC reference image. A second set of patches, for use with the 1995.4 WFPC2 images, had to be separately generated. The reason for this is shown in fig. 8.7. Each patch can be modeled as consisting of a collection of discrete blobs, each on its own ballistic trajectory in the origin's inertial frame. The motion of the blobs from epoch 1 to 2 will be manifested as increased separation in both x and y in the patch's co-moving reference frame. As long as this motion is truly ballistic in the

<sup>4</sup>Actually, auto-correlation.

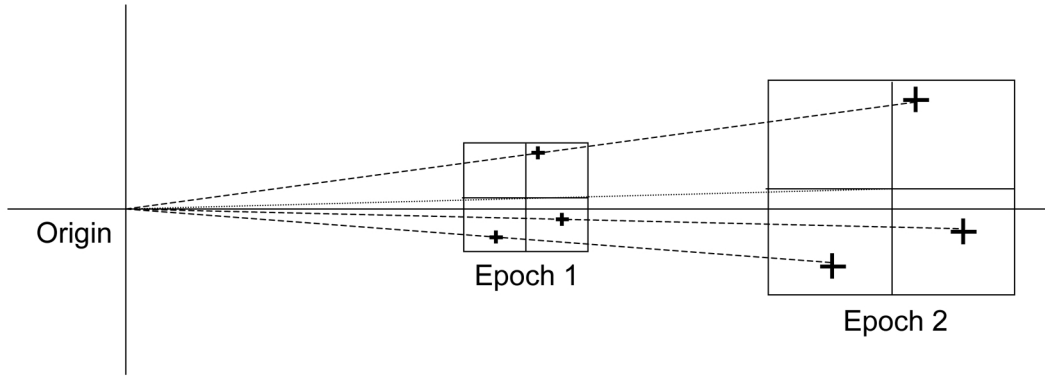


Figure 8.7: Visualization of patch expansion

origin's frame, the relative motion in the patch frame is exactly equivalent to scaling the patch by the ratio of the time from epoch 1 to epoch 2 to the time at epoch 1. For example, if the times for epoch 1 and 2 are given by  $t_1 = a$  and  $t_2 = 2a$ , then the relative motions are exactly equivalent to scaling the epoch 1 coordinates by a factor of two.

The aging process is time-reversible. In this case, we can take the 2003.9 patches and age them by a factor of 0.95 in order to simulate what the 2003.9 patches would have looked like in 1995.4, assuming an 1843 ejection date. The patch is reduced to 0.456 arcseconds; the central 0.45 arcseconds are then extracted and a new, 30 x 30 pixel “aged” patch is created at 15 mas per pixel resolution.

For some specialized cases (e.g., equatorial ejecta, the South Ridge), a variety of different scalings were tested in order to include the possibilities that the material was ejected at some time other than the Great Eruption. These cases are discussed in §9.

The process of aging the patches introduces a source of error. While it is true that point objects obey the scaling model described above, extended objects are problematic. Unless the extended object is expanding or contracting at the same rate as the bulk expansion of the overall material, the scaling process has the effect of incorrectly shrinking or expanding the extended objects. For example, if we consider the model described above (and shown in fig. 8.6), an object that has a  $\text{FWHM} = 10$  mas in epoch 1 would have a  $\text{FWHM} = 20$  mas in epoch 2. This was recognized by [Dowling(1996)], but the errors so introduced appear to have been sufficiently small so as to no affect the overall conclusions. This process will be simulated in order to estimate errors (§8.4; 8.5), at which point the magnitude of this error will be addressed.

### 8.3.2 Cross-correlation

The next step is the cross-correlation of the patches with the appropriate images. The non-aged patches were cross-correlated with the 2003.9 image using both a canonical “multiplicative” cross-correlation and the non-traditional “subtractive” method used in CD96 (see [Dowling(1996)] for implementation details). For epoch 1, the patches (15 mas per pixel) and the image (30 mas per pixel) were at two different resolutions. In order not to lose any information, the images were resampled without interpolation to 15 mas per pixel. The aged patches were then cross-correlated against this resampled image.

Initial results from using either multiplicative or subtractive cross-correlation

with the 1995.4 data were unsatisfactory. This appears to be due to instrumental differences between the HRC and the WFPC2 that resulted in the correlation being dominated by gain and offset differences rather than features. In order to overcome this problem, both the patches and the specific cross-correlation window from the image were converted from physical counts to units of standard deviation with a zero point equal to the mean of the particular window, so-called “Z scores” in statistics; see [Taylor(1997)]. Explicitly, the pixels were converted according to the following transformation:

$$I'_{x,y} = \frac{I_{x,y} - \bar{I}_{window}}{\sigma_{window}} \quad (8.1)$$

where  $I_{x,y}$  is the signal at position (x,y),  $\bar{I}_{window}$  is the mean signal and  $\sigma_{window}$  is the standard deviation for the overall window or patch. This transformation converts an input image with physical units representing counts per second to an image with a mean intensity of zero and individual pixel intensities given in units of image standard deviation. Converting the input images into standard deviation images in this way eliminated the instrumental differences (bias, gain, throughput, dark current, etc.) associated with trying to cross-correlate the HRC data with WFPC2 images. This transformation does not change the way an image “looks” (i.e., the relative intensities), but does “normalize” images from different instruments, significantly improving cross-correlation results.

### 8.3.3 Expansion velocity/date-of-origin calculation

The outputs of the cross-correlation process were two cross-correlograms: one each for the subtractive and the multiplicative techniques. These cross-correlograms were then used as input to the final step in the processing: calculation of the expansion velocity and date-of-origin for individual patches.

Relative patch positions were determined by finding the centroid of the peak positions in the cross-correlograms using a standard 2-D elliptical Gaussian centroiding routine. No significant differences were found between the multiplicative and subtractive results. The calculated patch positions were then compared to the central star position, determined using the Grid Search Method (GSM), described in detail in §3.4.1. This yielded a measurement of the separation of the patches from the central star in that epoch.

Separations were then compared between epochs for each patch. The annual expansion rate is given by:

$$r_{1-2} = \frac{d_2 - d_1}{d_1 \delta t} \quad (8.2)$$

where  $\delta t = 8.43$  years, the temporal baseline between the two epochs. Since second-epoch separation measurements are more accurate than first epoch, we use the second epoch patches and run the clock backwards, effectively shrinking them in order to simulate what they would have looked like at epoch 1:

$$r_{2-1} = \frac{d_2 - d_1}{d_2 \delta t} \quad (8.3)$$

The age of the patch at second epoch is then given by:

$$\Delta t = \frac{1}{r_{2-1}} \quad (8.4)$$

and the date of origin by:

$$D_{origin} = 2003.9 - \Delta t \quad (8.5)$$

### 8.3.4 Inter-epoch/inter-instrument plate-scale correction

As discussed previously in §3.7, the distortion correction for the WFPC2 data would seem to be accurate to a residual level of 0.01 pixels, or 0.5 mas RMS over the WFPC2 detectors. The HRC distortion correction is significantly more complicated, and the fourth-order correction applied during the MultiDrizzle process is thought to be good to the 0.1 pixel level (2.5 mas) RMS for this particular filter ([Anderson & King (2004)], [Anderson (2006)]). Furthermore, we are not aware of any definitive comparison of plate-scale transformations between the two instruments.

In order to correct for residual plate-scale differences between the two systems, the positions of a total of five stars (one bright and four very faint, distributed around the image outside the Homunculus) were measured on both WFPC2 F658N and HRC F660N reference images. A reference point was determined for each epoch by taking the mean position of the five stars and separations were measured for each star from the reference point in both epochs. Ratios between the first and second epoch separations were calculated and a mean value calculated. This mean ratio

was taken to be the residual plate-scale correction between the two epochs.

For the two images at hand, the ratio was determined to be 1.00063, that is, the second epoch image appeared 0.063% larger than it should have. Across the HRC image, this amounts to slightly more than half a pixel. This was applied as a correction factor for all second-epoch measured separations.

## 8.4 Simulation results

In order to validate the approach described above and quantify some of the sources of error, a simulation tool was written. The simulation tool generated the equivalent of first and second epoch images populated with multiple Gaussian “blobs.” Blob positions were defined for a WFPC2 epoch 1, and the blobs were added into a scene with realistic background and detector noise levels. Photon noise was also added. The epoch 1 positions were used to derive radial velocities, which were then used, along with a temporal offset and adjusted instrument parameters, to generate an HRC epoch 2 image. The blob positions were propagated ballistically from the first to the second epoch, thus simulating the expansion illustrated in fig.

8.7. One set of simulated images is shown in fig. 8.8.

The simulated images were then run through the cross-correlation processing described in §8.3.1—8.3.3, treating the simulated data exactly the same as if it were measurement data. The process correctly determined the date-of-origin (specified *a priori* in the simulation initial conditions) to within 1 year, thus validating the processing and indicating the systematic accuracy floor of the processing and data.

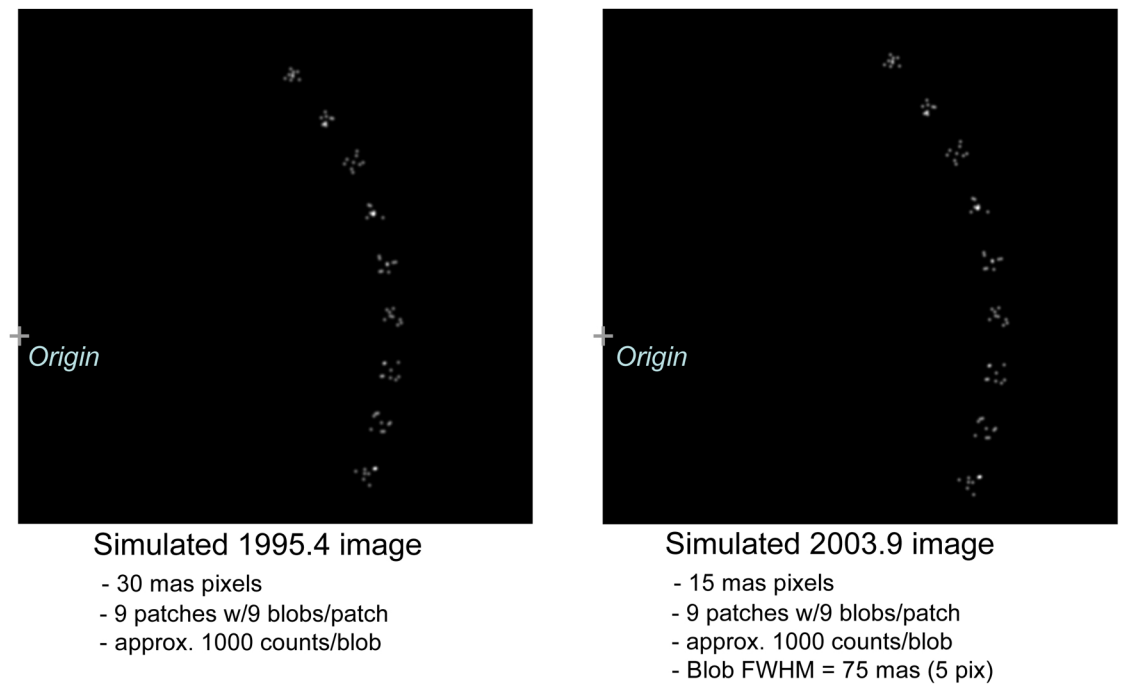


Figure 8.8: Simulated expansion images. Each blob is modeled as moving at constant velocity along a trajectory extending from the point marked “origin.” The simulated images are then used as input to the Cross-Correlation process to verify the processing and quantify errors.

Multiple cases were run, with variations such as variable background levels and photometrically inverted blobs (simulating dark rather than bright features). The results were statistically equivalent.

## 8.5 Error Estimates

What is the overall error associated with the data and techniques? The total error can be estimated by taking the root-sum-square combination of the individual sources of error. Individual error sources are described in the following subsections. In §8.5.5, the errors are combined and an overall error budget is provided.

### 8.5.1 Random centroiding

As discussed in Part I of this thesis, a reasonable approximation for random centroiding error is given by:

$$\sigma_{random} \approx \frac{FWHM}{SNR} \quad (8.6)$$

for a point source. For a given patch with  $n$  blobs, this becomes:

$$\sigma_{random} \approx \frac{FWHM}{SNR\sqrt{n}} \quad (8.7)$$

For the F658N WFPC2 data, the vast majority of the blobs are observed with an integration time of  $t_{int} = 400$  sec in the reference image. The typical peak flux rate for NW lobe features is 30–40 photons per second per pixel; the typical minimum

fluxes in the “valley” features are of order 6–7 photons per second per pixel. If we assume the latter represents the background flux from the Homunculus, the individual blob signal flux rates are approximately 28 photons per second per pixel. For a 400 sec integration time, the SNR for a typical blob is thus:

$$\begin{aligned}
SNR_{F658N} &\approx \frac{I_{blob}t_{int}}{\sqrt{(I_{blob} + I_{bg})t_{int}}} \\
&\approx \frac{I_{blob}\sqrt{t_{int}}}{\sqrt{I_{blob} + I_{bg}}} \\
&\approx \frac{28\sqrt{400}}{\sqrt{35}} \\
&\approx 95
\end{aligned}$$

For 2.5 pixel (75 mas) features, this yields a per feature random centroiding error of  $\sigma_{random} \approx 0.8$  mas. Assuming four blobs per patch as a lower limit, the contribution of random error to patch centroiding will be  $\sigma_{random,patch} \leq 0.4$  mas for first epoch data.

A similar analysis can be done for the F660N HRC data. Typical flux values are 13 photons per second per pixel for blob features and valley flux rates of 3 photons per second per pixel, yielding  $SNR_{F660N} \approx 110$  for a 1648 sec integration time. For 5 pixel (75 mas) features, this results in  $\sigma_{random} \approx 0.6$ ; with four blobs per patch, this gives an overall patch error upper limit of  $\sigma_{random,patch} \leq 0.3$  mas for second epoch data.

### 8.5.2 Residual distortion

As discussed in §8.3.4, based on information in the literature, the values quoted for the performance of the HST calibration routines, and discussions with STScI personnel, the RMS residual distortion for the F658N WFPC2 data is estimated to be 0.01 instrument pixels, or  $\sigma_{distortion} \approx 0.5$  mas, and 0.1 instrument pixels for the F660N HRC data, or  $\sigma_{distortion} \approx 2.5$  mas. This effect is taken to be systematic at patch scales<sup>5</sup>, thus, it is added in quadrature with the random error associated with patch location, and is not reduced by using multiple blobs.

### 8.5.3 Deconvolution effects

Deconvolution simulations were run to determine the effect of deconvolution on WFPC2 and HRC astrometry. It was found to introduce astrometric systematic errors at about the 0.1 pixel level. This references the input pixel size rather than the native instrument pixel size. For the F658N WFPC2 image, this results in  $\sigma_{decon} \approx 3$  mas, and for F660N HRC data  $\sigma_{decon} \approx 1.5$  mas. The F658N WFPC2 results are consistent with the 4 mas estimate for WFPC2 from [Dowling(1996)].

### 8.5.4 Central star position

Proper motions are calculated using the separation between the patch and the central star. The central star position has some uncertainty associated with it. Given the very large SNRs ( $SNR > 1000$  for the F660N data, for example), the

---

<sup>5</sup>That is, the residual astrometric errors due to uncorrected distortion do not reduce at a patch scale by averaging.

dominant source of error at the local level will be pixel phase effects. For the F658N data, the data are sampled at about 1.5 pixels per FWHM, or slightly undersampled. This suggests pixel phase error  $\sigma_{PPE} < 0.05$  pixels, or 2.3 mas for the WFPC2 data. The final HRC data is sampled at 4.5 pixels per FWHM, suggesting a pixel phase error of  $\sigma_{PPE} < 0.01$  pixels, or 0.15 mas for the second epoch data.

The other, perhaps more significant contribution to central star position error is due to the image registration, shifting and combination process that is used to generate the reference images. Misalignments due to misregistration will introduce a systematic offset between the few pixels around the central star that were contributed by the very short exposure image, and the Homunculus and outer ejecta region that was contributed by the deep exposure image.

The images were aligned using a cross-correlation routine that used the entire Homunculus. This is effectively a very large patch that is being correlated, so eqn. 8.7 can be used to estimate the error. How many features are there? The Homunculus consists of  $> 10^6$  pixels for the F658N data. Assuming one feature per 100 pixels, one gets  $n = 1000$ . The Homuncular SNR for the short exposure is in the ratio  $SNR_{short} = \sqrt{\frac{0.2}{400}} SNR_{long}$ , or  $SNR_{short} \approx 2$  for F658N. The accuracy of the cross-correlation is thus:

$$\begin{aligned}\sigma_{shift} &\approx \frac{75 \text{ mas}}{2\sqrt{1000}} \\ &\approx 1.2 \text{ mas}\end{aligned}$$

for the first epoch data.

Repeating the same calculations for the F660N data, we get  $SNR_{short} = \sqrt{\frac{0.4}{1648}} SNR_{long}$ , or  $SNR_{short} \approx 1.8$  for F660N. For  $n = 1000$  features, we get  $\sigma_{shift} \approx 1.3$  mas for the second epoch data.

The total “central star” error will be given by combining the error for centroiding the central star in the short exposures with the registration errors described above. This gives a combined error of  $\sigma_{cs} = 2.6$  mas for epoch 1, and  $\sigma_{cs} = 1.3$  mas for epoch 2. These values are used in Table 8.5.5.

### 8.5.5 Single-Patch Separation Estimated Total Error

The total estimated patch separation error can be estimated by taking the root-sum-square of the individual error components listed in §8.5.1—8.5.4. The results are shown in Table 8.5.5

Table 8.1: Estimated single-patch separation error: contributing components and total error.

Error source	1995.4 WFPC2	2003.9 HRC
	F658N (mas)	F660N (mas)
Random centroiding	0.4	0.3
Residual distortion	0.5	2.5
Deconvolution artifacts	3.0	1.5
Central Star position	2.6	1.3
<b>TOTAL</b>	4.0	3.2

### 8.5.6 Estimated single-patch expansion rate error

Eqn. 8.3 is used to calculate the expansion rate. We can estimate the error for the expansion rate by taking the partials with respect to  $d_1$  and  $d_2$ :

$$\begin{aligned}\sigma_r &= \sqrt{\left(\frac{\partial r_{2-1}}{\partial d_1} \sigma_{d_1}\right)^2 + \left(\frac{\partial r_{2-1}}{\partial d_2} \sigma_{d_2}\right)^2} \\ &= \sqrt{\left(\frac{-1}{d_2 \delta t} \sigma_{d_1}\right)^2 + \left(\frac{d_1}{d_2^2 \delta t} \sigma_{d_2}\right)^2}\end{aligned}$$

A patch dated from the Great Eruption would “typically” have  $d_1 = 4.0$  arcsec and  $d_2 = 4.2$  arcsec, where “typical” is approximately half-way from the central star to the edge of the Homunculus. If we insert these values along with  $\delta t = 8.43$  years and the error values from Table 8.5.5, the estimated expansion rate error is 0.01% per year, or 2 parts in one hundred for an expansion rate of 0.6% per year.

### 8.5.7 Estimated single-patch age error

The age of a given patch is calculated using eqn. 8.4. Repeating the approach from the previous section, the error in the age of the patch can be approximated by taking the partial derivatives of the eqn. 8.4, that is:

$$\begin{aligned}\sigma_{\Delta t} &= \sqrt{\left(\frac{\partial \Delta t}{\partial d_1} \sigma_{d_1}\right)^2 + \left(\frac{\partial \Delta t}{\partial d_2} \sigma_{d_2}\right)^2} \\ &= \sqrt{\left(\frac{d_2 \delta t}{(d_1 - d_2)^2} \sigma_{d_1}\right)^2 + \left(\frac{-d_1 \delta t}{(d_1 - d_2)^2} \sigma_{d_2}\right)^2}\end{aligned}$$

Inserting typical patch distances and the standard values for  $\delta t$  and  $\sigma_{d_1}$  and  $\sigma_{d_2}$  gives a result of  $\sigma_{\Delta t} = 4.5$  years.

### 8.5.8 Algorithm Error and Calculation of the Total Error

In §8.4, a series of simulations were run which resulted in age calculations with distributions of  $\sigma_{\Delta t} \approx 1$  year. The simulations were created so that none of the sources of error listed in Table 8.5.5 were present at any significant level. The result thus quantifies the level of inherent error introduced by the algorithm itself. As such, in order to understand the total error, the algorithm error should be added in quadrature as a systematic error to any total error calculation<sup>6</sup>. For single patches, this yields a total error in patch age of  $\sigma_{\Delta t} = 4.6$  years.

If we follow CD96 and M01, calculation of *the* date of origin of a particular feature is determined by using multiple patches. For example, the most likely date of origin for the NW lobe is given by taking the average date of origin for all the patches that are part of the NW lobe. According to the Central Limit Theorem (e.g., [Taylor(1997)]), the error associated with the date of origin is given by the standard deviation of the mean (SDOM), not by the standard deviation of the distribution of dates of origin for the patches. This is given by:

$$\sigma_{\Delta t, total} = \sqrt{\frac{\sigma_{\Delta t}^2}{n} + \sigma_{algorithm}^2} \quad (8.8)$$

$$= \sqrt{\frac{(4.6 \text{ years})^2}{n} + (1 \text{ year})^2} \quad (8.9)$$

---

<sup>6</sup>The assumption here is only that these systematic errors are uncorrelated with other errors such as random centroiding and pixel phase errors. There is no assumption that this error reduces over multiple observations; see eqn. 8.9.

As will be discussed in §9, different numbers of patches are used for different features.

Table 8.2 lists the estimates for each of these features.

Table 8.2: Estimated total error in determining feature age. Errors include patch error, algorithm error and number of patches per feature.

Feature	No. patches	$\sigma_{\Delta t, total}$ (years)
NW Lobe	77	1.2
SE Lobe	83	1.2
Paddle	13	1.9
NE Disk	23	1.5
SW Disk	22	1.5

There is some overlap between many patches. In order to account for this, the effective number of patches has been reduced by one-third.

### 8.5.9 Summary

The error analysis is summarized in the Table 8.3.

Table 8.3: Estimated errors: summary.

Type of error	Magnitude of error
Single patch sep. (1995.4)	4.0 mas
Single patch sep. (2003.9)	3.2 mas
Single patch exp. rate	0.01%
Single patch age	4.6 years
Feature age	1-2 years

I note that a single patch age distribution of  $\pm 4.6$  years may be enough to allow detection of temporal events separated by 5.52 years, that is, the period of the spectroscopic cycle. This will be discussed in more detail in §9.

## Chapter 9

### Homunculus and Equatorial Debris: Astrometric Measurement

#### Results

The next step is to apply the methodology developed in Chapter 8 to measurement of the ejecta around  $\eta$  Car. First, the method will be applied to the NW/SE lobe material, then to the equatorial debris. A second, alternate methodology (PAM, or the “Patch Alignment Method”) is used to confirm and further elucidate the Chapter 8 methodology. Discussion of the outer debris is presented in a following chapter (§11).

#### 9.1 NW Lobe: Initial Results

A total of 73 patches were selected for cross-correlation from the NW lobe. The locations of the patches are shown in fig. 9.1. The patches were chosen such that they were clearly part of the NW lobe system, with minimal chance of confusion with other systems such as the Paddle or Equatorial debris fields. The patches had also to be sufficiently far away from the central star such that the resultant cross-correlation was not dominated by the residual Airy diffraction pattern that is present near the central star, nor corrupted due to the steep gradients in this region. This minimum distance was found to be about 2 arcsec.

The cross-correlation analysis was conducted using the 1995.4 WFPC2 and

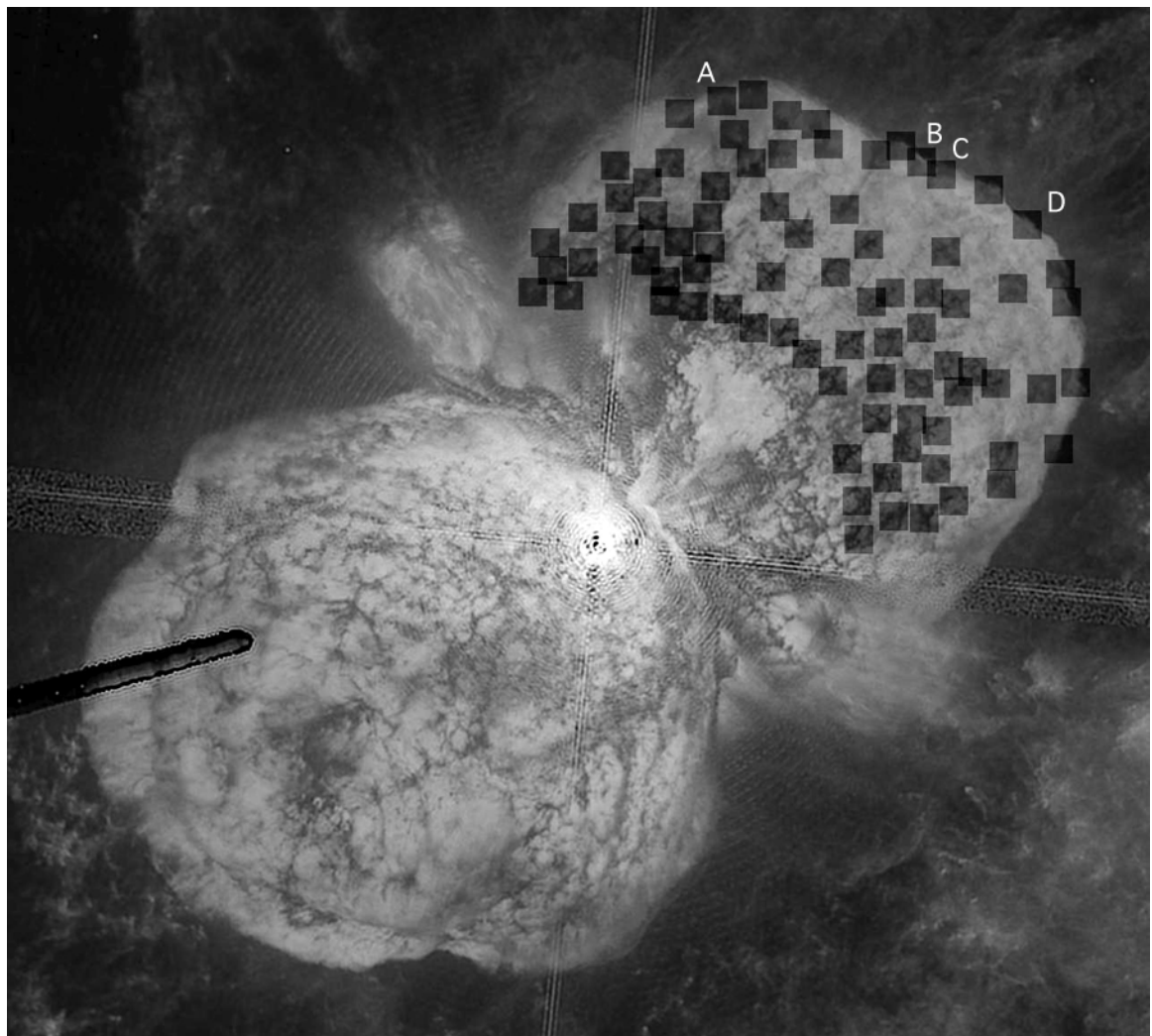


Figure 9.1: Locations of patches used for cross-correlation for the NW lobe of the Homunculus. Letters refer to specific patches discussed in text.

2003.5 HRC data as described in detail in §8. The shift in each patch’s pixel locations between the two epochs was converted to a projected (onto the plane-of-the-sky) separation velocity assuming a temporal baseline of 8.43 years and a distance of 2250 pc. The results are shown in fig. 9.2.

*Expansion velocity and expansion rate:* The top plot in fig. 9.2 shows the calculated expansion velocity, in km/sec, plotted as a function of separation at the 2003.5 epoch for all 73 NW lobe patches (fig. 9.1). Also shown is the best fit line for the expansion velocities. The residuals from the fit, shown in the middle plot, are distributed with a standard deviation  $\sigma = 14$  km/sec. The observed velocities are a linear function of the observed separations, confirming the “Hubble flow<sup>1</sup>” nature of the ejecta previously noted by CD96, SG98, M01, et al. The calculated expansion rate is  $r = (0.61 \pm 0.02)\%$  per year.

*Date of origin:* The date of origin calculated using the best fit to the expansion velocity data yields a date of  $1840.2^{+3.0}_{-2.9}$  years. On the other hand, the date of origin can be calculated by fitting a Gaussian to the dates of origins of the individual patches (bottom plot in fig. 9.2). This results in a date of origin estimate of  $1838.8 \pm 3.5$  years. Taking the mean between these two values gives a date of origin for the NW lobe of 1839.5 years.

---

<sup>1</sup>This term refers to a velocity system wherein velocity is a linear function of distance from some reference point.

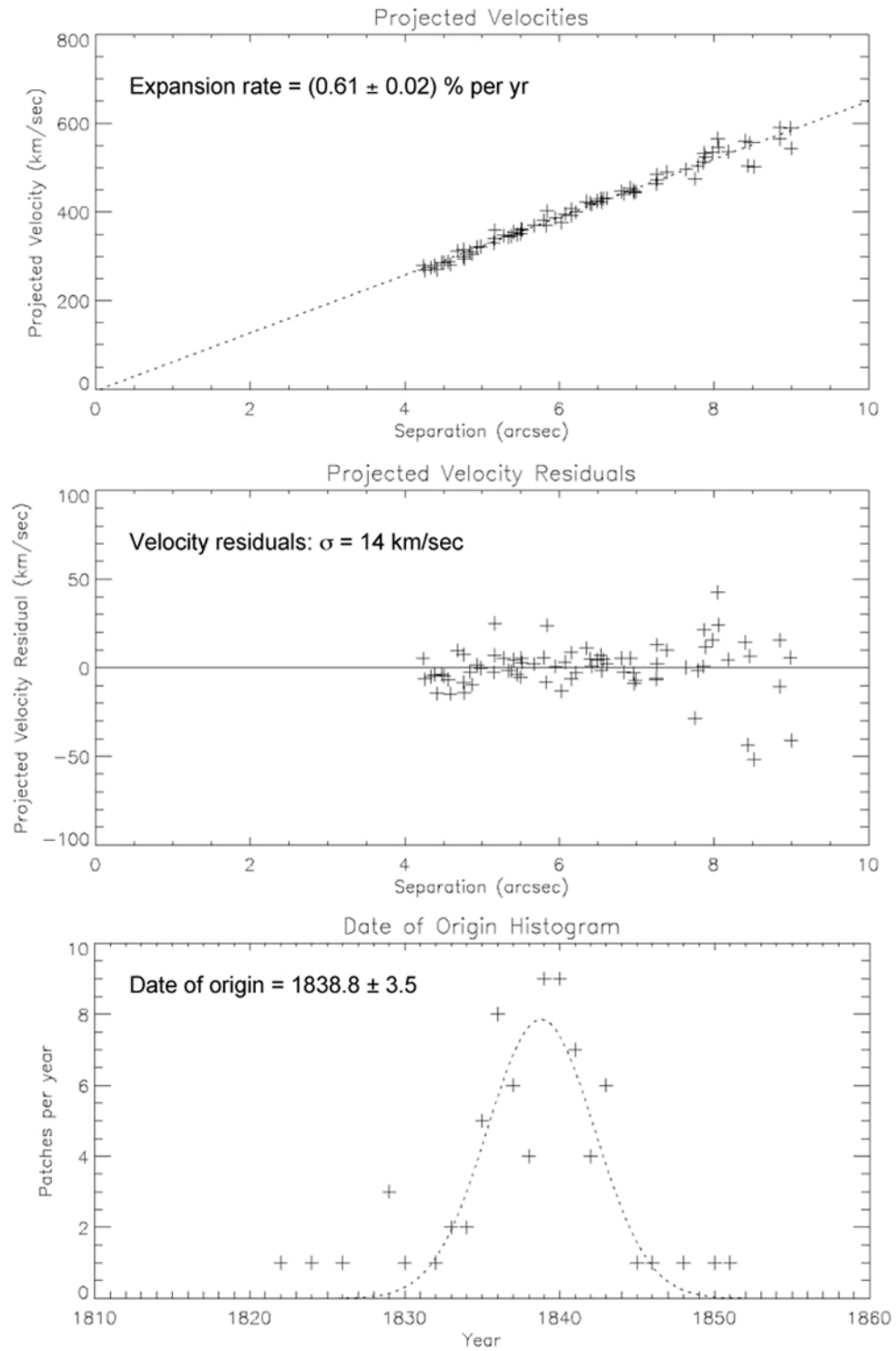


Figure 9.2: Astrometric results from NW lobe (uncorrected). (Top) Projected velocity vs. separation, (middle) projected velocity residuals vs. separation, (bottom) date of origin distribution.

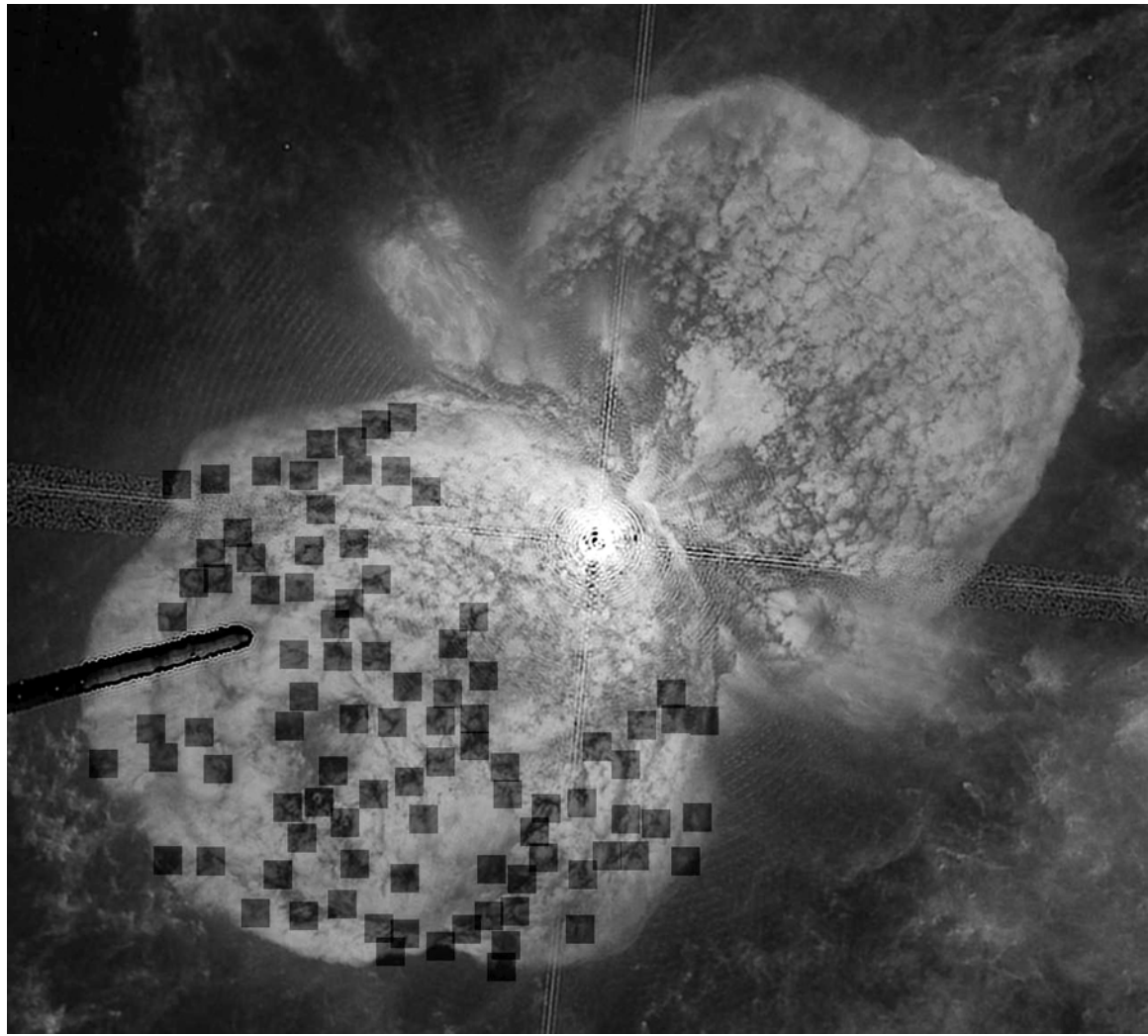


Figure 9.3: Locations of patches used for cross-correlation for the SE lobe of the Homunculus.

## 9.2 SE Lobe: Initial Results

A total of 84 patches were selected for cross-correlation from the SE lobe. The locations of the patches are shown in fig. 9.3. The results of the cross-correlation analysis are shown in fig. 9.2.

*Expansion velocity and expansion rate:* Figure 9.4 shows the calculated expansion velocity vs. separation and the best fit expansion velocity function (top), the

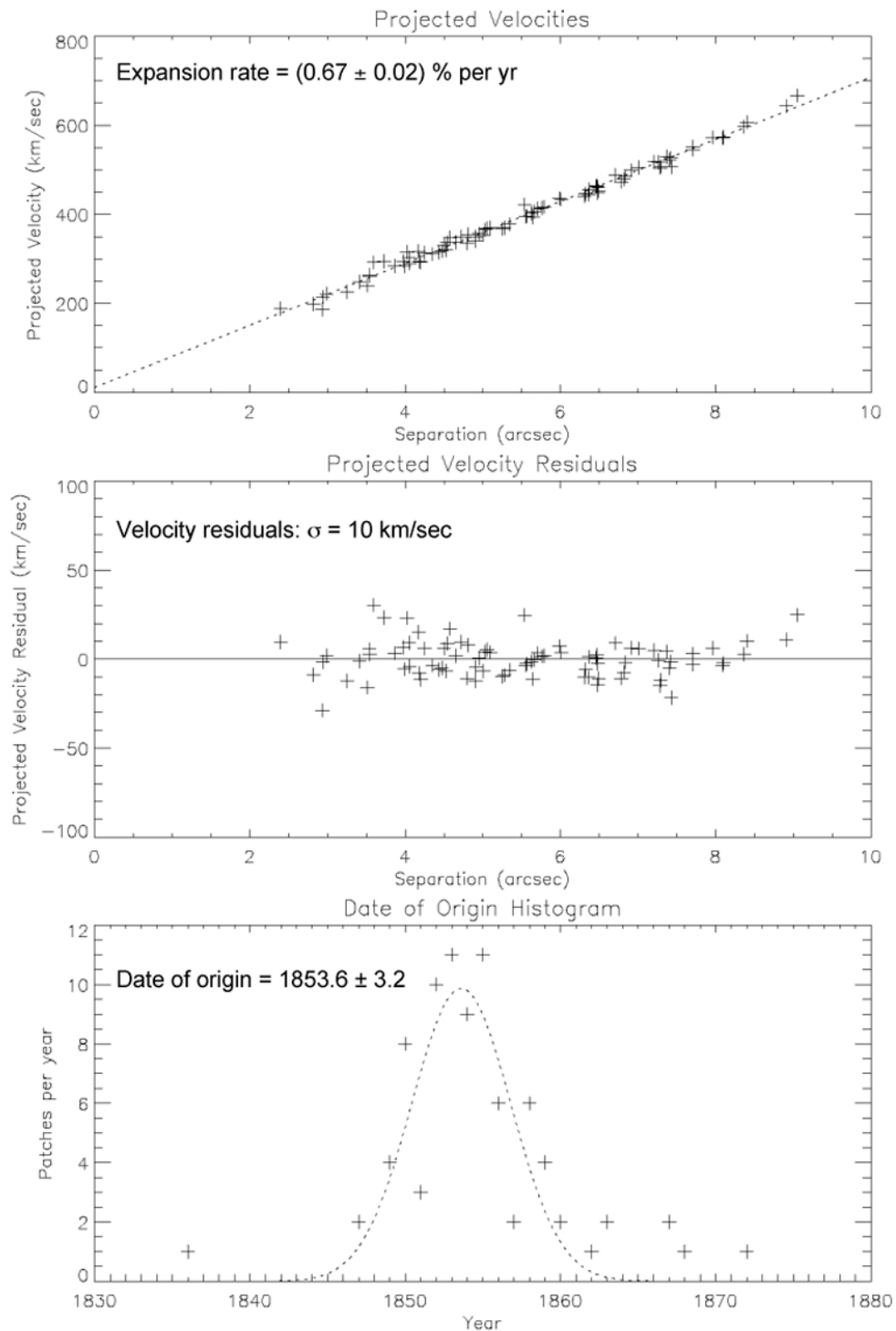


Figure 9.4: Astrometric results from SE lobe (uncorrected). (Top) Projected velocity vs. separation, (middle) projected velocity residuals vs. separation, (bottom) date of origin distribution.

velocity residuals (middle), and the distribution of individual patch dates of origin (bottom) for all 84 SE lobe patches. Fit residuals are distributed with a standard deviation  $\sigma = 10$  km/sec. As with the NW lobe, the SE ejecta shows a strongly linear relation between velocity and separation, confirming the ballistic nature of the ejecta field. The calculated expansion rate is  $r = (0.67 \pm 0.02)\%$  per year.

*Date of origin:* The date of origin calculated using the best fit to the expansion velocity data yields a date of  $1850.4^{+1.6}_{-1.5}$  years. The date of origin calculated by fitting a Gaussian to the distribution of the individual patch dates of origin results in a date of origin estimate of  $1853.6 \pm 3.2$  years. Taking the mean between these two values gives us a date of origin for the SE lobe of 1852.0 years.

### 9.3 Disagreements in Expansion Rates and Dates of Origin Between Lobes

Considered separately, the methodology has seemingly produced measurements of the Homunculus expansion rate and date of origin of very high precision. The residual velocities of  $\pm 14$  km/sec and  $\pm 10$  km/sec for the NW and SE lobes are significantly smaller than the CD96 and [Dowling(1996)] velocity residuals of 22-53 km/sec and equivalent to, if not somewhat better than the M01 residuals of 10-20 km/sec.

Considered together as part of an integrated system, however, the results are inconsistent at a statistically significant level. The SE lobe appears to be expanding significantly faster than the NW lobe (0.67 vs. 0.61% per year, with  $3\sigma$  difference

between the two values). As a result, the dates of origin for the two lobes differ by nearly 11 years, with the NW lobe apparently having been ejected a few years *before* and the SE lobe a few years *after* the Great Eruption.

Figure 9.5 is a composite plot of the two expansion velocity solutions that visually depicts the problem. As the plots show, there is a clear distinction between the two velocity systems, with the differences between the expansion velocity function much larger than the differences between these functions and the relevant data points. A similar effect was noted in SG98 and alluded to in [Dowling(1996)].

*Either* the effect is real and the two lobes were ejected a decade apart *or* there is a problem with either the methodology or the assumptions. Based on considerations of the physics, the latter seems much more likely than the former, so this possibility will be explored.

Examination of the upper plot in fig. 9.5 reveals that the radiant points (i.e., the zero-velocity points) for the two ejecta fields do not coincide at zero separation, as would be expected for a single ejecta system. The NW lobe's radiant point is at a small positive separation from the origin, while the SE lobe's radiant point is at a small negative separation from the origin. These results are consistent with one another and suggest that the radiant point is actually located northwest of the origin. We hypothesize that the radiant point for the single ejecta system is offset from the measured positions of the central star.

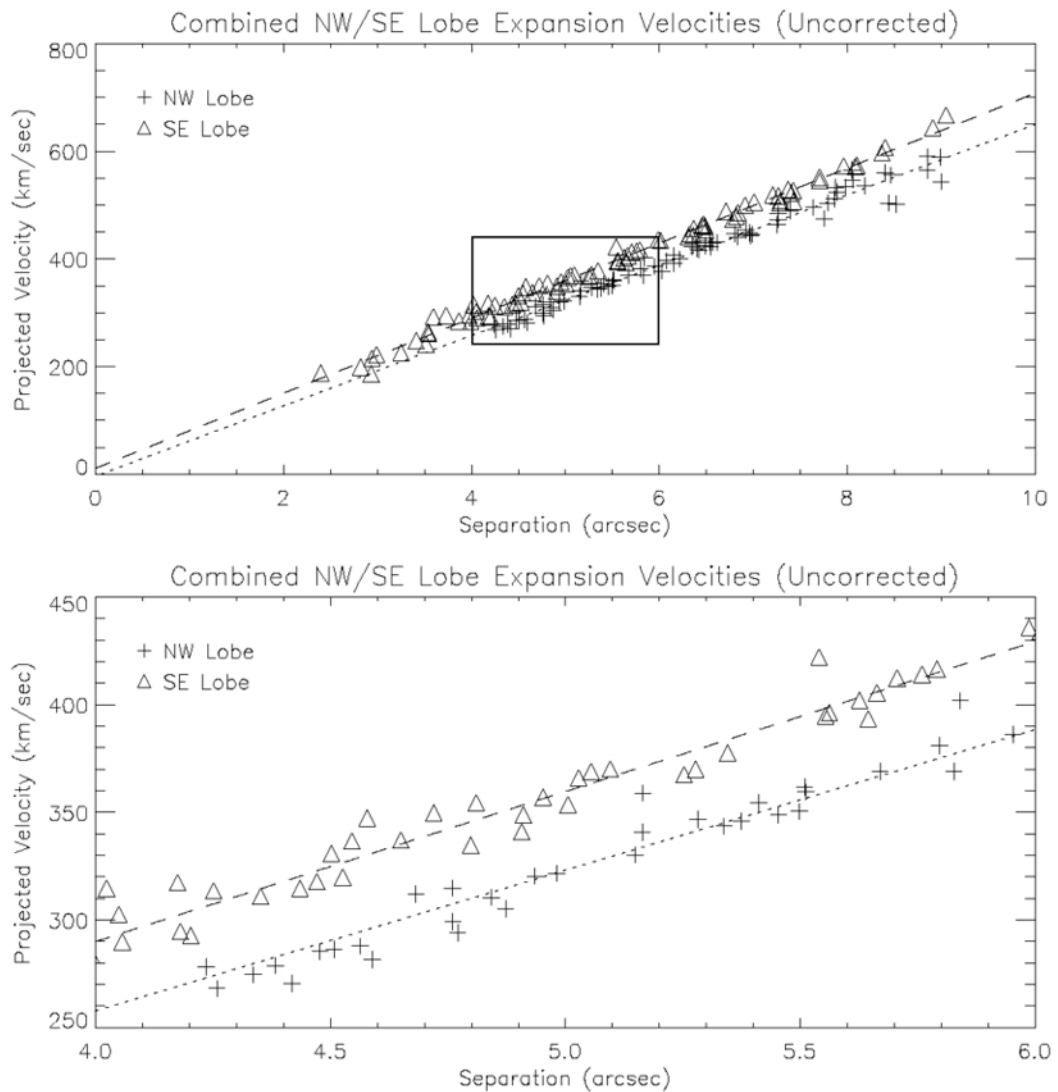


Figure 9.5: Comparison of NW and SE lobe expansion velocities. (Top) Expansion velocity plot showing two distinct velocity systems; rectangle denotes magnified region. (Bottom) Magnified region, clearly showing differences between NW and SE lobe results.

## 9.4 Revised Integrated Measurements and Results

To test this hypothesis, additional software was developed that varied the position of the central star over a grid of test positions and calculated a relevant metric for each position. In order to solve for the expansion rate and date of origin, the standard deviation of the velocity residuals of the combined NW and SE lobe data was minimized. The minimum was found at a 2003.9 offset of 0.4 mas relative to the 1995.4 central star position.

The revised integrated results for the Homunculus are shown in fig. 9.6. These results are clearly more sensible than the discrete results for the lobes considered separately. A single velocity system is now apparent, rather than two distinct systems. The errors are reduced significantly for all major metrics. The radiant point and the origin coincide within the limits of the expansion rate errors. Finally, the distribution of patch-ejection dates appears much more “Gaussian” than the distributions for the uncorrected lobes. These improvements are strong indicators that offset hypothesis is valid.

*Expansion rate:* The expansion rate of the best-fit expansion velocity line is  $r = (0.64 \pm 0.01)\%$ . As expected, this is between the results from the two lobes. This is slightly smaller than the CD96 expansion rate of  $r \approx 0.67$ , but consistent to within the limits of error. The fit residuals have a standard deviation of  $\sigma = 7.6$  km/sec, which is a significantly tighter distribution than either of the individual lobe results<sup>2</sup>. This is approximately twice as accurate as the velocities residuals in M01

---

<sup>2</sup>I note that this is not necessarily unexpected as it was this metric that was minimized.

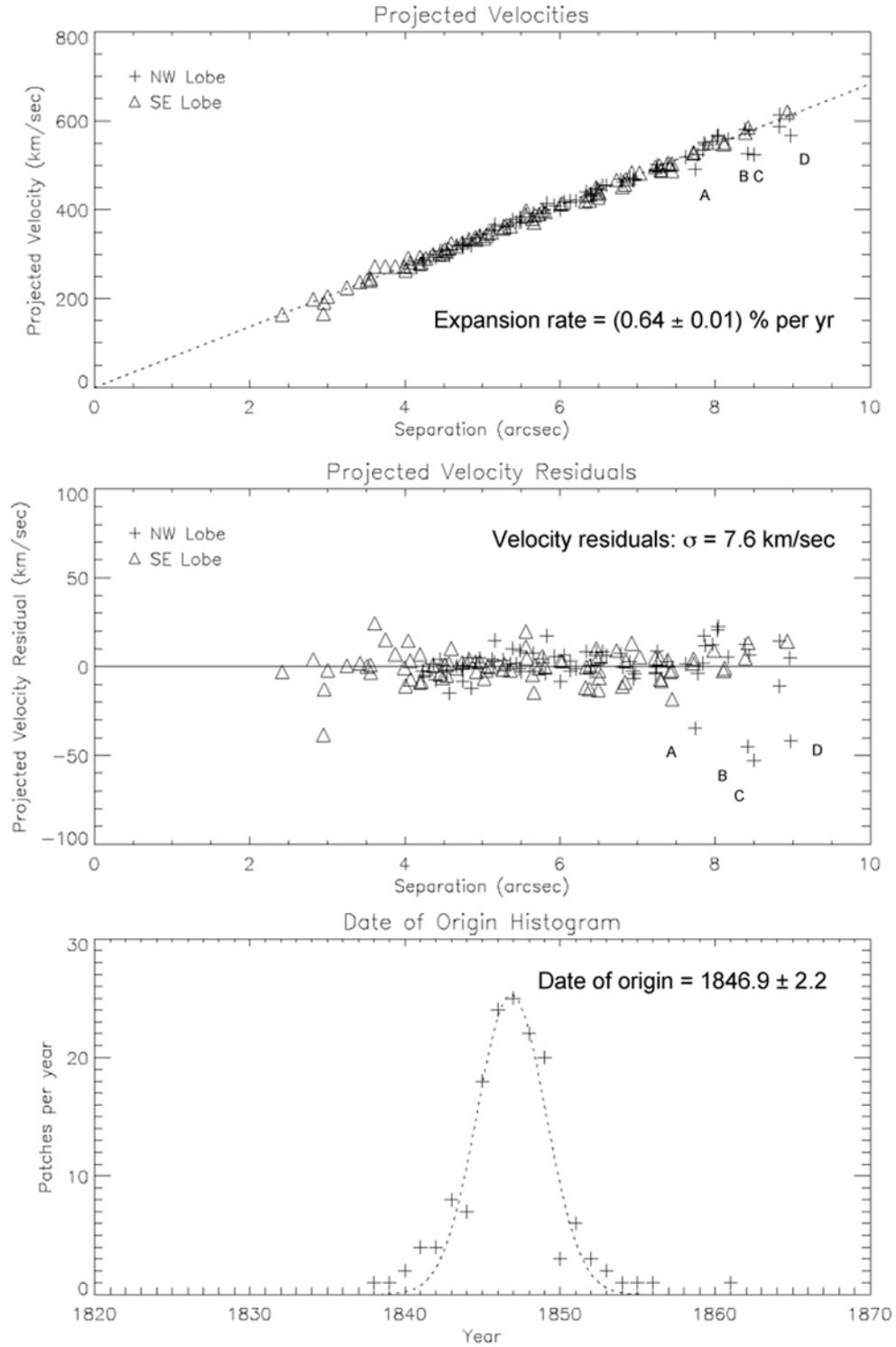


Figure 9.6: “Corrected” results for NW + SE lobes, using revised positions of central star to incorporate relative proper motion. (Top) Projected expansion velocity vs. separation and best-fit linear function, (middle) projected expansion velocity residuals, and (bottom) distribution of individual patch dates-of-origin. Note: letters A–D refer to four “slow” patches (see fig. 9.1); these patches were not used to calculate best-fit line.

and three times as accurate as the smallest residuals in CD96 and [Dowling(1996)].

*Date of origin:* The expansion rate-based date of origin is  $1847.3^{+2.2}_{-2.3}$ . As noted in the figure, the date of origin calculated by fitting a Gaussian to the distribution of individual patch dates of origin is  $1846.9 \pm 2.2$ , where 2.2 is the width of the date-of-origin distribution, not the SDOM. Since a total of 157 patches are being used, the SDOM will be much smaller than the distribution width. However, as noted in §8.5.8, there is a systematic error due to the algorithm that introduces a floor at about the 1-year level. With this in mind, we can combine the properly weighted expansion rate-based date of origin measurements with the result obtained by fitting a Gaussian to the distribution of individual patch dates of origin. Doing so results in a date-of-origin of  $1847.0 \pm 1.0$ .

This date is significantly different than that the one in CD96 and SG98 for either the lobe. It is in good agreement with the date from M01.

If the peak of the Great Eruption is coincident with the photometric peak period of 1843.3 to 1844.9 [Frew(2004)], the Homunculus date of origin comes three years later than mid-point of the peak eruption period, and two years after the end of the peak period. Given an error in the derived date of origin of  $\pm 1$  year, this is a statistically significant gap between the apparent photometric and kinematic (eruptive) peaks. This will be discussed in §10.1.1.

*Eruption Interval:* CD96 estimated the width of the date-of-origin distribution to be  $\sigma \approx 10$  years. The equivalent FWHM is given by

$$FWHM = (2\sqrt{2 \ln 2})\sigma \quad (9.1)$$

Taking the FWHM to represent the upper limit of the “interval” over which the eruption unfolded, the CD96 result gives an interval upper limit of 24 years. The interval upper limit from SG98 is 20 years. M01 quotes distribution width of 5 years, for an interval upper-limit of 12 years. My result, with a distribution significantly narrower than any of the previous results with a  $\sigma = 2.2$  years, yields an eruption interval upper limit of 4.7 years.

*Decelerating NW lobe ejecta?* Four patches at very large separations (see top and middle panels, fig. 9.6), while appearing to be part of the Homunculus velocity system, nevertheless have expansion velocities that are, statistically speaking, significantly lower than should be expected at their separations<sup>3</sup>. These are marked as patches A, B, C, and D in the plots. The patches have velocities that are  $4-6\sigma$  below the mean expansion velocity values for their positions. These four points were not used for the velocity fit, and they do not appear in the date of origin plot. From the binomial (Bernoulli) distribution, the probability that four out of a total of 157 patches would exceed  $4\sigma$  given a Gaussian distribution of residual velocities is  $P \approx 4 \times 10^{-8}$ , that is, very unlikely.

If these patches are not random, do they have any relation to one another? In fig. 9.1, the positions have been marked. They are not randomly distributed, but rather all are on the leading edge of the NW lobe of the Homunculus. This suggests either that they were ejected  $\approx 10$  years earlier than the rest of the Homunculus or that the leading edge is undergoing deceleration as it moves through the extra-Homuncular medium. This will be discussed in §10.2.1.

---

<sup>3</sup>With the result that the dates of origin of these four patches are in the mid-1830s.

*Evidence of a c. 1841 ejection event?* Close inspection of the bottom panel of fig. 9.6 reveals what appears to be an excess of patches correlated to dates of origin in the 1838–1842 range relative to what should be expected from the derived Gaussian distribution. Do these patches trace back to an earlier event?

One way to answer this question is to determine the probability of observing these data given the calculated Gaussian distribution. There are a total of eight events dated earlier than 1842.0. This date is  $2.2\sigma$  from the mean date of 1846.9. The probability of a single event occurring outside a  $2.2\sigma$  threshold is  $P = 0.0259$ . Using the binomial distribution, one can then calculate the probability of eight events occurring at or above this threshold given a total of 157 observations. We obtain  $P = 5\%$ ; in other words, there is a 95% probability that these eight events are *not* associated with the peak distribution and actually represent a distinct set of events<sup>4</sup>. It is thus probable that there was an earlier, much smaller eruptive event, peaked around 1841.

This is approximately five to six years before the main 1847 peak. From [Frew(2004)] (see fig. 1.3), the photometry indicated an 1837/1838 photometric spike, followed by the Great Eruption 5-6 years later. Thus, both photometry and ejecta analysis suggest a preliminary event approximately 5-6 years before the Great Eruption.

---

<sup>4</sup>One could argue that this is purely an effect of the fit statistics. In order to examine this possibility, one can consider the case where the peak is displaced to an earlier date by one fit standard deviation and  $\sigma$  is increased by one fit standard deviation. This represents the “most favorable” conditions for incorporating the 1841 material into main event. Given these conditions, we get an 80% probability that the 1841 material is not part of the peak eruption as modeled by the Gaussian distribution.

## 9.5 The Paddle and the Equatorial Debris

A total of 73 patches were selected for analysis for the Paddle, Northeast and Southwest equatorial debris regions. As shown in fig. 9.7, these consisted of 15 from the Paddle, 27 from the NE, and 31 from the SW Disk regions.

Each region was analyzed individually using the methodology previously employed with the NW and SE lobes. “Good” results were obtained for all three regions, where “good” means dates of origin with relatively small error bars. Date of origin results were  $DOO_{\text{Paddle}} = 1834 \pm 17$ ,  $DOO_{\text{NEDisk}} = 1851.3 \pm 6.8$ ,  $DOO_{\text{SWDisk}} = 1844.8 \pm 4.2$ , where  $1\sigma$  width of the Gaussians is the error metric. The composite ejection date (calculated using the three, properly weighted DOOs) is  $DOO = 1846.1 \pm 4.2$ .

The onset of the 1890 Lesser Eruption occurred in 1887 [Frew(2004)]. This is approximately 41 years after the composite ejection date of 1846.1. Given a standard deviation of 4.2 years, the Lesser Eruption date is thus 9.6 standard deviations after the 1846 ejection date. This result clearly shows that the Paddle, NW and SE equatorial features *did not* come from the 1890 Lesser Eruption, as claimed in SG98, but rather all three features originated in the Great Eruption of 1843–1844. The error in SG98 is most likely due to a combination of the relatively slow expansion velocity of the equatorial material, the limited number of data points used (one each for the NW disk, Paddle and SE disk) and the poor quality of the individual epoch data.

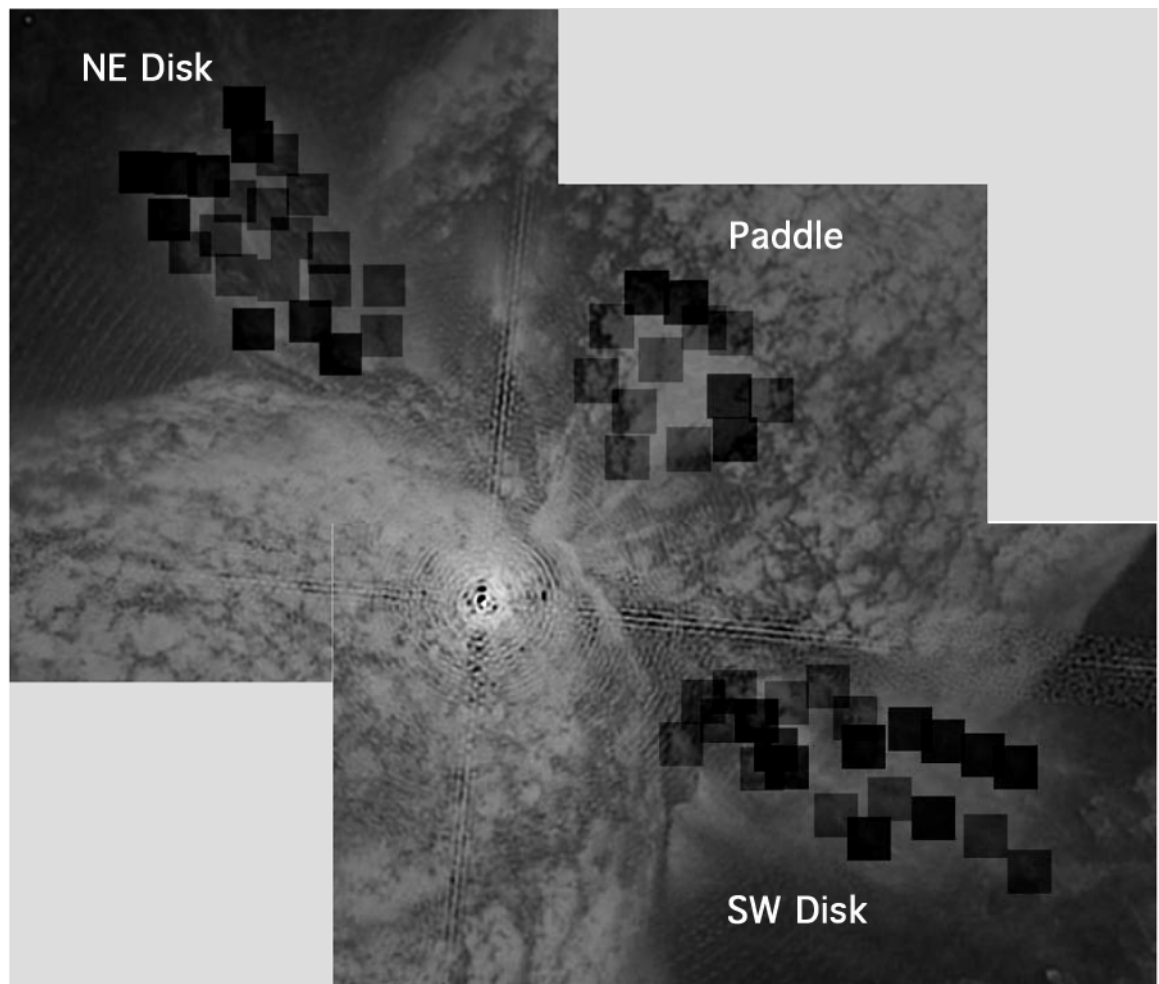


Figure 9.7: Locations of patches used for cross-correlation for the equatorial and “Paddle” features.

## 9.6 Confirmation of Integrated Results with Patch Alignment Method (PAM)

Despite the *relatively* good agreement between the Paddle, NE and SW Equatorial Disk results (§9.5) and the NW and SE Lobe results (§9.4), concerns remained about the methodology of offsetting the central star position and its causal effects on systematic differences between the five debris regions.

In order to address these concerns, a second methodology for measuring the astrometric expansion results was devised that was independent of central star positions. This methodology was then applied to all five components simultaneously in order to come up with a single, integrated solution and confirm previous results.

### 9.6.1 Overview of PAM

The “Patch Alignment Method” (PAM) uses the per-epoch measured patch positions as input, but unlike the primary methodology, does not calculate intra-epoch separation values from the central star. Rather, the inter-epoch positions are differenced and an inter-epoch velocity is calculated. Using the positions and the velocity, we can then “rewind the clock” to some arbitrary time in the past and calculate both the “center of expansion” (CoE) of the system (with each patch equally weighted) and the average distance of the patches from the CoE.

The efficacy of PAM is based on the assumption that the ejecta originated at some point  $(x_0, y_0)$  at some time  $t_0$ . Relative separations between two relatively current epochs  $(t_2, t_2)$  are propagated back in time. At each time step backwards

from  $t_1$ , the mean position and average distance of all patches are calculated. The calculations are run back in time until a minimum is passed;  $t_0$  is defined as the time when the minimum average distance obtains. This approach is more accurate than simply minimizing distances to trajectories, for example, in that the latter, purely geometric method ignores the temporal component of motion and is thus non-physical.

PAM also frees one from the constraints of calculating central star position and the associated error. The method is purely differential between the two epochs  $t_1$  and  $t_2$ , unlike the cross-correlation method, which requires the calculation of absolute positions within the image for a single epoch. The images can be shifted and rotated with respect to each other without modifying the basic PAM methodology.

### 9.6.2 PAM Results

Initial results with the PAM indicated that the NW and SE lobes were collapsing around two spatially separated radiant points. An analysis of the two reference images revealed why: a residual rotation of order  $0.15^\circ$  (9 arcmin) was present between the two epochs (presumably, a residual of the MultiDrizzle rotations). A counter-rotation was applied using PAM, fixing the problem. This revealed that the debris radiant was located approximately 5 pixels (80 mas), and at a  $PA \approx 297^\circ$ , from an origin defined by the photocenters of the central star. A shift was applied to compensate for this shift and the calculation was executed.

The resultant velocity field is shown in fig. 9.8 with the radiant nearly coinci-

dent with the origin<sup>5</sup> after the rotation and shift. The velocity field clearly shows both the Hubble-flow nature of the relationship between the velocity and distance of the ejecta from the radiant and also the two-dimensional nature of the projected ejecta field, with the velocity vectors pointing away from the radiant.

The results of rewinding the clock using the positions and velocities from fig. 9.8 is shown in fig. 9.9. An average separation distance of  $\bar{d} = 0.19$  arcsec occurs at  $t = 1848.2$ . The patches are contained in an area approximately 0.1% of the area of Homunculus at  $t = 2003$ .

Plots showing the patch distribution at four discrete epochs are shown in fig. 9.10. Going clockwise from upper left, the 1995.4 positions are shown, corresponding to the epoch 1 positions of the patches in the shifted reference frame; next, the positions at 1940.0 (a period of rapid brightening); next, the positions at 1890.0, the period of the Lesser Eruption; and finally, the 1848.2 positions. As can be seen in the final figure, virtually the entire debris field collapses into a region smaller than one square arcsecond simultaneously, visually confirming the coevality of the Homunculus and related debris. Figure 9.11 is a magnified view of the central one square arcsec at the 1848.2 epoch.

While figs. 9.10 and 9.11 make it clear that all of these regions originated during the period of the Great Eruption, there are still residual systematics in the results. In the lower left panel of fig. 9.10, the four “laggard” patches from the outer edge of the NW lobe have yet to enter the central box. A “rogue” patch from the SE lobe is headed off at relatively high speed in an easterly direction. The detailed

---

<sup>5</sup>Defined here as the epoch 2 (2003) input central star position.

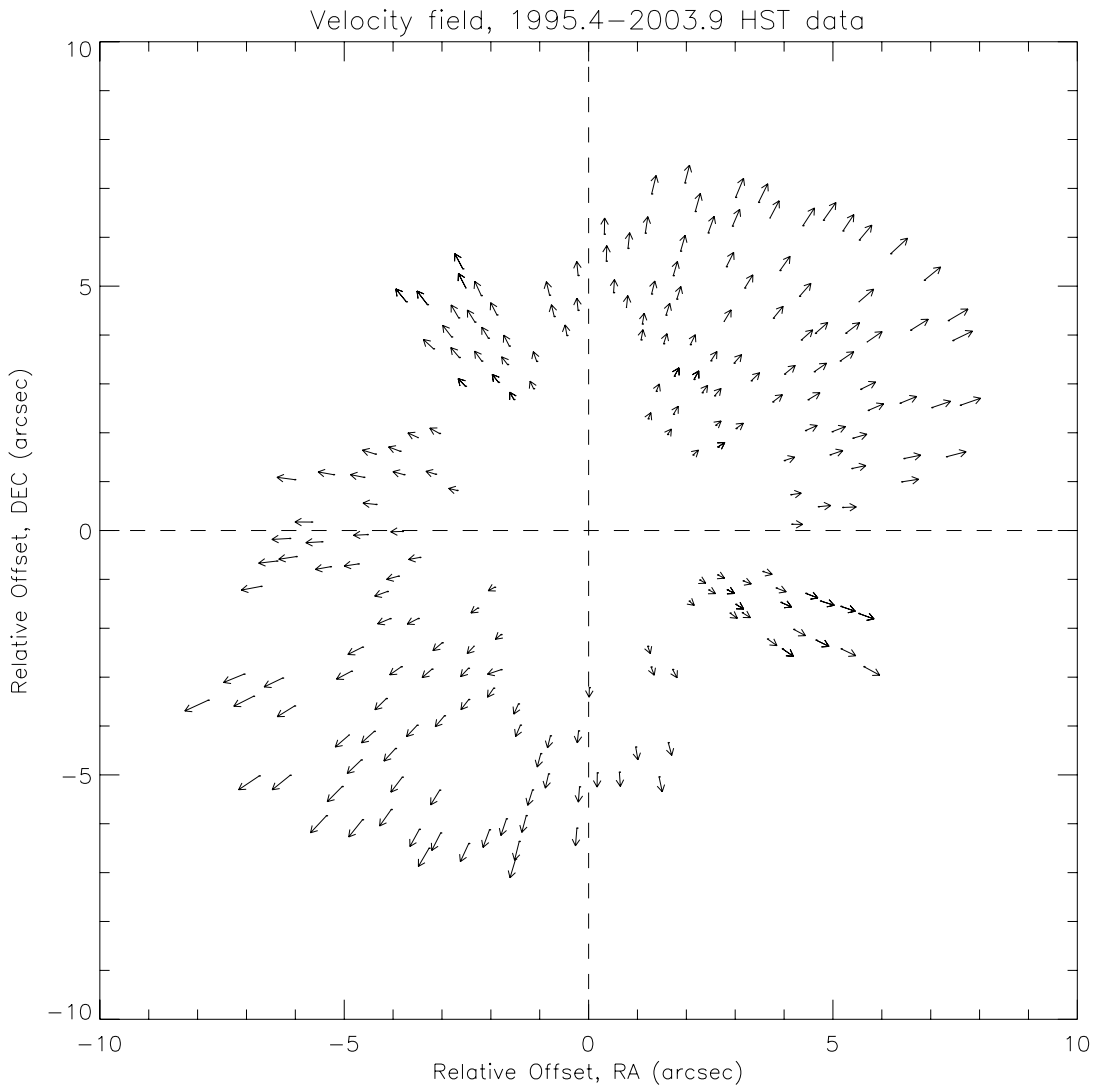


Figure 9.8: Velocity field for the 233 patches between the 1995.4 and 2003.9 epochs. The arrows extend from the 1995.4 position to the 2003.9 position, thus the magnitude represents the measured shift in patch position over 8.43 years. The plot includes NW and SE lobe as well as the Paddle and the NE and SW Equatorial Disk features. Epoch 1 has been rotated by  $\alpha = 0.152^\circ$  and shifted with respect to epoch 2.

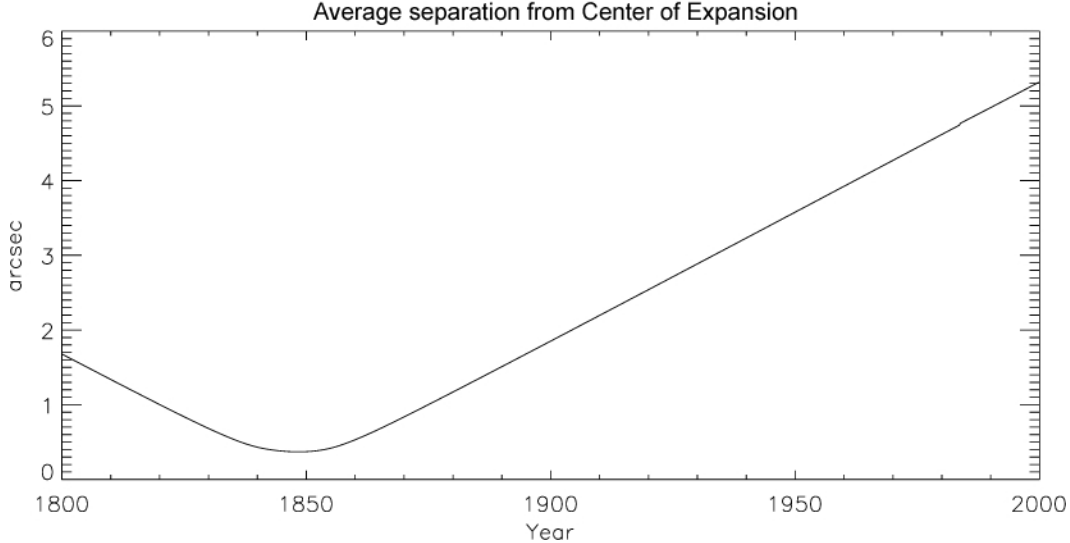


Figure 9.9: The average patch distance from the center of expansion as function of time. The average patch distance metric is minimized at  $t = 1848.2$ , with a value of  $\bar{d} = 0.19$  arcsec.

display in fig. 9.11 shows that some of the components (the NW and SE lobes and the Paddle) are well mixed in the central region, while both the NE and SW disk regions show residual systematics suggesting they are traveling at slightly higher than the velocities that would be expected.

These new results can be used to calculate expansion rates and dates of origin as was done earlier for the individual components. Figure 9.12 provides plots of both the projected expansion velocities (upper panel) and the fit residuals (lower panel) for all 233 patches.

The expansion velocity analysis of the AM output results in a calculated expansion rate of  $r = 0.64 \pm 0.01\%$  and a date of origin of  $t = 1846.8 \pm 1.1$ . These match well with the results derived for the two lobes only using the primary method (§9.4). Looking at the top panel of fig. 9.12, it is clear that the entire lobe and equatorial debris field represents a single velocity system tracing back to an eruption in

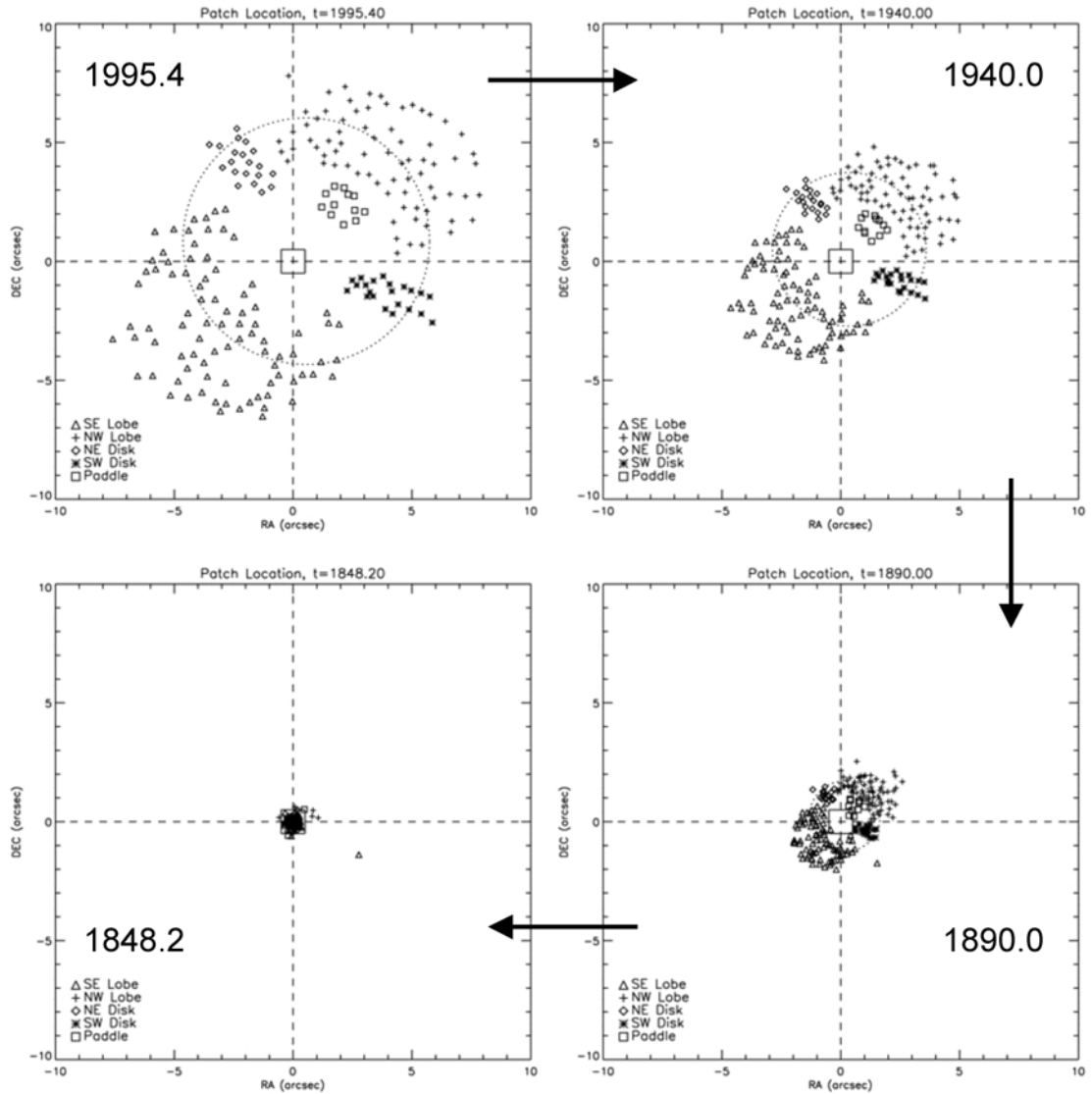


Figure 9.10: Time history of expansion of  $\eta$  Car Homunculus based on relative motions of 233 patches. Plots show position of each patch at approximately 50 year epochs. Plots are in reverse chronological order starting at upper left, showing 1995.4, 1940.0, 1890.0 and 1848.2. Circle indicates average separation radius at epoch, with each patch equally weighted. Small square box indicates central square arcsec (see fig. 9.11).

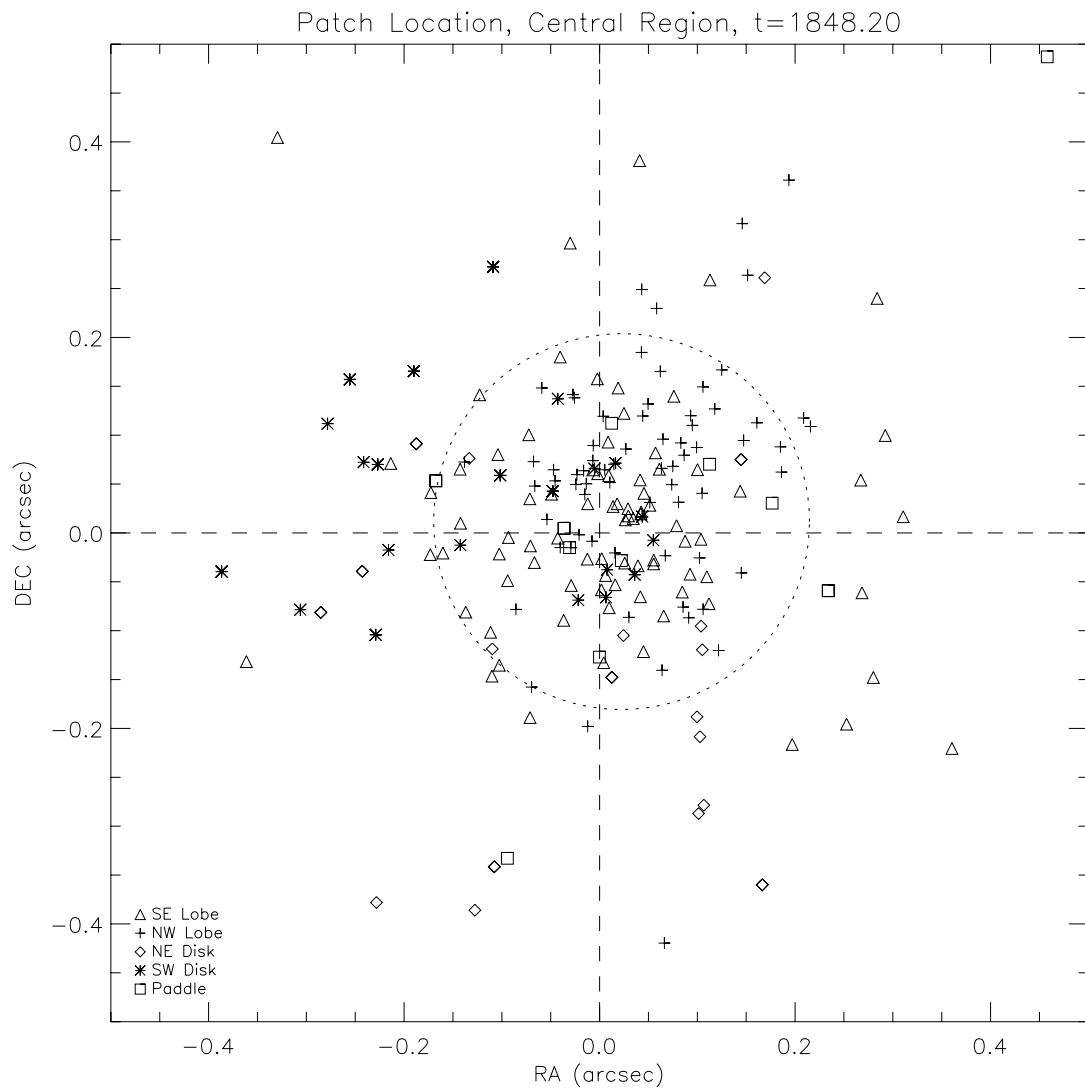


Figure 9.11: Central one square arcsec (see fig. 9.10) from 1848.2 epoch.

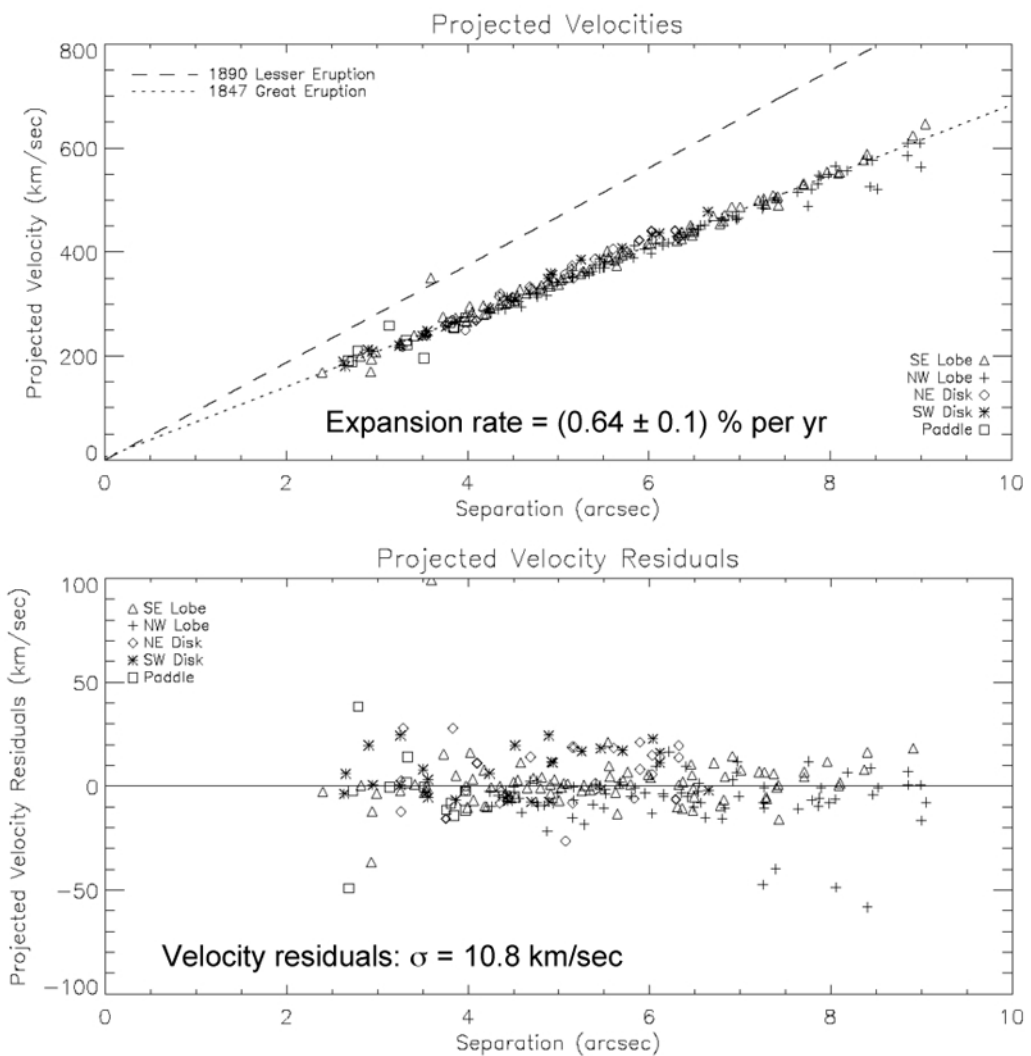


Figure 9.12: Expansion rates and velocities derived for entire, integrated field using alternate method. Expansion rate plot (upper frame) includes both best-fit solution (yielding a  $t = 1846.8$  date of origin) and the expected expansion velocity function for an 1890 eruption.

the 1840s, and that there is no 1890-era ejection event evident in any of the data analyzed<sup>6</sup>. Incorporating the equatorial features into the solution has increased the velocity noise to a little below 11 km/sec, but has not significantly changed any of the conclusions regarding expansion rate, age or date of origin.

Combining the date of origin results from the primary methodology with the two dates of origin derived using PAM<sup>7</sup>, we get a “composite” date of origin of  $t = 1847.3 \pm 1.0$ , where the one-year error represents the adopted systematic floor of the overall cross-correlation method.

## 9.7 Summary of Measurement Results

Using the cross-correlation methodology described in Chapter 8, the position and motion of 233 individual regions in  $\eta$  Car’s Homunculus and equatorial disk have been measured. These results confirm the “Hubble-flow” nature of the ejecta, that is, a strong linear relationship between distance and velocity. An expansion rate of  $r = 0.64 \pm 0.01\%$  per year has been derived and a date-of-origin of  $t_0 = 1847.3 \pm 1$  year determined, with a distribution width of the lobe date of origin features of  $\sigma = 2.2$  years. This implies an upper limit of the ejection interval of 4.7 years. The NW and SE lobes, the Paddle, and the NE and SW equatorial disk regions were all part of the Great Eruption event and are not associated (in whole or in part) with the 1890 Lesser Eruption. Using the alternative Patch Alignment Method (PAM) (§9.6.1),

---

<sup>6</sup>The single patch that appears to lie on the 1890 event is the “rogue” patch that is visible moving east in fig. 9.10. It does not point back to the central star, but rather appear to be an anomalous measurement.

<sup>7</sup>That is, the mean distance minimization ( $t = 1848.2$ ) and the expansion rate calculation ( $t = 1846.8$ ).

projecting the two-dimensional velocities back in time results in a close conjunction of all Homunculus patches around  $t \approx 1848$ , confirming the cross-correlation results.

## Chapter 10

### Analysis and Discussion of Homunculus Results

#### 10.1 Answering the Astrometric Questions

In §7.2, four questions regarding the debris fields around  $\eta$  Car were posed.

We can now answer the first three questions, which relate to the the Homunculus.

Discussion of the fourth question—related to outer debris—is deferred to Chapter 11.

##### 10.1.1 What is the date-of-origin for the Homunculus ejecta?

The date of origin for the Homunculus ejecta has been found to be  $t_0 = 1847.3 \pm 1.0$  years. This agrees well with M01’s date of  $1847.0 \pm 5.0$ . Based on their intra-epoch position accuracies and their temporal baselines (see Table §7.2), these are the two most accurate measurements of the date-of-origin available. One caveat before proceeding, however: M01’s second epoch is this analysis’ first epoch data, thus the two analyses are not independent and there may be correlation in some of the systematics. Mitigating this, however, is the fact that the 1995.4 WFPC2 data are this analysis’ *first* and M01’s *second epoch*. Systematic errors in patch positions in the 1995.4 data would manifest inversely in our respective analyses. For example, if the 1995.4 patch positions were systematically in error towards the central star, M01’s would derive a smaller expansion rate and this analysis would

derive a larger one. This is not seen, suggesting that shared systematics are not significant compared to other sources of error.

If the most accurate measurements of the ejecta date-of-origin is 1847.3, how does one reconcile that with the photometric record (e.g., [Frew(2004)])? The peak photometric period occurred from 1843.3–1844.9, fully three years (thus,  $3\sigma$ ) before the derived ejecta date of origin, a statistically significant difference.

The current central star luminosity is  $L_\eta \approx 4 \times 10^6 L_\odot$  [Cox et al.(1995)]. [Davidson & Humphreys(1997)] estimates an apparent V-band magnitude of  $m_v = 4$  for the central star were the ejecta material not present. An increase in brightness from a quiescent state of  $m_v = 4$  to  $m_v = -1$  during the photometric peak implies an increase of one hundred times in the V-band brightness of  $\eta$  Car. Adopting  $T_{eff} = 15000$  K (Table 6.1), a shift of the Wien radiation peak from 190 to 550 nm (representing, for example, an expansion of the stellar photosphere) would result in a maximum increase of  $5\times$  in V-band luminosity. Thus, as a lower limit, the star itself must have undergone an increase in luminous output of at least  $20\times$ . The total luminosity of the star during the photometric peak period would thus have been 80 million solar luminosities *or more*. For a star that is already sitting at the edge of the Eddington limit, there does not seem to be any physically realistic explanation as to how it could have increased its luminous output by a factor of twenty or more and yet not ejected material for three years.

Davidson & Humphreys conjectured that the Central Star was approximately the size of the orbit of Saturn during the photometric peak period

[Davidson & Humphreys(1997)]. Given the relationship:

$$L = \sigma T_{eff}^4 4\pi R^2 \quad (10.1)$$

between luminosity  $L$ , effective temperature  $T_{eff}$ , stellar radius  $R$ , and the Stefan-Boltzmann constant  $\sigma$ , the effective temperature can be calculated given the luminosity and radius. Adopting  $L_\eta = 8 \times 10^7 M_\odot$  and  $R = 9.4$  AU, the resultant effective temperature of the central star during the photometric peak was  $T_{eff} = 14,000$  K.

The energy flux density in watts per square meter is then given by the Stefan-Boltzmann law:

$$j^* = \epsilon \sigma T^4 \quad (10.2)$$

Adopting an emissivity  $\epsilon = 1$ , we get an energy flux density of  $j^* = 2.2 \times 10^9$  W m<sup>-2</sup> at the surface of the star. This is equivalent to over a million times the solar constant measured at the Earth's surface. This amount of radiation is equivalent to an outward pressure of 7.3 N m<sup>-2</sup> at the stellar surface.

Clearly, this amount of radiation pressure at the surface of the star should accelerate any ejected material. While a detailed analysis of absorption of radiation by material expelled by  $\eta$  Car is not within the scope of this thesis, we can demonstrate the plausibility of an hypothesis that radiation pressure near the surface of the star added a significant amount of  $\Delta V$  to the ejecta.

I consider an idealized test particle of emissivity  $\epsilon = 1.0$ , cross-section  $\sigma = 1$  cm<sup>2</sup> and mass  $m = 1$  g. If this particle is placed at the surface of the star ( $r_\eta = 9.4$

AU), the resultant radiation-induced acceleration<sup>1</sup> is  $a_{rad} = 0.73 \text{ m s}^{-2}$ . Assuming an initial ejection velocity of  $v_0 = 500 \text{ km sec}^{-1}$ , we can numerically evaluate the resultant equations of motion. After about 10 days, the particle will have accelerated to  $v = 870 \text{ km sec}^{-1}$  and traveled approximately 10 AU. Subsequent acceleration trails off rapidly due to the  $1/r^2$  relationship between the radiation pressure and the distance traveled; as a result, the test particle’s velocity converges at about 900 km/sec, thus the radiation has contributed  $\Delta V \approx 400 \text{ km sec}^{-1}$ , and observations of the resultant motion of the ejecta would derive a younger age (and later date of origin) than for a comparable, unaccelerated particle.

This is simply a plausibility argument. The actual  $\Delta V$  contributed by radiation pressure should be more along the lines of a few percent (of order tens of km sec<sup>-1</sup>). Detailed modeling and further analysis is required to address this question in more detail.

### 10.1.2 What is the ejection interval for the Great Eruption?

I derived an upper limit to the ejection interval of 4.7 years, where “interval” is defined as the FWHM of the temporal distribution of the date of origin metric. As noted in §9.4, every time the higher precision measurements are used to determine this quantity, the interval decreases. Furthermore, as shown in fig. 9.6, the distribution of the dates-of-origin appear highly Gaussian. There is no reason to expect the actual distribution of ejection dates to be Gaussian. Based on these two obser-

---

<sup>1</sup>The gravitational acceleration is  $a_{grav} = -0.008 \text{ m s}^{-2}$ , or approximately 1% of the radiation-induced acceleration (and similarly varies as  $1/r^2$ ); it is thus negligible and will be ignored in this analysis.

vations, one can infer that the measured interval is still dominated by measurement errors, and that the underlying distribution is smaller than 4.7 years. If 50% of the observed distribution is due to measurement error, a more realistic upper limit to the ejection interval is 3.3 years.

What are the physical implications of this? Recent work by Smith on the structure of the Homunculus using mid-wave IR have revised the estimated total mass ejected during the Great Eruption upward from  $\Delta M_{GE} = 2 - 3 M_{\odot}$  (e.g., [Davidson & Humphreys(1997)]) to  $\Delta M_{GE} = 10 - 20 M_{\odot}$  [Smith(2006)]. A mass ejection rate lower limit of  $\dot{M} \geq 3 M_{\odot} \text{ yr}^{-1}$  during the eruption period follows from this. Using the higher value for the ejected mass, or a shorter interval drives this already high rate even higher. This is a significant constraint for any future modeler of the Great Eruption.

### 10.1.3 What is (are) the ejection dates for the equatorial features?

The equatorial features<sup>2</sup> have been definitively dated to the Great Eruption. There is no evidence of any ejecta dating from after the Great Eruption period, or more specifically, the 1890 Lesser Eruption. The Great Eruption event thus featured *both* polar (the Homunculus) *and* equatorial ejecta, and was not just a polar event as implied by some authors ([Smith & Gehrz(1998)]). The need to explain both polar and equatorial features from the same event is a significant constraint on any Great Eruption modeler.

I note that close inspection of the equatorial features does not reveal the disk

---

<sup>2</sup>Here, “equatorial” refers to the axis-of-symmetry of the Homunculus.

that other authors have reported. While the presence of the NE and SW equatorial extensions, when combined with the Paddle, may be suggestive of a disk, recent results suggest that the Paddle is actually part of the NW Lobe front. This leaves the two extensions, which do not constitute a disk. It may be that they more closely resemble jets or sprays of material along the equatorial plane than components of an overall disk structure.

These results do not rule out the presence of equatorial material within 2 arcsec of the central star dating from later eruptions, as material that close-in was not analyzed. Any such material would, however, not be part of either the NE or SW equatorial extensions (see fig. 9.7).

## 10.2 Additional discussions

In addition to addressing the first three questions posed in §7.2, the Homunculus measurement results also bring up some new issues. These are discussed in the following three subsections.

### 10.2.1 Deceleration of leading edge of NW lobe

In §9.4, we found four patches (A–D) in the leading edge of the NW lobe that were moving significantly ( $> 3\sigma$ ) slower than they should have, given their membership in the Homunculus debris system. Further analysis using PAM (see bottom panel, fig. 9.12) confirms the general trend that the leading edge of the NW lobe appears to be moving more slowly than the rest of the Homunculus system.

For the NW Lobe region that is  $> 7$  arcsec from the central star, only 4 out of 23 patches (17%) lie above the velocity solution, while 14 out of 23 (61%) lie below.

These Homunculus results are consistent with the results for outer debris that will be described in §11.2, where material from a earlier ejections are found to be present in the northwest polar cap region. This earlier material appears to have caused deceleration of some high-velocity, extra-Homuncular Great Eruption ejecta that has penetrated the region. Taken together, these results strongly imply that the density of material in this NW polar cap region is higher than elsewhere, and that, as a result, deceleration at a detectable level is present in the NW lobe ejecta.

*A note on gravitational deceleration:* Is deceleration due to gravity relevant to the discussion of Homunculus (and later, outer) debris? The escape velocity at the star's photospheric surface (neglecting rotation) can be calculated by solving the orbital energy equation where the total energy equals 0:

$$E_{\text{orbital}} = PE + KE \quad (10.3)$$

$$0 = \frac{-GM_A m}{r} + \frac{1}{2} m V_{\text{esc}}^2 \quad (10.4)$$

$$V_{\text{esc}} = \sqrt{\frac{2GM_A}{r}} \quad (10.5)$$

The escape velocity for the “quiescent” (Hillier) radius of  $r = -0.28$  AU [Hillier et al.(2006)] is  $V_{\text{esc}} \approx 900$  km/sec. For the Great Eruption (Davidson) radius of  $r \approx 10$  AU [Davidson & Humphreys(1997)],  $V_{\text{esc}} \approx 150$  km/sec. At 2 arcsec—the innermost set of patches used for the cross-correlation analysis—Great Eruption ejecta will have lost a  $\Delta V \approx 143$  km/sec (out of 150 km/sec). At 9 arcsec—the

outermost set of patches—the ejecta will have lost an additional  $\Delta V \approx 4$  km/sec. Thus, there should be slight deceleration over the range of Homunculus material of magnitude 4 km/sec. Removing the ejecta from 9 arcsec to infinity would result in an additional  $\Delta V \approx 3$  km/sec. Thus gravitational deceleration is a real, though relatively small effect across the Homunculus. Future analyses using more accurate data will most likely need to model this effect. It is negligible, however, for the case of the outer lobe patches which appear to have decelerated (i.e., departed from the Hubble flow velocity) by  $\Delta V \approx 50$  km/sec.

### 10.2.2 Possible Great Eruption-Induced Impulse

One result from the PAM analysis was that there appears to be approximately 0.4 mas (1/40 pixel) difference between the 1995.4 and 2003.9 photocenters. While this is within the range of estimated central star image registration errors (see Table 8.5.9), it prompts the question: is there any significance to inter-epoch central star motion?

The unstated assumption for all previous has always been that the Central Star and the Homunculus ejecta are in the same inertial frame. A 1/40 pixel shift over 8.43 years translates to a 2 pixel shift over 160 years. Is it possible that this level of motion is real? If so, it could explain systematic differences in dates of origin between physically separated yet coeval ejecta features.

Current mass ejection estimates for the Great Eruption place a lower limit of  $\Delta M > 10 M_{\odot}$ , with a likely value closer to  $20 M_{\odot}$ , with virtually all of the

momentum going into the lobes. An asymmetry in the NW/SE lobe momentum at the 5% level would result in a net ejection of  $0.5 M_{\odot}$  mass (adopting Smith's lower limit). If we assume a typical ejecta velocity of  $500 \text{ km sec}^{-1}$  and an inclination angle of  $i \approx 45^\circ$ , the resultant impulse would change the plane-of-the-sky velocity of a  $M = 125 M_{\odot}$  central star by  $1.4 \text{ km sec}^{-1}$ . This is equivalent to  $0.3 \text{ AU yr}^{-1}$ , or  $0.1 \text{ mas yr}^{-1}$ . Over 8.43 years, the apparent motion would be approximately 1 mas, or twice that observed. Thus, relatively small asymmetries in the lobe momenta would result in observed motion of the central star with respect to the Homunculus. Additional analysis of possible stellar motion measured with respect to the Homunculus using increasingly longer baselines should be pursued to constrain this possible motion and the level of asymmetry in the lobe momenta.

### 10.2.3 Evidence of c. 1841 Ejecta?

As noted in §9.4, a statistical argument can be made based on the distribution of patch dates-of-origin that a small number of Homunculus patches were ejected  $\approx 6$  years before the Great Eruption (see fig. 9.6). If this is true, this may be a signature of the 5.52-year spectroscopic cycle ([Damineli(1996)]) in the ejection pattern of the Great Eruption. It is consistent with the possibility, discussed in §5.7.3, that the Great Eruption may represent sequential periastron passages, with the first one triggering, for example, a swelling of the primary, and the second one representing the actual Great Eruption caused, in this instance, by the passage of the secondary through the now-swollen photosphere of the primary.

While this conjecture is consistent with the observed pattern of ejection, it is not the only explanation. For example, there may be a component of the actual underlying ejection distribution (as opposed to the observed distribution) that is  $\approx 10$  years wide. We conclude that while this result is intriguing, it is not definitive.

#### 10.2.4 Equatorial Disk vs. Equatorial Streams

The standard interpretation of the equatorial debris is that it forms a disk, perhaps “tattered,” around the waist of the Homunculus lobes (e.g., [Davidson & Humphreys(1997)]). This presumes the Paddle feature was part of the equatorial debris. Current thought, however, is that the Paddle is part of the NW Lobe (e.g., [Smith et al.(2000)]), suggesting an equatorial “disk” may be more *trompe l’oeil* than real feature.

If anything, these results are consistent with equatorial “streams” (or, perhaps, jets) rather than a continuous disk. The NE equatorial features appear to be physically connected to the NN feature via the North Jet. Similarly, the SW equatorial features may be associated with the South Bar and the south wall features that have been dated to the Great Eruption. There is no *astrometric* evidence of “disk”-like features. In this case, spectroscopic/velocitmetric data would be extremely valuable in making this determination.

## Chapter 11

### Outer Debris: Astrometric Results

I now turn to the debris outside the Homunculus. Measuring the astrometric motions of these objects is extremely challenging for a couple of reasons. First, the SNR for the features is typically at least an order-of-magnitude smaller than Homunculus SNRs. Second, the debris do not obey a single Hubble law and appear to be a mix of ejecta from multiple past events, some of which may be decelerating.

Figure 11.1 is a normalized “difference image” showing relative motion between the 1995.4 and 2003.9 epochs. The brighter areas indicate motion into that region, while darker areas indicate motion out of that region. The image was created by subtracting a scaled and rotated version of the 1995.4 WFPC2 reference image (fig. 8.2) from 2003.9 HRC reference image (fig. 8.5) and dividing the resultant image by the latter.

The bright outline of the Homunculus is clearly visible, as well as many of the features discussed in the last chapter (e.g., the leading edge of the NE equatorial disk), all indicating motion away from the central region. The figure also shows that a complex ejecta field exists *outside* the Homunculus, with a variety of motions all pointing back towards the central region. Most notable of this outer debris are the “North Jet” and “South Bar” (or South Condensation) (see fig. 7.1). Other, fainter debris features surround the Homunculus.



Figure 11.1: Normalized difference image showing motion between 1995.4 and 2003.9. Lighter areas indicate net motion into the region; darker areas indicate net motion out of the region. Brightest regions include the leading edges of the Homunculus, the South Bar, the North Jet and the leading edge of the NE equatorial disk. Heavily mottled areas indicate reduced SNR regions where the longest exposure images were saturated due to blooming.

Do these features originate from the Great Eruption, or do they imply other eruptive events? In this chapter, I address this question by employing the cross-correlation technique described in Chapter 8. A total of 121 patches were selected for input to the cross-correlation process (see fig. 11.2). These patches were 0.96 arcseconds per side, or four times the area of the 0.48 arcseconds patches used for analysis of the Homunculus. This was necessitated by SNR considerations and the generally larger size of the features in the outer debris fields.

Approximately 25% of the patches failed to properly correlate. In order to supplement gaps in the correlation and add additional insight into the results, 16 stellar-like knots were selected and analyzed using more classical Gaussian centroiding measurements. These are discussed in the individual analysis sections.

The analysis is divided up into one section for each of the four quadrants marked in fig. 11.2. Since the results for the outer debris include multiple apparent velocity systems, rather than show expansion plots (as was done in Chapter 9), I will show results in terms of dates of origin for particular features or regions. Following description of the individual quadrants, I conclude this chapter with a discussion of the integrated results and the implications.

## 11.1 Northeast Quadrant

The primary feature of the NE quadrant is the “North Jet,” it two component condensations, called “North North” (NN) and “North South” (NS) (see fig. 7.1). The HRC image (see fig. 11.3) reveals a more detailed structure to the North Jet.

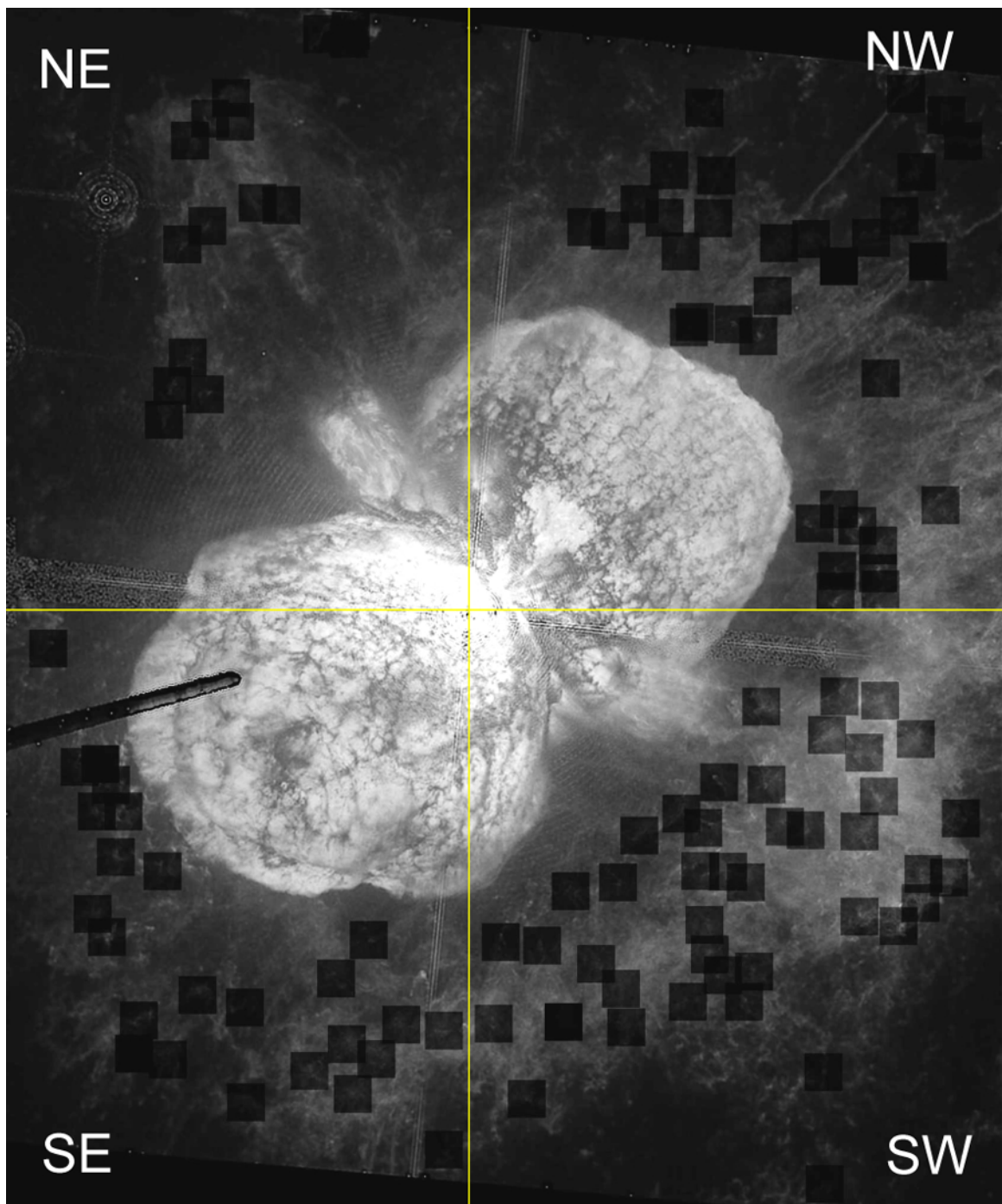


Figure 11.2: Outer debris cross-correlation patches. A total of 121 patches were used as inputs to the process described in Chapter 8. Patches are 0.96 arcseconds across vs. 0.48 arcseconds for the Homunculus. This was necessitated by the reduced signal-to-noise and the generally larger size of features in the outer fields. Not all patches converged on solutions.

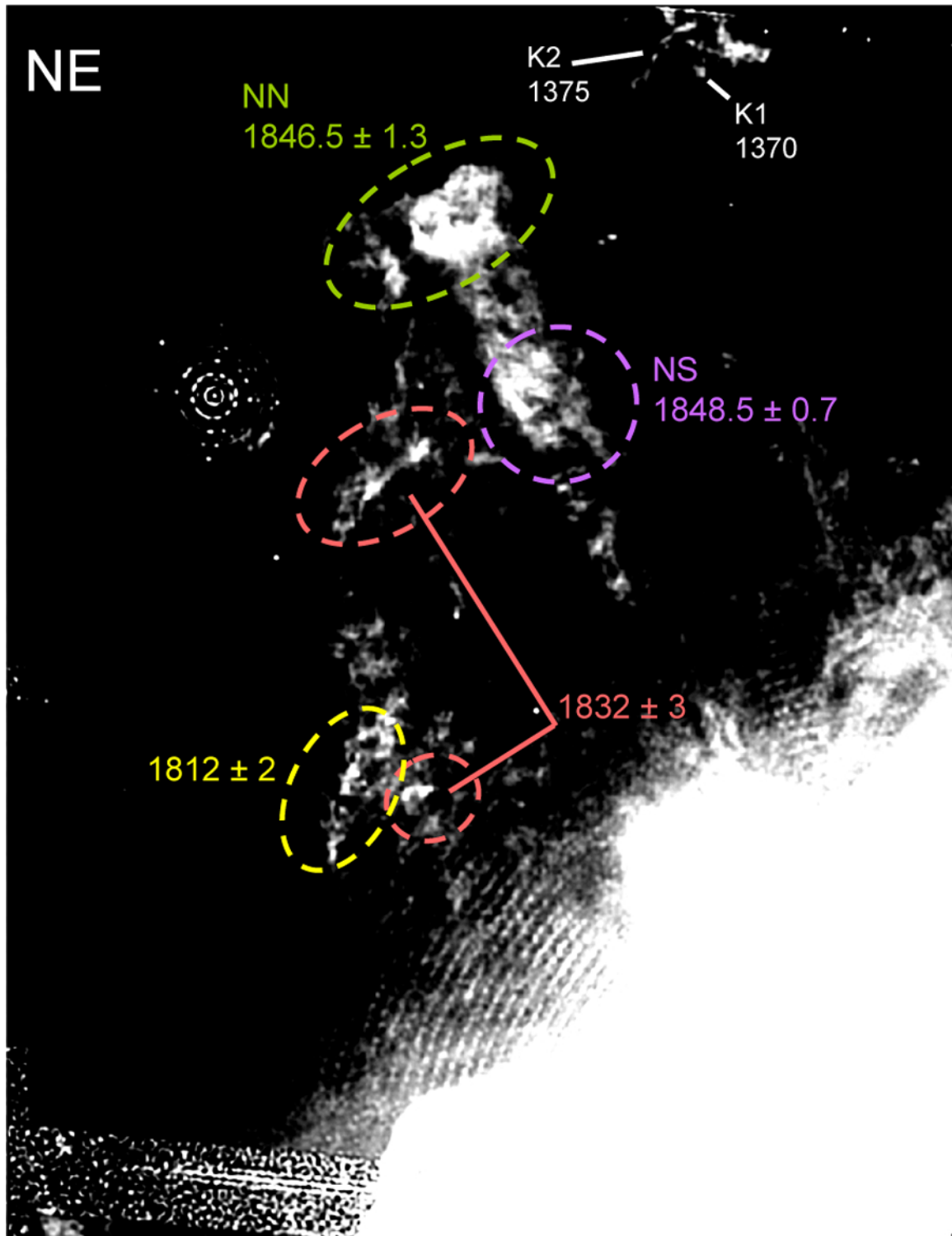


Figure 11.3: Outer debris, northeast quadrant. Cross-correlation dates of origin shown for specific features. Also shown are two knots (K1, K2), with dates of origin determined using standard centroiding techniques.

The jet consists of a central column that appears to trace back to the equatorial disk, along with a wall that trails off at about a  $45^\circ$  angle to the column. I note that with the higher HRC resolution the NS feature is not nearly as prominent as it is on lower resolution images.

The results, as shown in the figure, indicate that the column features (NN and NS) have ejection dates ( $\approx 1847$ ) clearly consistent with the Great Eruption. The northern wall feature is measured to have an ejection date of  $1832 \pm 3$ , while the southern wall feature shows an ejection date of  $1812 \pm 2$ . These features all appear to be part of the same structure; I conclude that the most likely explanation is that these are Great Eruption features that are decelerating as they encounter older, slower moving material from earlier events. Evidently, the trailing component of the wall has encountered more material, and hence has lost more velocity, than the leading edge. This is consistent with an ambient density gradient across the entire front, with the ambient material being densest in the south and gradually diminishing as one moves north until reaching NN, at which point it is sparse enough such that no appreciable deceleration can be detected.

I was unable to measure the nebular feature at the top of the HRC image using cross-correlation due to truncation of the image during the cross-correlation procedure. Instead, the positions of two knots (K1, K2) within the feature were measured in both epochs and motions and dates of origins were derived. The two knots are moving much more slowly than the nearby leading edge of the jet, and show a consistent date of origin of the 1370s.

## 11.2 Northwest Quadrant

I turn next to the NW quadrant. The ejecta in this region (see fig. 11.4) is characterized by a “halo” northwest of the Homunculus, extension of the South Ridge feature west of the Homunculus and the presence of the so-called “spike” or “whisker” features ([Weis et al.(1999)], [Morse et al.(2001)]), very high velocity, very narrow filaments extending from the central star out beyond the Homunculus.

As with the NE quadrant (§11.1), the analysis centered on cross-correlation of patches, supplemented by centroiding nine star-like knots. In this case, one of the knots (K9) appears to be a heavily-reddened background star<sup>1</sup>, selected as a check on the knot methodology.

As shown in fig. 11.4, a variety of velocity systems are apparent in this region. In general, the halo and some of the knots exhibit ejection dates in the 1780–1800 range. The halo, however, appears to be penetrated in a couple of regions by ejecta that dates from around 1823. This, presumably, is ejecta from the Great Eruption that has decelerated as it penetrated the halo, analogous to the decelerating North Jet components discussed in the previous section.

The northern tip of the South Ridge which extends into the southern part of this quadrant exhibits patch velocities consistent with an ejection date of  $1723 \pm 48$ . A single knot in this region (K8) exhibits a date of origin of 1790.

Thus, I find three statistically distinct velocity systems present in this quadrant: the South Ridge (1720s), the Halo ( $\approx 1790$ ) and Great Eruption (1820s).

---

<sup>1</sup>This star was one of the stars used for plate scale correction (see §8.3.4).

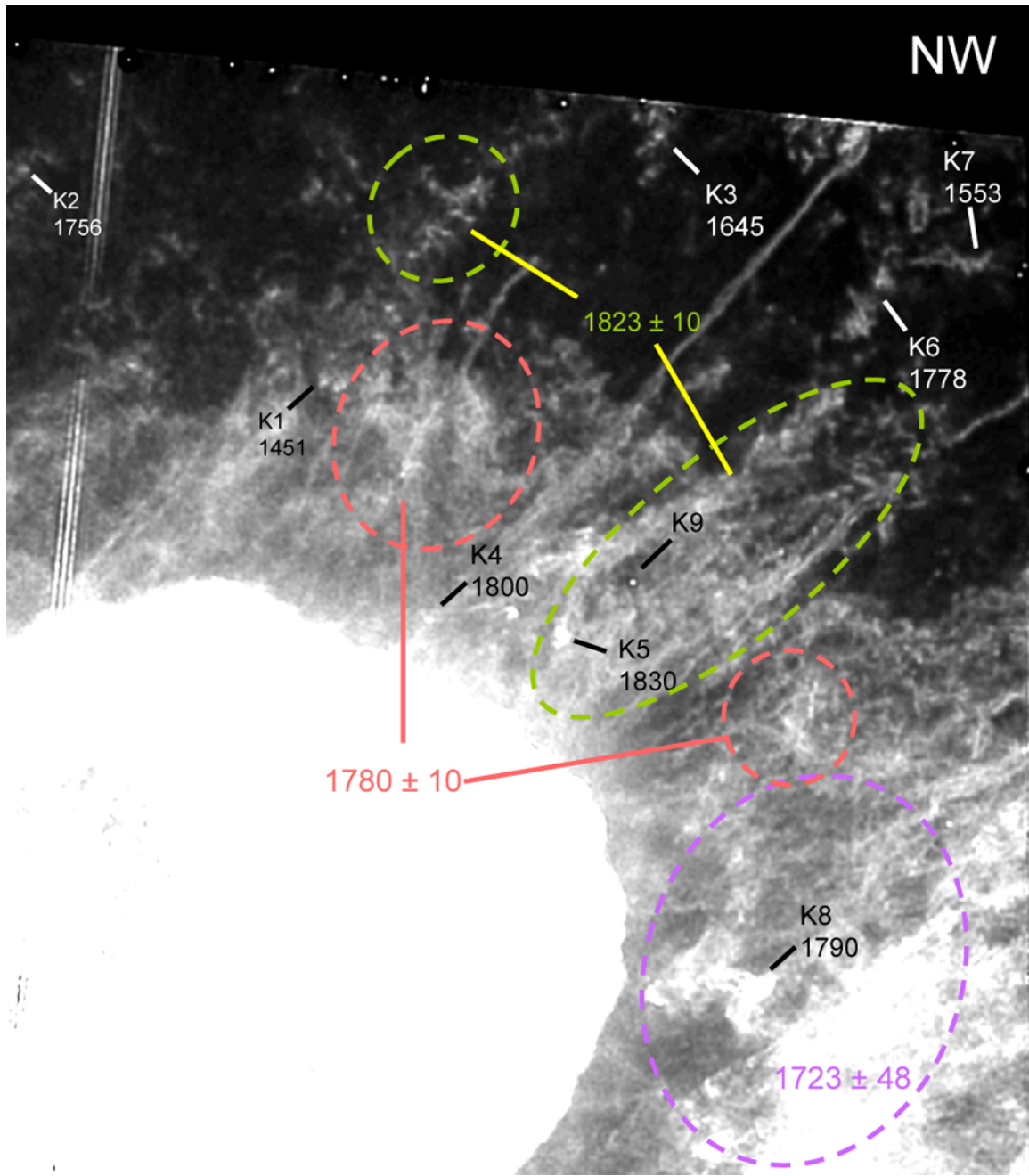


Figure 11.4: Outer debris, northwest quadrant. Cross-correlation dates of origin shown for specific features. Also shown are nine knots (K1–9), with dates-of-origin determined using standard centroiding techniques.

Attempts at cross-correlating spike patches did not produce satisfactory results; additional analysis is needed<sup>2</sup>. The “sanity check” star (knot K9) showed an expansion rate of  $< 0.001\%$ , which I interpret as reasonable validation of the methodology.

### 11.3 Southwest Quadrant Features

The SW quadrant is dominated by the South Ridge, which extends from the NW corner of the quadrant down to the SE corner (see fig. 11.5). Prominent smaller features include the South Bar, a relatively bright, straight line-like region 3-4 arcsec wide protruding from the leading edge of the South Ridge and a fainter, wall-like feature near the Homunculus, just inside the South Ridge.

Cross-correlation analysis reveals a complex mix of velocity systems and possible deceleration conditions. The “SW wall” feature is clearly associated with the Great Eruption, with multiple patch correlations indicating a date of origin of  $1840.0 \pm 0.2$ . The southern most region of the ridge indicates a date of origin of  $1732 \pm 26$ , while the adjacent region (clockwise in the figure) shows a date of origin of  $1670 \pm 34$ . The large South Ridge region between the South Bar and the Central Star show overall date of origin of  $1757 \pm 31$ , though some of the patches could not be properly dated for reasons discussed in the next paragraph.

The South Bar itself could not be dated using the standard cross-correlation methods. Changes in the relative intensities of the features—indeed, changes in the features themselves—for the bar and surrounding patches prevent much of this entire region from being dated. In this case, four “tie points”—distinctive features

---

<sup>2</sup>Various investigators have dated the spikes to the Great Eruption (e.g., [Weis et al.(1999)]).

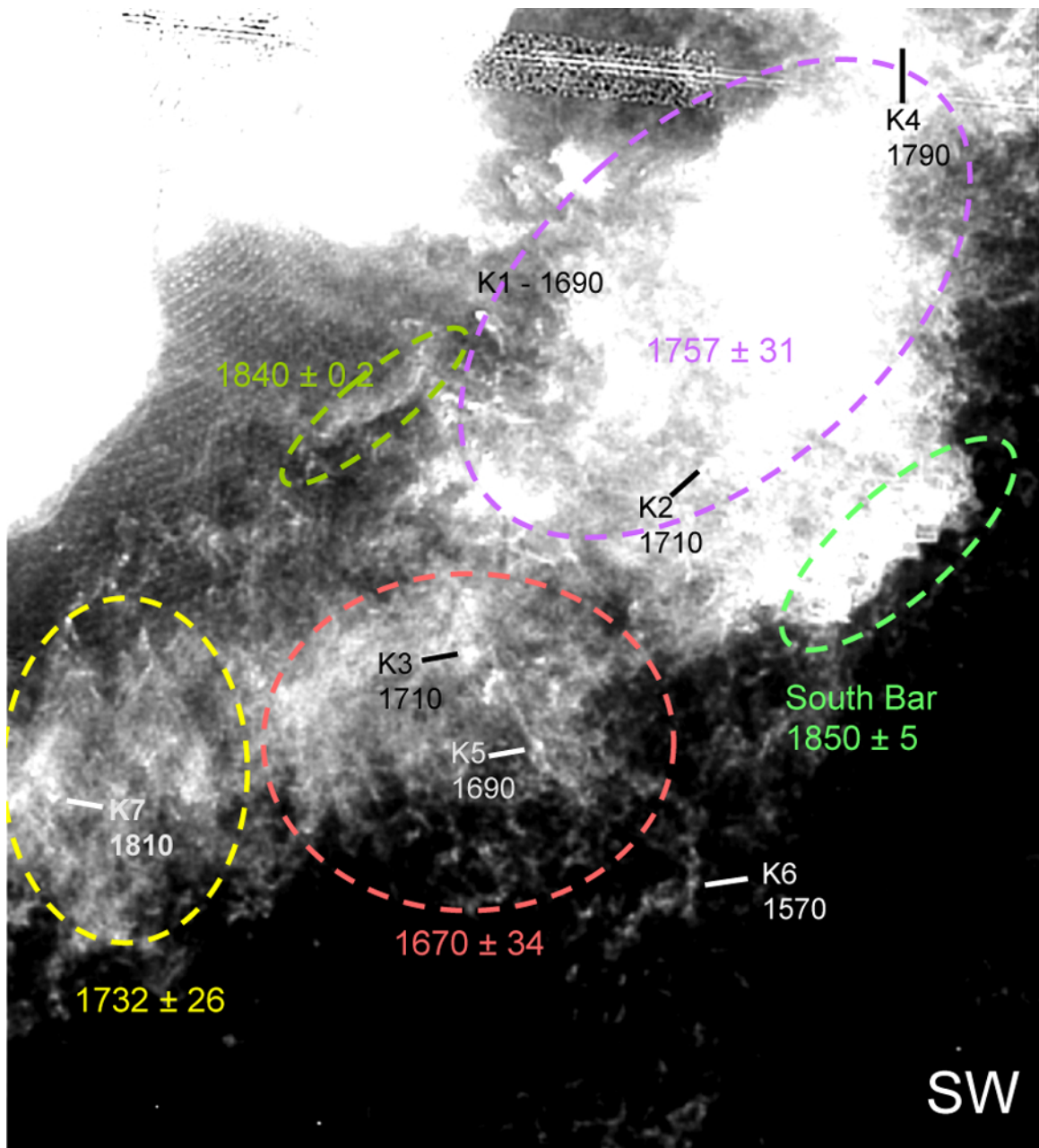


Figure 11.5: Outer debris, southwest quadrant. Cross-correlation dates of origin shown for specific features. Seven knots (K1–7) are shown with dates of origin determined using standard centroiding techniques. The South Bar feature did not cross-correlate properly due to brightness variations between epochs; here, the date of origin was determined by comparing four points on the leading edge of the feature between epochs.

on the leading edge of the bar, present in both epochs—were used to determine the velocity and date of origin for the overall bar. The results indicate a date of origin of  $1850 \pm 5$  for the bar, associating it clearly with the Great Eruption.

It thus appears either that the bar has penetrated through the South Ridge material or their alignment is an optical illusion. Given the fact that much of the ridge material behind the South Bar appears “disrupted” (e.g., quickly changing features, large spread in ejection dates, etc.) the former seems more likely than the latter. It is interesting to note that the South Bar does not appear to be decelerating—unlike the wall feature which is coeval, but which shows a statistically significant ten-year-older age than the Bar.

Based on these results, it is clear that the South Ridge is actually a mix of Great Eruption and earlier debris. There are numerous features embedded in the more quiescent ares of the Ridge which appear to date from around the 1730s. The faint trail of material that extends southwest of the 1670 region shows progressively earlier dates of origin, suggesting that the entire structure (and the 1670 region in the Ridge) may be decelerating, presumably due to higher density of ambient material. The results and this interpretation support a date of origin  $\approx 1730$  for the overall South Ridge structure, which agrees well with the results obtained previously for the South Ridge features in the Northwest Quadrant (§11.2).

## 11.4 Southeast Quadrant Features

The southeast quadrant features are shown in fig. 11.6. Proper motions and dates of origin were obtained for the ejecta near the SE Homunculus cap. Unfortunately, the combination of diffraction spikes in the 2003.9 and blooming in the 1995.4 data preclude the measurement of proper motions in the South Ridge extension into the SE Quadrant.

As shown in the figure, the ejecta breaks down into two general regions. Near the cap of Homunculus, the patch cross-correlation results indicate a date of origin of  $1815 \pm 9$ . Two of the four knots analyzed in this region indicate ejection dates around 1790. The region seems to consist of a mix of material ejected around 1790 with decelerating material from the Great Eruption.

The second region, south of the first region, also shows mixing between late seventeenth and early eighteenth centuries, with a derived date of origin of  $1801 \pm 24$ . The bright K1 knot, near the South Ridge extension, was dated to 1724.

These results suggest that the SE features consist of a mix of materials from a late 18th century eruption with younger material, most likely from the Great Eruption.

## 11.5 What are the ejection dates for the debris outside the Homunculus?

In §7.2, I proposed four questions regarding the kinematic nature of the Homunculus and the nearby ejecta. I have addressed the first three (dealing with the

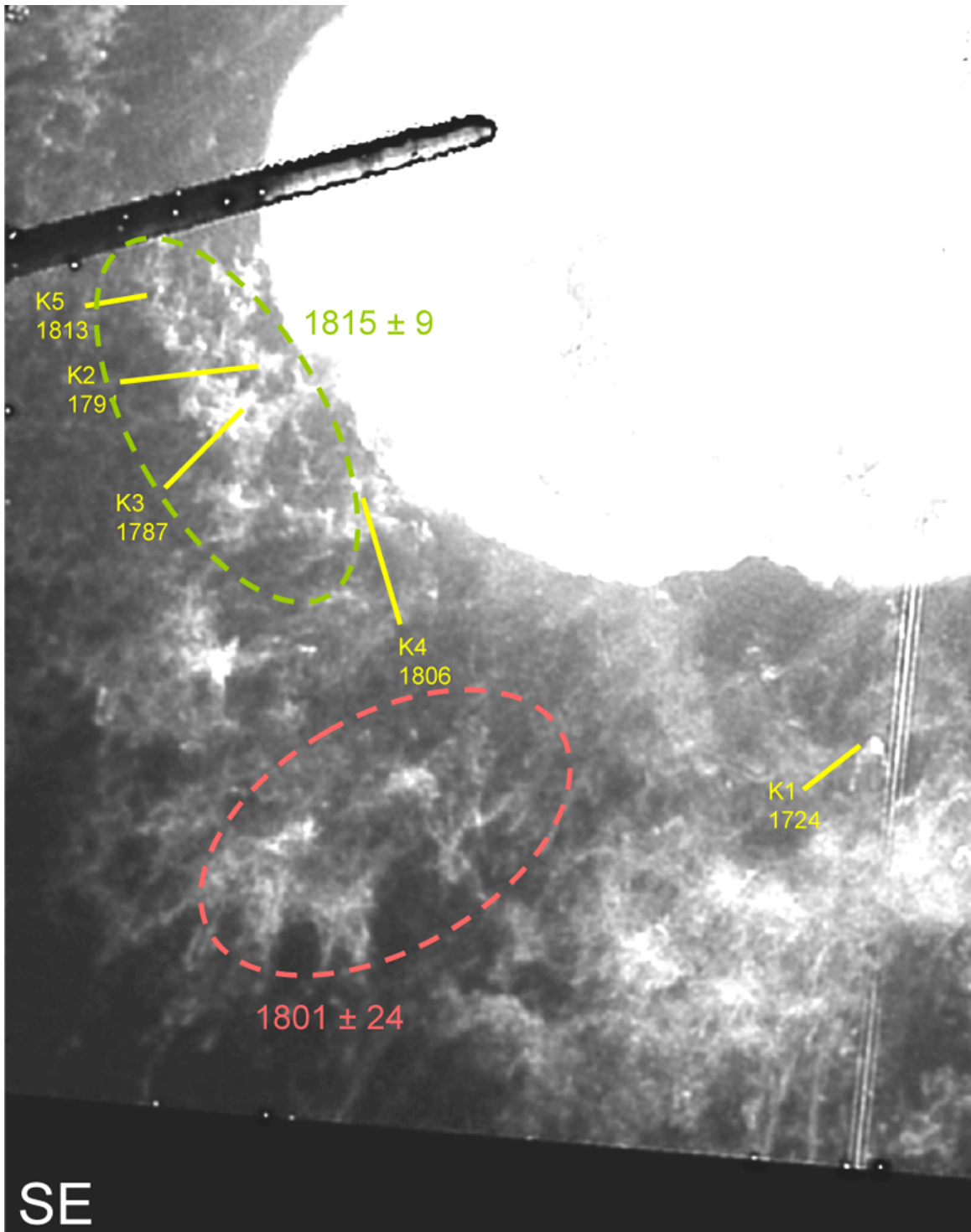


Figure 11.6: Outer debris, southeast quadrant. Cross-correlation dates of origin shown for specific features. Seven knots (K1–5) are shown with dates of origin determined using standard centroiding techniques. The extension of the South Ridge features (south of the Homunculus) did not support patch cross-correlation due to the combination of diffraction spikes in the 2003.9 and CCD blooming in the 1995.4 data.

Homunculus) in §10 . I now address the remaining question, viz.: what are the ejection dates for the debris outside the Homunculus?

In a certain sense, addressing the age of the Homunculus is straightforward because essentially all of the features are coeval and obey a Hubble-law linear relation between separation distance and velocity. In contrast, the outer debris fields consist of mixed velocity systems, some of which include deceleration features. Nevertheless, the features discussed in this chapter do sort into bins at a certain level, suggesting correlations with specific dates and implying possible ejection events and dates. Histograms for the polar cap and the South Ridge debris are shown in fig. ???. A “cartoon” view of the age-sorted debris is shown in fig. 11.7. In reverse chronological order, these are:

### 11.5.1 1840s Great Eruption

The South Bar and the North Jet (specifically, the NN and NS features) are clearly Great Eruption ejecta. Both features physically trace back to brighter equatorial region ejecta, and neither appears to have decelerated significantly during the intervening period. This suggests that the ambient material density in the regions these two features have passed through is relatively low.

The north-south wall in the NE quadrant appears to be physically connected to the North Jet. The material in the wall, however, shows dates of ejection earlier than the North Jet by 10–30 years. If they are part of the same ejecta system, this implies that the material is decelerating, presumably because it is passing through a

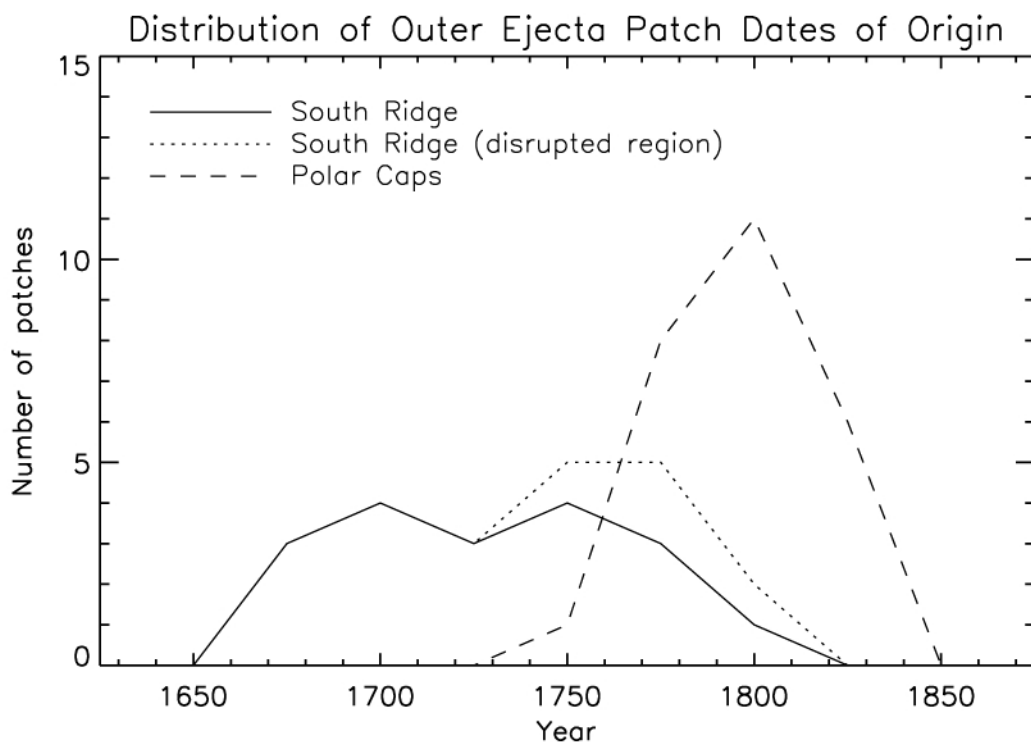


Figure 11.7: Histograms for the dates of origin for two outer debris fields. Both the South Ridge (solid line) and polar cap (dashed line) regions are shown. The dotted line indicates the “disrupted” region behind the South Bar. The polar cap regions show what appear to be mixing between Great Eruption (1840s)-era ejecta and earlier (pre-1800) ejecta. The South Ridge region appears to be a single feature, but is similarly penetrated by later, faster debris. In addition, some regions of the South Ridge appear to be decelerating, showing up as earlier ejection dates.

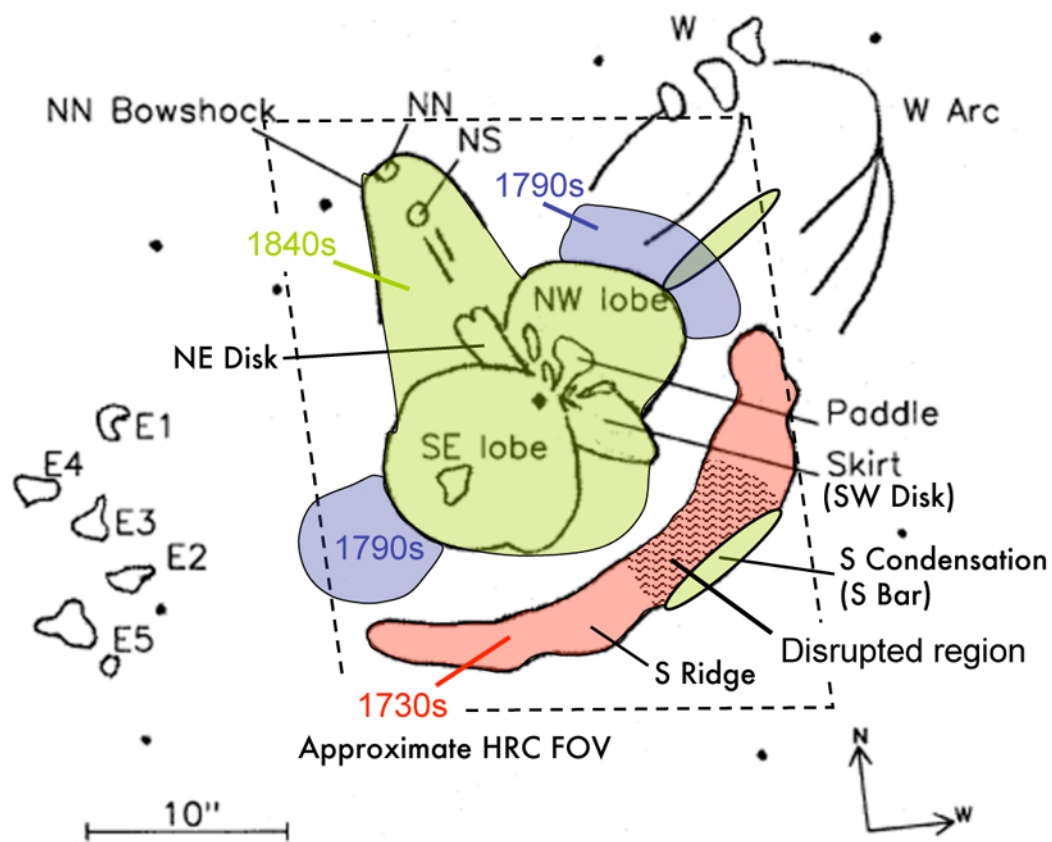


Figure 11.8: Ejecta fields dates of origin. Great eruption ejecta is indicated in green, 1790 polar ejection in purple, and 1730 ejecta in red. Also shown is the area of “disruption” behind the South Ridge. Compare to fig. 7.1.

relatively denser ambient medium. Furthermore, if the North Jet and wall material is part of the same ejecta structure, this implies that Great Eruption material can appear to be three decades older than it actually is.

Using the same logic, the  $1824 \pm 10$  ejecta northwest of the NW lobe cap is most likely Great Eruption ejecta that has slowed due to passage through the halo. The small, wall-like feature in the SW quadrant is also a Great Eruption feature that may be decelerating as it encounters the inner boundary of the South Ridge.

The material outside the southeast cap of the Homunculus is more difficult to characterize; it seems to be a mix of decelerating Great Eruption material with earlier ejecta.

The extra-Homunculus Great Eruption material, much like the Homunculus itself, consists of both equatorial and polar ejecta. The equatorial ejecta—primarily the North Jet NN and NS, and the South Bar—do not show significant deceleration, unlike the polar material. I infer from this that earlier eruptions preferentially deposited material deposited in the polar rather than equatorial regions.

### 11.5.2 c. 1790 Polar Ejection

In order to make sense out of the pre-Great Eruption debris, I will consider features with dates of origin earlier than 1820. Furthermore, a few features have anomalously long ages; in order not to skew the statistics, in this and the following section, I will consider only features that have dates of origin later than 1650.

Most of the halo material above the NW cap that is not the region penetrated

by the Great Eruption ejecta dates from the late 1700s and early 1800s. Similar dates of origin are found for various knots and features in the SW and SE quadrants. These features are found predominantly in the polar regions. There are a total of 23 such features, with a date of origin of  $1793 \pm 7$  (SDOM). Based on this result, I conclude that there was an ejection event in the 1790s time period that was predominantly polar in nature.

### 11.5.3 c. 1730 South Ridge Ejection

The South Ridge material is kinematically distinct from the 1790 polar material. I have identified a total of 43 features (patches and knots) in the South Ridge, and derive a date of origin of  $1733 \pm 7$  (SDOM) for these features. There is some evidence of deceleration (see discussion in §11.3) in portions of the ridge; I thus conclude that a 1733 date is most likely a lower limit and the actual event may have occurred a decade or two later; based on the distribution of material, I conclude that it was non-polar in nature, and fundamentally asymmetric in that most or all of the material was ejected south and west of the central star.

### 11.5.4 c. 1400 ejection

One intriguing result is the close correlation of dates for the slow-moving nebular feature north of the North Jet in the NE quadrant. Two separate reference points on the feature returned results indicating an ejection date in the 1370s. This particular feature is part of what appears to be a larger, extended structure of

phenomenologically similar features in the WFPC2 data. Unfortunately, the other features are outside the HRC field of view, so the statistics on a putative 1400 date of origin are limited. Nevertheless, based on the good agreement between the two reference points, it seems likely that an ejection around 1400 occurred and was responsible for some of the slower moving cloud-like features present to the northeast of the central star.

### 11.5.5 Correlation with Photometry

Is it possible to correlate these kinematic events with observations in the historical light curve data? Obviously, the Great Eruption ejecta correspond to the 1843–1844 photometric event. What about the 1790 event? According to Frew (see Table 2, [Frew(2004)])<sup>3</sup>, observers reported a brightness of  $m_V = 2.3$  in 1752, and brightness lower limits of  $m_V < 2.7$  in 1761.5 and 3.0 in 1773.4. An upper limit of  $m_V > 0.8$  is reported in 1800. The next observation is reported in 1823, with  $m_v = 2.0$ . These observations are thus *consistent with* a photometric brightening of  $\Delta m_V \approx 1.5$  during the period around 1800 and with a putative ejection event around this time.

What about the 1730 event? From Frew, we have observer reports of  $m_V = 3.4$  in 1687, followed by  $m_V > 2.0$  (1710),  $m_V > 1.0$  (1738),  $m_V = 2.3$  (1752), and  $m_V < 2.7$  (1761.5). These observations are consistent with a photometric brightening of one to two magnitudes in the period around 1740.

---

<sup>3</sup>Note that these observations are accorded lower credibility by Frew due, in part, to the fact some are limits rather than values; for this reason, they are not included on his plot (reproduced in fig. 1.3) but are included in his observational database.

No observational data are available earlier than c. 1600, so it is impossible to correlate the possible c. 1400 event with the photometric history of the star.

The photometry history is thus *consistent with* eruptions in the 1730 and 1790 timeframes, though it is clearly not definitive, given the limited accuracy and sparseness of sampling during this period. The photometric history is silent on the issue on any possible 1400 eruption.

The 1730 and 1790 dates fit a possible  $\approx 50$  year pattern for major eruptive events, viz: significant brightening around 2000 ([Smith et al.(2000)]), significant brightening around 1940 ([Davidson & Humphreys(1997)]; [Dorland et al.(2004b)]), the Lesser Eruption of 1890 ([Humphreys et al.(1999)]), and the Great Eruption of the 1840s (numerous authors, including this paper). If such a cycle does exist, the Great Eruption should have been preceded by “events” in the 1790s and 1740s . This may be pure coincidence; on the other hand, this may imply some fundamental 50-year quasi-cyclical property of the star or the system analogous to Damineli’s 5.52-year spectral cycle ([Damineli(1996)]).

## Chapter 12

### Conclusions: Astrometric Results for both Binarity and Ejecta Fields

In this dissertation, the most accurate visible-imaging data available has been used to address two significant questions: 1) is  $\eta$  Car a binary, and 2) what does the material surrounding the star tell us about its history? In the following two subsections (§12.1, 12.2), the findings with respect to these questions are summarized.

Obviously, the overall model explaining what it is we observe when we look at  $\eta$  Car must synthesize the binary and ejecta results. Although this is not a theoretical paper, in the final subsection (§12.3) thoughts on integrating the results into an overall model of the system are presented, and some possible areas of contradictions are noted.

#### 12.1 Binarity: Summary

In addressing the question of  $\eta$  Car's binarity, a total of eight epochs of short integration HST/ACS/HRC near ultra-violet (NUV) data were analyzed, each consisting of four 0.1 sec exposure images at an instrument resolution of 25 mas. These 32 images were calibrated and processed. Positions of the central star with respect to two field-reference stars were measured over the eight epochs using a methodology that combines the distortion-correction work of J. Anderson ([Anderson & King (2004)]; [Anderson (2006)]) with a sub-pixel centroiding tech-

nique developed in this dissertation. The overall method is shown to have residuals at the 0.25-mas level.

$\eta$  Car displays reflex motion at about the 2-mas level that is generally consistent with binary motion. The physical parameters of the system—derived by combining astrometric observational results with the work of previous authors—indicates the system consists of a  $125 M_{\odot}$  primary and  $25 M_{\odot}$  secondary with a total system semi-major axis of  $a = 15.6$  AU and an eccentricity of  $e = 0.95$ . As a result, separations of 0.78 AU at periastron and 32 AU at apastron are predicted<sup>1</sup>. This orbit agrees with that of many of the more recent models (derived, for example, from X-ray data) and excludes earlier models based primarily on spectroscopic observations which favored smaller eccentricities and similar primary/secondary masses. Based on ionization requirements, coevality of the Tr16 stars and stellar evolution arguments, the spectral class of the secondary is found to be O8/9 rather than WR, and the system is dated at 600,000 years old. Other system parameters are listed in Table 6.1.

In the current, quiescent state, neither system overflows its Roche lobe at any time during the orbit. Due to the highly eccentric nature of the orbits, however, a “swollen” primary or secondary would eject material away from the system’s center-of-mass, along the orbital equatorial plane, prior to overflowing into the other star’s Roche lobe as is typical of less eccentric orbits. Based on orbital energy considerations, the Great Eruption *may* be linked to a possible binary capture event.

---

<sup>1</sup>Note that the “quiescent” radii for  $\eta_A$  and  $\eta_B$  are 0.46 and 0.14 AU, respectively ([Hillier et al.(2006)]; during the Great Eruption, the radius of the primary is estimated at 10 AU ([Davidson & Humphreys(1997)])

## 12.2 Ejecta Fields: Summary

In order to address the nature and origin of the ejecta fields surrounding  $\eta$  Car, two epochs of HST data were used. The first epoch consisted of six F658n WF/PC2 images taken in 1995.4 that span integration times from 0.1 to 200 sec, with a native pixel resolution of 45.6 mas. The second epoch consisted of sixteen F660n ACS images taken during 2003.9, with integration times from 0.1 to 412 sec and an instrumental pixel resolution of  $\approx$  25 mas. With an 8.43-year baseline and the ACS data, this dataset represents the most accurate one available (by a factor of two or more) for proper motion measurements of the Homunculus and surrounding material.

These data were calibrated and reference images were created that integrated data from a range of exposure times that optimized signal-to-noise while eliminating saturation. Over three hundred patches were extracted from the 2003.9 reference image from both the Homunculus and outer debris regions. These patches were cross-correlated with both the 2003.9 and 1995.4 images, the latter after scaling the patches in order to reverse 8.43-years of expansion. Locations were determined for each one of these patches for both epochs, and separations from the central star were calculated. Inter-epoch differences in separation were calculated for each patch, yielding motion over the 8.43 year baseline. Expansion velocities and rates were calculated from these motions. From the expansion velocities, feature ages and dates of origin were derived.

A second method (PAM) was developed to check these results. This alternative

method compared patch locations directly between epochs rather than separations. This second method produced results consistent with the original, cross-correlation methodology.

As a result, the Homunculus was dated to  $1847.3 \pm 1.0$ , with an ejection interval upper limit of 3.3 years. As a result, the lower limit for the mass ejection rate over the ejection interval is  $\dot{M} > 3 M^{\odot} \text{ yr}^{-1}$ . The equatorial features were all definitively determined to be coeval with the Homunculus, as were the entire North Jet structure and both the South Bar and wall features. Estimates of the date of origin for the outer debris were less precise due to significantly reduced SNR and apparently decelerations. A polar debris structure dating from the 1790s is indicated, and the South Ridge appears to date from the 1730s, or perhaps a decade or two later due to correction for deceleration. Much older debris was also found, with indications of one nebular feature dating to the fourteenth century. Inspection of the photometric record is consistent with smaller (relative to the 1843 event) eruptions in the 1740 and 1800 timeframes.

### 12.3 Towards an integrated picture

Are the binary results compatible with or contradictory to the analysis of the ejecta? The primary findings of the binarity analysis—that  $\eta$  Car is a highly eccentric binary system whose orbital period is the source of the observed 5.52-year spectroscopic cycle—I would argue is *more* compatible with a single, massive eruption than one spread out over time. These new results have revised the ejection

interval upper limit down to 3 years, and appear to be “instrument-limited” still, implying the actual ejection interval may be much smaller. In this sense—viz., a very short eruption interval—the Homunculus results are consistent with the binary model.

Another aspect where there is agreement is in terms of the equatorial streams or jet features, i.e. the North Jet and NW equatorial “disk”<sup>2</sup> features on the one hand, and the South Bar, south wall and SE equatorial “disk” features on the other. In this paper, these are definitively dated to the Great Eruption. If one adopts the  $\approx$  10 AU diameter of  $\eta$  Car during the Great Eruption ([Davidson & Humphreys(1997)]) and then considers a binary system at periastron, the secondary would be *inside* the primary’s swollen photosphere. Without attempting to model the stellar atmospheres, one can say at a minimum that the special Roche Lobe overflow conditions described in §5.6.5 would be met in the region around both stars; as a result, the periastron passage would result in the ejection of material away from the system center-of-mass along the equatorial plane and aligned along the line of apsides, which is to say in two approximately anti-parallel jets. This is exactly what we see with the Great Eruption equatorial features. This material may be material ejected from the primary during periastron passage.

Finally, the ejecta pattern outside the Homunculus implies earlier events around 1790 and 1730. Is this consistent with the binary picture? As noted previously, it is certainly consistent with the subsequent behavior of the system, which has man-

---

<sup>2</sup>Here, nomenclature for the equatorial features (i.e., “disk”) were used for consistency; the results suggest there is not a coherent disk, however.

ifested significant photometric changes every 50 years or so. It is not clear how this would be directly related to a 5.52 year-period binary, but it may indicate some fundamental time scale associated with variations in the primary star itself, or may suggest the presence of a third star in a much longer period orbit. In any event, the coincidence of this 50-year cycle with close passage of the secondary *may* provide a starting point for explaining some of the phenomena associated with the Great Eruption.

## Appendix A

### Glossary

ACS	Advanced Camera for Surveys. A third-generation optical imaging instrument on the HST. As of early 2007, two of the three ACS instrument channels (WFC and HRC) had stopped functioning due to electronics problems.
AU	Astronomical Unit, defined as the mean orbital distance from the Earth to the Sun. $1 \text{ AU} \approx 1.5 \times 10^{11} \text{ m}$ .
DRIZZLE	Linear reconstruction algorithm used for HST data processing. See [Fruchter & Hook(2002)].
Equatorial	There are at least three possible interpretations of equatorial: 1) with respect to the Homunculus axis of symmetry, 2) w/r/t central star rotation axis, and 3) w/r/t a binary orbital plane. Unless otherwise noted, in this thesis, meaning 1 is implied. Note that there is strong reason to suspect that the Homunculus equatorial plane is closely aligned with the orbital plane.
FWHM	Full width at half maximum. The full width of a distribution measured at half the maximum value.
GO	General Observing. HST term for a discrete sequence of HST observations. Each GO is identified by a unique number.
H-D Limit	Humphreys-Davidson limit. An empirical limit on how luminous a star can be as a function of color (see fig. 1.5).
Homunculus	Name given by Gaviola (1950) to the bright nebula surrounding the primary star. Gaviola observed that the nebula looked like a small, fat man with his arms crossed.
HRC	High Resolution Channel. Part of the ACS instrument on-board HST. Offers the highest resolution imaging available on HST.
HST	Hubble Space Telescope
Hubble Flow	A velocity system wherein velocity is a linear function of distance from some reference point.
$L_{\odot}$	Solar luminosities. Stellar luminosity expressed in units where the luminosity of the Sun equals one. $1L_{\odot} \approx 3.8 \times 10^{33} \text{ ergs/s}$ .
$L_{\text{Eddington}}$	Eddington limit. Theoretical maximum stellar luminosity for a given mass.

LBV	Luminous Blue Variable. A class of very bright, variable stars of which $\eta$ Carinae is thought to be an extreme member.
$M_{\odot}$	Solar masses. Stellar mass expressed in units where the mass of the Sun equals one. $1M_{\odot} \approx 2.0 \times 10^{30}$ kg.
magnitude	Measure of apparent (“m”) or absolute brightness (“M”) of an astronomical object. Magnitude is given on a log scale, and is referenced to a specific, well-defined UV/optical/IR passband. The zero point is typically defined by the star Vega ( $\alpha$ Lyrae), and each increase in magnitude thus, a fifth magnitude star is 100 times fainter than a 0 magnitude star. Visible, or “V-band” magnitudes can be annotated by either the exponent “v” or “m”. Absolute magnitude, indicated by the letter “M” indicates the apparent magnitude, referenced to a distance of 10 parsecs.
mas	Milli-arcsecond. 1/1000th of one second of arc. 1 mas $\approx 4.84 \times 10^{-9}$ radians
MultiDRIZZLE	Implementation of the DRIZZLE algorithm (see above) which combines multiple images; see [Jedrzejewski et al.(2005)].
NIR	Near infra-red.
Parsec	Distance at which 1 AU appears to subtend 1 second of arc. 1 parsec $\approx 3.3$ light-years, 206,265 AU, or $3.2 \times 10^{16}$ m.
PPE	Pixel phase error. The error associated with centroiding an undersampled point-spread function (see Appendix C).
PoS	Plane of the sky.
SD	Standard deviation of the distribution.
SDOM	Standard Deviation of the Mean (as opposed to standard deviation of the distribution).
S-Dor	Sigma Doradus; “S-Dor events” are temporary reddenings in LBVs thought to be evidence of shell ejections (see §1.3). During a shell ejection event (or simply, a “shell event”), bolometric luminosity is constant; as a result, the effective surface temperature of the expanding shell (or “pseudo-photosphere”) decreases and the star appears to redden. When the temperature reaches the “opacity limit” the shell effectively becomes transparent and detaches from the star. At this point, the event terminates with the star observed to be at its “quiescent” color, surrounded by ejected material.
SNR	Signal-to-noise ratio
STIS	Space Telescope Imaging Spectrograph. Second generation imaging spectrometer aboard HST.

WFPC2	Wide field/planetary camera 2. A second generation HST instrument.
WR	A Wolf-Rayet star, thought to be the exposed He core of a massive star that has evolved off the Main Sequence.
ZAMS	Zero-Age Main Sequence. A star that is undergoing normal hydrogen burning. New stars evolve “onto” the main sequence of the Hertzsprung-Russell diagram where they spend most of their lifetime. At the end of the hydrogen burning phase, the stars evolve “off” the main sequence, eventually winding up as white dwarfs, neutron stars or black holes, depending on their initial masses.

## Appendix B

### Distance to $\eta$ Car

Much of the discussion in this thesis centers around the luminosity of  $\eta$  Car.

The standard reference for the star's bolometric luminosity is [Cox et al.(1995)], which found  $L_\eta \approx 5 \times 10^6 L_\odot$ . This was referenced, however, to a distance of 2.5 kpc, citing "Tapia et al. (1988)" Interestingly, [Tapia et al.(1988)] determines the distance to be  $2.4 \pm 0.2$  kpc. This discrepancy is difficult to resolve, since Cox et al. cite Tapia et al. in the text, but do not provide an entry in their reference section. It thus appears as if the reference distance is wrong in the canonical luminosity reference paper.

Since luminosity will vary as the square of the distance, a reduction in the distance from 2.5 to 2.4 kpc will reduce the derived luminosity from  $5 \times 10^6$  to  $4.6 \times 10^6 L_\odot$ . More recent work suggests that  $\eta$  is closer than 2.4 kpc. Because the derived luminosity depends on the square of this value, it is important to determine the distance as accurately as possible. What is the best estimate of the distance to  $\eta$  Car?

As noted in the discussion of [Cox et al.(1995)], the distance to Tr16 was calculated to be  $2.4 \pm 0.2$  kpc by [Tapia et al.(1988)] using analysis of interstellar reddening. Using spectroscopic analysis of expansion rate of the Homunculus, [Allen & Hillier(1993)] determined the distance to be  $2.2 \pm 0.2$  kpc. An al-

ternate argument based on reddening was used by [Davidson & Humphreys(1997)], which referenced work done by [Walborn(1995)] to determine the distance to be 2.3 kpc. In [Davidson et al.(2001)], expansion velocities are used to derive a value of  $2.25 \pm 0.18$  kpc. Using arguments of symmetry between the two lobes in the spectroscopic/velocimetric data, [Smith(2002)] derives a value of 2.25 kpc as the distance.

The unweighted mean value of these distances is 2.28 kpc, while the mode is 2.25 kpc. For consistency, I adopt 2.25 kpc as the reference distance to  $\eta$  Car, though note that the value is far from well established. This has the effect of reducing the derived luminosity to  $L_\eta = 4 \times 10^6 L_\odot$ , which is the value used in the discussion of binarity. Should the distance turn out to be larger than 2.25 kpc, the first-order effect would be a linear increase in the size of the primary, which would also drive a smaller increase in the size of the secondary. Adopting 2.4 kpc as an upper limit distance, the increase in primary mass would be approximately 7%.

## Appendix C

### Gaussian Centroiding and Pixel Phase Effects

High precision stellar astrometry is dependent to a large degree on the esoteric science of centroiding observed stellar point spread functions. Some concepts such as “pixel phase error” (PPE)<sup>1</sup> are not obvious. In this section, I describe some of the basic concepts and relationships.

#### C.1 Centroiding for Well-Sampled PSFs: FWHM and SNR Dependency

I begin by considering a simple theoretical model for centroiding. The centroiding process in its simplest form consists of two steps: first, a point source is observed, and second, a model PSF is fit to the observed data such that some metric (typically,  $\chi^2$ ) is minimized. The resultant centroid is the estimated position for the observed point source.

We approximate an actual instrumental PSF using a Gaussian distribution for purposes of this analysis. This approximation greatly simplifies the mathematical complexity while still producing realistic results. Adopting units where the peak amplitude is one, we can write our input PSF as:

---

<sup>1</sup>PPE is also known as “intra-pixel phase error,” “pixel phase bias,” and (by star tracker engineers) as “the S-shaped curve.”

$$y = \exp\left(\frac{-(x - x_0)^2}{2\sigma^2}\right) \quad (\text{C.1})$$

where  $x$  is the pixel,  $x_0$  is the photocenter, expressed in units of pixels,  $y$  is the measured signal for a given pixel, and  $\sigma$  is width in pixels of the Gaussian at one standard deviation, . We want to understand what the centroid error ( $\sigma_{x_0}$ ) is as a function of pixel and measured signal, so we invert the equation thus:

$$x_0 = x - \sigma \sqrt{-2 \ln y} \quad (\text{C.2})$$

This equation indicates that for a peak-normalized Gaussian PSF, and given a signal, a pixel, and knowledge of the underlying width of the Gaussian PSF, we can compute the centroid with a two-fold degeneracy (i.e., we can calculate how far it is from our reference pixel, but cannot determine direction without another measurement).

The error for the function  $x_0 = f(x, y)$  is given approximately by:

$$\sigma_{x_0} \approx \sqrt{\left(\frac{\partial}{\partial x} f(x, y) \sigma_x\right)^2 + \left(\frac{\partial}{\partial y} f(x, y) \sigma_y\right)^2} \quad (\text{C.3})$$

where  $\sigma_y$  is the error in  $y$ ,  $\sigma_x$  is the error in  $x$ , and  $\sigma_{x_0}$  is the error in  $x_0$  . In this example, we assume the error in identifying the pixel is negligible (i.e.,  $\sigma_x \approx 0$ ), so the first term on the right hand side goes to zero. Applying the remainder of eqn. C.3 to eqn. C.2 gives:

$$\sigma_{x_0} \approx \frac{\sigma}{y \sqrt{-2 \ln y}} \sigma_y \quad (\text{C.4})$$

When performing astronomical measurements, the Gaussian full width at half maximum (FWHM) is typically a more useful metric than the Gaussian standard deviation as it is relatively straightforward to measure from the data. The relationship between  $\sigma$  and the FWHM can be calculated using eqn. C.1. Substituting  $y = 0.5$ ,  $x = \text{FWHM}/2$ , and  $x_0 = 0$  into the equation, I get:

$$0.5 = \exp \frac{-(\text{FWHM}/2)^2}{2\sigma^2} \quad (\text{C.5})$$

Solving for  $\sigma$ , I get:

$$\sigma = \frac{\text{FWHM}}{\sqrt{8 \ln 2}} \quad (\text{C.6})$$

This result can be substituted into eqn. C.4 and that equation re-written in terms of the more practical FWHM metric:

$$\sigma_{x_0} = \frac{\text{FWHM}}{4y\sqrt{-\ln 2 \ln y}} \sigma_y \quad (\text{C.7})$$

This equation relates the error in measuring the intensity  $y$  to the derived error in the position of the Gaussian centroid. We consider only the case where photon noise dominates. The noise term  $\sigma_y$  is given by the square root of the total signal, and eqn. C.7 becomes:

$$\sigma_{x_0} = \frac{\text{FWHM}}{4\sqrt{-y \ln 2 \ln y}} \quad (\text{C.8})$$

The best place along the (now inverted) Gaussian to take the measurement is where the error is minimized. This is determined by taking the derivative of eqn.

C.8, setting it equal to zero, and solving for  $y$ :

$$\begin{aligned} \frac{d}{dy}\sigma_{x_0} &= \frac{d}{dy} \left( \frac{\text{FWHM}}{4\sqrt{-y \ln 2 \ln y}} \right) \\ 0 &= \frac{\ln \frac{1}{y} - 1}{8\sqrt{\ln 2(y \ln \frac{1}{y})^3}} (\text{FWHM}) \\ \frac{1}{e} &= y \end{aligned} \quad (\text{C.9})$$

The centroiding error is thus minimized at  $y = \frac{1}{e}$ , or, equivalently,  $(x - x_0) = \sqrt{2}\sigma \approx 1.4\sigma$ . The magnitude of the centroiding error is calculated by evaluating eqn. C.8 using this result for  $y$ , and noting the equality  $\text{SNR}(y) = \sqrt{y}$ , where  $\text{SNR}(y)$  is the signal-to-noise ratio at  $y$ :

$$\begin{aligned} \sigma_{x_0} &= \frac{\text{FWHM}}{4\text{SNR}(e^{-1})\sqrt{\ln 2 \ln e}} \\ &= \frac{\text{FWHM}}{4\text{SNR}(e^{-1})\sqrt{\ln 2}} \end{aligned} \quad (\text{C.10})$$

The signal to noise ratio at  $y$  is related to the peak SNR according to the following relation:  $\text{SNR}(e^{-1}) = e^{-1/2}\text{SNR}_{\text{peak}}$ . Substituting this into eqn. C.10 gives:

$$\begin{aligned} \sigma_{x_0} &= \left( \frac{e^{1/2}}{4\sqrt{\ln 2}} \right) \left( \frac{\text{FWHM}}{\text{SNR}_{\text{peak}}} \right) \\ &\approx 0.50 \frac{\text{FWHM}}{\text{SNR}_{\text{peak}}} \end{aligned} \quad (\text{C.11})$$

Equation C.11 shows the functional dependence of centroiding error on FWHM and SNR for the photon noise case, fitting a single point to one half of the PSF. It states that the error is linearly dependent on FWHM (as in the system noise limited case)

and inversely dependent on the peak SNR. Fitting multiple points tends to bring the prefactor up to of order unity. The basic relationship between centroiding error, FWHM and SNR is thus approximated by:

$$\sigma_{x_0} \approx \frac{\text{FWHM}}{\text{SNR}} \quad (\text{C.12})$$

From this equation, we see that the precision of the centroiding process is related directly to the width of the input PSF rather than the sampling grid. Thus, for example, for a given  $f/\#$  and detector resolution<sup>2</sup> (e.g., the HRC instrument), as one observes at longer and longer wavelengths, the centroiding error increases linearly with the increase in wavelength.

## C.2 Centroiding under-sampled PSFs: Pixel Phase Error

Equation C.12 implies that one should minimize the FWHM and maximize the SNR in order to achieve the smallest centroiding errors. If this were the only consideration, astrometric instrumentation would be designed such that the entire Airy disk were contained within a single pixel.

Of course, the assumption for the analysis is the previous section was that the PSF was well-sampled; this assumption breaks down as the PSF approaches a FWHM= 1 pixel. In the extreme limit, where the entire Airy disk is contained within a single pixel, there is indeed maximum SNR, but there is no spatial information on where *within* the pixel the photocenter is located. One can think of the centroiding

---

<sup>2</sup>Assuming a well-sampled PSF.

process as a sort of balance in which the relative intensities in the pixels adjacent to the central one provide the information about where within the central pixel the photocenter lies.

Figure C.1 is a grid of sampling and pixel phase offsets that graphically illustrate the errors that develop as sampling decreases below a critical threshold. Along the top row, the input Gaussian PSF (dashed line), the pixelated detector response (solid line), and the calculated Gaussian fit (dotted line) are shown for a sampling of  $\text{FWHM} = 2.5$  pixels for three photocenter offsets: 1) 0.0 pixels, i.e., the photocenter is coincident with the pixel center; 2) 0.25 pixels; and 3) 0.5 pixels, where the photocenter lies along a pixel boundary. The second and third rows show the same information, but for progressively lower sampling.

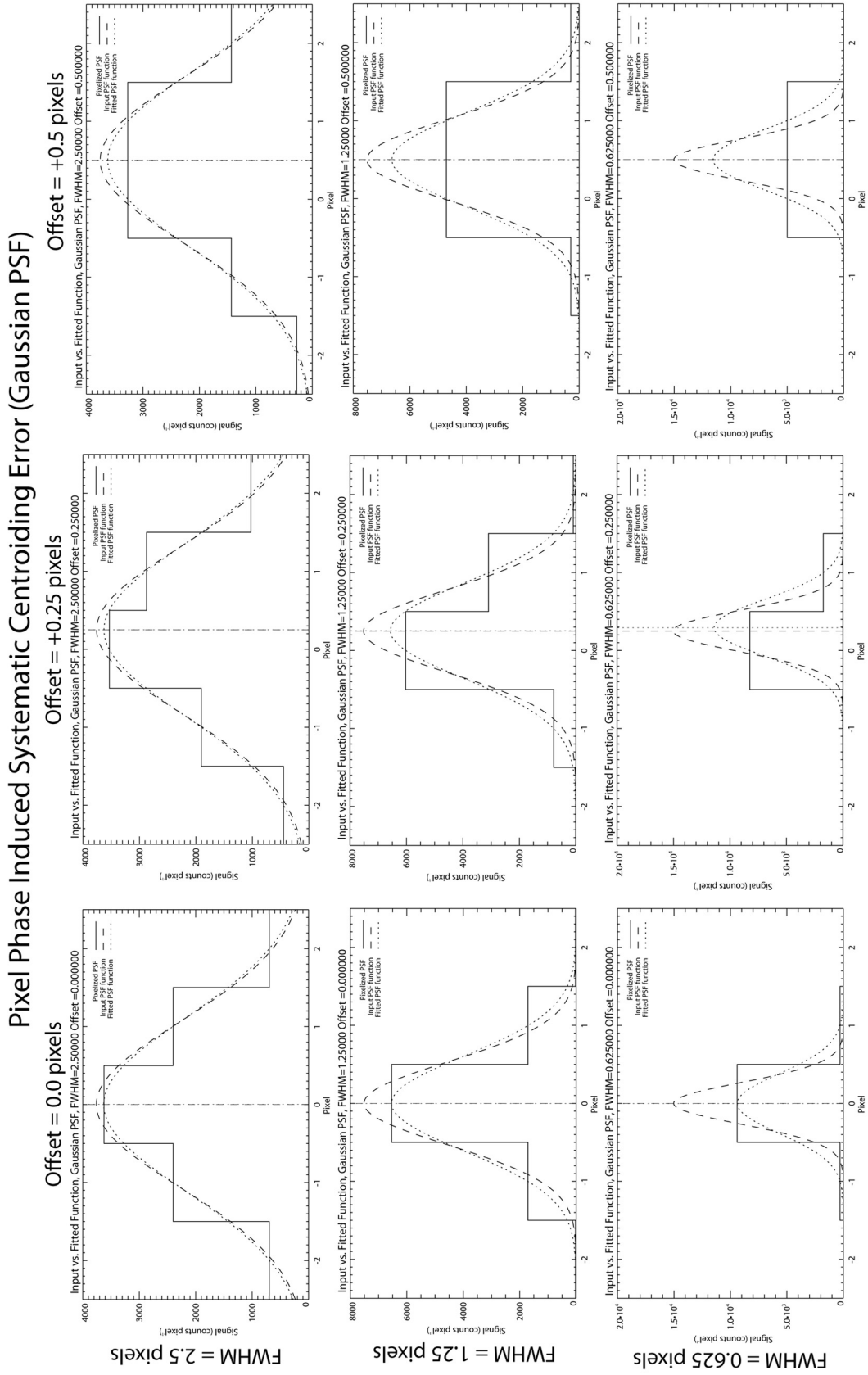


Figure C.1: Grid of pixel phase offset errors as a function of sampling and offset. Offset = 0.0 indicates the photocenter is in the center of the pixel; 0.5, along the pixel boundary. Dashed lines are actual (input) point spread functions, square lines are pixelized detector response to input PSFs, and dotted lines are the best fit Gaussian solutions.

At 2.5 pixels FWHM, the Gaussian fit to the detector response is a close match to the input PSF. There are slight mismatches on amplitude and width, but the centroid error is negligible. At 1.25 pixels FWHM, however, significant errors begin to develop. The photons in pixel +1, for example, are all equally weighted in terms of distance from the photocenter, despite the fact that virtually all of the photons entered the pixel near the boundary with pixel 0. This results in a significant overestimate of width, underestimate of peak amplitude, and a centroiding offset error. Because the fitting routine does not have sufficient spatial information, as the input detector response becomes asymmetric, the fitting algorithm develops a bias. This bias, or offset, is a function of the asymmetry of the detector response function. It is minimized at pixel phases 0 (photocenter = center of pixel) and 0.5 (photocenter = boundary of pixels) where the detector response is symmetric, and maximized at phase 0.25 (photocenter is halfway between center and boundary) where it is asymmetric. This pixel phase error (PPE) can be seen in the figure as an offset between the vertical lines indicating actual (dashed) and calculated (dotted) photocenters at photocenter offset 0.25 pixels. The bias can be seen for both FWHM =1.25 (slight) and FWHM=0.675 (more pronounced) pixel sampling cases.

### C.3 Optimal Sampling: A Simulation

For many applications, PPE is not an issue. For high precision astrometry, however, it is. The optimal sampling for astrometry can be calculated by varying the FWHM for a given input signal strength, and calculating both the random

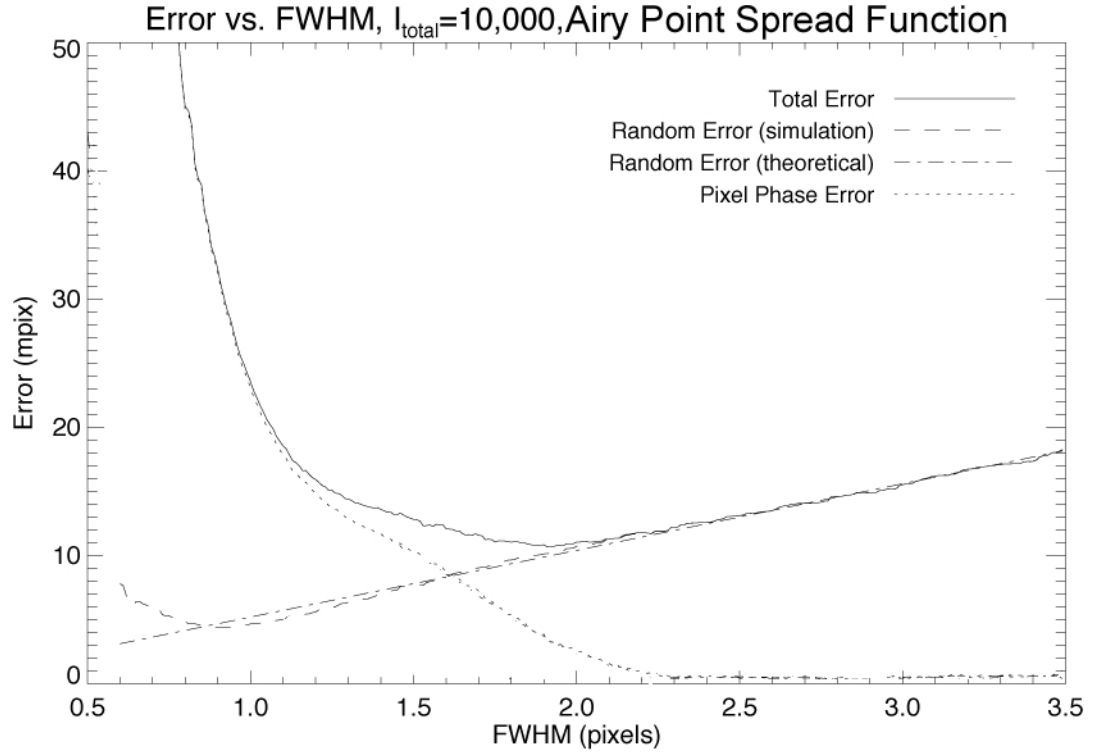


Figure C.2: Total centroiding error: simulation results. Total centroiding error is shown as a function of FWHM sampling. Also shown are the component error sources, i.e., random centroiding error and pixel phase error.

centroiding error (§C.1) and the PPE (§C.2). Fig. C.2 shows the results from a simulation of the centroiding process run over a variety of pixel phases for a total signal strength of 10,000 photons.

As shown in the figure, for a given SNR (=100), centroiding accuracy decreases linearly with FWHM in the well sampled ( $\text{FWHM} > 2$  pixels) regime. At around a sampling of  $\text{FWHM} \approx 2.3$  pixels, however, PPE begins to arise. At around  $\text{FWHM} \approx 1.7$  pixels, the two error sources cross and PPE becomes the dominant source of error. The total error, which is estimated as the root sum square of the random and PPE errors is minimized at around  $\text{FWHM} \approx 2.0$  pixels. For this particular

scenario, this is the optimal sampling for astrometric precision. At higher sampling, noise degrades the centroiding result, while at lower sampling, PPE does.

It should be noted that this analysis is a general discussion of errors associated with centroiding of astrometric images. The particular performance curve for any given instrument will be strongly dependent on the specifics of the instrument along with other considerations such as noise, dark current, PSFs, distortion, etc. The performance parameters of the HRC instrument for certain, specific filters are discussed in some detail in Chapter 3.

## BIBLIOGRAPHY

[Allen & Hillier(1993)] Allen, D. A., & Hillier, D. J. 1993, Proceedings of the Astronomical Society of Australia, 10, 338

[Anderson & King (2004)] J. Anderson & King, I. R. *Multi-filter PSFs and Distortion Corrections for the HRC*, HST Instrument Science Report ACS 2004-15, Baltimore, MD: Space Telescope Science Institute (2004)

[Anderson (2006)] J. Anderson, private communication, 2006

[Bevington & Robinson(2003)] Bevington, P. R., & Robinson, D. K. 2003, Data reduction and error analysis for the physical sciences, 3rd ed., by Philip R. Bevington, and Keith D. Robinson. Boston, MA: McGraw-Hill, ISBN 0-07-247227-8, 2003.,

[Bradt et al.(1993)] Bradt, H. V., Rothschild, R. E., & Swank, J. H. 1993, A&A Suppl., 97, 355

[Burkholder et al.(1997)] Burkholder, V., Massey, P., & Morrell, N. 1997, ApJ, 490, 328

[Carroll & Ostlie(1996)] Carroll, B. W., & Ostlie, D. A. 1996, Reading, Mass. : Addison-Wesley Pub., c1996.,

[Corcoran et al.(2001)] Corcoran, M. F., Ishibashi, K., Swank, J. H., & Petre, R. 2001, ApJ, 547, 1034

[Cox et al.(1995)] Cox, P., Mezger, P. G., Sievers, A., Najarro, F., Bronfman, L., Kreysa, E., & Haslam, G. 1995, *A&A*, 297, 168

[Currie et al.(1996)] Currie, D. G., et al. 1996, *AJ*, 112, 1115

[Currie (2007)] Currie, D. G. 2007, private communication

[Cutri et al.(2003)] Cutri, R. M., et al. 2003, The IRSA 2MASS All-Sky Point Source Catalog, NASA/IPAC Infrared Science Archive. <http://irsa.ipac.caltech.edu/applications/Gator/>,

[Dale & Davies(2006)] Dale, J. E., & Davies, M. B. 2006, *MNRAS*, 366, 1424

[Dame et al.(2001)] Dame, T. M., Hartmann, D., & Thaddeus, P. 2001, *ApJ*, 547, 792

[Damineli(1996)] Damineli, A. 1996, *ApJL*, 460, L49

[Damineli et al. (1997)] Damineli, A., Conti, P. S., & Lopes, D. F. 1997, *New Astronomy*, 2, 107

[Damineli et al.(1999)] Damineli, A., Stahl, O., Wolf, B., Kaufer, A., & Jablonski, F. J. 1999, *ASP Conf. Ser.* 179: *Eta Carinae at The Millennium*, 179, 221

[Damineli et al.(2000)] Damineli, A., Kaufer, A., Wolf, B., Stahl, O., Lopes, D. F., & de Araújo, F. X. 2000, *ApJL*, 528, L101

[Davidson(1987)] Davidson, K. 1987, *ApJ*, 317, 760

[Davidson(1989)] Davidson, K. 1989, ASSL Vol. 157: IAU Colloq. 113: Physics of Luminous Blue Variables, 101

[Davidson et al.(1995)] Davidson, K., Ebbets, D., Weigelt, G., Humphreys, R. M., Hajian, A. R., Walborn, N. R., & Rosa, M. 1995, AJ, 109, 1784

[Davidson & Humphreys(1997)] Davidson, K., & Humphreys, R. M. 1997, *Annu. Rev. Astron. Astrophys.*, 35, 1

[Davidson(1997)] Davidson, K. 1997, *New Astronomy*, 2, 387

[Davidson et al.(1997)] Davidson, K., Ebbets, D., Johansson, S., Morse, J. A., & Hamann, F. W. 1997, AJ, 113, 335

[Davidson et al.(1999)] Davidson, K., et al. 1999, AJ, 118, 1777

[Davidson et al.(2000)] Davidson, K., Ishibashi, K., Gull, T. R., Humphreys, R. M., & Smith, N. 2000, ApJL, 530, L107

[Davidson et al.(2001)] Davidson, K., Smith, N., Gull, T. R., Ishibashi, K., & Hillier, D. J. 2001, AJ, 121, 1569

[DeGioia-Eastwood et al.(2001)] DeGioia-Eastwood, K., Throop, H., Walker, G., & Cudworth, K. M. 2001, ApJ, 549, 578

[de Vaucouleurs(1952)] de Vaucouleurs, G. 1952, Leaflet of the Astronomical Society of the Pacific, 6, 244

[de Vaucouleurs & Eggen(1952)] de Vaucouleurs, G., & Eggen, O. J. 1952, PASP, 64, 185

[Dorland(2004a)] Dorland, B. N. 2004, Proc. SPIE, 5167, 302

[Dorland et al.(2004b)] Dorland, B. N., Currie, D. G., & Hajian, A. R. 2004, AJ, 127, 1052

[Dowling(1996)] Dowling, D. 1996, PhD Thesis, University of MD: College Park, MD

[Fabian et al.(1975)] Fabian, A. C., Pringle, J. E., & Rees, M. J. 1975, MNRAS, 172, 15P

[Feinstein et al.(1973)] Feinstein, A., Marraco, H. G., & Muzzio, J. C. 1973, A&A Suppl., 12, 331

[Figer et al.(1998)] Figer, D. F., Najarro, F., Morris, M., McLean, I. S., Geballe, T. R., Ghez, A. M., & Langer, N. 1998, ApJ, 506, 384

[Figer et al.(2004)] Figer, D. F., Najarro, F., & Kudritzki, R. P. 2004, ApJL, 610, L109

[Frew(2004)] Frew, D. J. 2004, Journal of Astronomical Data, 10, 6

[Fruchter & Hook(2002)] Fruchter, A. S., & Hook, R. N. 2002, PASP, 114, 144

[Garcia & Bianchi(2004)] Garcia, M., & Bianchi, L. 2004, ApJ, 606, 497

[Gaviola(1950)] Gaviola, E. 1950, ApJ, 111, 408

[Gonzaga(2005)] S. Gonzaga et al. 2005, *ACS Instrument Handbook*, v 6.0, Baltimore, MD: Space Telescope Science Institute

[Harwit(1988)] Harwit, M. 1988, *Astrophysical Concepts*, XV, 626 pp. 175  
figs.. Springer-Verlag Berlin Heidelberg New York. Also *Astronomy and  
Astrophysics Library*,

[Heintz(1978)] Heintz, W. D. 1978, *Geophysics and Astrophysics Monographs*, 15,  
[Heyer et al.(2004)] Heyer, Biretta, et al. 2004, *WFPC2 Instrument Handbook*, Ver-  
sion 9.0 (Baltimore: STScI).

[Hillier et al.(2001)] Hillier, D. J., Davidson, K., Ishibashi, K., & Gull, T. 2001,  
ApJ, 553, 837

[Hillier et al.(2006)] Hillier, D. J., et al. 2006, ApJ, 642, 1098

[Høg et al.(2000)] Høg, E., et al. 2000, AAP, 355, L27

[Humphreys & Davidson(1979)] Humphreys, R. M., & Davidson, K. 1979, ApJ, 232,  
409

[Humphreys & Davidson(1994)] Humphreys, R. M., & Davidson, K. 1994, PASP,  
106, 1025

[Humphreys et al.(1999)] Humphreys, R. M., Davidson, K., & Smith, N. 1999,  
PASP, 111, 1124

[Ipingle et al.(2005)] Ipingle, R. C., Sonneborn, G., Gull, T. R., Massa, D. L., & Hillier,  
D. J. 2005, ApJL, 633, L37

[Innes et al.(1927)] Innes, R. T. A., Dawson, B. H., & van den Bos, W. H. 1927,  
Johannesburg, S.A.: Union Observatory, 1927,

[Ishibashi et al.(1999)] Ishibashi, K., Corcoran, M. F., Davidson, K., Swank, J. H., Petre, R., Drake, S. A., Damineli, A., & White, S. 1999, ApJ, 524, 983

[Ishibashi(2001)] Ishibashi, K. 2001, ASP Conf. Ser. 242: Eta Carinae and Other Mysterious Stars: The Hidden Opportunities of Emission Spectroscopy, 242, 53

[Ishibashi et al.(2003)] Ishibashi, K., et al. 2003, AJ, 125, 3222

[Innes(1903)] Innes, R.T.A. 1903, Ann. Cape Obs., 9, 75B

[Janesick(2001)] Janesick, J. R. 2001, Scientific charge-coupled devices, Bellingham, WA: SPIE Optical Engineering Press, 2001, xvi, 906 p. SPIE Press monograph, PM 83. ISBN 0819436984,

[Jedrzejewski et al.(2005)] Jedrzejewski, R., Hack, W., Hanley, C., Busko, I., & Koekemoer, A. M. 2005, Astronomical Data Analysis Software and Systems XIV, 347, 129

[Koekemoer et al.(2002)] Koekemoer, A. M., Fruchter, A. S., Hook, R. N., & Hack, W. 2002, The 2002 HST Calibration Workshop : Hubble after the Installation of the ACS and the NICMOS Cooling System, Proceedings of a Workshop held at the Space Telescope Science Institute, Baltimore, Maryland, October 17 and 18, 2002. Edited by Santiago Arribas, Anton Koekemoer, and Brad Whitmore. Baltimore, MD: Space Telescope Science Institute, 2002., p.337, 337

[Krist(1995)] Krist, J. 1995, ASP Conf. Ser. 77: Astronomical Data Analysis Software and Systems IV, 77, 349

[Krist(2003)] J. Krist, *ACS WFC & HRC field-dependent PSF variations due to optical and charge diffusion effects*, HST Instrument Science Report ACS 2003-06, Baltimore, MD: Space Telescope Science Institute (2003)

[Lucy(1974)] Lucy, L. B. 1974, AJ, 79, 745

[Mardling(1995a)] Mardling, R. A. 1995, ApJ, 450, 722

[Mardling(1995b)] Mardling, R. A. 1995, ApJ, 450, 732

[Maeder(1989)] Maeder, A. 1989, ASSL Vol. 157: IAU Colloq. 113: Physics of Luminous Blue Variables, 15

[Meurer et al. (2002)] Meurer G.R., Lindler, D., Blakeslee, J. P., Cos, C., Martel, A. R., Tran, H. D., Bouwens, R. J., Ford, H. C. *et al.*, 2002, The 2002 HST Calibration Workshop : Hubble after the Installation of the ACS and the NICMOS Cooling System, Proceedings of a Workshop held at the Space Telescope Science Institute, Baltimore, Maryland, October 17 and 18, 2002. Edited by Santiago Arribas, Anton Koekemoer, and Brad Whitmore. Baltimore, MD: Space Telescope Science Institute, 2002., p.65

[Monet et al.(2003)] Monet, D. G., et al. 2003, AJ, 125, 984

[Morse et al.(1998)] Morse, J. A., Davidson, K., Bally, J., Ebbets, D., Balick, B., & Frank, A. 1998, AJ, 116, 2443

[Morse et al.(2001)] Morse, J. A., Kellogg, J. R., Bally, J., Davidson, K., Balick, B., & Ebbets, D. 2001, ApJL, 548, L207

[Pavlovsky et al. (2005)] C. Pavlovsky *et al.*, *ACS Data Handbook*, v 4.0, Baltimore, MD: Space Telescope Science Institute (2005)

[Perryman et al.(1997)] Perryman, M. A. C., et al. 1997, AAP, 323, L49

[Pittard & Corcoran(2002)] Pittard, J. M., & Corcoran, M. F. 2002, A&A, 383, 636

[Pliny the Younger (c. 100 AD)] Plinius, G. c. 100 AD, *Epistulae*, VI,16

[Pourbaix (2005)] Pourbaix, D. 2005, Presentation at Michelson Summer Workshop

[Press & Teukolsky(1977)] Press, W. H., & Teukolsky, S. A. 1977, ApJ, 213, 183

[Regös et al.(2005)] Regös, E., Bailey, V. C., & Mardling, R. 2005, MNRAS, 358, 544

[Richardson(1972)] Richardson, W. H. 1972, Optical Society of America Journal A, 62, 55

[Ringuelet(1958)] Ringuelet, A. E. 1958, Zeitschrift fur Astrophysik, 46, 276

[Rose(1998)] Rose, W. K. 1998, Advanced Stellar Astrophysics, by William K. Rose, pp. 494. ISBN 0521581885. Cambridge, UK: Cambridge University Press, May 1998.,

[Sepinsky et al.(2007)] Sepinsky, J. F., Willems, B., & Kalogera, V. 2007, ApJ, 660, 1624

[Soker(2005)] Soker, N. 2005, ApJ, 619, 1064

[Smith & Gehrz(1998)] Smith, N., & Gehrz, R. D. 1998, AJ, 116, 823

[Smith et al.(2000)] Smith, N., Morse, J. A., Davidson, K., & Humphreys, R. M. 2000, AJ, 120, 920

[Smith(2002)] Smith, N. 2002, MNRAS, 337, 1252

[Smith et al.(2003)] Smith, N., Gehrz, R. D., Hinz, P. M., Hoffmann, W. F., Hora, J. L., Mamajek, E. E., & Meyer, M. R. 2003, AJ, 125, 1458

[Smith et al.(2004)] Smith, N., Morse, J. A., Collins, N. R., & Gull, T. R. 2004, ApJL, 610, L105

[Smith(2006)] Smith, N. 2006, ApJ, 644, 1151

[Tapia et al.(1988)] Tapia, M., Roth, M., Marraco, H., & Ruiz, M. T. 1988, MNRAS, 232, 661

[Taylor(1997)] Taylor, J. 1997, “Introduction to Error Analysis, the Study of Uncertainties in Physical Measurements, 2nd Edition,” Published by University Science Books, 648 Broadway, Suite 902, New York, NY 10012, 1997.,

[van Genderen & The(1984)] van Genderen, A. M., & The, P. S. 1984, Space Science Reviews, 39, 317

[van Genderen et al.(1994)] van Genderen, A. M., de Groot, M. J. H., & The, P. S. 1994, A&A, 283, 89

[van Genderen et al.(2001)] van Genderen, A. M., de Groot, M., & Sterken, C. 2001, ASP Conf. Ser. 233: P Cygni 2000: 400 Years of Progress, 233, 59

[Verner et al.(2005)] Verner, E., Bruhweiler, F., & Gull, T. 2005, ApJ, 624, 973

[Walborn et al.(1978)] Walborn, N. R., Blanco, B. M., & Thackeray, A. D. 1978, ApJ, 219, 498

[Walborn(1995)] Walborn, N. R. 1995, Revista Mexicana de Astronomia y Astrofisica Conference Series, 2, 51

[Weis et al.(1999)] Weis, K., Duschl, W. J., & Chu, Y.-H. 1999, A&A, 349, 467

[Wolf(1989)] Wolf, B. 1989, A&A, 217, 87

[Zacharias(2003)] Zacharias, N. 2003, The Future of Small Telescopes In The New Millennium. Volume II - The Telescopes We Use, 67

[Zacharias et al.(2004)] Zacharias, N., Monet, D. G., Levine, S. E., Urban, S. E., Gaume, R., & Wycoff, G. L. 2004, American Astronomical Society Meeting Abstracts, 205,

[Zacharias (2006)] Zacharias, N. 2006, private communication

[Zahn(1977)] Zahn, J.-P. 1977, A&A, 57, 383